

CONTROL OF FRICTION BY IMPOSING VIBRATION
BETWEEN SLIDING SURFACES AND ITS INFLUENCE ON
THE EFFICIENCY OF GEARS

PRIYANG UDAYKANT JADAV

A thesis submitted in partial fulfilment of the requirements of the
University of the West of England, Bristol
for the degree of Doctor of Philosophy

Faculty of Environment and Technology,
University of the West of England, Bristol

September 2022



Abstract

The worm and wheel type gear arrangement is the usual choice for heavy duty applications requiring large operating torques. However, it is dominated by the sliding action of gear teeth which causes high frictional losses that significantly impact efficiency. The use of vibration is investigated as a method of reducing the frictional losses in worm gearing.

Pre-existing mathematical models that describe the mechanism of friction reduction due to in-plane vibration are further developed and executed analytically. Comparable results of friction reduction are obtained when the models are implemented into 3D finite element simulations of a sliding mass driven across a vibrating surface. The 3D numerical simulations are extended to evaluate the effect of vibration on friction in a worm gearset operating under load. Axial sinusoidal vibration applied to the worm enables an 80% reduction of input torque to generate the same output torque. This constitutes a five-fold increase in gearset mechanical advantage but a drop in overall system efficiency due to electrical power consumed to generate the vibration. The extent of input torque reduction is governed by the ratio of vibration velocity amplitude to the contact sliding velocity of the gearset.

Vibration experiments are conducted using a custom disc-on-disc friction test rig representing a contact similar to that of worm gearing. Test variables include lubricant type, vibration mode, vibration waveform, vibration frequency and sliding speed. In extension to previous studies that have investigated vibration-friction interactions only under dry pure-sliding conditions, disc-on-disc vibration experiments demonstrate presence of the friction reduction effect also under lubricated sliding-rolling conditions. Sinusoidal wave vibration produces greater friction reduction than triangular, and contrary to previous studies, transverse vibration experiments produce greater friction reduction than longitudinal.

As friction is intrinsic to the mechanics of everyday life, this research has relevance to any application seeking to reduce this dissipative contact force. In particular, this research shows that friction in lubricated sliding-rolling contact can be reduced by imposing vibration. In worm gearing this improves the mechanical advantage but impacts the overall system efficiency. This is not considered a problem if vibration can be temporarily activated for a momentary boost in mechanical advantage when it is most needed.

Contents

List of Figures.....	viii
List of Tables.....	xv
Acknowledgements.....	xvii
Abbreviations	xviii
Notations	xix

Chapter 1

Introduction	1
1.1. Motivation for Research	2
1.2. Aim and Objectives	3
1.3. Research Questions	4
1.4. Research Methodology	4
1.4.1. Research Philosophy	4
1.4.2. Research Type	5
1.4.3. Research Methods and Tools	5
1.4.4. Data Analysis Methods	5
1.5. Overview of Chapters	10

Chapter 2

Literature Review	12
2.1. Chapter Introduction	13
2.1.1. Types of Gears	13
2.1.2. Gear Terminology	14
2.1.3. Gear Ratio and Efficiency	18
2.1.4. History of Worm Gearing	19
2.1.5. Self-Locking Capability of Worm Gearing	19
2.1.6. Losses in a Worm Gearbox	20
2.2. Friction	21
2.2.1. Introduction to Friction	21
2.2.2. Contact Compliance	22
2.3. Lubrication	24

2.3.1.	Lubrication Regimes	24
2.3.2.	Mineral vs. Synthetic Oils	25
2.3.3.	Nanoparticles in Oil Lubricants	27
2.4.	Worm Gearing Materials	27
2.5.	Surface Coatings	29
2.6.	Gear Design Optimisation	31
2.7.	Imposed Vibration	34
2.7.1.	Normal Vibration	35
2.7.2.	Longitudinal Vibration	35
2.7.3.	Transverse vibration	37
2.7.4.	Practical applications of vibration	39
2.8.	Chapter Discussion and Conclusions	41

Chapter 3

Worm Gearing and Efficiency **43**

3.1.	Chapter Introduction	44
3.2.	Efficiency Sensitivity Analysis	44
3.2.1.	Worm Gearing Design Considerations	46
3.2.2.	Influence of Friction Reduction Method on Efficiency	48
3.2.3.	Influence of Worm Gearing Parameters on Efficiency	50
3.3.	Design Optimisation	52
3.3.1.	Permissible Torque	52
3.3.2.	Bending Stress	53
3.3.3.	Contact Stress	53
3.3.4.	Benchmark Worm Gearset Efficiency and Load Capacity	54
3.3.5.	Optimised Worm Gearset Efficiency and Load Capacity	56
3.4.	Chapter Discussion and Conclusions	60

Chapter 4

Analytical Friction Model with Vibration **61**

4.1.	Chapter Introduction	62
4.2.	Friction Model for Longitudinal Vibration	62
4.2.1.	Analytical Model Comprising Coulomb Friction	63
4.2.2.	Analytical Model Comprising Dahl Friction	64

4.2.3.	Analytical Simulations & Results	66
4.3.	Friction Model for Longitudinal Vibration with Drive Compliance	68
4.3.1.	Determination of Mechanical Drive Stiffness	71
4.4.	Friction Model for Transverse Vibration with Drive Compliance	72
4.5.	Friction Model for Coupled Longitudinal-Transverse Vibration	78
4.5.1.	First Phase of Motion	80
4.5.2.	Second Phase of Motion	82
4.5.3.	Consecutive Time Increments	83
4.5.4.	Model Validation for Longitudinal Mode	86
4.5.5.	Model Validation for Transverse Mode	89
4.5.6.	Results for Coupled Vibration Modes	91
4.6.	Chapter Discussion and Conclusions	93

Chapter 5

Numerical Simulation of Friction Model with Vibration **94**

5.1.	Chapter Introduction	95
5.2.	Introduction to Finite Element Contact Interactions	95
5.2.1.	Discretisation of Contact Pair Surfaces	95
5.2.2.	Contact Tracking Approaches	97
5.2.3.	Contact Normal Behaviour	97
5.2.4.	Friction Subroutine for Contact Tangential Behaviour	98
5.3.	Finite Element Simulations for Coupled Vibration	98
5.3.1.	Simulation Methodology	99
5.3.2.	Simulation Validation for Longitudinal Mode	100
5.3.3.	Simulation Validation for Transverse Mode	102
5.3.4.	Results for Coupled Vibration Modes	104
5.3.5.	Limitations of Modelling and Error Mitigation	105
5.4.	Chapter Discussion and Conclusions	106

Chapter 6

Experiments **107**

6.1.	Chapter Introduction	108
6.2.	The Need for a Custom Test Rig	108
6.3.	Preliminary Testing	109

6.3.1.	Features of the Preliminary Disc-on-Disc Test Rig	109
6.3.2.	Purpose of Preliminary Tests	112
6.3.3.	Surface Roughness Measurement	112
6.3.4.	Dry Sliding-Rolling Test and Results	115
6.3.5.	Greased Sliding-Rolling Test and Results	119
6.3.6.	Summary and Learning Outcomes	122
6.4.	Experimental Investigation	123
6.4.1.	Features of the Final Disc-on-Disc Test Rig	123
6.4.2.	Vibration Mode, Frequency, and Waveform	132
6.4.3.	Sonotrode Preload Selection	133
6.4.4.	Sonotrode Travel Range	134
6.4.5.	Noise Isolation	136
6.4.6.	Surface Roughness	137
6.4.7.	Sliding Velocity	139
6.4.8.	Normal Load Selection	139
6.4.9.	Lubricant Selection	140
6.4.10.	Test Matrix	141
6.4.11.	Data Capture	142
6.4.12.	Test Procedure	143
6.4.13.	Limitations of Experiments and Error Mitigation	145
6.5.	Transverse Vibration Test Results	146
6.5.1.	Torque Reduction due to Transverse Vibration	146
6.5.2.	Correlation of Torque Reduction with Accelerometer Data	150
6.5.3.	Normalised Torque vs. Previous Simulation	151
6.5.4.	Power loss Reduction due to Transverse Vibration	152
6.5.5.	Efficiency Improvement due to Transverse Vibration	152
6.6.	Longitudinal Vibration Test Results	157
6.6.1.	Torque Reduction due to Longitudinal Vibration	157
6.6.2.	Correlation of Torque Reduction with Accelerometer Data	160
6.6.3.	Normalised Torque vs. Previous Simulation	161
6.6.4.	Power loss Reduction due to Longitudinal Vibration	162
6.6.5.	Efficiency Improvement due to Longitudinal Vibration	162
6.7.	Wear Life Consideration	167
6.8.	Chapter Discussion and Conclusions	168

Chapter 7	
Worm and Wheel Simulation	170
7.1. Chapter Introduction	171
7.2. Worm Gearing Simulation Methodology	171
7.2.1. Geometry and Topology Adjustment	172
7.2.2. Simulation Domain	174
7.2.3. Simulation Steps and Boundary Conditions	176
7.2.4. Simulation Sets	177
7.3. Friction Model and Subroutine Modification	180
7.3.1. First Phase of Motion	181
7.3.2. Second Phase of Motion	182
7.3.3. Partial Derivatives	183
7.3.4. Consecutive Time Increments	188
7.3.5. Subroutine Validation	189
7.4. Worm Gearing Simulation Results	190
7.4.1. Comparison of Simulated vs. Theoretical Efficiency	190
7.4.2. Mesh Density and Element Types	191
7.4.3. Effect of Vibration on Input Torque	193
7.4.4. Coulomb Model Comparison	194
7.4.5. Effect of Vibration on Mechanical Advantage	195
7.4.6. Effect of Vibration on Efficiency	196
7.4.7. Limitations of Modelling and Error Mitigation	197
7.5. Chapter Discussion and Conclusions	199
Chapter 8	
Conclusions and Future Work	200
8.1. Overall Conclusions	201
8.2. Recommendations for Future Work	204
Bibliography	206

Appendices	221
Appendix A: Journal Article	222
Appendix B: Conference Article	231
Appendix C: Theoretical Calculations of Worm Gearsets	233
Appendix D: Abaqus® Friction Subroutine for Chapter 5	246
Appendix E: Abaqus® Friction Subroutine for Chapter 7.....	249

List of Figures

Figure 1.1: Worm gearing inside an actuator designed for operating valves (Rotork PLC, 2020).	2
Figure 2.1: Illustrations of common gear types classified by their shaft axes arrangement (a) parallel axis, spur gear external (b) intersecting axes, straight bevel gear (c) non-parallel and non-intersecting axes, worm gear.	14
Figure 2.2: Schematic of spur gear teeth with key terminology that applies also to wheel gear teeth (Budynas and Nisbett, 2011).	17
Figure 2.3: Schematic of worm gear teeth with key terminology (Radzevich, 2012).	17
Figure 2.4: Schematic of worm and wheel gear pair with key terminology (Budynas and Nisbett, 2011).	18
Figure 2.5: Coulomb friction schematic of body driven at constant velocity \mathbf{vd} over base surface.	22
Figure 2.6: Dahl (1968; 1976) friction schematic of body driven at constant velocity \mathbf{vd} over base surface. Elastic contact deformation \mathbf{s} and contact stiffness kt of lumped elastic asperity MN .	23
Figure 2.7: Influence of i on relationship between \mathbf{F} and \mathbf{x} during elastic slip phase, from $i = 0$ brittle material behaviour to $i = 2$ ductile material behaviour.	24
Figure 2.8: Schematic of the disc-on-disc test configuration of Fontanari <i>et al.</i> (2013). Steel 42CrMo4V disc loaded against dip lubricated bronze CuSn12 disc.	28
Figure 2.9: Comparison of stress distribution of original design against optimised geometry, (a) lead angle correction, (b) tip relief correction (Mao, 2007).	31
Figure 2.10: Formation of contact on worm (top) and wheel (bottom), (a) no misalignment, (b) with misalignment, (c) modified geometry (Litvin <i>et al.</i> , 2007).	32
Figure 2.11: Mesh checking of a worm gearset manufactured to BS 721 (British Standards Institution, 1983). (a) worm with blue dye driven against wheel, (b) blue dye transfer from worm to wheel demonstrates edge contact, (c) centre contact achieved by modified hobbing method of applying 2° tilt angle to cutting hob.	33
Figure 2.12: Contact points near the wheel addendum at low torque (left) and high torque (right) in EPS worm gearing (Watanabe, Shimizu and Terada, 2006).	34

Figure 2.13: EPS worm profile modification between its pitch line and outer diameter (Watanabe, Shimizu and Terada, 2006).	34
Figure 2.14: Time characteristics of Coulomb friction force during longitudinal vibration. Recreated from Kumar and Hutchings (2004).	36
Figure 2.15: Time characteristics of Dahl friction force during longitudinal vibration. $f = 4000$ Hz, $va = 0.75$ mm/s $>$ $vd = 0.5$ mm/s. Gutowski and Leus (2012).	37
Figure 2.16: Friction force during transverse vibration (a) vibration velocity vb is perpendicular to drive direction vd (b) top-down view of instantaneous forces acting on sliding body. FC opposes direction of relative velocity vr which deviates from direction of vd .	38
Figure 2.17: Friction force influencers.	42
Figure 3.1: Influence of friction reduction method on calculated worm gearing efficiency η_{z1-2} .	50
Figure 3.2: Graph showing influence of worm gearing parameters on calculated efficiency η_{z1-2} .	51
Figure 3.3: Coefficient of friction comparison between two different worm gearing standards.	56
Figure 3.4: Graphical comparison of benchmark vs. optimised η_{z1-2} and η_{AGMA} of four gearsets.	59
Figure 3.5: Graphical comparison of benchmark vs. optimised $M26k$, Mw , Ms and TG , all of four gearsets.	59
Figure 4.1: Simulink [®] longitudinal vibration model using Coulomb friction.	64
Figure 4.2: Simulink [®] longitudinal vibration model using Dahl friction.	66
Figure 4.3: Simulink [®] longitudinal vibration results, $va < x$.	67
Figure 4.4: Simulink [®] longitudinal vibration results, $va > x$.	68
Figure 4.5: Photo of experimental rig developed by Gutowski and Leus (2012) for longitudinal vibration investigation. 1: body, 2: base, 3: vibration exciter, 4: ring dynamometer, 5: fixed foundation, 6: constant velocity driver, 7-9: accelerometers.	69
Figure 4.6: Extension of Figure 2.6 to represent the longitudinal vibration experimental setup of Gutowski and Leus (2012). Structural stiffness kd and damping hd due to the drive system are also now included.	69

Figure 4.7: Simulink® longitudinal vibration model incorporating Dahl friction and drive compliance, based on Gutowski and Leus (2012).	70
Figure 4.8: Simulink® longitudinal vibration results by Gutowski and Leus (2012) at $f = 4000$ Hz, $va = 3 \cdot 10^{-3}$ m/s $>$ $vd = 0.5 \cdot 10^{-3}$ m/s.	71
Figure 4.9: Schematic of transverse vibration experimental setup of Gutowski and Leus (2015). Similar to Figure 4.6 except vibrating motion yb acts perpendicular to the direction of vd , causing change in magnitude and direction β of elastic deformation s .	73
Figure 4.10: Instantaneous forces acting on sliding body (Gutowski and Leus, 2015). Friction force F is sub-divided into two components, one parallel (Fx) and one perpendicular (Fy) to the direction of Fd .	73
Figure 4.11: Changes in magnitude and direction of elastic deformation s at consecutive phases of motion (Gutowski and Leus, 2015).	74
Figure 4.12: Simulink® transverse vibration model incorporating Dahl friction and drive compliance, based on Gutowski and Leus (2015).	77
Figure 4.13: Schematic of coupled longitudinal-transverse vibration. Combination of Figure 4.6 and Figure 4.9 such that vibrating motions xb and yb act simultaneously and in phase.	78
Figure 4.14: Instantaneous displacement vector of base vibrating along an axis at angle θ , separated into components xb and yb .	79
Figure 4.15. Change in magnitude and direction of deformation from s to $s1$ during a time increment Δt , due to incremental coupled base displacements Δxb and Δyb during sliding motion.	80
Figure 4.16: Simulink® friction model of coupled vibration incorporating Dahl friction and drive compliance.	85
Figure 4.17: Comparison of change in $FdvFds$ with kv , longitudinal vibration.	87
Figure 4.18: Comparison of time varying Fd at $kv = 6$, longitudinal vibration.	88
Figure 4.19: Comparison of time varying Fx at $kv = 6$, longitudinal vibration.	88
Figure 4.20: Comparison of change in $FdvFds$ with kv , transverse vibration.	90
Figure 4.21: Comparison of time varying Fd at $kv = 20$, transverse vibration.	90
Figure 4.22: Comparison of time varying Fx and Fy at $kv = 20$, transverse vibration.	91
Figure 4.23: Changes in $FdvFds$ with θ at selected values of kv .	92

Figure 5.1: Node-to-surface contact discretisation (Abaqus [®] , 2014c). Each slave node on the slave surface interacts with a point of projection normal to the master surface.	96
Figure 5.2: Contact pressure accuracy comparison of node-to-surface vs. surface-to-surface contact discretisation (Abaqus [®] , 2014c).	97
Figure 5.3: Comparison of linear vs. nonlinear pressure-overclosure relationship (Abaqus [®] , 2014d).	98
Figure 5.4: FEA simulation domain for coupled longitudinal-transverse vibration.	99
Figure 5.5: Change in $FdvFds$ with kv , longitudinal vibration. Abaqus [®] numerical results superimposed.	101
Figure 5.6: Comparison of time varying Fd at $kv = 6$, longitudinal vibration. Abaqus [®] numerical results superimposed.	101
Figure 5.7: Comparison of time varying Fx at $kv = 6$, longitudinal vibration. Abaqus [®] numerical results superimposed.	102
Figure 5.8: Comparison of change in $FdvFds$ with kv , transverse vibration. Abaqus [®] numerical results superimposed.	103
Figure 5.9: Comparison of time varying Fd at $kv = 20$, transverse vibration. Abaqus [®] numerical results superimposed.	103
Figure 5.10: Comparison of time varying Fx and Fy at $kv = 20$, transverse vibration. Abaqus [®] numerical results superimposed.	104
Figure 5.11: Changes in $FdvFds$ with θ at selected values of kv . Abaqus [®] numerical results superimposed.	105
Figure 6.1: Preliminary test rig.	110
Figure 6.2: Schematic of discs in preliminary test rig. Disc rotational speeds Ss and Sa are selected such that peripheral velocity vps exceeds vpa , thus the steel disc generates driving force Fa on the aluminium-bronze disc, and an opposite friction force FC acts on the steel disc.	111
Figure 6.3: Sectioned CAD image of disc and shaft subassemblies in preliminary rig.	112
Figure 6.4: Mean line (blue) of surface roughness profile.	113
Figure 6.5: Aluminium-bronze disc circumferential surface roughness measurement.	113
Figure 6.6: Aluminium-bronze disc lateral surface roughness measurement.	114
Figure 6.7: Pick-up on aluminium-bronze surface, comprising a diamond stylus transducer supported on the measuring surface by a pink skid.	114

LIST OF FIGURES

Figure 6.8: Graph showing effect of <i>FN</i> on <i>Ss</i> , <i>Sa</i> , <i>ims</i> and <i>ima</i> . Dry contact.	117
Figure 6.9: Graph showing effect of <i>FN</i> on <i>vsl</i> , <i>vro</i> and <i>R</i> . Dry contact.	117
Figure 6.10: Material transfer of aluminium-bronze onto steel disc during dry sliding-rolling test.	118
Figure 6.11: Graphs showing effect of <i>FN</i> on <i>Ts</i> and <i>Ta</i> . Dry contact.	118
Figure 6.12: Graph showing effect of <i>FN</i> on <i>Ss</i> , <i>Sa</i> , <i>ims</i> and <i>ima</i> . Greased contact.	120
Figure 6.13: Graph showing effect of <i>FN</i> on <i>vsl</i> , <i>vro</i> and <i>R</i> . Greased contact.	121
Figure 6.14: Graph showing effect of <i>FN</i> on <i>Ts</i> and <i>Ta</i> . Greased contact.	121
Figure 6.15: Photograph of disc-on-disc rig configured for transverse vibration.	124
Figure 6.16: Sectioned CAD image of rig in transverse vibration configuration.	125
Figure 6.17: Sectioned CAD image of disc and shaft subassemblies in transverse vibration configuration.	126
Figure 6.18: Sectioned CAD image of sonotrode.	127
Figure 6.19: Physik Instrumente piezo actuator model P-887.91.	128
Figure 6.20: Photograph of ancillary equipment for disc-on-disc rig.	129
Figure 6.21: Test rig equipment interface map.	130
Figure 6.22: Sectioned CAD image of disc-on-disc rig configured for longitudinal vibration.	131
Figure 6.23: Sectioned CAD image of disc and shaft subassemblies in longitudinal vibration configuration.	132
Figure 6.24: Vibration waveforms at $f = 750$ Hz, $ua = 0.016$ mm (a) sinusoidal (b) triangular.	133
Figure 6.25: PuTTY command terminal for vibration control.	133
Figure 6.26: Setup for measuring voltage output <i>Vl</i> from load cell at different loads.	134
Figure 6.27: Graph of measured voltage output <i>Vl</i> from load cell at different loads.	134
Figure 6.28: Sonotrode displacement response to steady voltage measured with clock dial displacement transducer clamped to magnetic stand. Sonotrode detached from rig.	135
Figure 6.29: Sonotrode displacement response to steady voltage measured with clock dial displacement transducer clamped to magnetic stand. Sonotrode attached to rig.	136
Figure 6.30: Noise isolation box.	137
Figure 6.31: Schematic showing dip lubrication of aluminium-bronze disc, peripheral disc velocities and normal load.	141

Figure 6.32: Effect of f on Ts . Transverse sinusoidal vibration, greased contact.	147
Figure 6.33: Effect of f on Ts . Transverse sinusoidal vibration, oil dip lubrication.	148
Figure 6.34: Effect of f on Ts . Transverse triangular vibration, oil dip lubrication.	149
Figure 6.35: Accelerometer position for transverse vibration measurements.	150
Figure 6.36: Influence of va on Ts reduction at applied transverse test frequencies.	151
Figure 6.37: Disc-on-disc transverse vibration test, change in $TsvTss$ with kv .	152
Figure 6.38: Effect of f on $Ploss_s$. Transverse sinusoidal vibration, oil dip lubrication.	153
Figure 6.39: Effect of f on $Ploss_s$. Transverse triangular vibration, oil dip lubrication.	154
Figure 6.40: Effect of f on $\Delta\eta_s$. Transverse sinusoidal vibration, oil dip lubrication.	155
Figure 6.41: Effect of f on $\Delta\eta_s$. Transverse triangular vibration, oil dip lubrication.	156
Figure 6.42: Effect of f on Ts . Longitudinal sinusoidal vibration, oil dip lubrication.	158
Figure 6.43: Effect of f on Ts . Longitudinal triangular vibration, oil dip lubrication.	159
Figure 6.44: Accelerometer position for longitudinal vibration measurements.	160
Figure 6.45: Influence of va on Ts reduction at applied longitudinal test frequencies.	161
Figure 6.46: Disc-on-disc longitudinal vibration test, change in $TsvTss$ with kv .	162
Figure 6.47: Effect of f on $Ploss_s$. Longitudinal sinusoidal vibration, oil dip lubrication.	163
Figure 6.48: Effect of f on $Ploss_s$. Longitudinal triangular vibration, oil dip lubrication.	164
Figure 6.49: Effect of f on $\Delta\eta_s$. Longitudinal sinusoidal vibration, oil dip lubrication.	165
Figure 6.50: Effect of f on $\Delta\eta_s$. Longitudinal triangular vibration, oil dip lubrication.	166
Figure 6.51: Comparison of transverse and longitudinal disc-on-disc normalised torque results. Superimposition of Figure 6.37 and Figure 6.46.	169
Figure 7.1: CAD model of worm gearset 3. Facets on tooth flanks of wheel gear caused by machining simulation.	172
Figure 7.2: CAD model of worm gearset 3 simplified for import into Abaqus®.	173
Figure 7.3: Worm gear as analytical rigid shell in Abaqus®.	173
Figure 7.4: Wheel gear tooth topology adjustment and mesh in Abaqus®.	174
Figure 7.5: Inside faces of wheel teeth constrained to centre point of wheel gear.	175

Figure 7.6: Worm and wheel finite element mesh with torsional stiffness AB .	175
Figure 7.7: Change in magnitude and direction of deformation from \mathbf{s} to $\mathbf{s1}$ during a time increment Δt , due to incremental displacements $\Delta \mathbf{x}$ and $\Delta \mathbf{y}$ as vibration is applied directly to the sliding body during sliding motion.	180
Figure 7.8: Comparison of change in $FdvFds$ with kv , new direct vibration friction model transverse results superimposed.	189
Figure 7.9: Comparison of change in $FdvFds$ with kv , new direct vibration friction model longitudinal results superimposed.	190
Figure 7.10: Input torque profile TB for simulation reference 33 in Table 7.2, per simulation steps in 7.2.3.	191
Figure 7.11: Worm gearing mesh densities a) coarse b) intermediate c) fine.	191
Figure 7.12: Change in $TBvTBs$ with kw for simulation set 3 at different mesh densities.	193
Figure 7.13: Comparison of change in $TBvTBs$ with kw for simulation set 1 and 2.	194
Figure 7.14: Change in $TBvTBs$ with kw , simulation set 3. Comparison of direct vibration friction model vs. Coulomb friction.	195
Figure 7.15: (a) Simulated influence of kw on $TBvTBs$, Ma and η_{sys} of a worm gearset compared to (b) empirical influence of kv on $TsvTss$ in disc-on-disc experiments.	196

List of Tables

Table 1.1: Research methods, tools and data analysis methods employed to address the research objectives and research questions, and their alignment with thesis chapters.	9
Table 2.1: Gear terms and their descriptions.	16
Table 2.2: Gear ratio and efficiency ranges of common gear types (Gonzalez, 2015; Designatronics Inc., 2020).	19
Table 3.1: Explanation of Appendix C efficiency and load capacity calculation spreadsheet.	45
Table 3.2: Input variables (green) and formulated values (grey) for efficiency calculation of worm gearset 2.	47
Table 3.3: Values of μ , v_{40} and v_{100} for efficiency comparison of different friction reduction methods. Input variables (green) and formulated values (grey).	49
Table 3.4: Summary of influence of worm gearing parameters on calculated efficiency $\eta_{z1} - 2$.	51
Table 3.5: Comparison of calculated benchmark efficiency and load capacity of four gearsets.	55
Table 3.6: Parametric constraints applied for worm gearset design optimisation.	57
Table 3.7: Comparison of optimised efficiency and load capacity of four gearsets.	58
Table 4.1: List of Simulink [®] basic longitudinal vibration simulations and input values.	66
Table 4.2: State-dependant variables for coupled vibration model of friction.	84
Table 4.3: Input values for comparison of pre-existing longitudinal vibration model with new coupled model.	86
Table 4.4: Input values for comparison of pre-existing transverse model with new coupled model.	89
Table 5.1: Abaqus [®] simulation steps for analysis of two planar contact surfaces.	100
Table 6.1: Circumferential surface Ra readings of discs for preliminary test rig.	115
Table 6.2: Lateral surface Ra readings of discs for preliminary test rig.	115
Table 6.3: Table of results for preliminary dry sliding-rolling tests, plotted in Figure 6.8 and Figure 6.9.	116
Table 6.4: Properties of Hydralube WIC Medium Compound grease.	119

Table 6.5: Table of results for preliminary greased sliding-rolling tests, plotted in Figure 6.12 and Figure 6.13.	120
Table 6.6: Circumferential surface Ra readings of discs, final rig.	138
Table 6.7: Lateral surface Ra readings of discs, final rig.	138
Table 6.8: Parameters used for calculation of Hertzian contact pressure.	140
Table 6.9: Properties of Fuchs Titan Gear MP SAE 80 mineral oil (Fuchs, 2011).	141
Table 6.10: Test matrix.	142
Table 6.11: Test data for steel disc at 750 Hz transverse sinusoidal vibration, oil lubrication, $V_{ms} = 1$ V.	143
Table 6.12: Effect of longitudinal vibration on weight loss of steel and aluminium-bronze discs.	167
Table 7.1: Sequential steps and boundary conditions for worm gearing numerical simulation with vibration applied.	177
Table 7.2: Conditions for vibration simulations of gearset 3.	179
Table 7.3: State-dependant variables for modified friction model.	188
Table 7.4: Worm gear and wheel gear global element sizes for the three simulated mesh densities.	192

Acknowledgements

I would like to thank my supervisors Dr. Ramin Amali and Dr. Oluwamayokun Adetoro for their guidance, constructive feedback, and support throughout this research.

I would also like to thank my colleagues at Rotork who have provided valuable input when needed; Kevin Sweet, Dr. Mike Evans, Ester Dunstan-Sewell, Simon Truelove, and Harry Willis.

Last but not the least, I would like to thank my family who have supported me immensely during this journey, especially my wife Rima and boys Hridan and Hriyan, whose love has driven me throughout. Their patience has enabled me to see this through to the end.

Abbreviations

ADI	Austempered ductile iron
AGMA	American Gear Manufacturers Association
AW	Anti-wear
B ₄ C	Boron carbide
CAD	Computer aided design
CCr	Carbon chromium
DLC	Diamond-like-carbon
EHL	Elastohydrodynamic lubrication
EP	Extreme pressure
EPS	Electronic power steering
FEA	Finite element analysis
Fe ₃ O ₄	Iron oxide
FZG	Forschungsstelle für Zahnräder und Getriebebau. English translation; Institute of Machine Elements - Gear Research Centre.
MEMS	Micro electro-mechanical systems
MoS ₂	Molybdenum disulphide
MoS ₂ /Ti	Molybdenum disulphide co-deposited with titanium
N/A	Not applicable
RPM	Revolutions per minute
TiAlN	Titanium aluminium nitride
TiN	Titanium nitride
TiO ₂	Titanium dioxide
VPN	Vickers pyramid number
WCC	Tungsten carbide carbon

Notations

Vector notations are signified by bold symbols. Units listed in the table below apply unless otherwise specified.

Symbol	Description	Unit
a	Peak acceleration of vibration of object	mm/s ²
A	Point attached to the sliding body	
A_r	Contact area	m ²
b	Hertzian contact area half-width	mm
B	Point at which constant drive velocity is applied	
c	Centre distance of gear pair	mm
d	Diameter of worm shaft	mm
d_a	Diameter of aluminium-bronze disc test specimen	mm
d_s	Diameter of steel disc test specimen	mm
D	Thickness of disc test specimen	mm
E_a	Modulus of elasticity of aluminium-bronze	N/mm ²
E_s	Modulus of elasticity of steel	N/mm ²
f	Vibration frequency applied to object in contact	Hz
F	Dahl friction force	N
F_a	Driving force on aluminium-bronze disc caused by the steel disc	N
F_c	Coulomb friction force	N
F_d	General term for applied drive force. Could be either F_{dv} or F_{ds}	N
F_{ds}	Signifies F_d in the absence of vibration	N
F_{dv}	Signifies F_d in the presence of vibration	N
F_g	Gravitational force due to mass of sliding body	N
F_N	Normal force	N
F_x	Component of Dahl friction force F acting parallel to axis X	N
F_y	Component of Dahl friction force F acting parallel to axis Y	N
F_z	Downward force due to pressure p	N
G_s	Modulus of rigidity of steel	N/mm ²
h_d	Structural damping coefficient of mechanical drive system	Ns/m
i	Shape parameter	

NOTATIONS

Symbol	Description	Unit
i_{ma}	Current drawn by motor driving the aluminium-bronze disc	amps
i_{ms}	Current drawn by motor driving the steel disc	amps
i_p	Current drawn by sonotrode	amps
k_d	Structural linear stiffness of mechanical drive system	N/m
k_D	Torsional stiffness of worm shaft	Nm/rad
k_t	Tangential contact stiffness	N/m
k_v	Dimensionless coefficient equal to v_a/v_d	
k_w	Dimensionless coefficient equal to v_a/v_g	
l	Length of worm shaft	mm
m	Mass of sliding object	kg
m_{min}	Minimum axial module	mm
m_{max}	Maximum axial module	mm
m_r	Mass of rig platform subassembly acting on disc-disc contact	kg
m_w	Dead mass	kg
m_{x1}	Axial module	mm
M	Endpoint of elastic asperity that freely interfaces with the base	
M_a	Mechanical advantage of gearing	
M_s	Permissible application-based wheel torque for strength, BS 721	Nm
M_w	Permissible application-based wheel torque for wear, BS 721	Nm
M_1	Calculated position of M at end of time increment	
M_{26k}	Permissible wheel torque for 26,000 hours life, per BS 721	Nm
n	Number of time intervals in a single vibration cycle	
n_1	Worm speed	RPM
n_2	Wheel speed	RPM
N	Endpoint of elastic asperity that is attached to the sliding body	
N'	Projection of endpoint N onto the XY plane	
N''	Calculated intermediated position of N' during time increment	
N'_1	Calculated final position of N' at end of time increment	
p	Pressure normal to contact	N/m ²
p_{max}	Maximum Hertzian contact pressure	N/mm ²
P_{loss_s}	Power loss due to frictional losses in steel disc drive	W
q_1	Diameter factor	

NOTATIONS

Symbol	Description	Unit
R	Slide-roll ratio of two discs	
Ra_1	Arithmetic mean surface roughness	μm
s	Contact's elastic deformation parallel to the sliding direction	m
s'	Calculated intermediate value of s during time increment	m
s_1	Calculated value of s at end of time increment	m
s_{max}	Maximum elastic contact deformation	m
\dot{s}	Velocity of contact's elastic deformation in the sliding direction	m/s
S_a	Speed of rotation of aluminium-bronze disc	RPM
S_s	Speed of rotation of steel disc	RPM
S_{ma}	Speed of rotation of motor driving the aluminium-bronze disc	RPM
S_{ms}	Speed of rotation of motor driving the steel disc	RPM
t	Time	s
t_v	Time at which vibration is activated	s
T_2	Wheel through-travel output torque	Nm
T_a	Torque measured by torque sensor for aluminium-bronze disc	Nm
T_{ba}	Torque losses from bearings in the aluminium-bronze disc drive	Nm
T_{bs}	Torque losses from bearings in the steel disc drive	Nm
T_B	General term for torque simulated at point B to drive worm shaft	Nm
T_{Bs}	Signifies T_B in the absence of vibration	Nm
T_{Bv}	Signifies T_B in the presence of vibration	Nm
$T_{G,all}$	Allowable application-based wheel torque, AGMA 6034-B92	Nm
T_R	Rated torque of valve actuator	Nm
T_s	Torque measured by torque sensor for steel disc	Nm
T_{ss}	Signifies T_s in the absence of vibration	Nm
T_{sv}	Signifies T_s in the presence of vibration	Nm
u	Instantaneous displacement of vibration	m
u_a	Amplitude of the displacement of vibration	m
U	Gear ratio	
v	Instantaneous velocity of vibration	m/s
ν_{40}	Kinematic viscosity at 40°C	mm^2/s
ν_{100}	Kinematic viscosity at 100°C	mm^2/s
ν_a	Amplitude of the velocity of vibration	m/s

NOTATIONS

Symbol	Description	Unit
v_d	Drive velocity	m/s
v_g	Sliding velocity between worm and wheel	m/s
v_{pa}	Peripheral linear velocity of aluminium-bronze disc	mm/s
v_{ps}	Peripheral linear velocity of steel disc	mm/s
v_r	Relative velocity of sliding during vibration	m/s
v_{r1}	Relative velocity v_r associated with 1 st phase of vibrating motion	m/s
v_{r2}	Relative velocity v_r associated with 2 nd phase of vibrating motion	m/s
v_{ro}	Roll velocity between two discs	mm/s
v_{sl}	Slide velocity between two discs	mm/s
V_l	Voltage output from load cell in sonotrode	mV
V_{ma}	Voltage supplied to the motor driving the aluminium-bronze disc	V
V_{ms}	Voltage supplied to the motor driving the steel disc	V
V_p	Voltage supplied to piezo actuator	V
V_w	Voltage wave output from vibration control box	V
x	Instantaneous displacement of sliding body parallel to axis X	m
\dot{x}	Instantaneous velocity of sliding body parallel to axis X	m/s
\ddot{x}	Instantaneous acceleration of sliding body parallel to axis X	m/s ²
x_b	Instantaneous displacement of vibrating base parallel to axis X	m
\dot{x}_b	Instantaneous velocity of vibrating base parallel to axis X	m/s
x_A	Instantaneous displacement of point A	m
x_B	Instantaneous displacement of point B	m
y	Instantaneous displacement of sliding body parallel to axis Y	m
\ddot{y}	Instantaneous acceleration of sliding body parallel to axis Y	m/s ²
y_b	Instantaneous displacement of vibrating base parallel to axis Y	m
\dot{y}_b	Instantaneous velocity of vibrating base parallel to axis Y	m/s
Y_w	Material factor	
z_1	Number of starts on worm	
z_2	Number of teeth on wheel	
α	Angle defining direction of v_{r1} in relation to axis X	degree
α_n	Normal pressure angle	degree
β	Angle defining direction of v_{r2} in relation to axis X	degree
γ_{m1}	Worm lead angle	degree

NOTATIONS

Symbol	Description	Unit
ϵ_a	Poisson's ratio of aluminium-bronze	
ϵ_s	Poisson's ratio of steel	
ϵ	Energy	J
η_{AGMA}	Worm gearset efficiency per AGMA 6034-B92	%
η_{z1-2}	Worm gearset efficiency per PD ISO/TR 14521	%
η_{ges1-2}	Worm gearbox system efficiency per PD ISO/TR 14521	%
η_s	Efficiency of the steel disc drive	%
η_{sys}	Overall efficiency of worm gearset and vibration system	%
η_y	Coefficient of transverse vibration when base is vibrating	
η_y^*	Coefficient of transverse vibration when body is vibrating	
θ	Angle describing the mode of in-plane vibration	degree
μ	Coefficient of friction	
μ_{AGMA}	Coefficient of friction reported by AGMA 6034-B92	
μ_{zm}	Mean tooth coefficient of friction	
π	The numeric constant Pi	
σ_a	Wheel bending stress at rated torque T_R	N/mm ²
σ_c	Wheel contact stress	N/mm ²
τ_{crit}	Critical friction stress	N/m ²
τ_{eqv}	Equivalent friction stress caused by τ_x and τ_y	N/m ²
τ_x	Component of friction stress acting parallel to axis X	N/m ²
τ_y	Component of friction stress acting parallel to axis Y	N/m ²
ω	Angular frequency	rad/s
\leftarrow	Leftward arrow over symbol; value before activating vibration	
\rightarrow	Rightward arrow over symbol; value after activating vibration	
$\bar{\quad}$	Bar over symbol; vector between two points	
\sim	Tilde over symbol; average value	
\square	Boxed symbol; state-dependant variable	

Chapter 1

Introduction

1.1. Motivation for Research

The global market for industrial gearboxes is projected to reach US\$43.6 billion by 2025 (Global Industry Analysts Inc., 2020). By the same year the market size for worm gears has a forecast increase to US\$610.5 million, from US\$578.8 million in 2019 (Global Info Research, 2020). This demand is driven by increasing adoption of automation across varied industries and applications to make processes more reliable, improve safety and increase productivity.

Gearboxes are vital for powering automation equipment as they deliver mechanical power in various combinations of speed and torque. Popular gearbox designs range from using spur, helical and bevel gears to planetary and worm gears. Present day gearboxes are capable of interfacing with digitised controls, enabling amalgamation of mechanical, electrical and information technologies. An example of this are valve actuators (Figure 1.1), which typically feature a motor driven worm gear shaft meshed with a wheel gear. This constitutes the worm gearset, which operates submerged in an oil bath within a sealed enclosure. The wheel gear produces output torque used to operate many types of valves while sensors in the actuator measure torque and valve position which is displayed on the actuator's user interface.

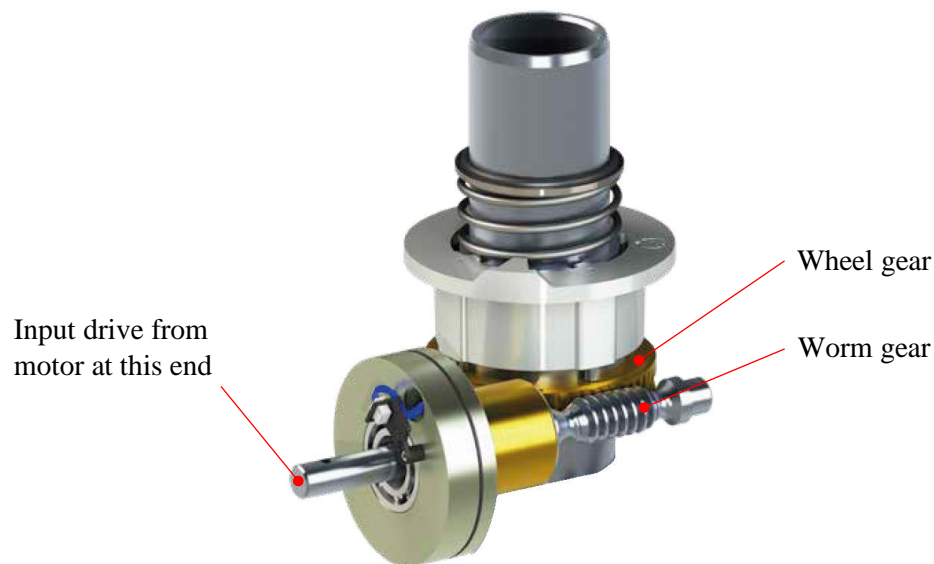


Figure 1.1: Worm gearing inside an actuator designed for operating valves (Rotork PLC, 2020).

Due to their many advantages, worm gearsets are chosen for many other applications, such as elevators, conveyors, rudders, and heavy machinery such as presses

and rolling mills. However, by nature of their design worm gearsets are inefficient (Designatronics Inc., 2020). A fundamental consideration for the design of a gearbox is its operating efficiency. Given that worm gearing demand is on the rise, research on improving its efficiency would make a significant contribution to industry.

Increased efficiency of a worm gearset means less input torque to the worm is necessary to achieve the same output torque from the wheel. For example, a 15:1 ratio worm gearset that produces 150 Nm of wheel output torque and is 50% efficient would require $150/(15 \cdot 0.5) = 20$ Nm of worm input torque. The same gearset at 80% efficiency would require only $150/(15 \cdot 0.8) = 12.5$ Nm of worm input torque to generate the same output torque. Assuming the rotational speed remains unchanged, this is equivalent to 37% reduction in power.

Reduced torque load on the motor would reduce heat and could also lead to downsizing of components in the drivetrain to subsequently reduce weight and material cost.

1.2. Aim and Objectives

The aim of this research is to investigate a novel method of improving worm gearing efficiency and to quantify the potential benefits through experimental testing, mathematical modelling, and simulations. To achieve this research aim, the specific research objectives are:

- i. Identify existing and emerging methods of reducing friction between loaded contacts.
- ii. Use worm gearing design standards to calculate the theoretical efficiency improvement gained by imposing vibration compared to other methods of reducing friction.
- iii. Develop mathematical models to describe the contact mechanics associated with friction force reduction in the presence of in-plane vibration and validate the analytical models against pre-existing simulation results.
- iv. Develop numerical simulations of friction force reduction by in-plane vibration using finite element method and compare results with analytical method.
- v. Produce a custom friction test rig to conduct vibration experiments of a contact representative of worm gearing and evaluate empirical results.
- vi. Perform 3D finite element simulations of vibration applied to a worm gearset, evaluate efficiency results, and quantify the benefits.

1.3. Research Questions

Driven by the research objectives, the key research questions that this study seeks to answer are:

- i. How does theoretical efficiency improvement due to imposed vibration compare to that of other friction reduction methods, such as lubricants and surface coatings?
- ii. What are the limitations of existing analytical models for computing friction force reduction in presence of in-plane vibration?
- iii. Are finite element simulations to numerically compute friction force reduction by vibration a viable alternative to overcome the limitations of analytical method?
- iv. Can the friction reduction effect due to vibration be produced in sliding-rolling type contact that is typical of gearing?
- v. Can the friction reduction effect due to vibration be produced when the contact is lubricated?
- vi. How does friction reduction due to triangular waveform of vibration compare to sinusoidal waveform that is used as the norm?
- vii. What is the effect of vibration on efficiency of a worm gearset simulated using finite element analysis?

1.4. Research Methodology

The purpose of research methodology is to identify the philosophical underpinnings of the research and to outline the specific research methods, tools and data analysis methods employed.

The objectives in 1.2 and research questions in 1.3 establish the focus, highlighting what is to be achieved. The research methods and tools (1.4.3) identify the methods by which research data is collected to address the objectives and research questions. Methods of analysing the collected data are then identified (1.4.4).

1.4.1. *Research Philosophy*

This research is based on the philosophy of positivism, which adheres to the view that reality is objective and only factual knowledge gained through measurement is trustworthy (Eriksson and Kovalainen, 2016). Experimental results are not influenced by feelings or opinions of the researcher but are based on measured and recorded test data. This is the underlying ideology in scientific studies and drives the need for quantitative

research data. Like experiments, simulations produce also quantitative data, however, results of simulations depend on assumptions made when establishing the simulation domain and its boundary conditions, see 7.4.7.

1.4.2. *Research Type*

This research is of the deductive type, meaning that existing theories from which phenomena can be explained are developed to expand existing knowledge base ((Eriksson and Kovalainen, 2016). Mathematical models and experiments that are already established for evaluating the influence of vibration on friction force are further developed. This is because pre-existing work only applies to dry contacts that exhibited pure sliding while subjected to sinusoidal vibration. This research expands current knowledge of friction to lubricated contacts that exhibit sliding-rolling action while subjected to sinusoidal or triangular wave vibration. It also demonstrates transition from pre-existing analytical procedures to numerical simulations for evaluation of the complex contact conditions posed by meshing gear teeth that are subjected to vibration.

1.4.3. *Research Methods and Tools*

Listed in Table 1.1 are the research methods and tools employed for this work. Research methods and tools describe how the research data is collected to address the research objectives (1.2) and research questions (1.3).

1.4.4. *Data Analysis Methods*

Table 1.1 also lists the data analysis methods employed for this work. Data analysis involves visualisation and interpretation of the collected research data to make comparisons and draw conclusions.

Research objective	Research question	Research method	Tools used	Data analysis method	Thesis chapter
i	i	Review of literature on methods of reducing friction	World Wide Web.	Critical commentary on findings of prior research.	Chapter 2
ii	i	Examination of cause-and-effect relationships using standardised worm gear formulae, detailed gear drawings, and published coefficients of friction as secondary data.	Microsoft® Excel.	Collation of cause-and-effect data in Microsoft® Excel, plotted as bar graphs or line graphs, to show the effect of a multitude of variables on worm gearing efficiency and torque capacity.	Chapter 3
iii	ii	Analytical execution of existing mathematical procedures and of the developed analytical model.	Matlab Simulink®.	Extraction of Simulink® simulation data to Microsoft® Excel to plot the analytically simulated effect of vibration on friction force.	Chapter 4

Research objective	Research question	Research method	Tools used	Data analysis method	Thesis chapter
iv	iii	Finite element simulations for numerical implementation of the developed analytical model.	Intel [®] Visual Fortran Composer XE 2013, Microsoft [®] Visual Studio 2012, Abaqus [®] 6.14.	Extraction of Abaqus [®] simulation data to Microsoft [®] Excel to plot the numerically simulated effect of vibration on friction force. Comparison with analytical results by superimposition of graphical data.	Chapter 5

Research objective	Research question	Research method	Tools used	Data analysis method	Thesis chapter
v	iv, v, vi	Experimentation to fill knowledge gap regarding the influence of sinusoidal and triangular wave vibration on friction force in lubricated sliding-rolling contact. Perform each test run twice to check consistency of empirical data. Test matrix, data capture and test procedure as detailed in 6.4.10-6.4.12.	Siemens® Solid Edge, Picoscope® Oscilloscope, Arduino®, PuTTY, preliminary test rig (6.3.1), final test rig and ancillary devices (6.4.1), Taylor Hobson Surtronic 3+ surface roughness measurer, G-clamps (Figure 6.26), clock dial displacement transducer and magnetic stand (Figure 6.28), noise isolation box (Figure 6.30), accelerometer model A/127 by DJB Instruments (Figure 6.35, Figure 6.44) into a National Instruments® NI9234 data acquisition module and cDAQ9174 chassis, National Instruments® Signal Express.	Processing of data logged by Picoscope® Oscilloscope and transfer into Microsoft® Excel for evaluation of changes in torque, speed and motor current due to the application of vibration. Graphical visualisation of the effect of vibration frequency on torque, power loss and efficiency. Processing of accelerometer data logged by National Instruments® Signal Express and transfer into Microsoft® Excel for evaluation of the effect of vibration frequency on vibration velocity amplitude.	Chapter 6

Research objective	Research question	Research method	Tools used	Data analysis method	Thesis chapter
vi	vii	Finite element simulations to evaluate the effect of vibration on efficiency of a worm gearset.	Intel [®] Visual Fortran Composer XE 2013, Microsoft [®] Visual Studio 2012, Abaqus [®] 6.14.	Extraction of Abaqus [®] simulation data to Microsoft [®] Excel to plot the numerically simulated effect of vibration on torque required to drive a worm gearset, and the consequential effect on gearset mechanical advantage and efficiency.	Chapter 7

Table 1.1: Research methods, tools and data analysis methods employed to address the research objectives and research questions, and their alignment with thesis chapters.

1.5. Overview of Chapters

Chapter 2 provides a literature review of worm gearing, friction, and conventional methods employed for friction reduction. Control of friction using vibration is discussed as a developing field of research and a knowledge gap is identified in terms of its viability with gearing.

Building on knowledge from chapter 2, sensitivity studies in chapter 3 theoretically assess the potential benefit of inducing vibration to improve worm gearing efficiency, compared to other conventional friction reduction methods. Comprehensive design calculations are also employed to assess opportunities for optimising the design of worm gearsets. The research hypothesis is established by vibration highlighted as having the most potential to reduce friction and thus improve gear efficiency.

Chapter 4 develops deeper understanding of contact mechanics via mathematical modelling. A new analytical friction model for vibration based on two separate pre-existing models is developed to describe how friction force is influenced by vibration induced in the plane of contact. The new model applies to dry sliding contact between two 3D planar surfaces, where the normal contact pressure is constant.

To evaluate more complex contacts such as those of multiple concurrent gear teeth, where normal contact pressures change as teeth enter and exit the gear mesh, one must turn from analytical to numerical methods such as FEA. By implementing the new friction model into a FEA software tool, Chapter 5 demonstrates the ability to achieve numerical results matching analytical results of dry sliding between 3D planar surfaces. This sets the foundation for use of numerical method to simulate the influence of vibration on worm gearing in chapter 7.

Chapter 6 details the features of a custom disc-on-disc test system followed by its use to conduct friction experiments. Experiments investigate the effect of vibration on lubricated sliding-rolling contact friction, building upon theoretical analyses from previous chapters by advancing towards a worm gearset-like contact. Test variables include vibration mode, vibration waveform, vibration frequency, lubricant type, and sliding speed.

Chapter 7 describes the conduct of 3D finite element vibration simulations performed on a worm gearset. It builds upon previous chapters 4 and 5 to further modify the mathematical friction model and simulate the influence of vibration on worm gearset mechanical advantage and system efficiency.

Chapter 8 contains overall conclusions drawn from this thesis and recommendations are made to further develop this research.

Abbreviations and notations used throughout, together with their descriptions, are included for clarity within the front matter of this thesis.

Chapter 2

Literature Review

2.1. Chapter Introduction

As this research is associated with worm gearing and friction, a basic understanding of these two fields is necessary. Therefore, this chapter begins with an introduction to gears with a focus on the characteristics on worm gearing that differentiate it from other gear types.

Friction in gears, like in most other mechanical systems, is undesired. One of the main aims in gear system design is to reduce friction as it causes wear, generates heat, and thereby reduces the efficiency of the system. A basic introduction to friction is given in this chapter since a comprehensive review requires a deep dive into friction modelling, which is better fitting in chapter 4. Recent advances in friction modelling with vibration (Gutowski and Leus, 2011; 2012; 2015; 2020) chiefly incorporate the Dahl (1968; 1976) friction model, hence other friction models are not considered.

Literature regarding conventional methods employed to reduce friction is reviewed to identify a gap in knowledge that is later evaluated further to establish the focus for research.

2.1.1. *Types of Gears*

Gears are machine elements that transmit rotary motion and power by the successive engagements of teeth on their periphery. Gears have been in use for more than three thousand years and in current times are used in a diverse range of applications spanning industries including automotive, industrial, marine, aerospace and medical. Gears range by size as large as 30 metres in diameter and vary in materials from plastics to high-strength steels (Davis, 2005).

A wide variety of gear types are in existence, each serving a range of different functions. They can be classified by the arrangement of shafts on which they are mounted, as per Figure 2.1. Geometric arrangement of the apparatus being actuated, the space available, the desired gear ratio and efficiency are all factors that influence selection of the appropriate gear type for an application.

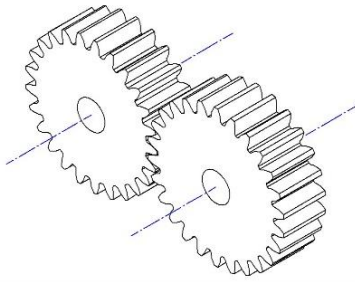
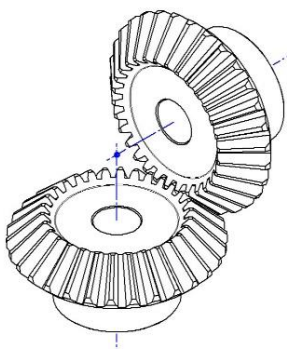
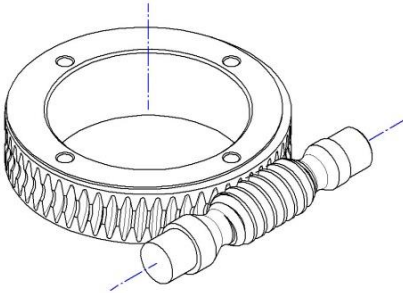
Shaft axes arrangement	Gear type	Illustration of axes arrangement
Parallel axes	Spur gear external (right) Spur gear internal Helical gear external Helical gear internal Herringbone gear	 <p>(a)</p>
Intersecting axes	Straight bevel gear (right) Spiral bevel gear Face gear	 <p>(b)</p>
Non-parallel and non-intersecting axes	Worm gear (right) Crossed helical gear Hypoid gear	 <p>(c)</p>

Figure 2.1: Illustrations of common gear types classified by their shaft axes arrangement

(a) parallel axis, spur gear external (b) intersecting axes, straight bevel gear (c) non-parallel and non-intersecting axes, worm gear.

2.1.2. Gear Terminology

Key gear terms used in this thesis are described in Table 2.1 with supporting schematics Figure 2.2, Figure 2.3 and Figure 2.4.

Terminology	Description
Addendum	Distance between the pitch circle and tip of gear teeth (Figure 2.2, Figure 2.3).
Arithmetic mean roughness Ra_1	Surface roughness of the machined gear teeth.
Axial module m_{x1}	Ratio of the wheel's pitch circle diameter to the total number of wheel gear teeth.
Axial pitch	Distance between two corresponding points of adjacent threads parallel to the worm gear axis (Figure 2.3).
Centre distance c	Distance between the centres of the meshed gear pair (Figure 2.4).
Contact ratio	The mean number of teeth that are in contact to share the load during transmission. As one pair of teeth exits the gear mesh, a succeeding pair of teeth must have already started action.
Crowning	A type of modification that applies thinning of teeth at the ends of the face width such that the tooth thickness gradually reduces from the centre (Figure 2.2). This helps to concentrate the contact zone near the centre of the face width.
Dedendum	Distance between the pitch circle and root of gear teeth (Figure 2.2, Figure 2.3).
Diameter factor q_1	Ratio of pitch diameter of worm to its axial module
Efficiency	A measure of useful work performed by the gearset, calculated by dividing the mechanical advantage by the gear ratio.
Face width	Width of gear teeth measured parallel to the gear axis (Figure 2.2).
Flank	Curved surface on the side of gear teeth (Figure 2.2).
Gear mesh stiffness	The ability of gear teeth to resist deformation under load when meshed.
Gear ratio U	Ratio of the angular speed or number of revolutions of the input gear to the angular speed or revolutions of the output gear. Also equivalent to the number of wheel teeth divided by the number of starts on the worm.
Lead angle γ_{m1}	Angle of the helix of gear teeth as shown in Figure 2.4.

Material factor Y_W	Enables inclusion of the influence of the wheel material of coefficient of friction.
Mechanical advantage	An increase in torque that a gearset produces. It is the ratio of the real output torque produced from the input torque applied into the gearset. Due to losses in the gear mesh the mechanical advantage is always lower than the gear ratio.
Normal pressure angle α_n	As shown in Figure 2.3.
Number of starts on worm z_1	The number of helical threads on the worm. The worm may have a single start or multiple starts. For a single start worm, each 360° rotation of the worm advances the wheel by one tooth. For a double start worm, each 360° rotation of the worm advances the wheel by two teeth, and so forth.
Pitch circle	Imaginary circle (Figure 2.2) between the tip and root of gear teeth that is concentric to the gear along its axis. If the gear pair are designed correctly, their pitch circles are tangent to one another. The pitch circle of the wheel gear is tangent to the pitch line of the worm gear (Figure 2.4).
Pitch diameter	Diameter of the pitch circle.
Tip relief	A type of modification that applies thinning of teeth at their tip to prevent excessive dynamic contact loads as gear teeth enter the mesh (Figure 2.2).
Tooth root	The innermost part of the gear tooth profile where the dedendum is measured (Figure 2.2, Figure 2.3).
Tooth thickness	Thickness of tooth measured on the pitch circle (Figure 2.2).
Tooth tip	The outermost part of the gear tooth profile where the addendum is measured (Figure 2.2, Figure 2.3).
Transmission error	Deviation of the actual angular position of the driven gear compared to its theoretical angular position when the driving gear is running at constant speed. The higher the transmission error, the greater the risk of dynamic variation in operating speed and torque, implying operational inconsistency and higher noise levels.

Table 2.1: Gear terms and their descriptions.

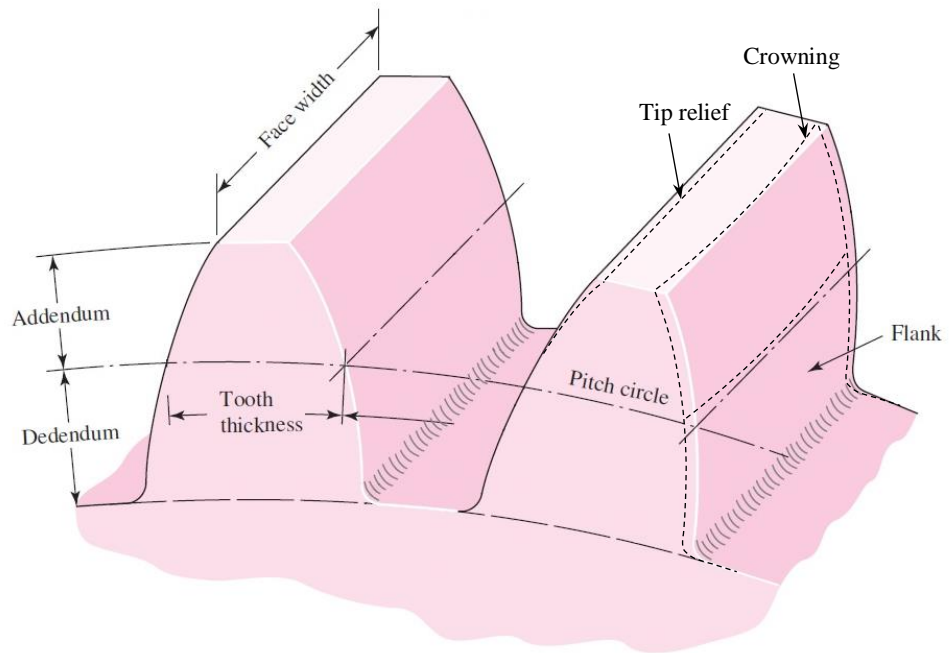


Figure 2.2: Schematic of spur gear teeth with key terminology that applies also to wheel gear teeth (Budynas and Nisbett, 2011).

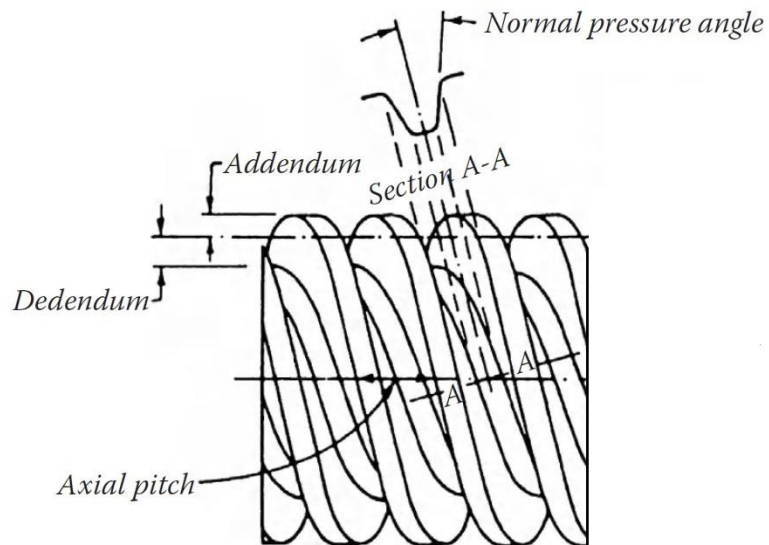


Figure 2.3: Schematic of worm gear teeth with key terminology (Radzevich, 2012).

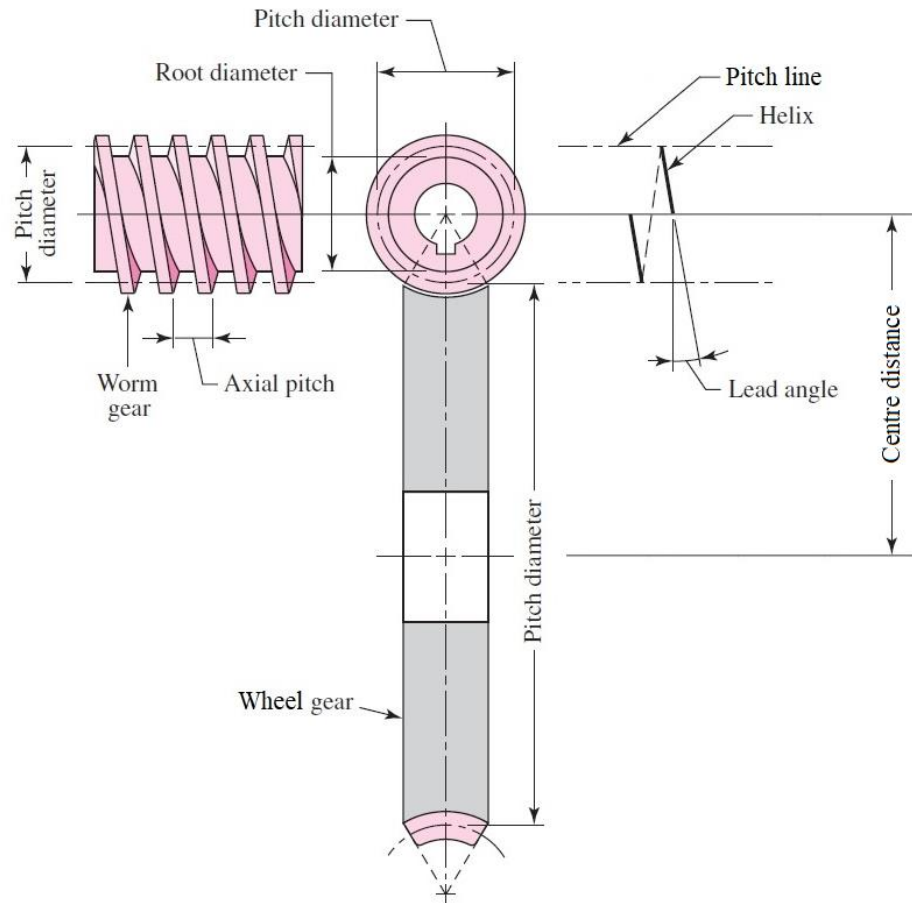


Figure 2.4: Schematic of worm and wheel gear pair with key terminology (Budynas and Nisbett, 2011).

2.1.3. Gear Ratio and Efficiency

A general guide on gear ratios and efficiency ranges of common gear types is presented in Table 2.2. Gear efficiency is largely affected by the way in which gear teeth mesh. Spur, helical and bevel gears have a predominantly rolling tooth contact, which makes very efficient meshing action. However, their normal ratio range consists of relatively low gear ratios. It is possible to obtain higher ratios through multiple-stage configurations, but this reduces efficiency while increasing backlash, space consumption and weight (Davis, 2005).

In contrary, worm gearing allows for significantly higher ratios, enabling radical increase of output torque with just a single gear stage. The worm and wheel teeth mesh in a predominantly sliding contact action, which causes greater frictional loss. Worm gearing efficiency varies significantly with gear ratio, hence the wide efficiency range for this type.

Gear type	Normal ratio range	Efficiency range
Spur	1:1 to 6:1	98 to 99.5%
Helical	3:2 to 10:1	98 to 99%
Straight bevel	3:2 to 5:1	98 to 99%
Hypoid	10:1 to 200:1	96 to 98%
Worm gear	5:1 to 300:1	30 to 90%

Table 2.2: Gear ratio and efficiency ranges of common gear types (Gonzalez, 2015; Designatronics Inc., 2020).

2.1.4. *History of Worm Gearing*

In the early 19th century worm gearing efficiency was not seriously considered. Grinding of worm teeth was unheard of as a manufacturing process, and little was known of correct tooth geometries and their relation to efficiency. Use of worm gears in England began around 1908 for commercial motor vehicles. Meanwhile, in USA slow vehicular speed and large loads of the motor truck necessitated designers to turn towards worm gearing for a considerable speed reduction in the final drive. Prior to 1912, this reduction was obtained in two stages using bevel gears and chain drive.

Early efforts in gear improvement were devoted to heat treatment and material improvements. Passenger carrying brought new requirements in the way of higher speeds, greater acceleration, and quietness. It was recognised that the worm should be made from heat treated steel for a hardened surface, and the wheel from a bronze-based material which would burnish down and increase its hardness at the point of highest contact pressure.

Very few brass foundries could produce a gear bronze meeting the requirements of the developing worm gearing. Testing of a well-advertised and highly recommended grade of bronze showed that the gear could run for several days under light load but was destroyed in 30 minutes when the load and speed were doubled to levels of a motor truck (Calkins, 1926). Since these times significant advances have been made in the development of worm gearing, and gearing in general, as detailed in subsequent sections of this literature review.

2.1.5. *Self-Locking Capability of Worm Gearing*

An important characteristic of worm gearing is that the worm drives the wheel, but the wheel cannot always back-drive the worm. This self-locking capability is

dependent on the value of the friction angle $\arctan(\mu)$, in relation to the worm lead angle γ_{m1} , and is explained by the following relationship (Radzevich, 2012):

$$\text{If } \begin{cases} \gamma_{m1} < \arctan(\mu) & \text{worm gearing is self-locking} \\ \gamma_{m1} \geq \arctan(\mu) & \text{worm gearing is reversible (not self-locking)} \end{cases} \quad (1)$$

If the lead angle is smaller than the friction angle, then theoretically the gearing is self-locking. This provides an important function in actuation as it means the gearset will act as a secondary brake, maintaining position when the motor that drives the worm is switched off or removed for maintenance. Smaller lead angles enable higher gear ratios but cause more sliding of gear teeth, resulting in increased friction and consequently reduced efficiency. Self-locking worm gearsets are thus associated with low efficiency and result in considerable power loss if used continuously. Efficiency improvement can make worm gearing reversible, depending on the gear ratio. A highly efficient worm gearset may require an anti-back-drive mechanism to maintain system non-reversibility.

2.1.6. *Losses in a Worm Gearbox*

A worm gearbox is compact. It comprises worm and wheel gears on two non-parallel and non-intersecting shafts, with bearings and oil seals in an enclosed oil bath. These machine elements attribute to four mechanical transmission power losses; tooth friction losses, bearing losses, sealing losses and oil churning losses (Childs, 2019).

Bearing losses are a result of friction between bearing rollers and bearing races that support shafting within the unit. Seals retain lubricating oil within the gearbox while preventing dirt and water ingress into it. Since the lip of an oil seal rides against a rotating shaft, friction is developed at this interface. As the gears rotate, their teeth continuously strike and displace oil. Mechanical power is absorbed by this action of oil churning.

While bearings, seals and oil influence the overall efficiency of the system, the greatest loss in efficiency is associated with the predominantly sliding contact friction between the worm and wheel teeth (Bobak, 2009). Since tooth friction losses are the largest contributor to low efficiency, an improvement of this has potential to yield the most benefit for worm gearing applications. Review of literature is thus aimed at the subject of reducing friction between gear teeth.

2.2. Friction

2.2.1. Introduction to Friction

Friction forces are present when two surfaces in contact enter relative motion; an event so intrinsic to mechanics of everyday life and important in a multitude of applications that it has been acknowledged since ancient times, when friction associated with moving large stone blocks had to be overcome to build the pyramids (Wriggers, 2006).

The dissipative character of friction and its significance to all contact problems has impelled experimental research since the 15th century when Leonardo Da Vinci made the first known quantitative studies in this subject, as reviewed by Hutchings (2016). His immense contribution to the field of tribology did not fully surface until the late 1960s when several caches of his notebook pages were discovered, uncovering his notable observations that precede the development of the laws of friction adopted today (Pitenis, Dowson and Sawyer, 2014).

Dowson (1998) refers to the studies of Guillaume Amontons who in 1699 enunciated these observations, thus the contribution of Da Vinci is often neglected. Amontons believed that friction is the result of work done to lift one surface over the roughness of another. The proposition that friction is due to the roughness on surfaces was further elaborated by Bernard Forest B elidor in 1737 by representation of rough surfaces with spherical asperities, followed by Leonhard Euler in 1750, who first distinguished between static and kinetic friction.

Popova and Popov (2015) indicate that by the late 1780s, Charles Augustin Coulomb had investigated friction as a function of many factors including the nature of the materials in contact, their surface area, normal load, time of repose, temperature and humidity. Coulomb was the first to formulate friction force as an equation:

$$\mathbf{F}_C = \mu \mathbf{F}_N \tag{2}$$

Figure 2.5 schematises a body being driven at constant drive velocity \mathbf{v}_d over a base. Drive velocity \mathbf{v}_d creates a drive force \mathbf{F}_d on the body, opposite to which acts friction force \mathbf{F}_C of equal magnitude. The velocity of the body is equal to the externally applied drive velocity, $\dot{\mathbf{x}} = \mathbf{v}_d$. Downward external pressure in addition to the body's mass generates a reaction force \mathbf{F}_N . The total displacement of the body is \mathbf{x} . The base can

be static in which case $\mathbf{x}_b = \dot{\mathbf{x}}_b = 0$, or it can be vibrated with oscillatory displacement \mathbf{x}_b and velocity $\dot{\mathbf{x}}_b$.

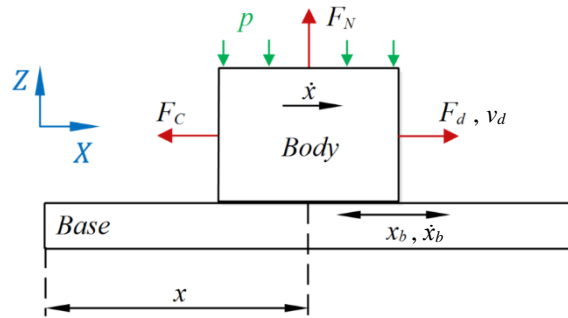


Figure 2.5: Coulomb friction schematic of body driven at constant velocity \mathbf{v}_d over base surface.

Coefficient of friction μ in (2) ranges typically between 0.1 for polished oiled metal surfaces to 1 for rough dry surfaces (Bird, 2001). A comprehensive review by Oden and Martins (1985) highlights that friction theories of the eighteenth and early nineteenth centuries explain frictional behaviour in terms of rigid interlocking surface asperities. Coulomb friction thus only considers an object as either static when $\mathbf{F}_d < |\mathbf{F}_C|$, or under macroscopic relative motion when $\mathbf{F}_d > |\mathbf{F}_C|$.

2.2.2. Contact Compliance

Friction models can be divided into two groups, namely static and dynamic. Static models derived from the Coulomb model assume that relative motion between rubbing surfaces does not occur at rest. Dynamic models derived from the Dahl (1968) friction model assume that small pre-sliding displacements occur, and the friction force is a function of these displacements. This property has been confirmed by detailed experimental studies (Dahl, 1968; Dahl, 1976; Liang, Fillmore and Ma, 2012).

As discovered by Dahl (1968; 1976), when an external drive force is applied on a static body in contact with another, an intermediate motion of one surface over the other occurs before the bodies enter macroscopic relative motion. This intermediate pre-sliding displacement, also known as elastic slip, is a result of surface asperities that are considered to deflect. These deformable contacting asperities between the sliding body and base can be modelled as a single lumped elastic asperity MN (Figure 2.6). Endpoint N of the lumped asperity is attached to the sliding body, while the free endpoint M interfaces with the base.

In development to Figure 2.5, Figure 2.6 shows the external drive force F_d creating an elastic deformation s of the lumped elastic asperity MN . As asperities undergo increased strain, yielding occurs and the two surfaces start to break free of each other. During this time, plastic deformation of asperities takes place. Finally, asperity rupture occurs leading to formation of further surface irregularities which will continuously undergo strain and rupture as sliding takes place. Thus, in Dahl's friction model it is assumed that friction force F is associated with the tangential contact stiffness k_t (Figure 2.6), and elastic deformation s of the contact:

$$F = k_t s \quad (3)$$

The value of k_t in real contacts is dependent on surface roughness of the contact pair, the type of material, lubrication and normal contact pressure p .

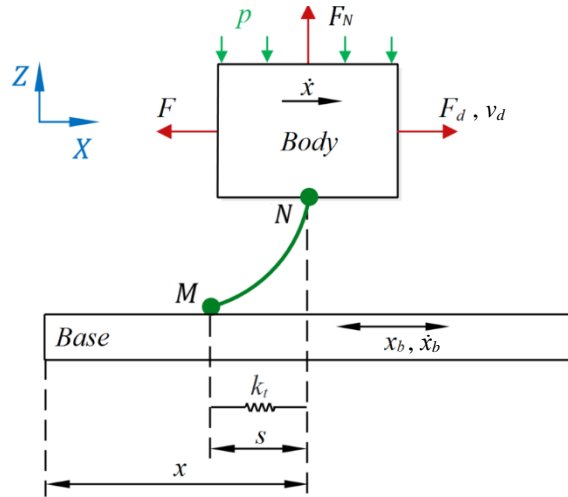


Figure 2.6: Dahl (1968; 1976) friction schematic of body driven at constant velocity v_d over base surface. Elastic contact deformation s and contact stiffness k_t of lumped elastic asperity MN .

The force-displacement relationship is modelled by the following differential equation (Dahl, 1976):

$$\begin{aligned} \frac{dF}{dx} &= k_t \left[1 - \frac{F}{F_c} \operatorname{sgn}(\dot{x}) \right]^i \\ &= k_t \left[1 - \frac{k_t s}{\mu F_N} \operatorname{sgn}(\dot{x}) \right]^i \end{aligned} \quad (4)$$

$d\mathbf{F}$ and $d\mathbf{x}$ are the incremental friction force and incremental displacement respectively, and $\dot{\mathbf{x}}$ the instantaneous velocity of the body in the direction of sliding. Parameter i determines the shape of the relationship between \mathbf{x} and \mathbf{F} during elastic slip (Figure 2.7). $i = 0$ describes brittle material behaviour, where \mathbf{F} linearly increases with \mathbf{x} at a gradient k_t , until the maximum friction force \mathbf{F}_C is reached and the surfaces break away. As the value of i approaches 2 the material behaviour becomes ductile producing a non-linear response of \mathbf{F} which is asymptotic to the value of \mathbf{F}_C (Dahl, 1976).

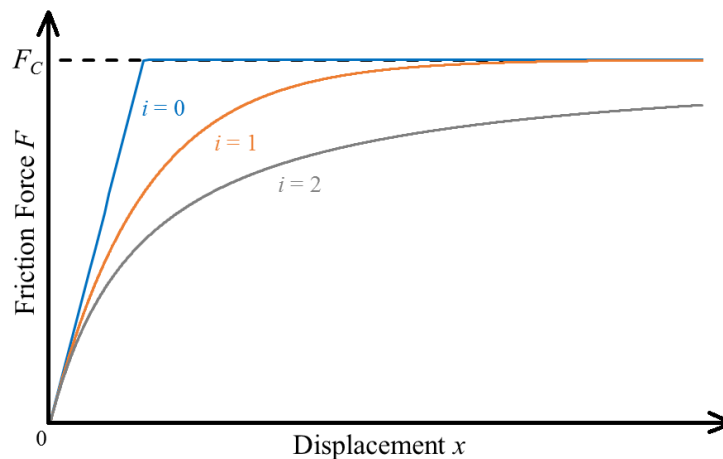


Figure 2.7: Influence of i on relationship between \mathbf{F} and \mathbf{x} during elastic slip phase, from $i = 0$ brittle material behaviour to $i = 2$ ductile material behaviour.

2.3. Lubrication

A lubricant is any substance that reduces friction and wear when present between interacting surfaces. High operating torques and sliding speeds in worm gearing generate high levels of frictional heat. Wear debris is also produced, particularly from the sacrificial wheel material. It is thus common practice in worm gearboxes that the gears remain submerged in an oil bath. The oil dissipates the heat and carries wear debris away from the contact.

2.3.1. Lubrication Regimes

Oil lubrication regimes can be divided into three fundamental types: full-film, boundary, and mixed lubrication. The regime in which a gearset operates depends on rotational speed, load, surface roughness and lubricant viscosity (Budynas and Nisbett,

2011). It is entirely possible for the same gearset to operate in different regimes as these conditions change.

Full-film regime requires an adequate lubricant supply. The moving gear surfaces pull the lubricant into the contact zone at a sufficiently high speed, creating a high-pressure film that separates the load carrying surfaces such that no asperity contact occurs. Full-film separation of sliding surfaces is called hydrodynamic lubrication, and that of rolling surfaces is called elastohydrodynamic lubrication (EHL).

Full-film lubrication in gearboxes is not always possible, particularly when starting and reversing. A reduction in speed of the interacting surfaces, an increase in contact load, or an increase in lubricant temperature leading to reduced viscosity, are all factors that can reduce lubricant film thickness. Gear lubricants with extreme pressure (EP) or anti-wear (AW) additives help protect the surfaces when this happens. The additives cohere to the surfaces, forming a sacrificial layer.

Boundary lubrication is when surface asperities are only separated by the additives, or by lubricant films only several molecular dimensions in thickness. Thus, in boundary lubrication the additives become determinant, whereas in full-film condition the chemical composition of the lubricant is most important (Brandão *et al.*, 2012). Asperity interaction is high in boundary lubrication, and this causes high friction, heat and wear.

The transition from full-film to boundary lubrication is not sudden. It is probable that a mixed regime occurs first, and as the surfaces move closer together, boundary lubrication becomes predominant (Budynas and Nisbett, 2011).

2.3.2. *Mineral vs. Synthetic Oils*

Industrial gear oils consist of a base oil and chemical substances called additives. The performance classification of a gear oil depends on the quality and type of base oil, and the combination of additives used. 85-95% of the composition typically constitutes the base oil, and additives account for 5-15% (Bartels and Bock, 2017).

Gear oils fall into two categories: mineral and synthetic. Mineral oils are refined from crude oil whereas synthetic oils are man-made, with scientifically designed molecules produced from chemical synthesis (Daniel and Paulus, 2019). Both types have been extensively researched.

A test rig developed by the Institute of Machine Elements - Gear Research Centre (FZG) is commonly used to evaluate fluid lubrication and wear protection properties at

the interface of a gear pair subjected to known load stages. The gears are spur type, but different profiles can be used to achieve varying slide-roll ratios. Experiments by Hargreaves and Planitz (2009) evaluate the energy efficiency of six EP industrial mineral oils, comparing power consumption with each in an FZG test rig. The lubricants are of industrial equivalence from various manufacturers, having the same viscosity grade and FZG load capacity. However, the difference in power consumption between the worst and best performing oils is 3.24 and 2.77 kW, equating to a difference of 14.6%. This is significant considering their use in high-powered industrial machines. The study shows that differences in chemical composition between different manufacturers has a significant influence on lubricant performance.

Synthetic lubricants adopted in gear applications include ester, polyalphaolefin and polyglycol based oils. Although developed decades ago, their considerably higher cost means their use on a large technical scale has only slowly increased. Environmental awareness has led to a growing interest in biodegradable synthetic oils. FZG tests by Martins *et al.* (2005) show that biodegradable ester oil enables μ reduction exceeding 20% compared to mineral oil. Moreover, according to Brandão *et al.* (2012) biodegradable ester only reduces μ in full-film regime, not under boundary lubrication. This highlights the important role of oil additives under boundary lubrication, the choice of which is constrained by biodegradability.

The consumption of polyalphaolefin, the most common type of synthetic oil, has increased enormously in the last two decades according to Dresel (2017). Höhn, Michaelis and Hinterstoißer (2009) refer to FZG test results by Doleschel (2003) which indicate that compared with mineral oil, gear friction can be reduced by 10 to 20% with polyalphaolefin, and an immense 20 to 30% with polyglycol oil. The results align with helical gearbox tests by Marques *et al.* (2014) which also show improved efficiency when substituting mineral oil with polyalphaolefin, but even more so by using polyglycol which reduced power loss by 30%.

For worm gearing also, the best results have been obtained when switching over to polyglycol oil (Siebert, 2011; Mautner *et al.*, 2015). However, when the wheel gear is made of aluminium alloy, such as aluminium-bronze, reaction in the load zone may increase wear (Kajdas, Karpińska and Kulczycki, 2010). Polyglycol compatibility tests should consider wear life as well as efficiency improvement of worm gearing.

2.3.3. Nanoparticles in Oil Lubricants

With the development of nanotechnology, research of nanoparticles has been driven into the field of lubrication. Xu, Zhao and Xu (1996) show that diamond nanoparticles immersed in oil possess excellent load carrying capacity and friction reduction properties. In agreement with findings of Dwyer-Joyce, Sayles, Ioannides (1994), nanoparticles penetrate the rubbing surfaces, and a ball bearing type effect is created where nanoparticles tumble through the contact. Much like the effect of EP or AW additives described in 2.3.1, the nanoparticles form a boundary lubrication film that prevents the rubbing faces from coming into direct contact. Shen, Luo and Wen (2001) further add that diamond nanoparticles form a thicker lubricant film than that with just the base oil. Chu, Hsu and Lin (2010) have experimented with different concentrations of immersion. Their highest test concentration of 3% is most favourable in terms of both friction reduction and wear loss.

Within the past decade, metallic nanoparticles such as Iron Oxide Fe_3O_4 (Zhou *et al.*, 2013) and Titanium Dioxide TiO_2 (Ingole *et al.*, 2013; Wu *et al.*, 2018) have also been shown to reduce friction and wear. The outstanding advantage of using such additives is that by magnetic decantation they can easily be isolated from the used lubricant for disposal.

2.4. Worm Gearing Materials

It is accepted practice to adopt a hard-soft material pair to prevent scuffing from the high degree of sliding in the worm gearing mesh. The historically most common selection for worm gearing is a bronze wheel with a hardened steel worm (Calkins, 1926). This coupling is characterised by a low μ between 0.05 and 0.10 for the most common sliding speeds (British Standards Institution, 1983; Fontanari *et al.*, 2013).

An inevitable consequence of this arrangement is that wheel gear teeth are subjected to a much higher wear rate than the worm. This is largely tolerated in view of worm gearing advantages presented in 2.1.3 and 2.1.5. Moreover, the use of sacrificial wheel material is beneficial to the running-in of new gears as it prevents the problems related to improper surface finishing, inaccurate tooth profiles and minor misalignments in assembly.

Fontanari *et al.* (2013) have investigated wear damage mechanisms occurring in the steel-bronze tribological pair by performing lubricated sliding-rolling tests in a disc-on-disc configuration. In Figure 2.8 the steel 42CrMo4V and bronze CuSn12 disc

specimens of outer diameters 54 mm and 26 mm, thickness 8 mm, are dip lubricated in a polyglycol oil tank, the temperature of which is maintained at 80°C to reproduce severely loaded working conditions. At 4.14 m/s the peripheral velocity of the steel disc is faster than the bronze.

Tests show that depending on contact pressure different wear mechanisms such as scuffing, pitting and spalling can take place at different sliding distances. At high contact pressure, pitting already occurs after the running-in phase, linked to a progressive decrease in μ . The surface craters formed from pitting act as small lubricant tanks enabling better lubrication of disc contact. It is believed that local pressure applied on the lubricant entrapped inside the craters is responsible for the coalescence of pits into large craters, producing the crushing of a surface layer and consequently material removal (Budynas and Nisbett, 2011).

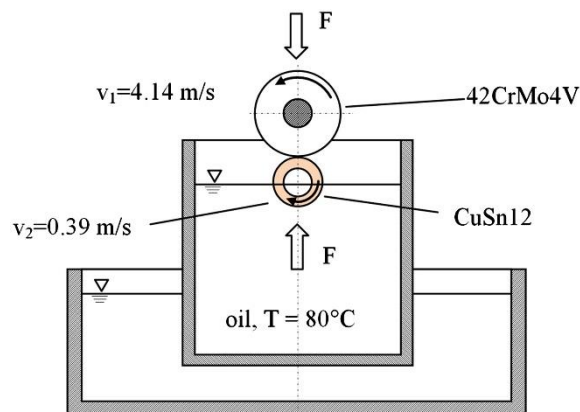


Figure 2.8: Schematic of the disc-on-disc test configuration of Fontanari *et al.* (2013).

Steel 42CrMo4V disc loaded against dip lubricated bronze CuSn12 disc.

Use of a bronze wheel severely limits the allowable gear contact pressure (Sharif, Evans and Snidle, 2006), therefore metallurgists have developed specific alloys to minimise wear of the bronze constituent while maintaining its benefits and increasing its load capacity. Alloys such as aluminium-bronze, manganese-bronze and tin-bronze provide higher strength and hardness, reduced wear and better corrosion resistance without detrimental effect on μ (Russo, 2013).

Austempered Ductile Iron (ADI) gears have been used since the mid-1970s by large automobile manufacturers such as General Motors, BMW, Renault, and FIAT among others. Under commercial interests the results of extensive test programs undertaken with different ADI gears remain unpublished (Magalhães and Seabra, 1998).

Several studies consider ADI for use as gear material (Tsukamoto *et al.*, 1990; Magalhães, Seabra and Sá, 2000; Martins, Seabra and Magalhães, 2008; Magalhães, Martins and Seabra, 2012). An investigation using the same setup as in Figure 2.8 tests the ductile iron-bronze tribological pair (Fontanari *et al.*, 2016), however, as with most ADI studies the focus is on wear performance with limited consideration of the impact on μ and thus efficiency. Nonetheless, research shows ADI can improve wear resistance of a sliding-rolling contact if the appropriate lubricant is used.

2.5. Surface Coatings

Surface coating technology has significantly improved in the current century, providing higher load capacity from greater protection against surface failures, and lower μ where high sliding velocities and gear contact stresses are coupled with inadequate lubricant film thickness (Martins, Amaro and Seabra, 2008). Of the many surface coatings reported in literature, those based on molybdenum disulphide (MoS_2), titanium nitride (TiN), boron carbide (B_4C), tungsten carbide carbon (WCC) and diamond-like-carbon (DLC) are widely used in gearing.

The crystal structure of MoS_2 has tendency to deteriorate when exposed to moisture (Li *et al.*, 2020). Its tribological properties, as with other coatings, are improved with the co-deposition of other elements or compounds, for example, titanium. The performance benefits of MoS_2/Ti coating are demonstrated through disc-on-disc, pin-on-disc, FZG and transfer gearbox tests by Amaro *et al.* (2005). A low value of μ in the range 0.04-0.045 is reported with 0.5% efficiency improvement of the gearbox, and a significant increase in load capacity attributing to an increase of up to 77% power transmission capability. Similar tests by Martins, Amaro and Seabra (2008) have shown MoS_2/Ti to outperform carbon chromium (CCr), and when deposited on top of titanium aluminium nitride (TiAlN) it can decrease the value of μ by a significant 48% (Yongliang and Sunkyu, 2006). The low friction benefit of MoS_2/Ti is further backed up by the work of He, Lyu and Her (2010) as well as Singh *et al.* (2015). Recently undertaken research reduces the impact of moisture on performance of MoS_2 based coatings (Cao *et al.*, 2019; Li *et al.*, 2020)

Mao, Sun and Bell (2006) have conducted gear tests with TiN coating, compared with an uncoated but case-hardened specimen, as well as duplex treated (TiN coated over case-hardened) specimen. The three variants respectively have 2 times, 10 times, and 55 times better wear performance compared to untreated gears. An important note from this

is that surface coatings are of high hardness and thus work best when the substrate is also hardened. Otherwise, there is a sharp transition from the hard coating to the soft base metal which can deform under load and cause the coating to break away.

Joachim, Kurz and Glatthaar (2004) have shown exceptional tribological benefits of B₄C and WCC coated gears, where $\mu < 0.04$ with WCC. This equates to μ reduction of up to 30% compared to uncoated gears. However, the results are highly application dependent, so the coating-lubricant interaction is questionable as well as compatibility with additives.

Xiao *et al.* (2014) conclude that WCC and DLC coatings are more suitable than TiN for high-speed heavy-duty gears. DLC coatings are receiving increased interest in recent years due to their extreme hardness, excellent wear resistance and low friction characteristics, together with high thermal and chemical stability making them strong contenders against other coating types (Tamura *et al.*, 2016; Zahid *et al.*, 2017; Aboua *et al.*, 2018; Espejo *et al.*, 2018; Laderou *et al.*, 2020).

Considerable effort has been, and still is, devoted to assessing the performance and compatibility of coatings with different lubricants (Weck *et al.*, 2002; Feng and Xia, 2012; Moorthy and Shaw, 2012; Kondo *et al.*, 2013; Yazawa, Minami and Prakash, 2014). The method by which coatings are deposited onto surfaces also influences their characteristics (Hulka *et al.*, 2015).

Evidently, coatings provide a degree of lubricity to the contact to increase gearing load capacity and improve efficiency. However, for coatings to work effectively the substrate surface must not only be very hard, but also have a smooth finish to optimise its bond with the coated layer. A surface finishing process followed by a hardening process adds component cost. Moreover, the coatings themselves can be expensive as they require dedicated deposition processes and tight control of conditions. Tribological properties are affected by variables such as the coating deposition processes, coating material properties and thickness, presence of lubricant and additives, surface roughness and temperature.

Sliding-rolling contacts are considered in research of coatings, however, for material combinations discussed in 2.4 for worm gearing, the research is sparse. There is no benefit in coating the bronze-based wheel gear since this is sacrificial by design. Disc-on-disc tests by Benedetti *et al.* (2017) show promising wear improvement when coating the steel counterpart with WCC and DLC, but further work is necessary to realise the impact on efficiency.

2.6. Gear Design Optimisation

Assembly misalignment and shaft deflection at high load and speed cause changes in stress levels and location of the contact zone between interacting gear teeth. It is possible to optimise loaded contact behaviour of helical gears by making small adjustments to the lead angle and tip relief using FEA (Mao, 2007). Lead angle correction (Figure 2.9a) improves contact stress distribution so that the high local stresses are better distributed across the face width of gear teeth. Tip relief correction (Figure 2.9b) of the original over-relieved design enables contact at the tip of gear teeth to start earlier, improving contact ratio and dynamic load sharing while reducing noise (Mao, 2007; Abdullah and Jameel, 2015; Cirelli *et al.*, 2020).

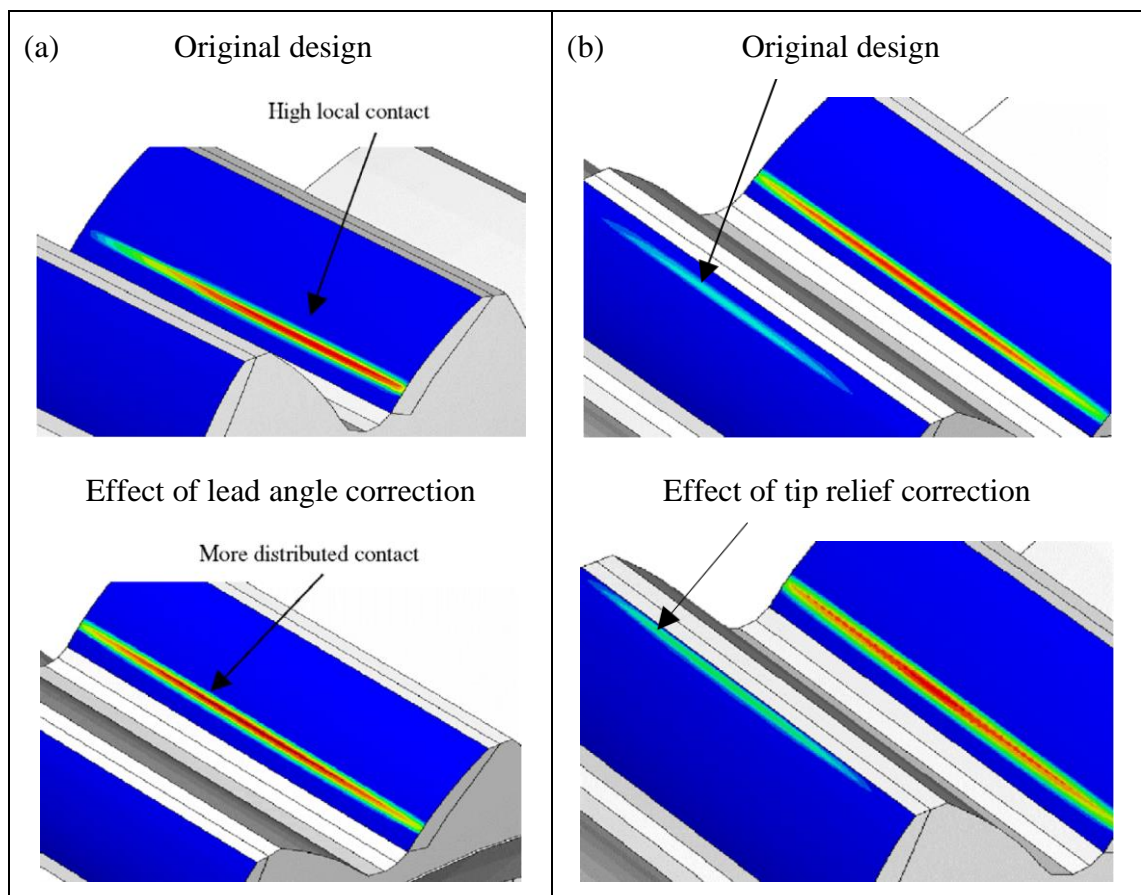


Figure 2.9: Comparison of stress distribution of original design against optimised geometry, (a) lead angle correction, (b) tip relief correction (Mao, 2007).

Worm gearing contact characteristics can be improved likewise, hence considerable modelling and simulation effort has gone into design optimisation and its effect on mesh stiffness, tooth interference, transmission errors and loaded contact behaviour (Yang, Su and Gentle, 2001; Su and Qin, 2003; Xu, Qin and Shi, 2006; Deng,

Wang and Horstemeyer, 2013). Manufacturing the wheel with a cutting hob identical to the worm creates line contact between gear teeth, and high contact stresses occur on the edge of the thread surfaces (Figure 2.10a). Assembly misalignment and load deflection change line contact to edge contact (Figure 2.10b). Oversizing the cutting hob generates a crowned wheel tooth contact surface (Fang and Tsay, 2000; Litvin *et al.*, 2007), creating an elliptical contact zone under load (Figure 2.10c). Consequently, the contact becomes centralised, reducing sensitivity to misalignment. Centre contact also encourages reduced contact pressure and better lubricant entry, thus improving gear efficiency.

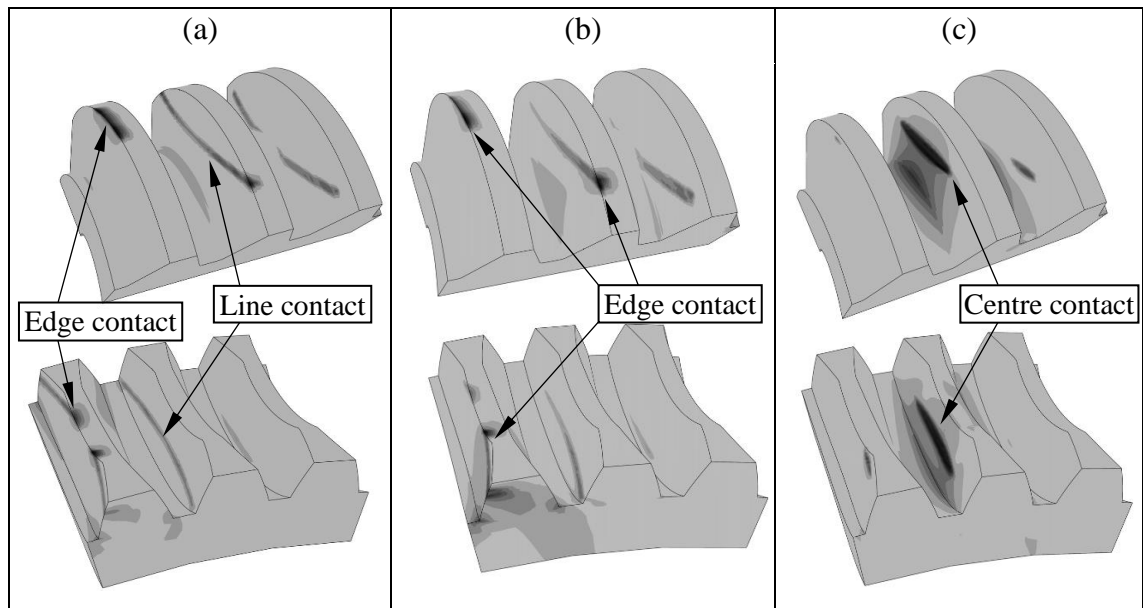


Figure 2.10: Formation of contact on worm (top) and wheel (bottom), (a) no misalignment, (b) with misalignment, (c) modified geometry (Litvin *et al.*, 2007).

Despite of tooth crowning by an oversized hob, a study of geometric interference of worm and wheel gear teeth by Sohn and Park (2016) shows that edge contact can still occur at higher lead angles since the crowned profile becomes increasingly asymmetric. To make crowning symmetric a modified hobbing method of applying a tilt angle to the cutting hob is proposed by Sohn and Park (2017). This method does not require special machinery or hob geometry.

To comprehend and demonstrate the benefit of applying a tilt angle to the cutting hob, mesh checks performed at a gear manufacturer are shown in Figure 2.11. Figure 2.11a shows mesh checking of a worm gearset that has been manufactured to BS 721 (British Standards Institution, 1983), where the wheel teeth have been cut with a 12% oversized hob. The worm gear with blue dye applied is driven against the wheel gear. In

Figure 2.11b blue dye transfer from worm to wheel demonstrates edge contact. Centre contact, Figure 2.11c, is achieved when tilting the cutting hob by an angle of 2° which is maintained during machining of the wheel teeth. The extent of hob oversize and tilt angle required to achieve centre contact depends on size and geometry of teeth.

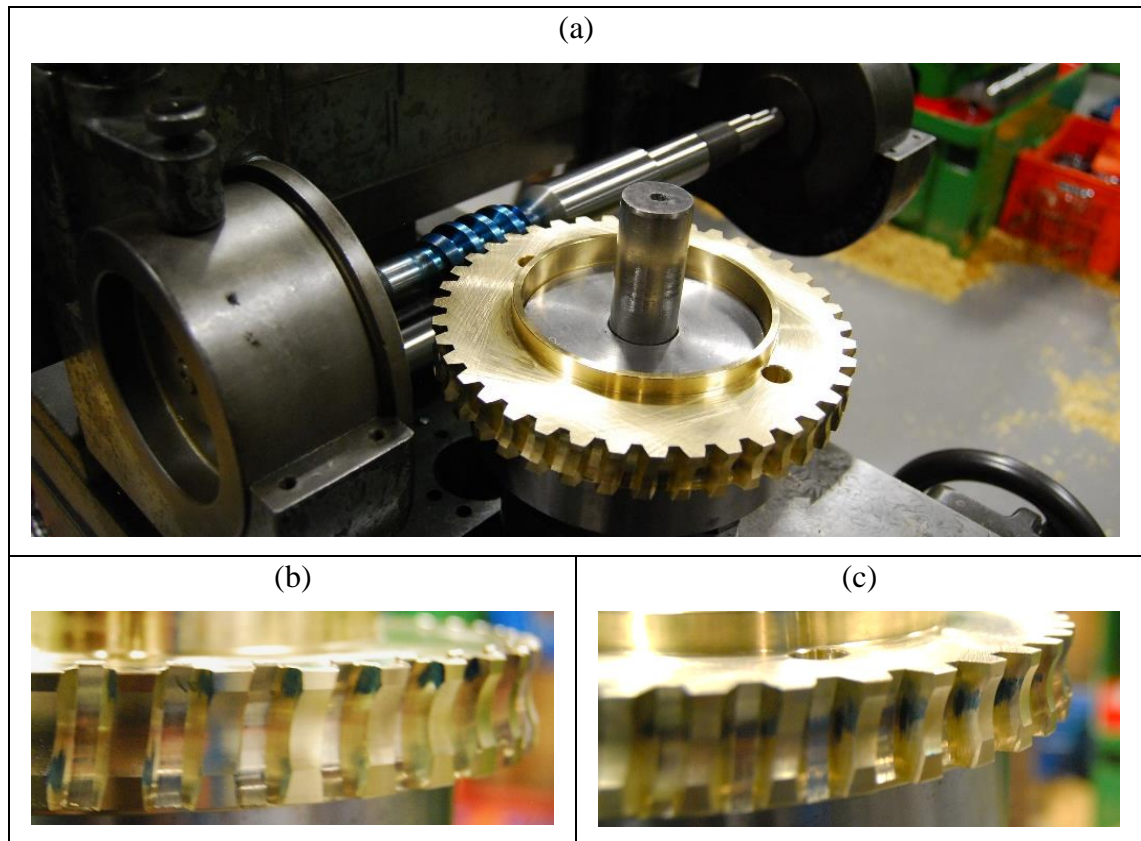


Figure 2.11: Mesh checking of a worm gearset manufactured to BS 721 (British Standards Institution, 1983). (a) worm with blue dye driven against wheel, (b) blue dye transfer from worm to wheel demonstrates edge contact, (c) centre contact achieved by modified hobbing method of applying 2° tilt angle to cutting hob.

Worm gearing in an automotive electronic power steering (EPS) system has been enhanced to address higher torque requirements while reducing the space envelope (Watanabe, Shimizu and Terada, 2006). It is considered that an efficient gear profile is one that works near the addendum of the wheel, as per Figure 2.12. The worm in this case is made from steel and the wheel from polymer, so as torque increases the wheel teeth elastically deflect and the number of contact points increase (Figure 2.12). For the contact points to remain at the wheel addendum at high torque, the worm profile between its pitch line and outer diameter must be modified per Figure 2.13.

Metal-on-polymer combinations are commonly found only in light load applications such as automotive components and robotics (Linquip, 2021). Industrial machinery demands the strength of metallic wheels which, compared to polymer wheels, would reduce elastic deflection of teeth.

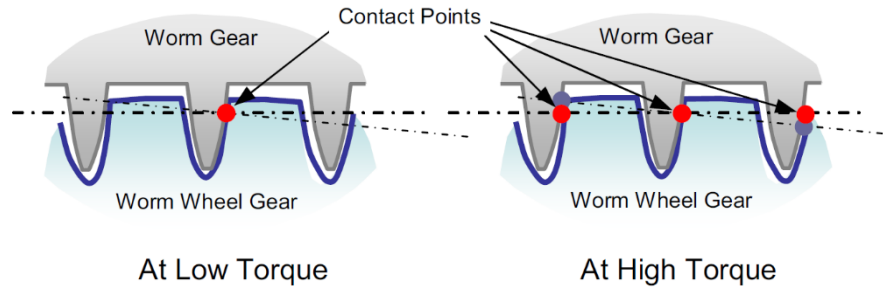


Figure 2.12: Contact points near the wheel addendum at low torque (left) and high torque (right) in EPS worm gearing (Watanabe, Shimizu and Terada, 2006).

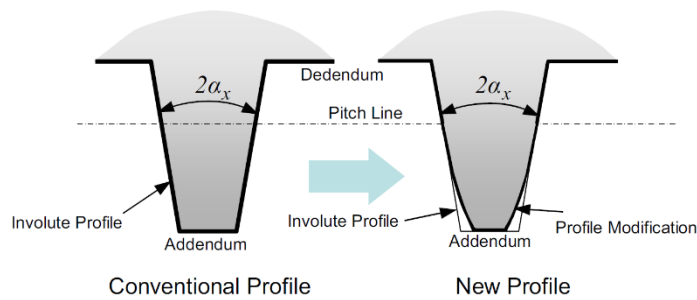


Figure 2.13: EPS worm profile modification between its pitch line and outer diameter (Watanabe, Shimizu and Terada, 2006).

2.7. Imposed Vibration

A practically utilised method of friction reduction and one that has been the subject of theoretical analyses for several decades is the phenomenon of reduced friction force between surfaces subjected to vibration. On one hand, frictional forces may cause undesired vibrations due to stick-slip motion at the contact. Conversely, literature presented in this part of the review suggests that imposed vibration can significantly reduce the friction force between contacting surfaces.

Vibration is applied to the contact by exciting one of the contact bodies in either the normal, longitudinal, or transverse mode. Normal vibration is perpendicular to the plane of contact, transverse is in the plane of contact but perpendicular to the sliding direction, and longitudinal is in the plane of contact and collinear with the sliding direction. Each mode of vibration has a different mechanism by which friction is reduced.

2.7.1. Normal Vibration

The first work investigating the influence of vibration on friction dates to a study by Baker, Claypoole and Fuller (1952) in which they determined that static μ under influence of imposed normal vibration can be minimised to almost zero. Experiments by Fridman and Levesque (1959) in the frequency range 6000-42000 Hz, and by Godfrey (1967) in the range 20-1000 Hz also showed rapid decrease in μ . While pulling a known mass over a surface under normal vibration, periodic changes in contact electrical resistance indicated reduced metal-to-metal contact. Lenkiewicz (1969) also concluded that normal vibration causes changes in the real contact area, creating a floating effect of the sliding object. Hess and Soom (1991) further found that up to 10% reduction of friction force occurs when there is no loss of contact. In this century, custom built pin-on-disc tribometers have shown a decrease in μ with increasing vibration frequency in the range 120-600 Hz, and amplitude 0.015-0.225 mm. This effect was observed between combinations of metallic (Abdo and Tahat, 2008) and non-metallic surfaces (Chowdhury and Helali, 2008). Interestingly, the wear rate of steel-steel contact has also been shown to reduce with normal vibration (Chowdhury and Helali, 2007).

2.7.2. Longitudinal Vibration

Many studies prove that friction can also be reduced by imposing in-plane vibration, either longitudinal or transverse (Mitskevich, 1968; Skåre and Ståhl, 1992; Mutuonga and Onoda, 1995; Littmann, Storck and Wallaschek, 2001; Kumar and Hutchings, 2004). Consider a body of material (Figure 2.5) sliding at constant driven velocity $\dot{\mathbf{x}} = \mathbf{v}_d$ over a base that is vibrating longitudinally i.e., along the same axis at sinusoidal velocity $\dot{\mathbf{x}}_b$. The amplitude of this sinusoidal velocity is denoted v_a . The relative velocity at any instance in time is:

$$\mathbf{v}_r = \mathbf{v}_d - \dot{\mathbf{x}}_b \quad (5)$$

As shown in Figure 2.14, during a single vibration cycle when $\dot{\mathbf{x}}_b > \mathbf{v}_d$, then \mathbf{v}_r in accordance with relationship (5) becomes negative. Therefore, if the amplitude v_a of sinusoidal velocity exceeds drive velocity \mathbf{v}_d then the relative velocity \mathbf{v}_r periodically changes sign. Change in sign constitutes change in direction of \mathbf{v}_r . Since friction force \mathbf{F}_c always opposes the direction of relative velocity \mathbf{v}_r , its periodic change in direction also causes a periodic change in the direction of \mathbf{F}_c . This results in a reduced average friction force during the vibration cycle. Therefore, the reduction of average friction force

occurs as a result of cyclic instantaneous changes in the direction of the friction force vector \mathbf{F}_C , only possible when the condition $v_a > v_d$ is satisfied.

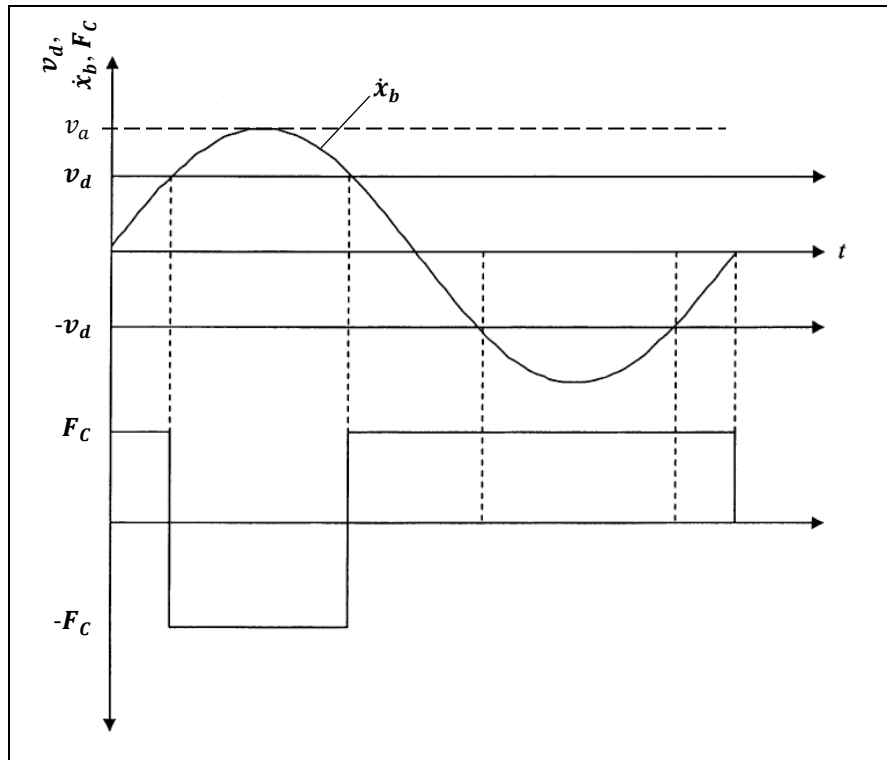


Figure 2.14: Time characteristics of Coulomb friction force during longitudinal vibration. Recreated from Kumar and Hutchings (2004).

This is true where Coulomb friction is assumed, however, as described in 2.2.2 real contact surfaces exhibit an elastic pre-sliding displacement resulting from the elastic deformation of surface asperities. Therefore, the Dahl friction model provides more realistic contact behaviour. Consider the same body of material (Figure 2.6) sliding at constant velocity v_d over the longitudinally vibrating base. The friction force \mathbf{F} is now a function of the elastic contact deformation \mathbf{s} . In this case, the continually changing magnitude and direction of relative velocity \mathbf{v}_r causes the magnitude and direction of elastic deformation \mathbf{s} to change. As a result, in accordance with (3), the friction force \mathbf{F} also changes in a continuous periodic fashion (Figure 2.15).

The condition $v_a > v_d$ must still be satisfied for friction force reduction to occur, however, Gutowski and Leus (2011; 2012) have shown that at small differences between v_a and v_d , the average friction force can reduce without the change in sign of the friction vector, as shown in Figure 2.15, where \mathbf{F} periodically reduces in magnitude but does not change sign. However, as the ratio v_a/v_d increases, the periodic troughs in the \mathbf{F} plot reduce in magnitude and eventually change sign.

In friction reduction estimations, use of simplified models based on the static Coulomb model of friction in which the contact elastic slip is not included creates inconsistency with experimental results. Gutowski and Leus (2011; 2012) showed that significantly better agreement with experiments is achieved by conducting analyses using dynamic friction models, such as the Dahl (1976) model. Dynamic friction models produce a continuous change of the friction force profile (Figure 2.15) as opposed to static friction models which predict stepwise change (Figure 2.14) in the presence of vibration.

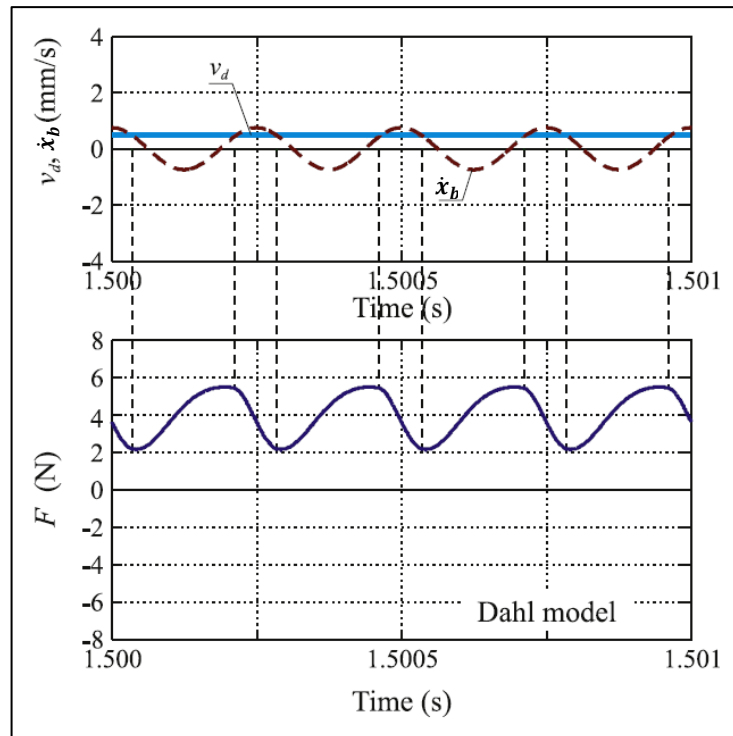


Figure 2.15: Time characteristics of Dahl friction force during longitudinal vibration.

$f = 4000 \text{ Hz}$, $v_a = 0.75 \text{ mm/s} > v_d = 0.5 \text{ mm/s}$. Gutowski and Leus (2012).

2.7.3. Transverse vibration

In the case of transverse vibration (Figure 2.16a), vibration velocity \dot{y}_b occurs along an axis perpendicular to the sliding velocity $\dot{x} = v_d$. This causes changes in the magnitude and direction of relative velocity v_r of vibration (Figure 2.16b). This variable vector of relative velocity of sliding oscillates around the sliding direction causing oscillations of the friction force vector F , resulting in a sub-division of this force into two components, one parallel (F_x) and one perpendicular (F_y) to the direction of motion.

Magnitude of F_x which opposes sliding velocity v_d is smaller than F hence friction in the direction of sliding is reduced. This mechanism is based on Coulomb

friction, therefore, analytical models based on this mechanism (Mutuonga and Onoda, 1995; Littmann, Storck and Wallaschek, 2001; Kumar and Hutchings, 2004) have shown large discrepancy with experimental results.

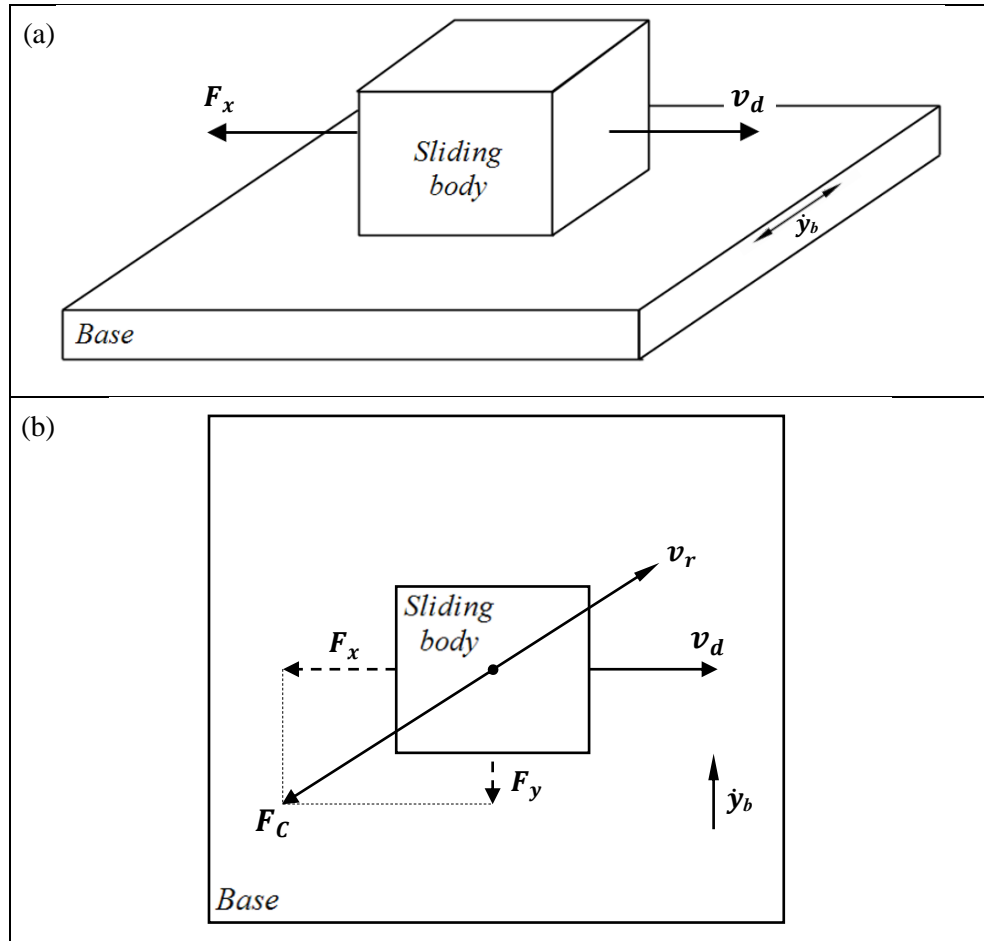


Figure 2.16: Friction force during transverse vibration (a) vibration velocity \dot{y}_b is perpendicular to drive direction v_d (b) top-down view of instantaneous forces acting on sliding body. F_c opposes direction of relative velocity v_r which deviates from direction of v_d .

As with longitudinal vibration (2.7.2), Gutowski and Leus (2015) again demonstrated that much better agreement with transverse vibration experiments is achieved by utilising an analytical model which incorporates Dahl friction. The principle is the same with Dahl friction in that the friction force vector is sub-divided into components F_x and F_y . However, it is the magnitude and direction of elastic deformation s , as a result of relative velocity v_r , that governs the magnitude and direction of the friction force vector. Chapter 4 describes this in more depth as part of analytical model development.

2.7.4. *Practical applications of vibration*

One patent filed by Seibu Electric & Machinery Co., Ltd. (Mori, Kukita and Shimada, 2014) indicates it is feasible to reduce friction in worm gearing by applying vibration, and thereby improve efficiency. The patent claims that while the worm is rotationally driven, its angular velocity via a motor control system can be repeatedly fluctuated at a frequency of 2500 Hz such that the worm is oscillated in the rotational direction. Such motion creates longitudinal vibration; vibration that is in the plane of contact and in the direction of sliding. Vibration control is performed by the electronics and existing motor so there is no need for an additional vibration generating device. Furthermore, the patent claims that the system can be programmed such that vibration is active only when the higher torque output from the actuator is most necessary; this is typically during the initial opening stage or final shutting stage of the valve. This control makes it possible to achieve higher mechanical advantage while still maintaining the self-locking feature of worm gearing.

Considerable research in wider domains has been devoted to exploiting the phenomenon of reduced friction due to vibration. In the sheet metal deep drawing process Jimma *et al.* (1998) have shown that vibrating the drawing die at ultrasonic (above the human audibility limit of 20 kHz) frequency of 28 kHz enables deeper steel cups to be formed. This is due to reduced friction between the sheet metal surface and the drawing die caused by vibration. Siegert and Ulmer (2001) have shown it is possible to further reduce friction by having the drawing dies vibrate parallel to the drawing direction. Wu *et al.* (2021) have investigated the effect of 20 kHz ultrasonic vibration, compared to low frequency vibration in the range 50-200 Hz, concluding that ultrasonic vibration obtains greater friction reduction but also causes more wear and adhesion.

In the emerging field of micro electro-mechanical systems (MEMS) glass is a highly desired material due to its excellent optical properties, chemical stability, and ability to bond to silicon, however, its hardness and brittleness makes micromachining of glass a challenge (Hof and Abou Ziki, 2017). To tackle this, Egashira, Mizutani and Nagao (2002) have used an ultrasonically vibrated glass workpiece to drill microholes of diameter 10 μm . Imposing vibration has been shown to decrease cutting force, extended tool life, increase tool penetration, and produce smoother machined surfaces with no cracks around the rim of the hole.

In the food industry, vibrating cutting blades have become increasingly popular to reduce cutting force, improve the quality of cut and reduce deformation of soft foods

due to the reduction of friction (Liu *et al.*, 2014). The reduction of cutting force is a function of the vibration velocity amplitude and vertical cutting velocity of the blade (Zahn *et al.*, 2006). Arnold *et al.* (2009) conclude that due to reduced friction force the material does not stick to the blade, making vibration particularly effective for cutting viscoelastic and viscoplastic foods. It is also good for fragile and heterogeneous products such as cakes and pastry that would deform under a pressing force. Schneider *et al.* (2009) further add that the texture of the food being cut has a big influence on the extent of friction force reduction. Open porous structures such as short pastry, bread and cake benefit less in terms of friction reduction compared to foods like cheese and sausage that form closed plane surfaces with the blade whilst being cut. In the latter, vibration normal and parallel to the blade's sliding motion also significantly reduce friction force.

Vibration has also been applied to friction stir welding. Friction stir welding is a method by which a rotary tool under pressure produces frictional heat and plastic deformation to permanently join two metallic workpieces together. Large torque and downward force on the rotary tool are needed to generate the necessary heat and plastic material flow. Applying ultrasonic vibration to this process reduces welding loads, increases the fluidity of plastic material, and enhances microstructural properties to improve the weld quality (Xiaochao *et al.*, 2013; Amini and Amiri, 2014; Gao, Wu and Padhy, 2017). Determination of the friction reduction due to vibration between the tool and workpiece is a prerequisite for determining the heat generated during friction stir welding. Numerical simulations by Yang, Wu and Shi (2018) map the friction coefficient on the tool surface, clearly indicating that longitudinal, transverse and normal directions of vibration produce very different friction coefficient distributions.

Interest in the relationship between vibration and friction is further promoted by advanced applications that do not specifically aim to reduce macroscale friction by imposing vibration, however, they do exploit the interdependency of the two entities. Examples are harvesting of vibration energy generated by friction (Wang *et al.*, 2018), travelling wave ultrasonic motors used for focus adjustment in camera lenses (Storck *et al.*, 2002; Liu *et al.*, 2019), vibrating structures in space (Tong *et al.*, 2019) and marine (Jin, Liu and Zhou, 2019) applications, and the rapid development of nanotribology (Socoliuc *et al.*, 2006; Wang *et al.*, 2020).

2.8. Chapter Discussion and Conclusions

Review of literature affirms that a wide variety of gears can be classified by their shaft arrangement. Worm gearing, which operates on parallel and non-intersecting shaft axes, allows for significantly higher gear ratios compared to other gear types, enabling radical increase of output torque in a compact arrangement. An important characteristic of worm gearing is the self-locking capability. However, high frictional losses occur owing to the predominantly sliding contact interactions. As a result, tooth friction losses in worm gearboxes are more significant than bearing, sealing and oil churning losses. Reducing tooth friction would thus yield most benefit from an efficiency standpoint.

Friction is a collection of many complex mechanical and chemical phenomena. Friction forces couple macroscopic mechanical degrees of freedom of contacting objects to the microscopic degrees of freedom which occur, for instance, as heat or plastic deformation of a multitude of small contacts between shearing surfaces, called asperities. Friction can be reduced by many means, Figure 2.17. A hardened steel worm with an alloyed bronze wheel have long been established as the best tribological pair for worm gears. Improvement in surface finish is known to have a further efficiency benefit. Extensive literature is also available comparing different lubricants and coatings, as well as optimising the design of gear teeth.

The type of oil, its viscosity and additives that constitute the lubricant play an important role in the overall efficiency of a gearbox. The purpose of gear oil is to avert boundary lubrication regime such that friction and wear are reduced, and to provide a median by which frictional heat and wear debris are transferred away from the contact. A changeover from mineral to synthetic oils is an effective way of improving efficiency. Fundamental studies such as chemistry, thermodynamics and fluid mechanics must be utilised in developing a lubricant.

Coatings are primarily used to reduce surface damage at high loads with friction reduction being a secondary benefit. A good tribological system must have a compatible selection of materials, lubricant, and coating.

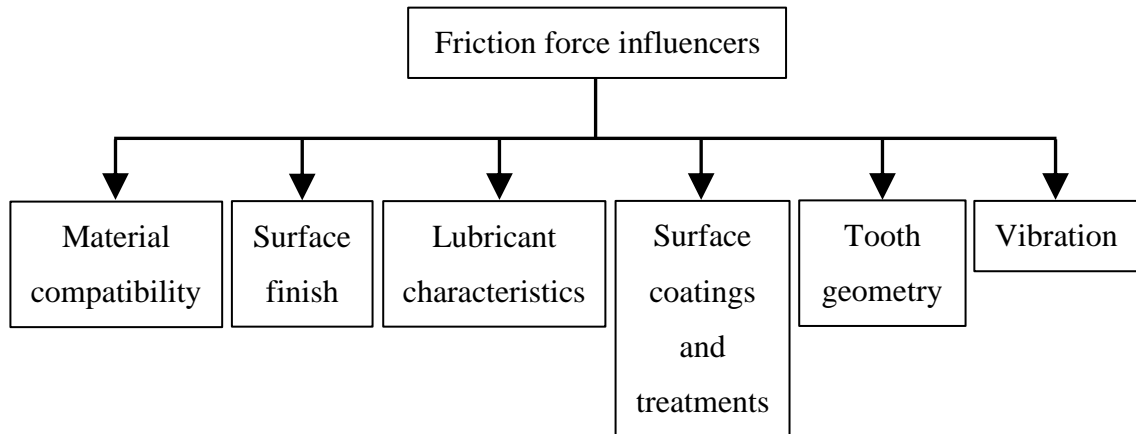


Figure 2.17: Friction force influencers.

Control of friction using vibration is still a developing field of research. Friction is substantially reduced by imposing vibration to the system. The mode of applied vibration also has an influence whereby each mode has differing contact mechanics. When two planar surfaces are in contact, longitudinal vibration has greater friction reduction effect than transverse. Although the phenomenon is exploited in many applications, limited literature studying its relevance to gearing is available. One patent filed by Seibu Electric & Machinery Co., Ltd. (Mori, Kukita and Shimada, 2014) indicates it is feasible to reduce worm gearing friction by applying vibration, and thereby improve efficiency. Furthermore, the patent claims the system can be programmed such that vibration is active only when elevated torque output from the gearset is most necessary. This control makes it possible to achieve a temporarily increase in mechanical advantage while still maintaining the self-locking feature of worm gearing when vibration is deactivated.

Lack of literature regarding the use of vibration to improve gearing efficiency indicates there is a knowledge gap. Learning from literature review is carried forward into chapter 3, in which the different means of friction reduction are compared in terms of their influence on theoretical gear efficiency. This is then used to establish the research focus.

Chapter 3

Worm Gearing and Efficiency

3.1. Chapter Introduction

Building upon knowledge from review of literature, this chapter explores the identified knowledge gap by theoretically assessing the influence of vibration on worm gearing efficiency. A sensitivity analysis calculates theoretical efficiency when vibration is applied compared to when lubricants or coatings are utilised. The purpose of this is to compare the potential efficiency benefit of vibration with other friction reduction means.

The analysis is then extended for a detailed worm gearset design study to optimise gear parameters for maximum theoretical efficiency, while paying attention to not compromise the load capacity of the gearset.

Results of the sensitivity analysis and design optimisation study are reviewed to confirm the route forward for research.

3.2. Efficiency Sensitivity Analysis

Appendix C has efficiency and load capacity calculation spreadsheets for four different worm gearsets. This selection is made to span a range of physical gearset sizes, increasing in centre distance and torque capacity from gearset 1 to 4. This is so that the study of the influence of design optimisation on efficiency in 3.3 is not based solely on one gearset. The calculation spreadsheets are generated using formulae from multiple standards, listed in Table 3.1. For completeness, formulae utilised from these standards are also included in Appendix C. Gearset 2 has been selected for the efficiency sensitivity analysis as this is the most popular size from the four gearsets.

Spreadsheet column range	Description
A-E	Theory from PD ISO/TR 14521 (British Standards Institution, 2011) to calculate gearset efficiency. This standard specifies formulae for calculating the values of gear design parameters and factors relating to the gear size, tooth geometry, material, and surface roughness, which all feed into the calculation of gearset efficiency.
G-K	Theory from BS 721 (British Standards Institution, 1983) to calculate permissible torque, explained in 3.3.1. These columns are not used for sensitivity analysis but to assess load capacity in 3.3.4 and 3.3.5. In addition to worm gearing design formulae that are echoed by PD ISO/TR 14521, standard BS 721 enables determination of factors associated with the speed and torque at which the worm gearsets are expected to operate. Based on these factors the standard provides formulae to calculate the maximum torque that a gearset can output based on its wear life requirement and load bearing capacity.
M-Q	Calculation of efficiency, wheel bending stress and permissible torque based on AGMA theory (American Gear Manufacturers Association, 1992; Budynas and Nisbett, 2011). Bending stress is explained in 3.3.2. These columns are not used for sensitivity analysis but to assess load capacity in 3.3.4 and 3.3.5. AGMA theory provides an alternative set of formulae for worm gearing design compared to British standards PD ISO/TR 14521 and BS 721. It features factors associated with loading and load distribution, as well as accuracy requirements to enable calculation of gearset efficiency, wheel bending and contact stresses, and maximum allowable torque to satisfy the wear life requirement.

Table 3.1: Explanation of Appendix C efficiency and load capacity calculation spreadsheet.

Only columns A-E are of interest initially, to calculate worm gearing efficiency η_{z1-2} , and total gearbox system efficiency η_{ges1-2} . Green spreadsheet cells in Appendix C identify manual data entry cells. Grey cells contain formulae from the relevant standards (Table 3.1) thus their values are automatically computed based on manual data

entered. For consistency, the notations used herein are taken from PD ISO/TR 14521 (British Standards Institution, 2011), which has a comprehensive set of efficiency formulae considering:

- i. Worm gearing design parameters such as centre distance c , gear ratio U and axial module m_{x1} to name a few.
- ii. Type of base oil such as mineral, polyalphaolefin, polyglycol.
- iii. The four factors required to calculate mean tooth coefficient of friction: size factor, geometry factor, material factor and roughness factor.
- iv. Four power losses; meshing, idle running, bearing loss and sealing loss.
- v. Output torque from the wheel gear

3.2.1. Worm Gearing Design Considerations

Standard BS 721 (British Standards Institution, 1983) recommends normal pressure angle of 20° as a guideline to avoid undercutting at the wheel tooth root during manufacture. When designing worm gearing from first principles, the centre distance c and gear ratio U can be selected based on the size and speed requirements. The number of starts z_1 on the worm and the number of wheel teeth z_2 depend on c and U . The diameter factor q_1 of value between 6 and 12 is advised by BS 721. Worms that have identical values of q_1 and z_1 are regarded as being geometrically similar since these two parameters alone determine the worm lead angle γ_{m1} . Knowing the values of c , U , z_1 , z_2 , q_1 and γ_{m1} , the minimum and maximum axial module m_{min} and m_{max} are then calculated. The selected axial module m_{x1} is a value between m_{min} and m_{max} .

If self-locking is desired, it is recommended that q_1 be as low as possible. This method of selecting q_1 permits an initial calculation that is checked for acceptability, and if necessary, iterative changes can be made to maintain the gear design within acceptable limits. Values of q_1 from 12 upwards are seldom required except when the worm is bored.

In the case of a valve actuator (Figure 1.1) the worm gearset is submerged in a bath of mineral oil. The wheel completes a set number of turns to complete a full stroke of opening or closing a valve. At the end of stroke, the output torque from the wheel quickly peaks to a maximum value as the valve is driven into its seat by the actuator. The maximum torque that can be delivered is known as the rated torque T_R . During a stroke the wheel is subjected to lower torque, usually $1/3$ of T_R . This is known as through-travel output torque T_2 . Since the gearing experiences T_R at end of stroke and T_2 through stroke,

gear load capacity for strength is based on T_R whereas load capacity for a desired wear life is based on T_2 .

All factors and losses in columns A-E of the Appendix C calculation spreadsheet can be determined from the parameters listed in Table 3.2. Values of μ , v_{40} and v_{100} assume mineral oil Fuchs Titan Gear MP SAE 80 as gear lubricant, the properties of which are listed in Table 6.9. Worm gearset 2 in Table 3.2 has calculated efficiency $\eta_{z1-2} = 38\%$. The gearbox system efficiency η_{ges1-2} is reduced to 31% due to other estimated power losses such as those caused by bearings and seals. As tooth friction reduction has been established in 2.1.6 as most beneficial for worm gearing efficiency, the gear efficiency η_{z1-2} is of more relevance for sensitivity analysis than the overall gearbox efficiency η_{ges1-2} .

Parameter	Symbol	Value	Unit
Normal pressure angle	α_n		degree
Centre distance	c		mm
Gear ratio	U		
Number of starts on worm	z_1		
Diameter factor	q_1		
Worm lead angle	γ_{m1}		degree
Axial module	m_{x1}		mm
Worm speed	n_1		RPM
Sliding velocity	v_g		m/s
Kinematic viscosity at 40°C	v_{40}		mm ² /s
Kinematic viscosity at 100°C	v_{100}		mm ² /s
Material factor	Y_W		
Arithmetic mean roughness	Ra_1		µm
Coefficient of friction	μ		
Rated torque of valve actuator	T_R		Nm
Wheel through-travel output torque	T_2		Nm
Calculated gear efficiency	η_{z1-2}	38	%
Calculated gearbox efficiency	η_{ges1-2}	31	%

Table 3.2: Input variables (green) and formulated values (grey) for efficiency calculation of worm gearset 2.

3.2.2. Influence of Friction Reduction Method on Efficiency

The influence of different lubricants, coatings and vibration on calculated worm gearing efficiency η_{z1-2} are compared, based on their estimated effect on μ as suggested by the reviewed literature. Estimated values of μ and corresponding sources of data for this analysis are listed in Table 3.3. Mineral oil Fuchs Titan Gear MP SAE 80 is used as the baseline against which other friction reduction means are compared. $\mu = 0.0715$ is based on theory from PD ISO/TR 14521 (British Standards Institution, 2011). Tests by Marques *et al.* (2014) with a polyalphaolefin oil suggest $\mu = 0.0550$. Polyglycol oil Klübersynth UH1 6-640 further reduces μ to 0.0170 (Siebert, 2011). Kinematic viscosity values v_{40} and v_{100} also change with lubricant.

Zhou *et al.* (2013) report 30% μ reduction by adding Fe_3O_4 nanoparticles to mineral oil, whereas Chu, Hsu and Lin (2010) report approximately 50% reduction with diamond nanoparticles. MoS_2/Ti coating in mineral oil shows up to 42% μ reduction compared to uncoated gears, which is further improved to 49% reduction when applied to superfinished gears (Martins, Amaro and Seabra, 2008). DLC coating reduces μ by up to 30% in mineral oil (Tamura *et al.*, 2016).

Since the aforementioned μ reductions are associated with tests conducted in mineral oil, it is assumed for simplicity that the same percentage reductions apply to the baseline mineral oil in Table 3.3.

In the application of vibration, the larger the magnitude of ratio v_a/v_d , the greater the reduction of μ (Gutowski and Leus, 2015). Transverse and longitudinal sinusoidal vibration applied to dry sliding contact respectively reduce μ by 90% and 95% when the velocity ratio is high, $v_a/v_d = 20$. The experimental setup for vibration constitutes a body of known mass driven at constant velocity over a vibrating base. It is assumed the same reduction applies for lubricated contact. These assumptions are made because tests with a wide range of mineral oils have been reported in previous studies and it is not possible to correlate their chemical composition with the published results. In addition to oil composition, the tribological test type and conditions such as normal load, sliding speed, surface finish and coating thickness all vary from one study to another. The assumptions thus enable an approximation of how efficiency is influenced by the different methods of friction reduction.

Means of friction reduction	μ	v_{40}	v_{100}
Mineral oil, Fuchs Titan Gear MP SAE 80	0.0715	92	10
	PD ISO/TR 14521 (British Standards Institution, 2011)	(Fuchs, 2011)	
Polyalphaolefin oil	0.0550	324.38	35.27
	(Marques <i>et al.</i> , 2014)	(Marques <i>et al.</i> , 2014)	
Polyglycol oil, Klübersynth UH1 6-640	0.0170	460	80
	(Siebert, 2011)	(Klüber Lubrication, 2018)	
Fe ₃ O ₄ nanoparticles added to mineral oil	0.0500	92	10
	(Zhou <i>et al.</i> , 2013)	(Fuchs, 2011)	
Diamond nanoparticles added to mineral oil	0.0357	92	10
	(Chu, Hsu and Lin, 2010)	(Fuchs, 2011)	
MoS ₂ /Ti coating in mineral oil	0.0415	92	10
	(Martins, Amaro and Seabra, 2008)	(Fuchs, 2011)	
MoS ₂ /Ti coating on superfinished gears in mineral oil	0.0365	92	10
	(Martins, Amaro and Seabra, 2008)	(Fuchs, 2011)	
DLC coating in mineral oil	0.0500	92	10
	(Tamura <i>et al.</i> , 2016)	(Fuchs, 2011)	
Vibration	0.0036	92	10
	(Gutowski and Leus, 2015)	(Fuchs, 2011)	

Table 3.3: Values of μ , v_{40} and v_{100} for efficiency comparison of different friction reduction methods. Input variables (green) and formulated values (grey).

Altering μ , v_{40} and v_{100} per Table 3.3 results in changes in efficiency η_{z1-2} presented by Figure 3.1. Change from mineral to polyalphaolefin oil increases η_{z1-2} by

6%. Improved efficiency can be obtained by adding nanoparticles or using coatings without change of oil. Change to polyglycol oil gives better efficiency over all oils, coatings and nanoparticles considered. Figure 3.1 suggests the best efficiency η_{z1-2} can be achieved by imposing vibration. This supports the research knowledge gap concluded in 2.7.4 and further strengthens the need for research focus on gear efficiency improvement via vibration induced friction reduction.

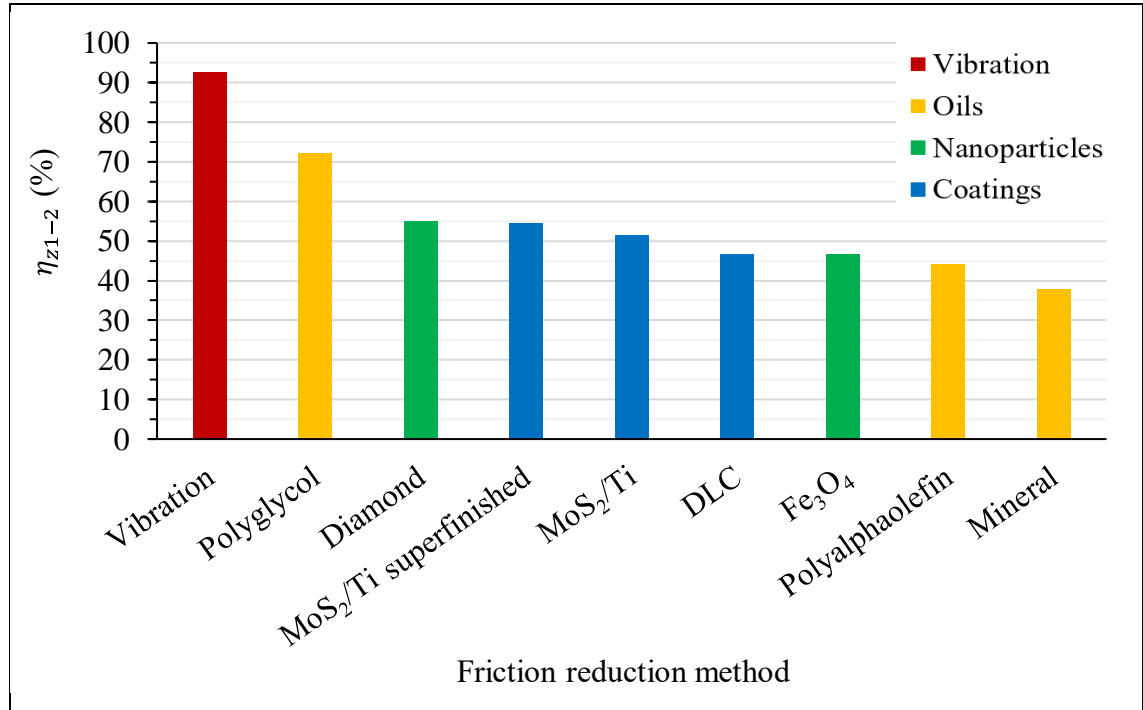


Figure 3.1: Influence of friction reduction method on calculated worm gearing efficiency η_{z1-2} .

3.2.3. Influence of Worm Gearing Parameters on Efficiency

This part of the sensitivity analysis studies the influence of adjusting worm gearing parameters on η_{z1-2} . Input gear variables in Table 3.2 (green) are individually increased in 5% intervals up to 40%. Excluded from this analysis are z_1 since a 40% increase rounded to the nearest whole number still equates to 1 start, v_{40} and v_{100} as these are oil parameters, Y_W which only changes with wheel material, and T_R which according to PD ISO/TR 14521 (British Standards Institution, 2011) influences overall gearbox efficiency η_{ges1-2} but not worm gearing efficiency η_{z1-2} .

The effect on η_{z1-2} is displayed in Figure 3.2 and summarised in Table 3.4. Increasing the value of α_n , c or n_1 has positive influence on η_{z1-2} , whereas U , q_1 , m_{x1} and Ra_1 have negative influence. α_n and Ra_1 have a small influence on η_{z1-2} compared

to c and U . For this gearset an increase of U by over 27%, or an increase of m_{x1} by over 37%, generates a mathematical error due to negative numbers in the calculation of η_{z1-2} .

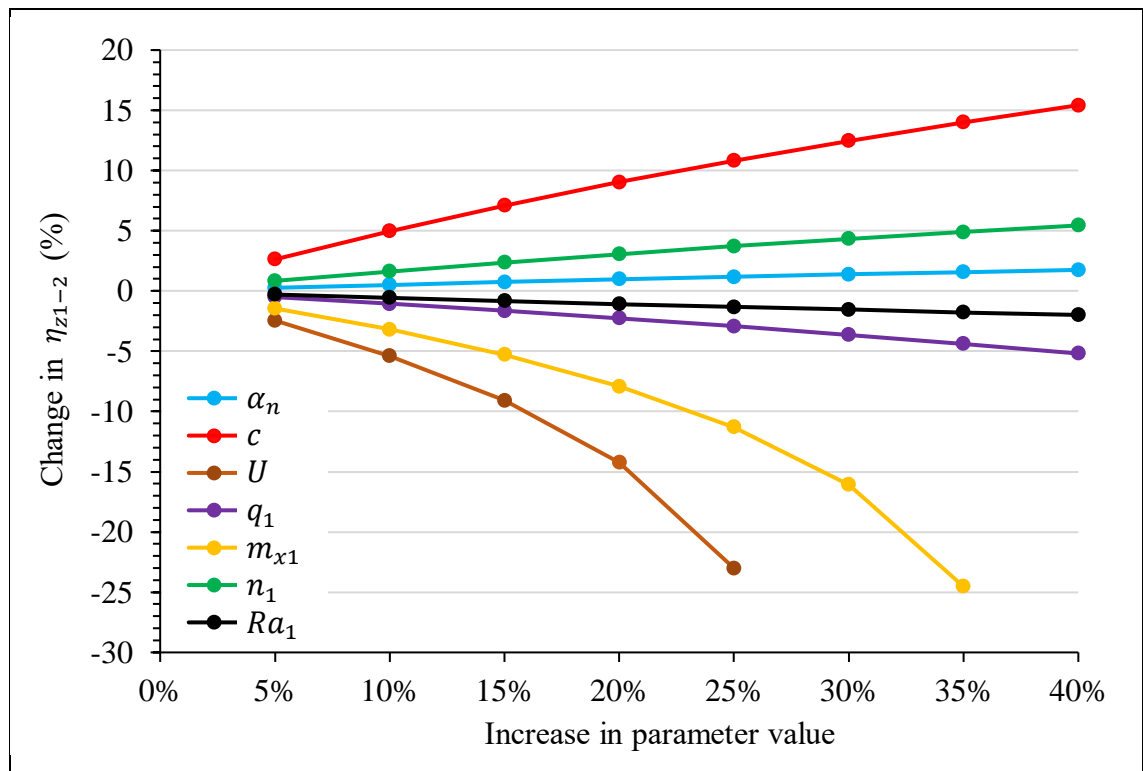


Figure 3.2: Graph showing influence of worm gearing parameters on calculated efficiency η_{z1-2} .

Parameter	Symbol	Effect on η_{z1-2}
Normal pressure angle	α_n	40% increase changes η_{z1-2} by +2%
Centre distance	c	40% increase changes η_{z1-2} by +15%
Gear ratio	U	25% increase changes η_{z1-2} by -23%
Diameter factor	q_1	40% increase changes η_{z1-2} by -5%
Axial module	m_{x1}	35% increase changes η_{z1-2} by -25%
Worm speed	n_1	40% increase changes η_{z1-2} by +5%
Arithmetic mean roughness	Ra_1	40% increase changes η_{z1-2} by -2%

Table 3.4: Summary of influence of worm gearing parameters on calculated efficiency η_{z1-2} .

Ideally, improving gear efficiency should not require redesign of other system components. Figure 3.2 shows that centre distance c has the most positive impact on

efficiency, however, the enclosure containing the worm gearset would also then have to be enlarged, which would increase the product weight and space envelope.

U is selected at design stage to achieve the required T_R , and n_1 is a characteristic of the drive motor powering the worm gear. Changing nominal worm speed requires a change to the motor's physical makeup.

Since the values of c , U and n_1 must be maintained, efficiency improvement can only be achieved by adjusting α_n , q_1 , m_{x1} and Ra_1 . Further analysis in 3.3 aims to maximise efficiency by concurrently optimising these four parameters.

3.3. Design Optimisation

In 3.2.3, it is identified that α_n , q_1 , m_{x1} and Ra_1 are the only worm gearing parameters that can be adjusted to influence efficiency without instigating redesign of other system components. In the previous analysis each parameter is individually adjusted on a single gearset. In this section the four parameters are concurrently optimised to achieve maximum efficiency of worm gearsets. While doing so, gearset load capacity is also given attention since this is also an important consideration in gear design.

The design optimisation study is an extension of the efficiency sensitivity analysis in 3.2, in which only Gearset 2 (Appendix C) is analysed. Gearset 1, 3 and 4 (Table 3.5) are also evaluated in this extended study. The selection not only covers a range of gear sizes but also different gear ratios and operating speeds. A prior understanding of the terms permissible torque, bending stress and contact stress is necessary for this analysis, see 3.3.1-3.3.3.

3.3.1. Permissible Torque

As per Table 3.1, columns G-K of the Appendix C efficiency and load capacity calculation spreadsheets are set up to calculate the permissible torque of worm gearsets using theory from BS 721 (British Standards Institution, 1983). Likewise, columns M-Q are based on AGMA theory (American Gear Manufacturers Association, 1992; Budynas and Nisbett, 2011). The permissible torque of a worm gearset is limited by consideration of contact stress and bending stress, which respectively affect wear and strength. Consequently, the capacity of a worm gearset to deliver torque is determined using calculations concerned with wear and strength.

As explained in 3.2.1, gear load capacity for strength is based on T_R whereas load capacity for a desired wear life is based on T_2 . Therefore, when designed to BS 721 (British Standards Institution, 1983) worm gearsets must meet the following permissible torque criteria; $M_w > T_2$ and $M_s > T_R$. The lower of the two values M_w and M_s should be selected as the wheel permissible torque limit.

BS 721 (British Standards Institution, 1983) permissible torque calculations are based on worm gearing operating life of 26,000 hours. For any other life requirement, a method of conversion is suggested by the standard. In this case, the application requires wear life of 500,000 wheel revolutions. M_w for each gearset is thus based on the equivalent running time for this number of revolutions. The permissible wheel torque for strength M_s is based on 1/10 of the equivalent running time.

The diction in AGMA 6034-B92 (American Gear Manufacturers Association, 1992) is allowable wheel torque $T_{G,all}$ for which the calculation is based on a nominal service life of 25,000 hours.

3.3.2. *Bending Stress*

Most load resisting components are designed to withstand a particular level of stress in the main body of the component. When this stress becomes exorbitant, excessive deflection, yielding and even fracture can occur. Stress associated with excessive deflection is termed bending stress. AGMA 6034-B92 (American Gear Manufacturers Association, 1992; Budynas and Nisbett, 2011) only considers bending stress in wheel teeth since worm teeth are inherently much stronger.

3.3.3. *Contact Stress*

When two curved surfaces roll, or roll and slide against one another with sufficient force, there is shear stress in the contact zone which is largest just below the contact surface. This contact stress can be more significant than bending stress in certain cases. Examples of this, other than gear teeth, are the contact stress between a locomotive wheel and rail, and between a ball bearing and bearing race. The contact stresses are cyclic in nature.

It is postulated that a surface fatigue failure is initiated by this maximum shear stress and then propagated rapidly to the surface. The lubricant then enters the crack that is formed and under pressure eventually expels material from the contact region (Budynas and Nisbett, 2011). The fact that contact stresses frequently lead to fatigue failure explains

why these stresses limit the load carrying capacity of gears. For this very reason, standards BS 721 (British Standards Institution, 1983) and AGMA 6034-B92 (American Gear Manufacturers Association, 1992) encourage consideration of contact stress as well as bending stress during gear design.

3.3.4. Benchmark Worm Gearset Efficiency and Load Capacity

Benchmark calculations of efficiency and load capacity of four worm gearsets are performed. Key parameters for the calculations are listed in Table 3.5, extracted from Appendix C. Results in red are of most interest for comparing the different gearsets, and for comparison with optimised gearsets in 3.3.5.

Gearsets 1 to 4 increase in physical size; value of c gets larger (Table 3.5). v_g coincidentally increases despite the variation in U . Since the lubricant, worm and wheel materials, and method of manufacture are consistent regardless of size, the values of v_{40} , v_{100} , Y_W and Ra_1 do not change.

$\eta_{ges1-2} < \eta_{z1-2}$ in all cases due to other system losses. In comparison to η_{z1-2} , the AGMA 6034-B92 (American Gear Manufacturers Association, 1992) calculated gearing efficiency η_{AGMA} is much higher. This is due to differences in the coefficient of friction μ and μ_{AGMA} reported by the two standards (Figure 3.3), as well as differences in the efficiency equations (6) and (7).

$$\eta_{z1-2} = \left(\frac{\tan \gamma_{m1}}{\tan(\gamma_{m1} + \tan^{-1} \mu_{zm})} \right) 100 \quad (6)$$

$$\eta_{AGMA} = \left(\frac{\cos \alpha_n - \mu_{AGMA} \tan \gamma_{m1}}{\cos \alpha_n + \mu_{AGMA} \cot \gamma_{m1}} \right) 100 \quad (7)$$

There is also difference between M_{26k} and $T_{G,all}$ as equations from the two standards differ. Equations are based on empirical data, and it is likely that British and American standard tests were not like-for-like. $T_{G,all} > M_{26k}$ for gearsets 1-3 and vice versa for gearset 4.

The application requires operating life below 26,000 hours, therefore, permissible torques M_w and M_s exceed M_{26k} . The gearsets comply with BS 721 (British Standards Institution, 1983) criteria stated in 3.3.1; $M_w > T_2$ and $M_s > T_R$.

Owing to differing gear parameters, the wheel tooth bending stress σ_a does not increase with T_R .

Parameter	Symbol	Worm and wheel gearset			
		1	2	3	4
PD ISO/TR 14521					
Normal pressure angle	α_n	■	■	■	■
Centre distance	c	■	■	■	■
Gear ratio	U	■	■	■	■
No. of starts on worm	z_1	■	■	■	■
Diameter factor	q_1	■	■	■	■
Worm lead angle	γ_{m1}	■	■	■	■
Axial module	m_{x1}	■	■	■	■
Worm speed	n_1	■	■	■	■
Sliding velocity	v_g	■	■	■	■
Kinematic viscosity, 40°C	ν_{40}	■	■	■	■
Kinematic viscosity, 100°C	ν_{100}	■	■	■	■
Material factor	Y_W	■	■	■	■
Arithmetic mean roughness	Ra_1	■	■	■	■
Coefficient of friction	μ	■	■	■	■
Mean tooth coefficient of friction	μ_{zm}	■	■	■	■
Rated torque of actuator	T_R	■	■	■	■
Through-travel output torque	T_2	■	■	■	■
Calculated gear efficiency	η_{z1-2}	41	38	73	66
Calculated gearbox efficiency	η_{ges1-2}	28	31	68	58
BS 721					
Permissible torque, 26,000 hrs	M_{26k}	29	88	151	556
Permissible torque for wear	M_w	83	238	440	1557
Permissible torque for strength	M_s	75	262	385	2743
AGMA 6034-B92					
Calculated gearing efficiency	η_{AGMA}	78	69	91	82
Wheel bending stress at T_R	σ_a	256	480	402	356
Allowable torque, 25,000 hrs	$T_{G,all}$	51	119	194	517

Table 3.5: Comparison of calculated benchmark efficiency and load capacity of four gearsets.

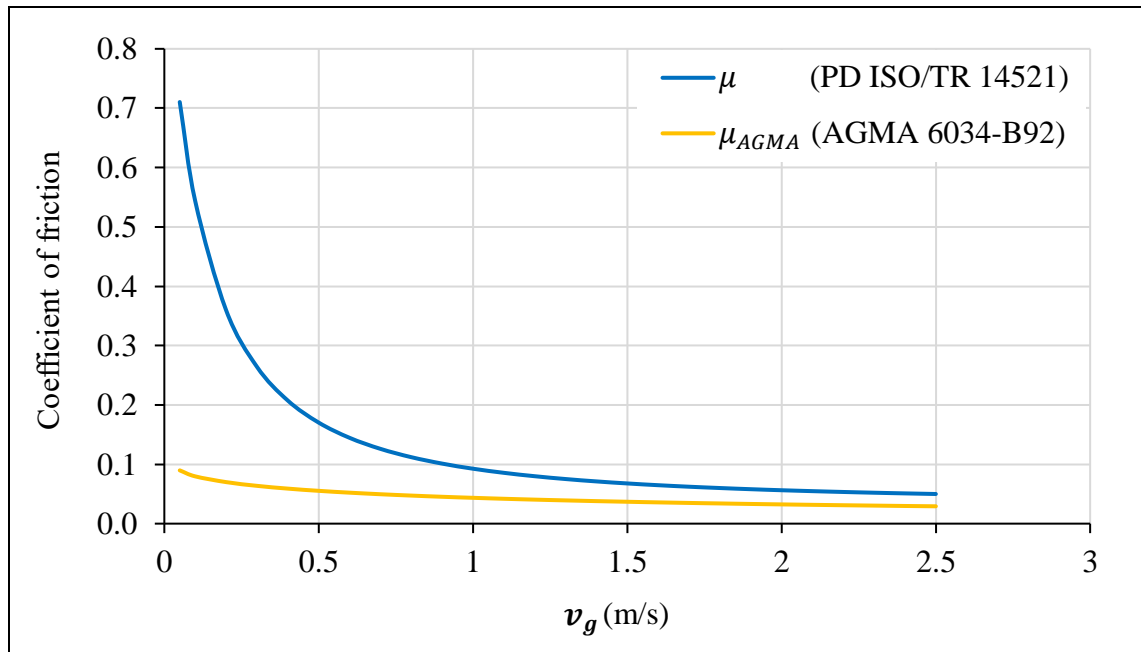


Figure 3.3: Coefficient of friction comparison between two different worm gearing standards.

3.3.5. Optimised Worm Gearset Efficiency and Load Capacity

The outcome from 3.2.3 is that α_n , q_1 , m_{x1} and Ra_1 are the only worm gearing parameters that can be adjusted to influence efficiency. Microsoft® Solver, an add-in for Microsoft® Excel, can find the maximum possible value of η_{z1-2} based on limits on the values of other cells. The objective is to maximise η_{z1-2} without reducing the BS 721 permissible torques M_w and M_s . To achieve this, the parametric constraints listed in Table 3.6 are applied.

The resultant optimised gearsets are detailed in Table 3.7. Comparison with Table 3.5 shows that α_n increases to 30° for all gearsets, q_1 and σ_a increase for gearset 3 only, changes in m_{x1} are small, and Ra_1 is reduced to $0.8 \mu\text{m}$. The calculated efficiencies of benchmark and optimised gearsets are compared by Figure 3.4. There is increase of η_{z1-2} in all cases, but the same is not true for η_{AGMA} .

The permissible wheel torques of benchmark and optimised gearsets are compared by Figure 3.5. Values of M_{26k} are close to those of $T_{G,all}$ despite being calculated from two different standards. Efficiency improvement in Figure 3.4 causes a slight increase of M_w in the optimised gearsets, but no change to M_s . To restate from 3.3.1, the lower of the two values M_w and M_s should be selected as the wheel permissible torque limit. Taking this into consideration, Figure 3.5 shows that design optimisation makes very little improvement on the maximum torque that can be delivered by these gearsets.

Parameter symbol	Applied constraint	Justification
α_n	$20 \leq \alpha_n \leq 30$	BS 721 (British Standards Institution, 1983) recommends $\alpha_n = 20^\circ$ but up to 30° is possible according to Budynas and Nisbett (2011)
q_1	$6 \leq q_1 \leq 12$	Recommended by BS 721
m_{x1}	$m_{min} \leq m_{x1} \leq m_{max}$	Recommended by BS 721
Ra_1	$0.8 \leq Ra_1 \leq 1.6$	It is assumed that modern manufacturing processes can achieve an improved surface finish of hobbed wheel teeth
η_{z1-2}	Maximum value	Objective is to maximise η_{z1-2}
M_w	$\geq M_w$ pre-optimisation	Objective is to not reduce M_w
M_s	$\geq M_s$ pre-optimisation	Objective is to not reduce M_s

Table 3.6: Parametric constraints applied for worm gearset design optimisation.

Parameter	Symbol	Worm and wheel gearset			
		1	2	3	4
PD ISO/TR 14521					
Normal pressure angle	α_n	■	■	■	■
Centre distance	c	■	■	■	■
Gear ratio	U	■	■	■	■
No. of starts on worm	z_1	■	■	■	■
Diameter factor	q_1	■	■	■	■
Worm lead angle	γ_{m1}	■	■	■	■
Axial module	m_{x1}	■	■	■	■
Worm speed	n_1	■	■	■	■
Sliding velocity	v_g	■	■	■	■
Kinematic viscosity, 40°C	ν_{40}	■	■	■	■
Kinematic viscosity, 100°C	ν_{100}	■	■	■	■
Material factor	Y_W	■	■	■	■
Arithmetic mean roughness	Ra_1	■	■	■	■
Coefficient of friction	μ	■	■	■	■
Mean tooth coefficient of friction	μ_{zm}	■	■	■	■
Rated torque of actuator	T_R	■	■	■	■
Through-travel output torque	T_2	■	■	■	■
Calculated gear efficiency	η_{z1-2}	48	45	79	72
Calculated gearbox efficiency	η_{ges1-2}	31	36	73	63
BS 721					
Permissible torque, 26,000 hrs	M_{26k}	34	100	162	599
Permissible torque for wear	M_w	95	273	473	1677
Permissible torque for strength	M_s	75	262	385	2743
AGMA 6034-B92					
Calculated gearing efficiency	η_{AGMA}	80	73	90	82
Wheel bending stress at T_R	σ_a	230	400	424	346
Allowable torque, 25,000 hrs	$T_{G,all}$	45	100	198	503

Table 3.7: Comparison of optimised efficiency and load capacity of four gearsets.

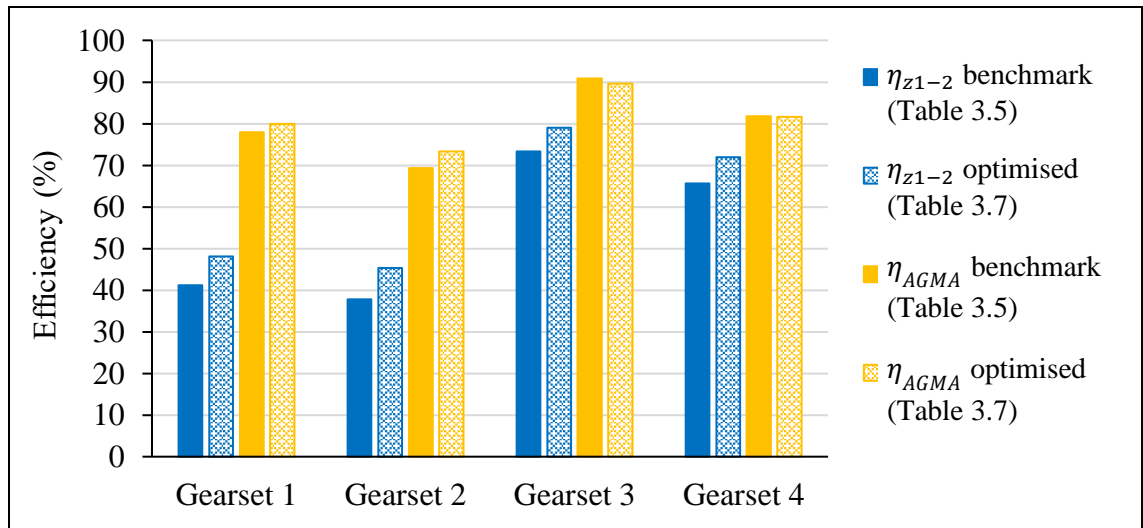


Figure 3.4: Graphical comparison of benchmark vs. optimised η_{z1-2} and η_{AGMA} of four gearsets.

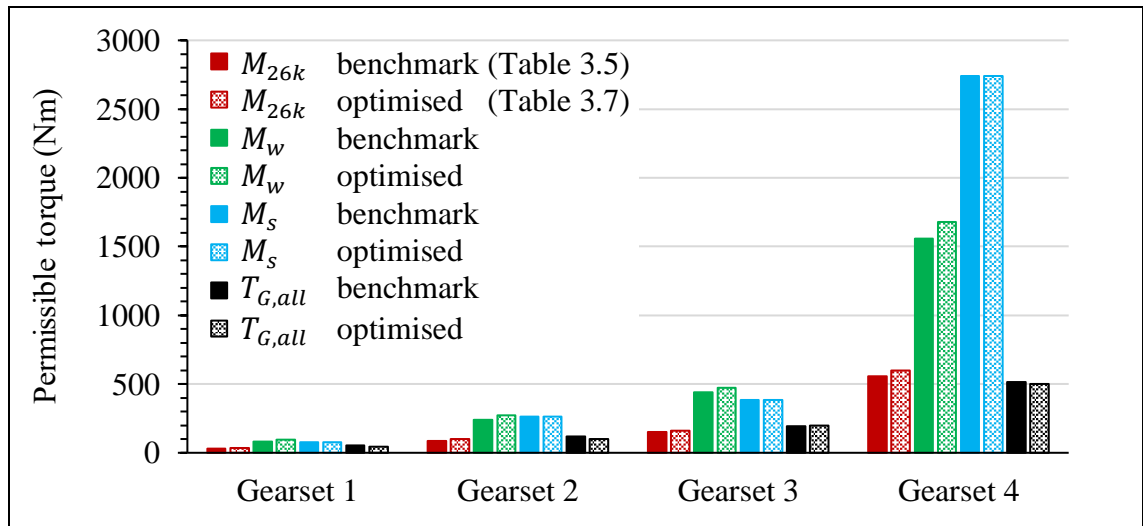


Figure 3.5: Graphical comparison of benchmark vs. optimised M_{26k} , M_w , M_s and $T_{G,all}$ of four gearsets.

3.4. Chapter Discussion and Conclusions

A worm gearing calculation spreadsheet has been created comprising efficiency and load capacity equations from three different standards. Initially, the calculation sheet has been utilised for an efficiency sensitivity analysis. The first part of this analysis has investigated the sensitivity of efficiency to the different means of friction reduction identified by literature review. Using estimated values of μ based on data from various previous studies, the analysis indicates that imposed vibration results in the best worm gearing efficiency improvement, outperforming use of synthetic oils, the addition of oil nanoparticles and use of coatings. This further supports the conclusion in section 2.7.4 wherein research of friction reduction via imposed vibration is identified as a favourable research path.

The second part of the sensitivity analysis has investigated the sensitivity of efficiency to changes in worm gearing parameters. The desire to maintain product space envelope and avoid major redesign of other system components narrows the number of optimisable gear design parameters to just four.

Calculated benchmark efficiency and load capacity of four different gearsets have been compared with improved variants where the four adjustable gear design parameters have been concurrently optimised. While design optimisation adds 7% onto the efficiency η_{z1-2} benchmark (Figure 3.4), there is relatively small improvement to the load capacity of the gearsets (Figure 3.5). In Figure 3.1, an additional 7% to the efficiency η_{z1-2} with mineral oil would put design optimisation at $\eta_{z1-2} = 45\%$, a relatively small efficiency improvement compared to the other friction reduction methods.

Imposing vibration to reduce friction still stands as the most promising method of improving gear efficiency. Chapters 2 and 3 both indicate the need to delve deeper into this field of research, so in the next chapter deeper understanding of contact mechanics is developed via mathematical modelling.

Chapter 4

Analytical Friction Model with Vibration

4.1. Chapter Introduction

Previous chapters have highlighted control of friction using vibration as a developing field. Each mode of vibration has different contact mechanics, and while this phenomenon is exploited in many applications, there is a knowledge gap for its viability in gears. The theoretical evaluation of the influence of vibration on worm gearing efficiency in chapter 3 indicates positive results. For deeper understanding of the mechanisms of friction reduction due to vibration an appreciation of recent mathematical models is necessary.

To date the most comprehensive research into mathematically explaining friction reduction in presence of vibration has been conducted by Gutowski and Leus (2011; 2012; 2015; 2020) for in-plane vibration. Models describing normal vibration have not developed to the same extent, however, finite element method where impact of surfaces can be simulated are potentially a way of achieving this. It is therefore necessary to first understand existing in-plane vibration models. Gutowski and Leus (2011; 2012; 2015) have developed two different mathematical models in Matlab Simulink® to calculate the friction force between contact surfaces subjected to vibration, one model for longitudinal mode and the other for transverse. A brief account of these models is given in this chapter, based on which a new single combined analytical model is developed to evaluate friction force reduction during any in-plane mode of vibration, beyond just longitudinal or transverse. The work in this chapter is thus an extension of sections 2.7.2 and 2.7.3.

4.2. Friction Model for Longitudinal Vibration

Longitudinal vibration can be modelled in a basic two-dimensional domain, depicted by Figure 2.5 and Figure 2.6; vibration x_b of the base occurs parallel to the direction of sliding velocity \dot{x} of the body. Transverse vibration requires modelling in a three-dimensional domain. Longitudinal mode is thus the simplest place to start for comprehending current friction models for vibration. For further simplicity, Coulomb friction (Figure 2.5) is assumed initially, before progressing onto analytical modelling with Dahl friction (Figure 2.6).

4.2.1. Analytical Model Comprising Coulomb Friction

In Figure 2.5 a body slides at constant velocity \dot{x} over a base vibrating with sinusoidal displacement x_b . Uniformly distributed pressure p is applied to the body. The values for \dot{x} , F_N , μ and f are selected per Table 4.1, where F_N is determined from:

$$p = 42333 \text{ N/m}^2$$

$$A_r = 1.2 \cdot 10^{-3} \text{ m}^2$$

$F_N = pA_r = 50.8 \text{ N}$. The body is assumed zero mass, thus has no contribution to F_N .

The relative velocity is:

$$\mathbf{v}_r = \dot{x} - \dot{x}_b = \begin{cases} \dot{x} & \text{if } \dot{x}_b = 0, \text{ i.e. stationary base} \\ \mathbf{v}_r & \text{if } \dot{x}_b \neq 0, \text{ i.e. vibrating base} \end{cases} \quad (8)$$

Sinusoidal displacement x_b of vibration is given by:

$$\mathbf{x}_b = \begin{cases} u_a \sin(\omega t) & \text{if } t \geq t_v \\ 0 & \text{if } t < t_v \end{cases} \quad (9)$$

where u_a is the amplitude of the displacement of vibration, ω the angular frequency, and t_v the time at which vibration is activated. Equation (9) acts as a switch, activating vibration when $t \geq t_v$. The velocity \dot{x}_b of sinusoidal motion is given by differentiating x_b :

$$\dot{x}_b = \frac{d\mathbf{x}_b}{dt} = \begin{cases} u_a \omega \cos(\omega t) & \text{if } t \geq t_v \\ 0 & \text{if } t < t_v \end{cases} \quad (10)$$

The direction and thus the sign of F_C is always opposite to the direction of \mathbf{v}_r .

If $\dot{x}_b > \dot{x}$, then \mathbf{v}_r is negative, therefore F_C is positive.

If $0 \leq \dot{x}_b < \dot{x}$, then \mathbf{v}_r is positive, therefore F_C is negative.

If $\dot{x}_b < 0$, then \mathbf{v}_r is positive, therefore F_C is negative.

The following equation for Coulomb friction is the vector form of (2) which satisfies all the above three conditions:

$$\mathbf{F}_C = -\mu F_N \text{sgn}(\mathbf{v}_r) \quad (11)$$

The product $u_a\omega$ is the amplitude v_a of vibration velocity, hence:

$$v_a = u_a\omega = u_a2\pi f \quad (12)$$

If $v_a > \dot{x}$ then F_C will repeatedly change sign during vibration. The drive force F_d is equal and opposite to F_C , therefore:

$$F_d = -F_C = \mu F_N \text{sgn}(v_r) \quad (13)$$

Since \dot{x}_b and hence v_r in accordance with (8) change during vibration, (13) determines F_d at every time increment $\Delta t = 10^{-6}$ s. The Simulink® model for determining F_d during longitudinal vibration using Coulomb friction per equations (8)-(13) is shown in Figure 4.1. Green blocks indicate configurable input values for computation. The computation starts at $t = 0$ s. The ‘Vibration Switch’ performs the ‘if’ function in (9), activating x_b when $t \geq t_v$.

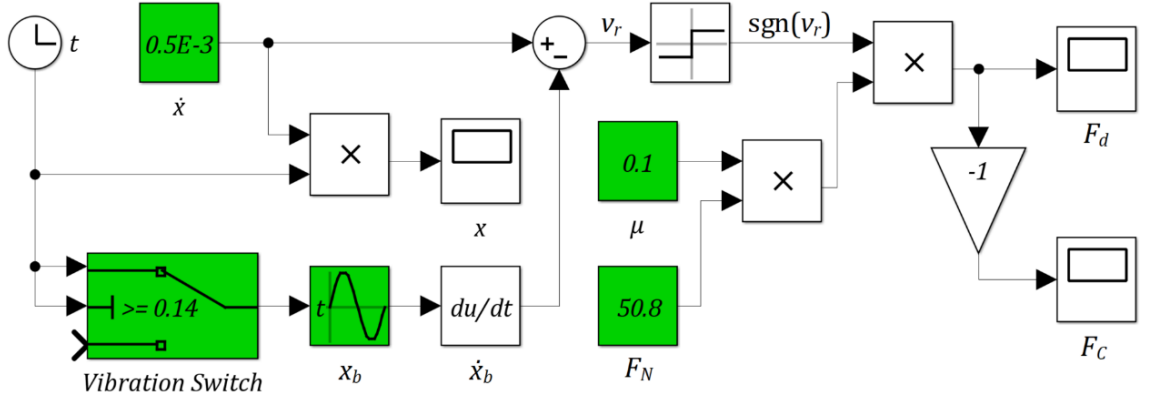


Figure 4.1: Simulink® longitudinal vibration model using Coulomb friction.

4.2.2. Analytical Model Comprising Dahl Friction

As described in 2.2.2, a more realistic approach is to use Dahl (1968; 1976) friction which includes contact compliance. Incremental friction force dF based on (3), and incremental displacement dx are described as follows:

$$dF = k_t ds \quad (14)$$

$$dx = \dot{x} dt \quad (15)$$

Substituting (14) and (15) into (4) gives:

$$\begin{aligned}\frac{k_t d\mathbf{s}}{\dot{\mathbf{x}} dt} &= k_t \left[1 - \frac{k_t \mathbf{s}}{\mu \mathbf{F}_N} \operatorname{sgn}(\dot{\mathbf{x}}) \right]^i \\ \frac{d\mathbf{s}}{dt} &= \dot{\mathbf{x}} \left[1 - \frac{k_t \mathbf{s}}{\mu \mathbf{F}_N} \operatorname{sgn}(\dot{\mathbf{x}}) \right]^i\end{aligned}\quad (16)$$

(16) describes the relationship between the velocity of elastic deformation and the instantaneous velocity $\dot{\mathbf{x}}$ of the sliding body. $\dot{\mathbf{x}}$ can be treated as the relative velocity \mathbf{v}_r . Therefore (16) can be written in a generalised form which considers both the non-vibrating and vibrating cases:

$$\frac{d\mathbf{s}}{dt} = \dot{\mathbf{s}} = \mathbf{v}_r \left[1 - \frac{k_t \mathbf{s}}{\mu \mathbf{F}_N} \operatorname{sgn}(\mathbf{v}_r) \right]^i \quad (17)$$

Gutowski and Leus (2011; 2012; 2015; 2020) have shown good agreement of analytical models with experimental results, as stated in 2.7.2 and 2.7.3. To maintain consistency with their work the value $i = 1$ is used for all computations. The significance of this parameter is explained by Figure 2.7. At the point of breakaway, $\mathbf{F}_c = \mathbf{F}$ and elastic deformation \mathbf{s} is at its maximum value s_{max} . k_t can thus be calculated based on s_{max} :

$$\begin{aligned}\mathbf{F}_c &= \mathbf{F} \\ -\mu \mathbf{F}_N \operatorname{sgn}(\mathbf{v}_r) &= -k_t s_{max} \operatorname{sgn}(\mathbf{v}_r) \\ k_t &= \frac{\mu \mathbf{F}_N}{s_{max}}\end{aligned}\quad (18)$$

Longitudinal vibration is a one-dimensional problem in a two-dimensional domain; Figure 2.6, vibration \mathbf{x}_b acts parallel to the direction of \mathbf{v}_d , therefore, deformation \mathbf{s} of elastic asperity MN occurs in one dimension. In this case (17) can be readily used and its integration determines \mathbf{s} during each time increment $\Delta t = 10^{-6}$ s. The computed value of \mathbf{s} then solves (3). The Simulink[®] model for computing \mathbf{F}_d during longitudinal vibration using Dahl friction per equations (3), (8)-(10), (17) and (18) is shown in Figure 4.2.

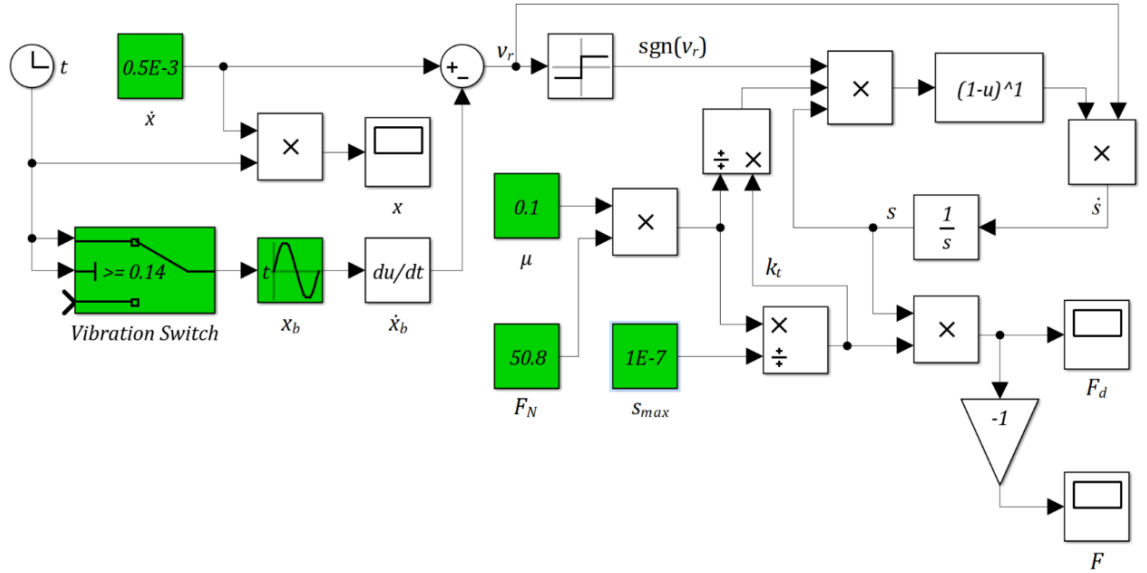


Figure 4.2: Simulink® longitudinal vibration model using Dahl friction.

4.2.3. Analytical Simulations & Results

Six longitudinal vibration Simulink® simulations are performed, listed in Table 4.1. Simulations L_{1-Sim} and L_{2-Sim} are performed with the Coulomb friction-vibration model (Figure 4.1), with $v_a < \dot{x}$ and $v_a > \dot{x}$ respectively. s_{max} is not applicable here since Coulomb friction has no contact compliance.

The remaining simulations are performed with the Dahl friction-vibration model (Figure 4.2). $v_a < \dot{x}$ applies for L_{3-Sim}, and vice versa for L_{4-Sim} to L_{6-Sim}. s_{max} is increased from 10^{-7} to 10^{-5} m.

Ref.	\dot{x} (m/s)	F_N (N)	μ	f (Hz)	v_a (m/s)	s_{max} (m)	Friction Model
L _{1-Sim}	$0.5 \cdot 10^{-3}$	50.8	0.1	200	$0.2 \cdot 10^{-3}$	-	Coulomb (Figure 4.1)
L _{2-Sim}					$1 \cdot 10^{-3}$	-	
L _{3-Sim}					$0.2 \cdot 10^{-3}$	10^{-7}	Dahl (Figure 4.2)
L _{4-Sim}					$1 \cdot 10^{-3}$	10^{-7}	
L _{5-Sim}					$1 \cdot 10^{-3}$	10^{-6}	
L _{6-Sim}					$1 \cdot 10^{-3}$	10^{-5}	

Table 4.1: List of Simulink® basic longitudinal vibration simulations and input values.

In each simulation, the respective model is used to plot F_d against time t . For condition $v_a < \dot{x}$, results are presented in Figure 4.3. Under this condition vibration does not reduce F_d , regardless of whether Coulomb or Dahl friction is used.

Periodic F_d reduction due to longitudinal vibration only occurs when $v_a > \dot{x}$, Figure 4.4. Under this condition Coulomb friction generates a square-wave of F_d ; when $v_r > 0$, F_d is positive and its magnitude equal to F_C , but when $v_r < 0$ the sign of F_d is reversed. By introducing Dahl friction, periodic changes in F_d are described by a smooth wave since relative motion at the contact affects the instantaneous magnitude of s , and consequently F_d . Increasing s_{max} from 10^{-7} to 10^{-5} decreases the extent of periodic F_d reduction until eventually a change in sign of the force vector does not occur. The results agree with the work of Gutowski and Leus (2011), who also concluded that under longitudinal vibration the condition $v_a > \dot{x}$ must be satisfied for friction reduction to occur.

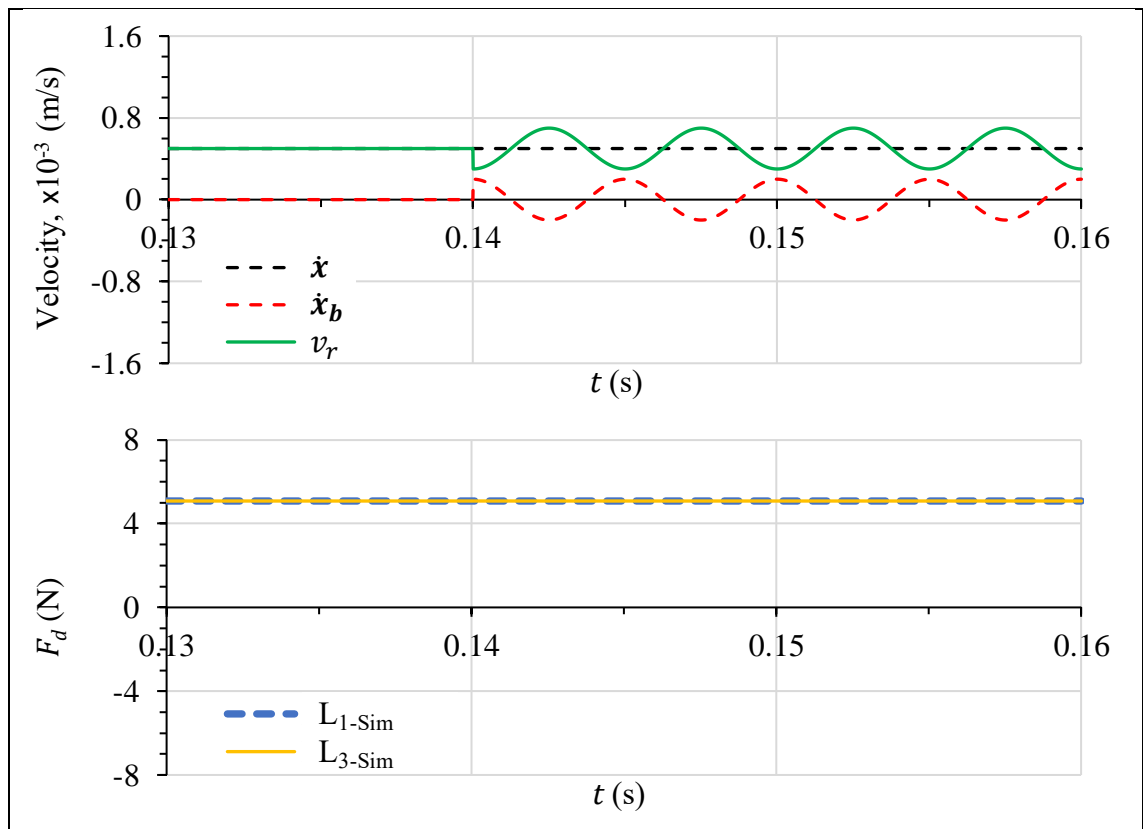


Figure 4.3: Simulink[®] longitudinal vibration results, $v_a < \dot{x}$.

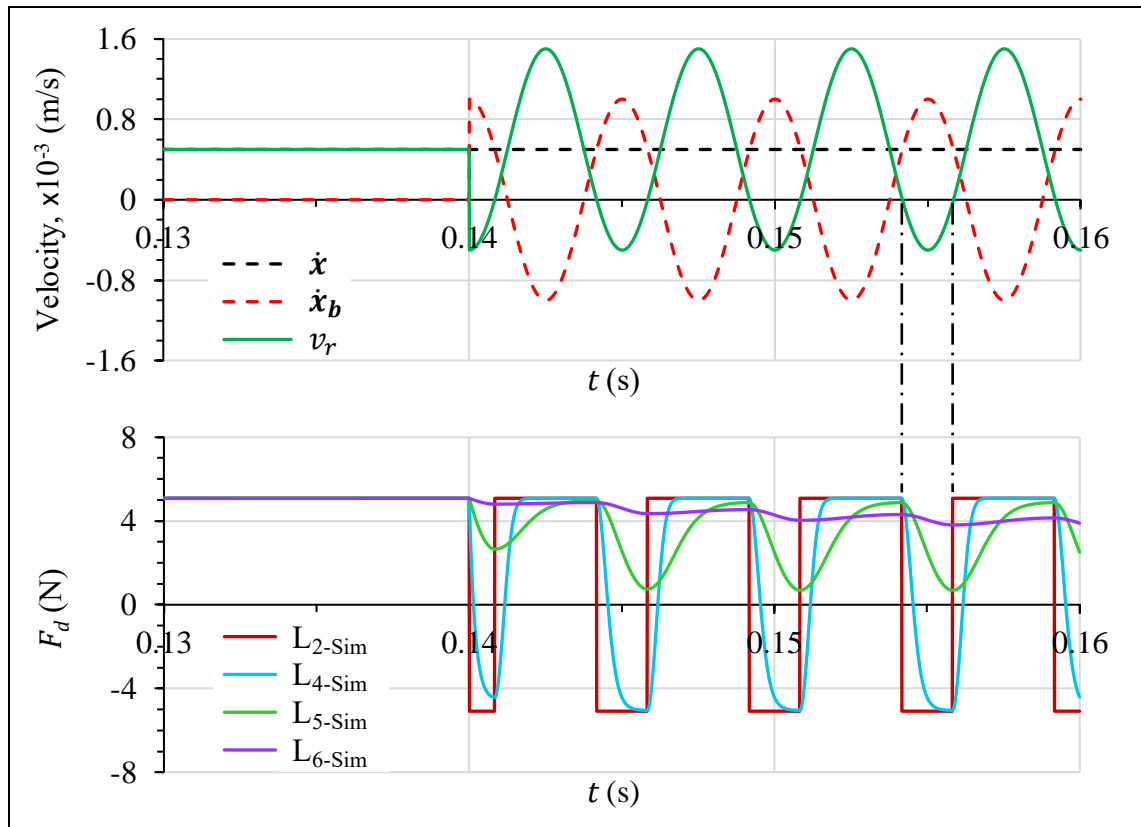


Figure 4.4: Simulink® longitudinal vibration results, $v_a > \dot{x}$.

4.3. Friction Model for Longitudinal Vibration with Drive Compliance

Figure 4.5 shows the test rig developed by Gutowski and Leus (2012) to investigate the influence of longitudinal vibration on friction force. It comprises a body pulled over a base by a driver travelling at constant velocity. During body sliding motion, activation of the exciter makes the base vibrate, while changes in drive force are registered by a ring dynamometer.

To achieve agreement with experimental results Gutowski and Leus (2012) have established that friction models for vibration, while considering compliance of the contact zone (4.2.2), must also include compliance of the mechanical drive system. The driver and dynamometer (Figure 4.5) are elements of the drive system that introduce structural stiffness and damping. Exclusion of these system characteristics, as is the case in Figure 2.6, causes inaccuracy of simulation results. Therefore, development of Figure 2.6 to Figure 4.6 more accurately represents the experimental setup of Gutowski and Leus (2012).

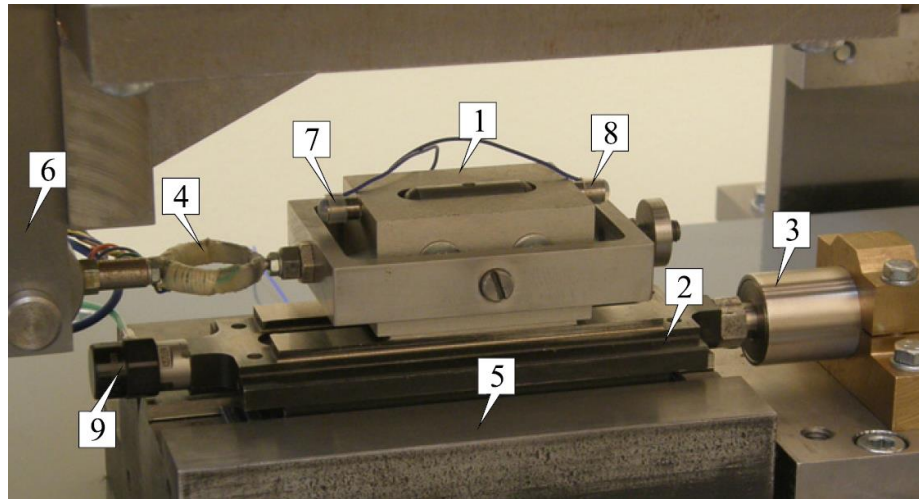


Figure 4.5: Photo of experimental rig developed by Gutowski and Leus (2012) for longitudinal vibration investigation. 1: body, 2: base, 3: vibration exciter, 4: ring dynamometer, 5: fixed foundation, 6: constant velocity driver, 7-9: accelerometers.

Structural stiffness k_d (Figure 4.6) is known and zero structural damping is assumed, hence $h_d = 0$. Movement of body mass m over the vibrating base is imposed by constant drive velocity v_d applied at point B , while a proportion of sinusoidal vibration applied to the base is also transferred to the body, corresponding to an instantaneous external drive force F_d . \dot{x} is thus no longer a constant velocity. F_d is transferred to point A of the sliding body via the drive system.

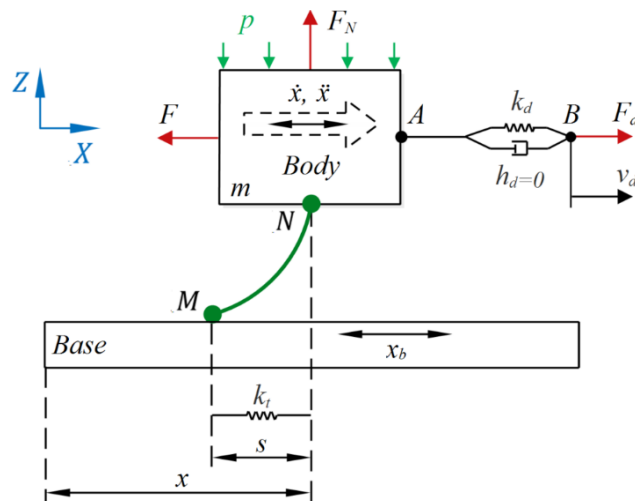


Figure 4.6: Extension of Figure 2.6 to represent the longitudinal vibration experimental setup of Gutowski and Leus (2012). Structural stiffness k_d and damping h_d due to the drive system are also now included.

The derivation and experimental verification of the longitudinal vibration model which includes drive compliance is detailed by Gutowski and Leus (2012). The key equations are included here for reference later in this thesis. The equation describing the body's motion along the X axis is:

$$m\ddot{x} = F_d - F \quad (19)$$

Since the sliding body also receives a proportion of vibration from the base, the distance between points A and B continually changes. Therefore, F_d is a function of the variable elastic deformation of the mechanical drive's components. Assuming the drive system has linear elastic characteristic, F_d is calculated by:

$$\begin{aligned} F_d &= k_d[x_B - x_A] \\ &= k_d[v_d t - x] \end{aligned} \quad (20)$$

Substituting (20) and (3) into (19) gives:

$$m\ddot{x} = k_d[v_d t - x] - k_t s \quad (21)$$

The Simulink[®] model proposed by Gutowski and Leus (2012) which incorporates (3), (8)-(10), (17), (18) and (21) to include compliance of the drive system is shown in Figure 4.7.

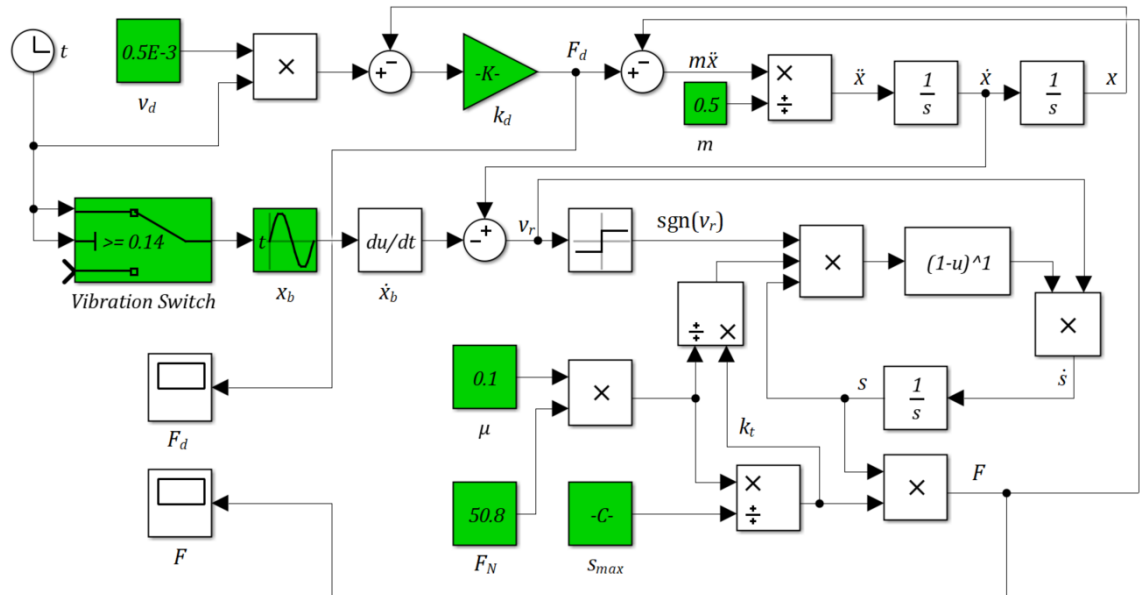


Figure 4.7: Simulink[®] longitudinal vibration model incorporating Dahl friction and drive compliance, based on Gutowski and Leus (2012).

4.3.1. Determination of Mechanical Drive Stiffness

Stiffness k_d of the mechanical drive system is not explicitly specified by Gutowski and Leus (2012), however, it can be calculated from the graphical information provided by the authors (Figure 4.8). The right-hand side of Figure 4.8 brings the notations in line with those used in this thesis.

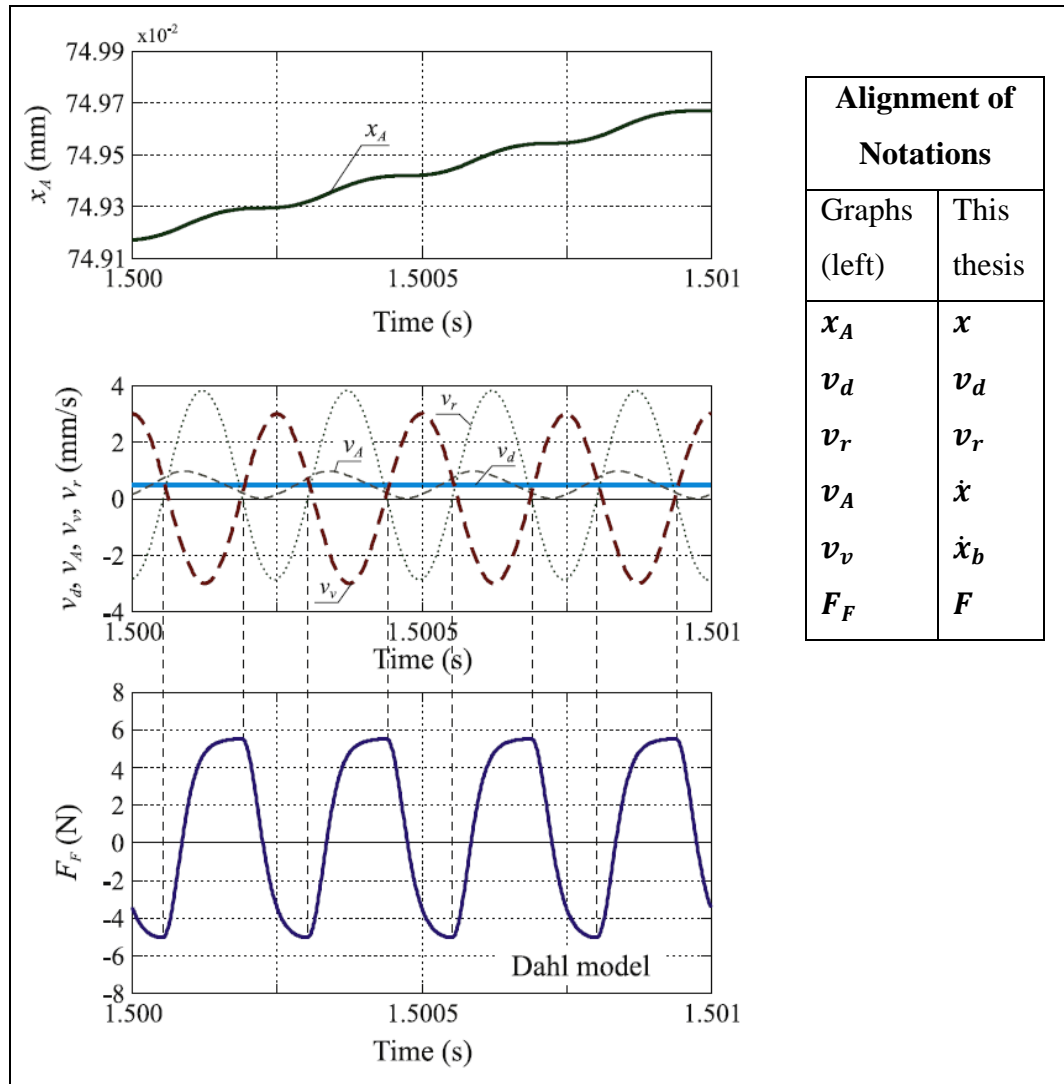


Figure 4.8: Simulink® longitudinal vibration results by Gutowski and Leus (2012) at

$$f = 4000 \text{ Hz}, v_a = 3 \cdot 10^{-3} \text{ m/s} > v_d = 0.5 \cdot 10^{-3} \text{ m/s}.$$

Data acquired from Figure 4.8 using a graph digitiser:

At $t = 1.500001386 \text{ s}$, $\dot{x} = 0.1833 \cdot 10^{-3} \text{ m/s}$

At $t = 1.500006410 \text{ s}$, $\dot{x} = 0.2234 \cdot 10^{-3} \text{ m/s}$, $x = 0.749175 \cdot 10^{-3} \text{ m}$, $F = -3.91128 \text{ N}$

Data given by Gutowski and Leus (2012):

$$m = 0.5 \text{ kg}$$

$$v_d = 0.5 \cdot 10^{-3} \text{ m/s}$$

Substituting into (21) gives:

$$0.5 \left(\frac{\Delta \dot{x}}{\Delta t} \right) = k_d [(0.5 \cdot 10^{-3} \cdot 1.500006410) - 0.749175 \cdot 10^{-3}] - \mathbf{F}$$

$$\begin{aligned} k_d &= \frac{0.5 \left(\frac{\Delta \dot{x}}{\Delta t} \right) + \mathbf{F}}{(0.5 \cdot 10^{-3} \cdot 1.500006410) - 0.749175 \cdot 10^{-3}} \\ &= \frac{0.5 \left(\frac{(0.2234 - 0.1833)10^{-3}}{1.500006410 - 1.500001386} \right) - 3.91128}{(0.5 \cdot 10^{-3} \cdot 1.500006410) - 0.749175 \cdot 10^{-3}} \\ &= 96068 \text{ N/m} \end{aligned}$$

This value of k_d is used throughout. Results of the pre-existing friction model for longitudinal vibration (Figure 4.7) are presented in 4.5.4. An understanding of the more complicated transverse vibration friction model proposed by Gutowski and Leus (2015) is given in the following section. Knowledge of both models is necessary to develop the new model in 4.5.

4.4. Friction Model for Transverse Vibration with Drive Compliance

Transverse vibration is a two-dimensional problem in a three-dimensional domain, Figure 4.9. Vibration \mathbf{y}_b acts perpendicular to the direction of \mathbf{v}_d , therefore, deformation \mathbf{s} of elastic asperity MN now occurs on the two-dimensional plane of sliding XY . (17) can no longer be used readily like it is for longitudinal vibration.

A mathematical model for computing \mathbf{F} and \mathbf{F}_d during transverse vibration exists. The intention is not to give a full account of the model here as it is already detailed by Gutowski and Leus (2015). Only the key relationships are extracted since this model will be further developed in 4.5. The transverse vibration model is more complex than the longitudinal since the trajectory of motion of the body sliding over the vibrating base is a superposition of two motions; the first caused by \mathbf{F}_d , and the second by the transfer of

transverse motion \mathbf{y}_b from the base to the sliding body. N' is the projection of N on the XY plane (Figure 4.9).

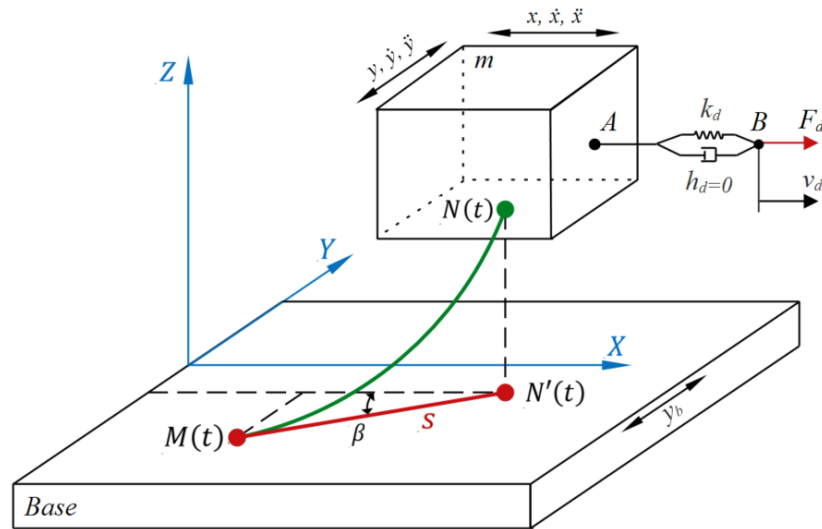


Figure 4.9: Schematic of transverse vibration experimental setup of Gutowski and Leus (2015). Similar to Figure 4.6 except vibrating motion \mathbf{y}_b acts perpendicular to the direction of \mathbf{v}_d , causing change in magnitude and direction β of elastic deformation \mathbf{s} .

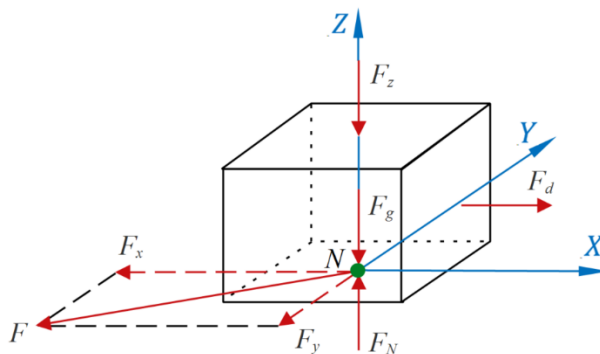


Figure 4.10: Instantaneous forces acting on sliding body (Gutowski and Leus, 2015).

Friction force \mathbf{F} is sub-divided into two components, one parallel (\mathbf{F}_x) and one perpendicular (\mathbf{F}_y) to the direction of \mathbf{F}_d .

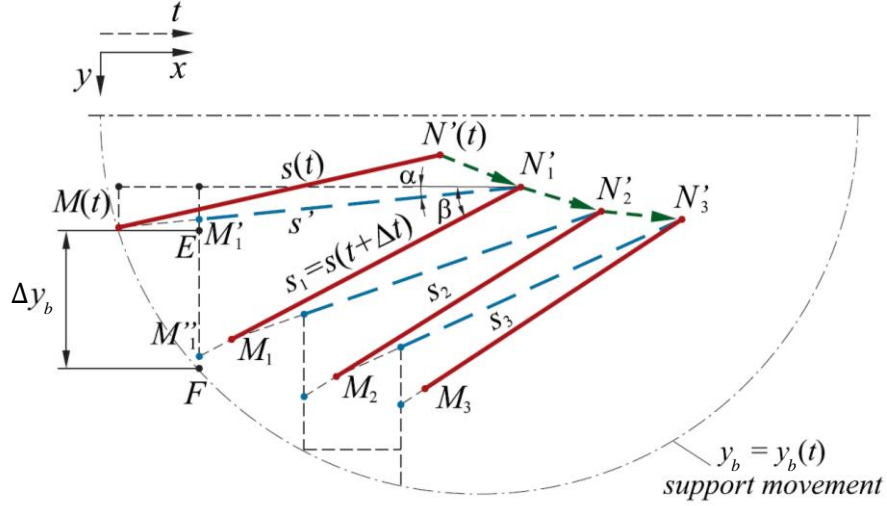


Figure 4.11: Changes in magnitude and direction of elastic deformation \mathbf{s} at consecutive phases of motion (Gutowski and Leus, 2015).

During a consecutive time increment Δt , Figure 4.11 illustrates how M and N' change their relative positions. Consequently, \mathbf{s} undergoes change in its magnitude and direction from $\mathbf{s}(t)$ at the beginning of the first time increment to $\mathbf{s}_1(t + \Delta t)$ at the end of the increment. In the subsequent time increment, further change in relative positions of M and N' causes further change in magnitude and direction of elastic deformation from $\mathbf{s}_1(t + \Delta t)$ to $\mathbf{s}_2(t + 2\Delta t)$, and so forth. During any time increment endpoints M and N' change positions simultaneously, but from a mathematical standpoint this motion can only be described by computing the effect of each end point in turn. Therefore, the change in elastic deformation during each time increment is separated into two phases. In the first phase the intermediate deformation \mathbf{s}' is analysed as a result of N' moving to position N'_1 . In the second phase the final deformation \mathbf{s}_1 is analysed as a result of M moving to position M_1 .

Coordinates of M and N' at the start of the increment are:

$$M(t) = [M_x(t), M_y(t)] \quad (22)$$

$$N'(t) = [N'_x(t), N'_y(t)] \quad (23)$$

and at the end of the increment:

$$M(t + \Delta t) = M_1 = [M_{1x}, M_{1y}] \quad (24)$$

$$N'(t + \Delta t) = N'_1 = [N'_{1x}, N'_{1y}] = [\mathbf{x}, \mathbf{y}] \quad (25)$$

$\mathbf{s}(t)$ is determined from initial coordinates (22) and (23):

$$\mathbf{s}(t) = \sqrt{[N'_x(t) - M_x(t)]^2 + [M_y(t) - N'_y(t)]^2} \quad (26)$$

Due to superposition of motions caused by \mathbf{F}_d and \mathbf{y}_b (Figure 4.9), two equations of motion apply concurrently:

$$m\ddot{\mathbf{x}} = \mathbf{F}_d - \mathbf{F}_x \quad (27)$$

$$m\dot{\mathbf{y}} = \mathbf{F}_y \quad (28)$$

where \mathbf{F}_x and \mathbf{F}_y are components of \mathbf{F} (Figure 4.10), and \mathbf{F}_d is still computed by (20). In the first phase of motion the intermediate elastic deformation \mathbf{s}' is given by:

$$\begin{aligned} \mathbf{s}' &= \mathbf{s} + \Delta\mathbf{s} \\ &= \mathbf{s} + \mathbf{v}_{r1} \left[1 - \frac{k_t \mathbf{s}}{\mu \mathbf{F}_N} \operatorname{sgn}(\mathbf{v}_{r1}) \right]^i \Delta t \end{aligned} \quad (29)$$

where \mathbf{v}_{r1} is the relative velocity associated with the first phase of motion. Direction of \mathbf{v}_{r1} in relation to axis X is determined by angle α (Figure 4.11). Within the same time increment Δt , in the second phase of motion, the base undergoes transverse vibration (Figure 4.9-Figure 4.11) imposed by:

$$\mathbf{y}_b = \begin{cases} u_a \sin(\omega t) & \text{if } t \geq t_v \\ 0 & \text{if } t < t_v \end{cases} \quad (30)$$

$$\dot{\mathbf{y}}_b = \frac{d\mathbf{y}_b}{dt} = \begin{cases} u_a \omega \cos(\omega t) & \text{if } t \geq t_v \\ 0 & \text{if } t < t_v \end{cases} \quad (31)$$

Note the similarity of (30) and (31) with (9) and (10). In the second phase of motion $\Delta\mathbf{y}_b$ of transverse vibration is only partially transferred to endpoint M of the lumped elastic asperity. Therefore, displacement $\overline{\mathbf{M}'_1 \mathbf{M}''_1}$ (Figure 4.11) is only a proportion of the transverse vibration displacement $\Delta\mathbf{y}_b = \overline{\mathbf{EF}}$. This proportion is defined by the transverse vibration transfer coefficient η_y , hence:

$$\overline{\mathbf{M}'_1 \mathbf{M}''_1} = \eta_y \Delta\mathbf{y}_b \quad (32)$$

The consequence of this is a further change of elastic asperity deformation from an intermediate \mathbf{s}' to final magnitude \mathbf{s}_1 :

$$\begin{aligned}
 \mathbf{s}_1 &= \mathbf{s}' + \Delta \mathbf{s}' \\
 &= \mathbf{s}' + \mathbf{v}_{r2} \left[1 - \frac{k_t \mathbf{s}'}{\mu \mathbf{F}_N} \operatorname{sgn}(\mathbf{v}_{r2}) \right]^i \Delta t
 \end{aligned} \tag{33}$$

where \mathbf{v}_{r2} is the relative velocity associated with the second phase of motion. Direction of \mathbf{v}_{r2} in relation to axis X is determined by angle β (Figure 4.11).

Knowing the magnitude of \mathbf{s}_1 and its direction determined by angle β , as well as the coordinates $[\mathbf{x}, \mathbf{y}]$ of point N'_1 , it is possible to determine the coordinates of point M_1 at which the endpoint M is placed after lapse of Δt :

$$M_{1x} = M_x(t + \Delta t) = \mathbf{x} - \mathbf{s}_1 \cos \beta \tag{34}$$

$$M_{1y} = M_y(t + \Delta t) = \mathbf{y} + \mathbf{s}_1 \sin \beta \tag{35}$$

Friction force components \mathbf{F}_x and \mathbf{F}_y are based on Dahl friction (3):

$$\mathbf{F}_x(t + \Delta t) = k_t \mathbf{s}_1(t + \Delta t) \cos \beta \tag{36}$$

$$\mathbf{F}_y(t + \Delta t) = k_t \mathbf{s}_1(t + \Delta t) \sin \beta \tag{37}$$

M_{1x} and M_{1y} computed at the end of interval Δt are then substituted into (22) as $M_x(t)$ and $M_y(t)$ at the start of the next time interval $2\Delta t$. Likewise, \mathbf{x} and \mathbf{y} are substituted into (23) as $N'_x(t)$ and $N'_y(t)$.

At consecutive intervals ($3\Delta t, 4\Delta t, \dots, n\Delta t$) the cycle of equations (22)-(37) is repeated. Figure 4.12 is the Simulink[®] model for this computation. The transverse vibration transfer coefficient value $\eta_y = 0.71$ gives best alignment of the model to results of experiments performed under the conditions $f = 3000$ Hz, $\mathbf{F}_N = 50.08$ N, $k_t = 67.29 \cdot 10^6$ N/m² and \mathbf{v}_d in the range 0.0001-0.0033 m/s (Gutowski and Leus, 2015).

Results of the pre-existing friction model for transverse vibration (Figure 4.12) are presented in 4.5.5. With knowledge of the pre-existing friction models for longitudinal and transverse vibration (4.3 and 4.4), it is possible to combine the two into a newly developed friction model for coupled longitudinal-transverse vibration in 4.5. This makes it possible to evaluate friction force reduction during any in-plane mode of vibration, beyond just longitudinal or transverse.

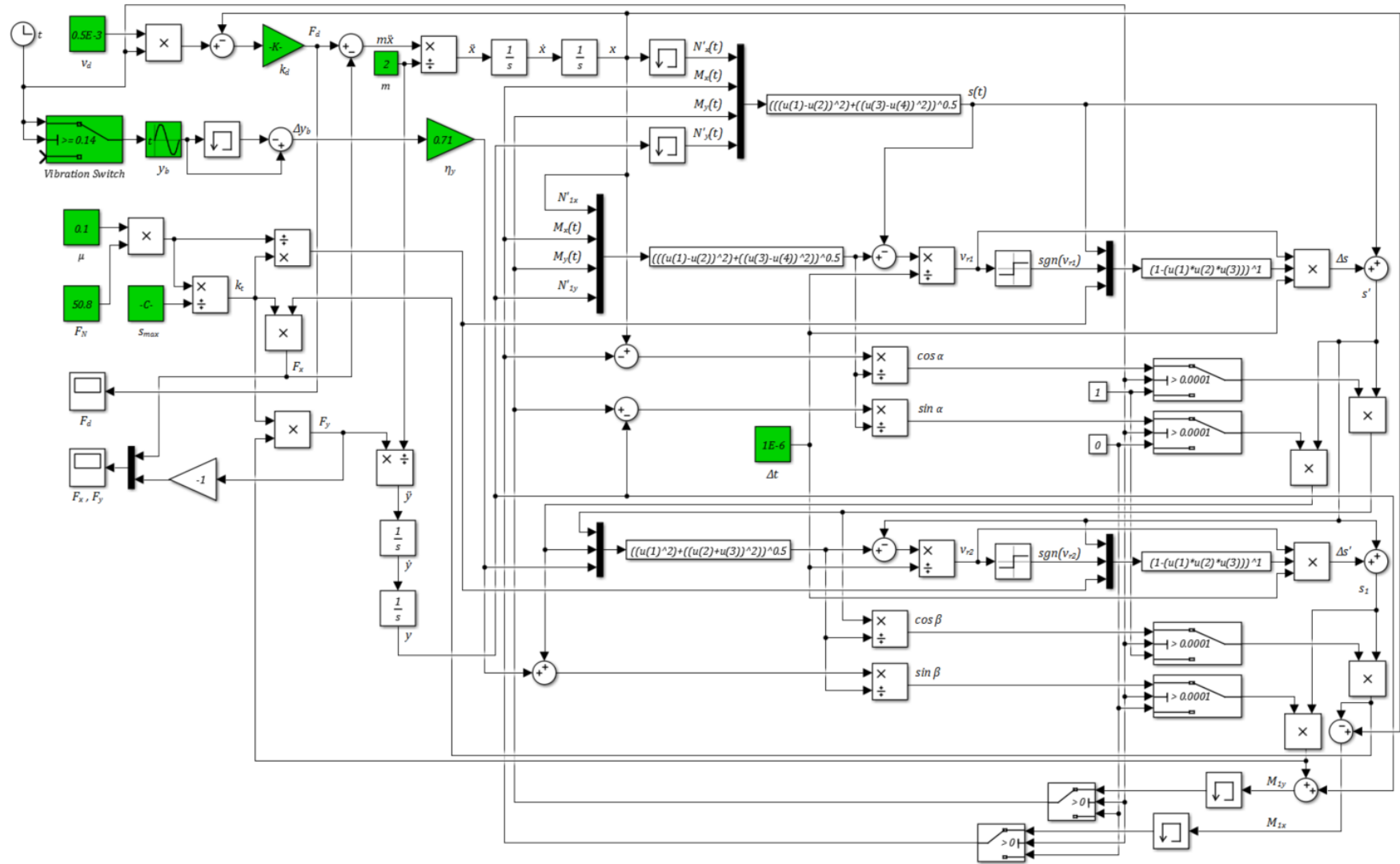


Figure 4.12: Simulink[®] transverse vibration model incorporating Dahl friction and drive compliance, based on Gutowski and Leus (2015).

4.5. Friction Model for Coupled Longitudinal-Transverse Vibration

Previous sections of this chapter have described the development of pre-existing friction models for longitudinal (4.3) and transverse vibration (4.4). Computation for either longitudinal or transverse vibration requires use of separate analytical models for each mode. This section presents the development of these pre-existing models by combining them into a single analytical model to compute F_x , F_y and F_d during longitudinal, transverse and coupled longitudinal-transverse vibration. Previous models 4.3 and 4.4 are used as basis for validating the new model. Publications regarding the new model and its validation (Udaykant Jadav, Amali and Adetoro, 2018a; 2018b) are included in Appendix A and Appendix B.

In the following work (Udaykant Jadav, Amali and Adetoro, 2018a) it is shown that the friction model for transverse vibration (4.4) can be extended for use in any mode of in-plane vibration. An extension of Figure 4.9 is Figure 4.13, wherein vibration is coupled such that longitudinal and transverse components x_b and y_b act simultaneously and in phase. Figure 4.10 still applies for instantaneous forces acting on the sliding body.

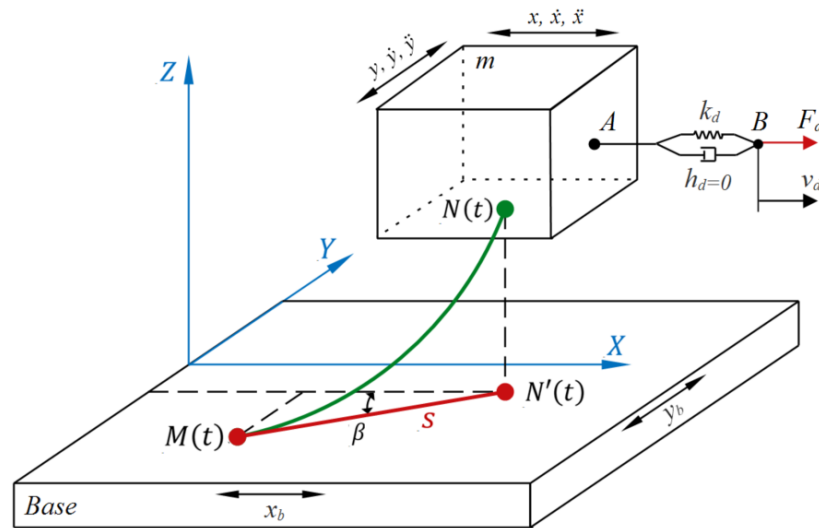


Figure 4.13: Schematic of coupled longitudinal-transverse vibration. Combination of Figure 4.6 and Figure 4.9 such that vibrating motions x_b and y_b act simultaneously and in phase.

The coupled motion is mathematically equivalent to applying vibration along an axis that is at an arbitrary angle θ relative to the direction of sliding, Figure 4.14. θ thus describes the mode of in-plane vibration.

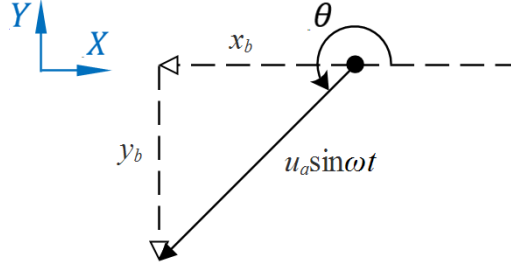


Figure 4.14: Instantaneous displacement vector of base vibrating along an axis at angle θ , separated into components x_b and y_b .

The trajectory of motion of the body sliding over the vibrating base is a superposition of three motions; the first caused by F_d , the second by y_b , and the third by x_b . All three of these motions influence the magnitude and direction of s .

The new coupled model follows formulation described by the sequence of equations henceforth. For clarity, boxed symbols indicate state-dependant variables; their value calculated in the previous time increment is stored for use in the current time increment.

In similarity to 4.4, during a time increment Δt , M and N' (Figure 4.15) change their relative positions thus s undergoes a change in its magnitude and direction from $s(t)$ at the beginning of the time increment to $s_1(t + \Delta t)$ at the end of the increment. Coordinates of M and N' , and magnitude of $s(t)$ at the start of the increment are given by:

$$M(t) = [M_x(t), M_y(t)] = [\boxed{M_{1x}}, \boxed{M_{1y}}] \quad (38)$$

$$N'(t) = [N'_x(t), N'_y(t)] = [\boxed{N'_{1x}}, \boxed{N'_{1y}}] = [\boxed{x}, \boxed{y}] \quad (39)$$

$$s(t) = \boxed{s_1} \quad (40)$$

and at the end of the increment by (24) and (25).

During Δt , M and N' change their relative positions (Figure 4.15). This change is separated into two phases. In the first phase the intermediate deformation s' is analysed as a result of motion of point N' to N'_1 . In the second phase the final deformation s_1 is

analysed as a result of motion of point M'^1 to M'^2 . The displacement from M'^1 to M'^2 is described by components $\overline{M'^1M'^2_x}$ and $\overline{M'^1M'^2_y}$.

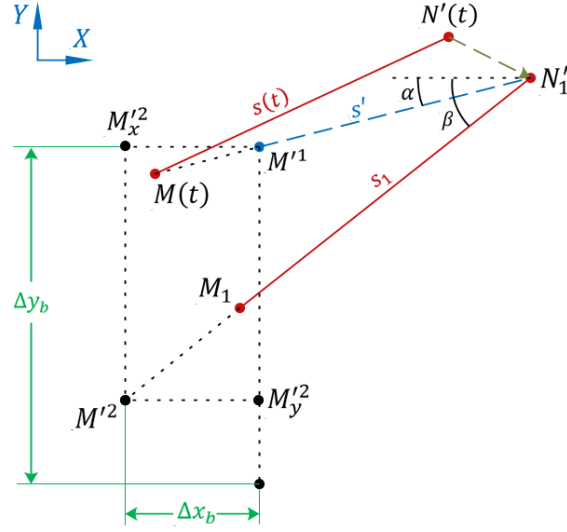


Figure 4.15. Change in magnitude and direction of deformation from \mathbf{s} to \mathbf{s}_1 during a time increment Δt , due to incremental coupled base displacements $\Delta \mathbf{x}_b$ and $\Delta \mathbf{y}_b$ during sliding motion.

Since N is rigidly connected with the sliding body (Figure 4.13), its coordinates $[\mathbf{x}, \mathbf{y}]$ in the XY plane can be described by manipulating (27) and (28):

$$m\ddot{\mathbf{x}} = \mathbf{F}_d - \mathbf{F}_x$$

$$\Delta \mathbf{x} = \iint \frac{\mathbf{F}_d - \mathbf{F}_x}{m} dt dt - \boxed{\iint \frac{\mathbf{F}_d - \mathbf{F}_x}{m} dt dt} \quad (41)$$

$$\mathbf{x} = \Delta \mathbf{x} - \boxed{\Delta \mathbf{x}_b} + \boxed{\mathbf{x}} \quad (42)$$

$$m\ddot{\mathbf{y}} = \mathbf{F}_y$$

$$\mathbf{y} = \iint \frac{\mathbf{F}_y}{m} dt dt \quad (43)$$

where \mathbf{F}_d , \mathbf{F}_x , \mathbf{F}_y and $\Delta \mathbf{x}_b$ are determined by (20), (36), (37) and (53) respectively. In (20), \mathbf{x} is now determined by (42).

4.5.1. First Phase of Motion

In the first phase of motion, during a consecutive time interval Δt , displacement of the sliding body moves point N' to N'_1 (Figure 4.15). At the same instance, M moves

along the path \overline{MN}'_1 to position M'^1 . Consequently, deformation \mathbf{s} changes to an intermediate \mathbf{s}' with a new magnitude and direction. Instantaneous direction of this deformation is determined by angle α , whilst the change in its magnitude by an increment $\Delta\mathbf{s}$, evaluated using (17). Therefore, the magnitude of deformation \mathbf{s}' after this first phase of motion is calculated by:

$$\begin{aligned} \mathbf{s}' &= \mathbf{s} + \Delta\mathbf{s} \\ &= \boxed{\mathbf{s}_1} + \mathbf{v}_{r1} \left[1 - \frac{k_t \boxed{\mathbf{s}_1}}{\mu F_N} \text{sgn}(\mathbf{v}_{r1}) \right]^i \Delta t \end{aligned} \quad (44)$$

Relative velocity \mathbf{v}_{r1} along the line of action of the lumped elastic asperity is determined by:

$$\mathbf{v}_{r1} = \frac{\overline{MN}'_1 - \overline{MN}'}{\Delta t} = \frac{\overline{MN}'_1 - \mathbf{s}}{\Delta t} = \frac{\overline{MN}'_1 - \boxed{\mathbf{s}_1}}{\Delta t} \quad (45)$$

where:

$$\begin{aligned} \overline{MN}'_1 &= \sqrt{[N'_{1x} - M_x(t)]^2 + [M_y(t) - N'_{1y}]^2} \\ &= \sqrt{[x - \boxed{M_{1x}}]^2 + [\boxed{M_{1y}} - y]^2} \end{aligned} \quad (46)$$

Direction of \mathbf{v}_{r1} in relation to axis X is determined by angle α (Figure 4.15)

where:

$$\sin \alpha = \begin{cases} \frac{\boxed{M_{1y}} - y}{\overline{MN}'_1} & \text{if } t > t_v \\ 0 & \text{if } t \leq t_v \end{cases} \quad (47)$$

$$\cos \alpha = \begin{cases} \frac{x - \boxed{M_{1x}}}{\overline{MN}'_1} & \text{if } t > t_v \\ 1 & \text{if } t \leq t_v \end{cases} \quad (48)$$

The ‘if’ conditions in (47) and (48) are necessary to avoid errors in the formulation when dividing by $\overline{MN}'_1 = 0$.

4.5.2. Second Phase of Motion

Within the same time increment Δt , in the second phase of motion, in accordance with Figure 4.14, the base undergoes coupled longitudinal-transverse vibration such that the longitudinal component \mathbf{x}_b and transverse component \mathbf{y}_b act simultaneously and in phase. The instantaneous displacement \mathbf{u} of this oscillation along the axis of vibration is given by:

$$\mathbf{u} = \begin{cases} u_a \sin \omega t & \text{if } t \geq t_v \\ 0 & \text{if } t < t_v \end{cases} \quad (49)$$

Displacement components \mathbf{x}_b and \mathbf{y}_b (Figure 4.14) are thus given by:

$$\mathbf{x}_b = \mathbf{u} \cos \theta \quad (50)$$

$$\mathbf{y}_b = \mathbf{u} \sin \theta \quad (51)$$

and the instantaneous velocity \mathbf{v} of this oscillation along the axis of vibration is given by:

$$\mathbf{v} = \begin{cases} u_a \omega \cos \omega t & \text{if } t \geq t_v \\ 0 & \text{if } t < t_v \end{cases} \quad (52)$$

where $u_a \omega = v_a$ as per (12).

In longitudinal vibration where θ is 0° or 180° (Figure 4.14), \mathbf{x}_b repeatedly changes direction while \mathbf{y}_b remains zero. In transverse vibration where θ is 90° or 270° , \mathbf{y}_b repeatedly changes direction while \mathbf{x}_b remains zero. During any other vibration mode, the direction of both \mathbf{x}_b and \mathbf{y}_b will change.

After the lapse of Δt , the base incremental displacements $\Delta \mathbf{x}_b$ and $\Delta \mathbf{y}_b$ (Figure 4.15) are:

$$\Delta \mathbf{x}_b = \mathbf{x}_b - \boxed{\mathbf{x}_b} \quad (53)$$

$$\Delta \mathbf{y}_b = \mathbf{y}_b - \boxed{\mathbf{y}_b} \quad (54)$$

The effect of incremental displacement $\Delta \mathbf{x}_b$ is described by (42), whereas the effect of $\Delta \mathbf{y}_b$ by (55). As per the transverse vibration model in 4.4 (Gutowski and Leus, 2015), $\Delta \mathbf{y}_b$ is only partially transferred to endpoint M , therefore, the displacement $\overline{M^1 M_y^2}$ of point M^1 comprises only a part of the incremental displacement $\Delta \mathbf{y}_b$ of the base:

$$\overline{M^1 M_y^2} = \eta_y \Delta \mathbf{y}_b \quad (55)$$

where η_y is the transverse vibration transfer coefficient from 4.4 introduced by Gutowski and Leus (2015). Consequently, in this second phase of motion, intermediate deformation \mathbf{s}' changes to final magnitude \mathbf{s}_1 . Instantaneous direction of this deformation is determined by angle β (Figure 4.15), whilst the change in its magnitude by an increment $\Delta\mathbf{s}'$. In similarity with the previous phase (4.5.1), $\Delta\mathbf{s}'$ can be evaluated using (17). Therefore, the final magnitude \mathbf{s}_1 after this second phase of motion is calculated by (33), in which relative velocity \mathbf{v}_{r2} along the new line of action of the lumped elastic asperity is determined by:

$$\mathbf{v}_{r2} = \frac{\overline{N'_1 M'^2} - \overline{N'_1 M'^1}}{\Delta t} = \frac{\overline{N'_1 M'^2} - \mathbf{s}'}{\Delta t} \quad (56)$$

where:

$$\begin{aligned} \overline{N'_1 M'^2} &= \sqrt{[\mathbf{s}' \cos \alpha]^2 + [\mathbf{s}' \sin \alpha + \overline{M'^1 M'^2}]^2} \\ &= \sqrt{[\mathbf{s}' \cos \alpha]^2 + [\mathbf{s}' \sin \alpha + \eta_y \Delta y_b]^2} \end{aligned} \quad (57)$$

Direction of \mathbf{v}_{r2} in relation to axis X is determined by angle β (Figure 4.15)

where:

$$\sin \beta = \begin{cases} \frac{\mathbf{s}' \sin \alpha + \eta_y \Delta y_b}{\overline{N'_1 M'^2}} & \text{if } t > t_v \\ 0 & \text{if } t \leq t_v \end{cases} \quad (58)$$

$$\cos \beta = \begin{cases} \frac{\mathbf{s}' \cos \alpha}{\overline{N'_1 M'^2}} & \text{if } t > t_v \\ 1 & \text{if } t \leq t_v \end{cases} \quad (59)$$

The ‘if’ conditions in (58) and (59) are necessary to avoid errors in the formulation when dividing by $\overline{N'_1 M'^2} = 0$. The coordinates of point M_1 after lapse of Δt are then determined by (34) and (35), and friction components \mathbf{F}_x and \mathbf{F}_y by (36) and (37).

4.5.3. Consecutive Time Increments

The values of state-dependant variables listed in Table 4.2 computed during Δt are carried forward to the next consecutive time increment $2\Delta t$. At consecutive increments ($3\Delta t, 4\Delta t, \dots, n\Delta t$) the sequence of equations (38)-(59), including (20) and (33)-(37), is repeated. The Simulink[®] friction model for coupled longitudinal-transverse

vibration based on these equations is shown in Figure 4.16. Blue blocks indicate additional operations and differences compared to the pre-existing transverse model (Figure 4.12) proposed by Gutowski and Leus (2015). Green blocks, as with previous schematics, indicate configurable input values for the computation.

State-dependant variable	Computed during Δt by	Carried forward to $2\Delta t$ for use as
$\iint \frac{F_d - F_x}{m} dt dt$	(41)	$\boxed{\iint \frac{F_d - F_x}{m} dt dt}$ in (41)
x	(42)	\boxed{x} in (39) and (42)
y	(43)	\boxed{y} in (39)
x_b	(50)	$\boxed{x_b}$ in (53)
y_b	(51)	$\boxed{y_b}$ in (54)
Δx_b	(53)	$\boxed{\Delta x_b}$ in (42)
s_1	(33)	$\boxed{s_1}$ in (40), (44) and (45)
M_{1x}	(34)	$\boxed{M_{1x}}$ in (38), (46) and (48)
M_{1y}	(35)	$\boxed{M_{1y}}$ in (38), (46) and (47)

Table 4.2: State-dependant variables for coupled vibration model of friction.

The Simulink[®] coupled vibration model, Figure 4.16, is executed in longitudinal mode (see 4.5.4), followed by transverse (see 4.5.5), then coupled modes (see 4.5.6). Longitudinal and transverse results are validated against those from pre-existing models, Figure 4.7 and Figure 4.12, which themselves are already verified against experimental data (Gutowski and Leus, 2012; Gutowski and Leus, 2015). Results presented in sections 4.5.4-4.5.6 have been published in a journal article, Appendix A (Udaykant Jadav, Amali and Adetoro, 2018a).

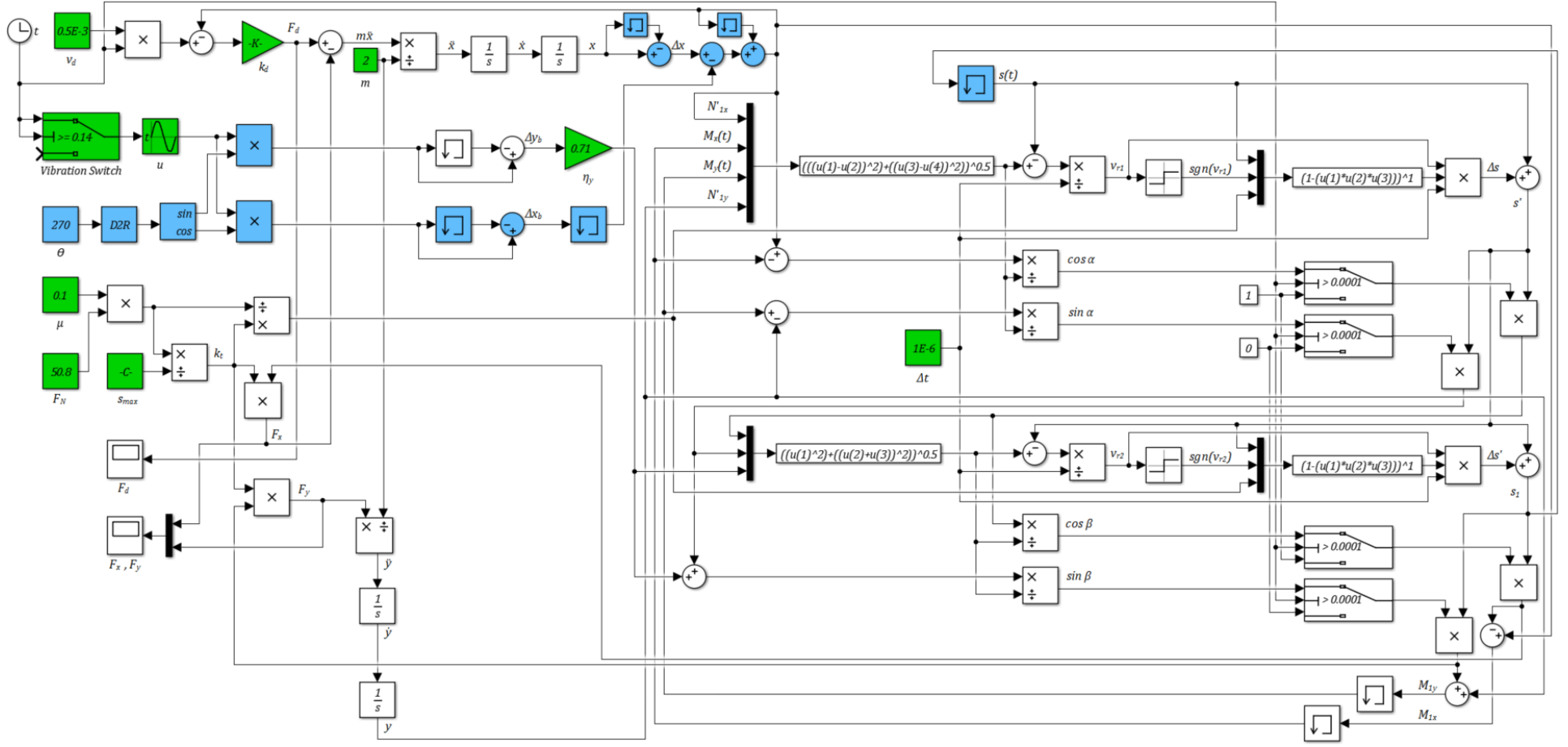


Figure 4.16: Simulink® friction model of coupled vibration incorporating Dahl friction and drive compliance.

4.5.4. Model Validation for Longitudinal Mode

The pre-existing longitudinal model (Figure 4.7) and the coupled model (Figure 4.16) have been executed with identical input values, listed in Table 4.3. η_y , θ and Δt are only applicable to the coupled model. Since \mathbf{y}_b in (51) remains zero at $\theta = 0^\circ$ or 180° , $\overline{\mathbf{M}'^1 \mathbf{M}'^2}$ given by (55) also remains zero, therefore, η_y has no influence on longitudinal vibration results. The value of k_d has been determined in 4.3.1. The magnitude s_{max} is selected using (18) such that $k_t = 80 \cdot 10^6$ N/m. The total simulation time of 1 s has been used.

Parameter	Input value for pre-existing model	Input value for new coupled model
v_d	$0.5 \cdot 10^{-3}$ m/s	$0.5 \cdot 10^{-3}$ m/s
k_d	96068 N/m	96068 N/m
m	0.5 kg	0.5 kg
t_v	0.14 s	0.14 s
f	4000 Hz	4000 Hz
μ	0.1	0.1
F_N	55 N	55 N
s_{max}	$6.875 \cdot 10^{-8}$ m	$6.875 \cdot 10^{-8}$ m
η_y	N/A	0.71
θ	N/A	0°
Δt	N/A	$1 \cdot 10^{-6}$ s

Table 4.3: Input values for comparison of pre-existing longitudinal vibration model with new coupled model.

Figure 4.17 illustrates the computed variability of drive force F_{dv} under the influence of longitudinal vibration in relation to the magnitude F_{ds} of this force without vibration, as a function of a dimensionless coefficient $k_v = v_d/v_d$. Each data point on the graph corresponds to the result of a single simulation. Results from the pre-existing model form a trend indicated by the dashed line. Superimposed longitudinal vibration results from the new coupled model show very good agreement with the pre-existing model by Gutowski and Leus (2012). In longitudinal vibration there is no reduction of drive force when $k_v \leq 1$.

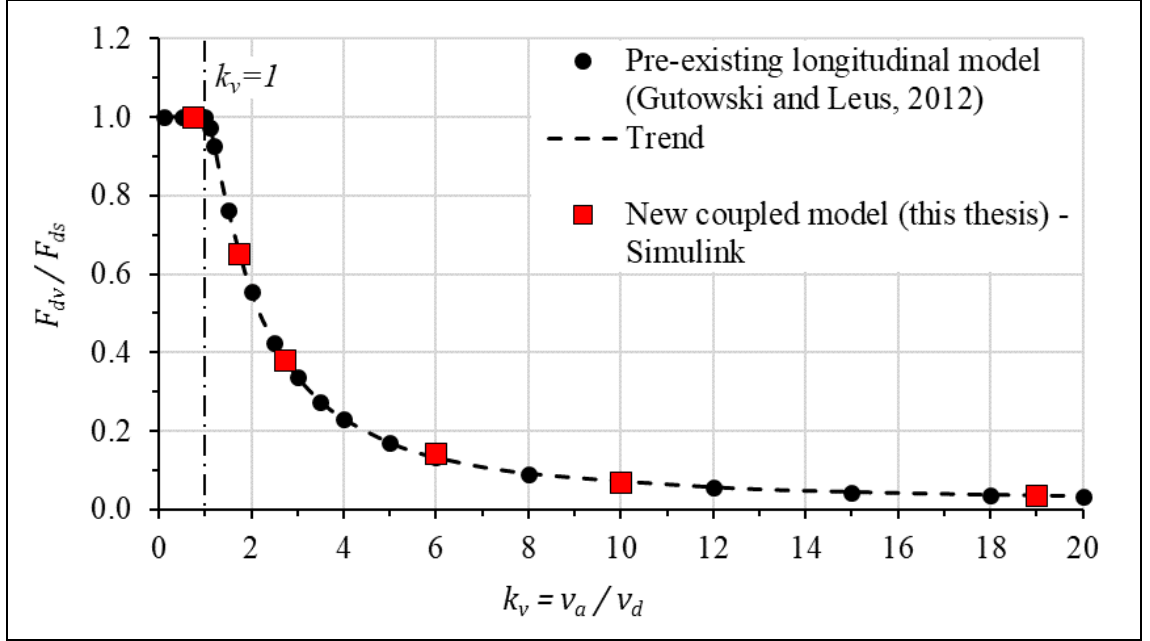


Figure 4.17: Comparison of change in F_{dv}/F_{ds} with k_v , longitudinal vibration.

Changes in F_d and F_x with time, computed using the new model when $k_v = 6$ ($v_a = 3 \cdot 10^{-3}$ m/s) are plotted in Figure 4.18 and Figure 4.19 in comparison to results from the pre-existing longitudinal vibration model (4.3). Simulations begin with the body stationary, hence $F_d = 0$ N at $t = 0$ s (Figure 4.18). Application of v_d at $t > 0$ s causes elastic deformation s to increase, resulting in a steady rise in F_d until $t \approx 0.12$ s, at which time breakaway occurs due to F_d reaching the magnitude $F_c = \mu F_N = 5.5$ N. Vibration activation at $t = 0.14$ s significantly reduces the magnitude of F_d as the body continues to slide. A characteristic of the new model is that it produces greater undulation of F_d . This is due to the computation of x , equation (42), being different to how x is determined in the pre-existing longitudinal model. This undulation diminishes as the vibration mode θ approaches transverse at 90° and 270° , see Figure 4.21. The reduced drive force F_{dv} due to vibration is thus determined by averaging its magnitude within a single cycle:

$$F_{dv} = \frac{1}{n} \sum_{n=1}^n F_{dv_n}(t + \Delta t_n) \quad (60)$$

where n is the number of time intervals into which a single vibration cycle is divided:

$$n = \frac{1}{f \Delta t} \quad (61)$$

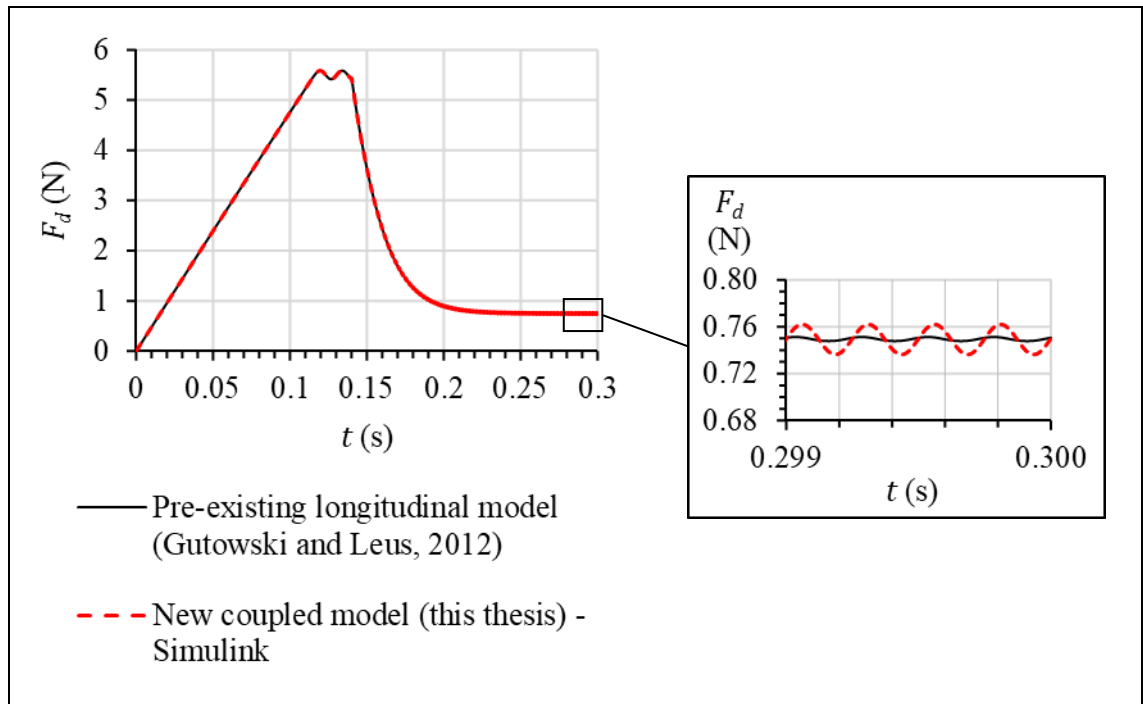


Figure 4.18: Comparison of time varying F_d at $k_v = 6$, longitudinal vibration.

F_d reduces due to cyclic changes in opposing friction force F_x , both in magnitude and direction (Figure 4.19). The average value of F_x reduces from $\mu F_N = 5.5$ N without vibration to a lower value when vibration is activated. Analytical F_x results of the new model show an exact match to the pre-existing longitudinal model.

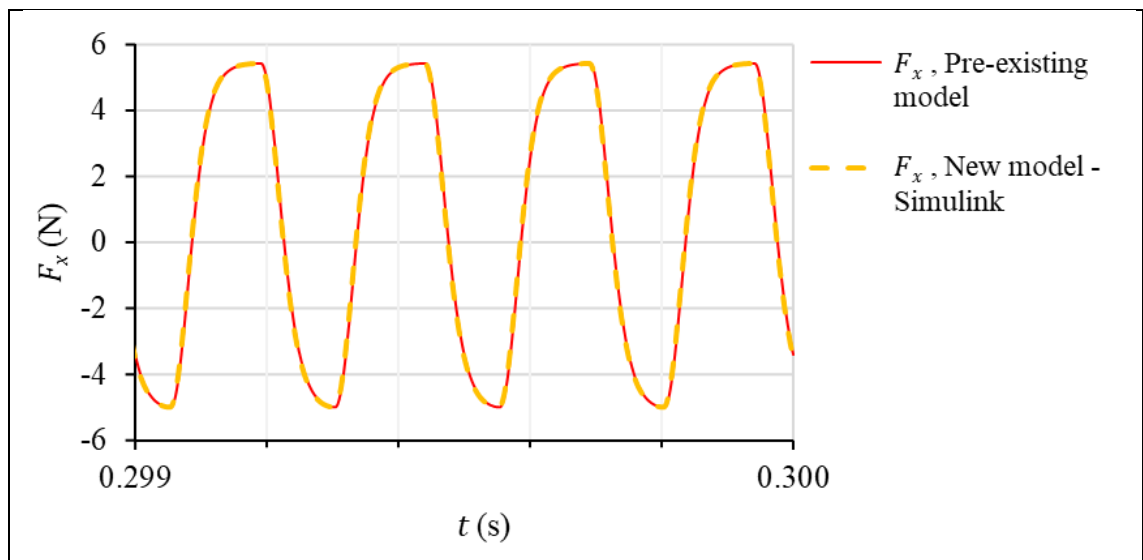


Figure 4.19: Comparison of time varying F_x at $k_v = 6$, longitudinal vibration.

4.5.5. Model Validation for Transverse Mode

The pre-existing transverse model (Figure 4.12) and the coupled model (Figure 4.16) have been executed with identical input values, listed in Table 4.4. As in 4.5.4, θ and Δt are only applicable to the coupled model. The magnitude s_{max} is selected using (18) such that $k_t = 67.29 \cdot 10^6$ N/m. The total simulation time of 1 s has been used.

Parameter	Input value for pre-existing model	Input value for new coupled model
v_d	$0.5 \cdot 10^{-3}$ m/s	$0.5 \cdot 10^{-3}$ m/s
k_d	96068 N/m	96068 N/m
m	2 kg	2 kg
t_v	0.14 s	0.14 s
f	3000 Hz	3000 Hz
μ	0.1	0.1
F_N	50.8 N	50.8 N
s_{max}	$7.549 \cdot 10^{-8}$ m	$7.549 \cdot 10^{-8}$ m
η_y	0.71	0.71
θ	N/A	270°
Δt	N/A	$1 \cdot 10^{-6}$ s

Table 4.4: Input values for comparison of pre-existing transverse model with new coupled model.

Figure 4.20 illustrates the computed variability of normalised drive force F_{dv}/F_{ds} under the influence of transverse vibration, as a function of a dimensionless coefficient $k_v = v_a/v_d$. Superimposed transverse vibration results from the new coupled model show very good agreement with the pre-existing model by Gutowski and Leus (2015). Unlike longitudinal vibration, in transverse vibration there is reduction of drive force when $k_v \leq 1$.

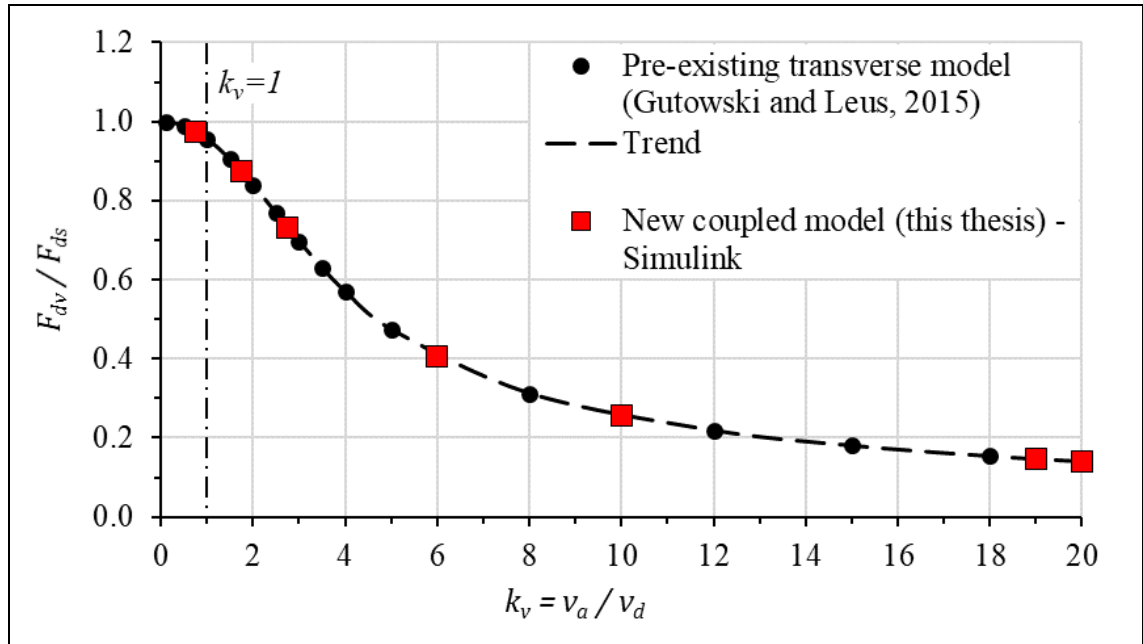


Figure 4.20: Comparison of change in F_{dv}/F_{ds} with k_v , transverse vibration.

Changes in F_d , and friction force components F_x and F_y with time, computed using the new model when $k_v = 20$ ($v_a = 10 \cdot 10^{-3}$ m/s) are plotted in Figure 4.21 and Figure 4.22 in comparison to results from the pre-existing transverse vibration model (4.4). Breakaway occurs when F_d reaches magnitude $F_C = \mu F_N = 5.08$ N. Vibration activation at $t = 0.14$ s significantly reduces the magnitude of F_d as the body continues to slide.

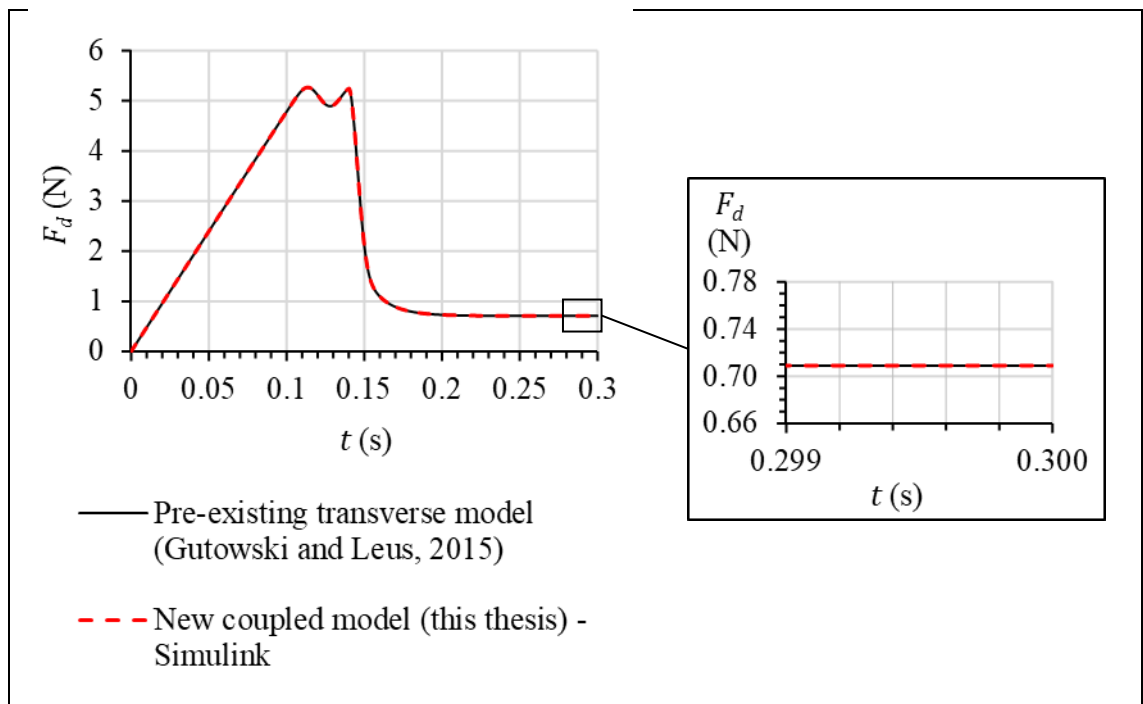


Figure 4.21: Comparison of time varying F_d at $k_v = 20$, transverse vibration.

At $k_v = 20$, F_x undergoes cyclic changes only in magnitude whereas F_y changes in magnitude and direction (Figure 4.22). The average value of F_x reduces from $\mu F_N = 5.08$ N without vibration to a lower value when vibration is activated, hence the reduction in opposing force F_d . Analytical results of the new model show an exact match to the pre-existing transverse model.

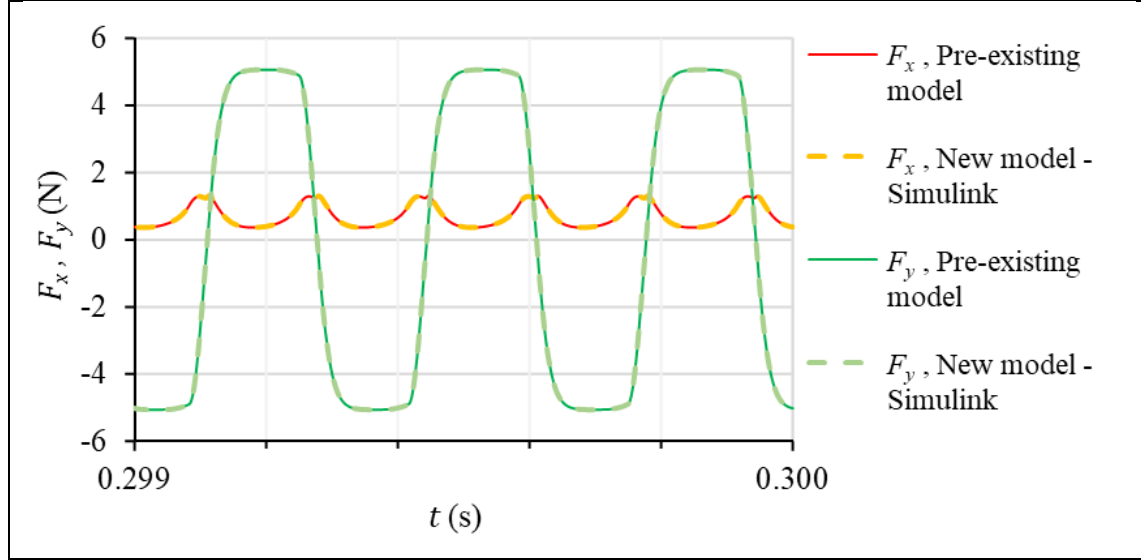


Figure 4.22: Comparison of time varying F_x and F_y at $k_v = 20$, transverse vibration.

4.5.6. Results for Coupled Vibration Modes

The coupled model (Figure 4.16) has been executed with values listed in Table 4.4. Simulations have been performed at selected values of k_v (2, 3, 4, 6, and 20), and at each k_v simulations in 25 different vibration modes θ have been performed.

As stated in 4.4, the best fit for the pre-existing transverse vibration model against experiments performed at $f = 3000$ Hz, $F_N = 50.08$ N, $k_t = 67.29 \cdot 10^6$ N/m² and v_d in the range 0.0001-0.0033 m/s, is achieved by setting the transverse vibration transfer coefficient to $\eta_y = 0.71$ (Gutowski and Leus, 2015). Since coupled vibration simulations satisfy these conditions, $\eta_y = 0.71$ is assumed for all vibration modes.

The results of normalised drive force F_{dv}/F_{ds} are plotted in Figure 4.23 with corresponding trends for each value of k_v . Increase in k_v causes decrease in drive force. The greatest reduction of drive force is achieved by longitudinal mode ($\theta = 0^\circ, 180^\circ$), regardless of the value of k_v . The shape of curve F_{dv}/F_{ds} between longitudinal and transverse modes is always symmetrical about $\theta = 180^\circ$. This suggests the same friction reduction effect can be obtained at multiple values of θ .

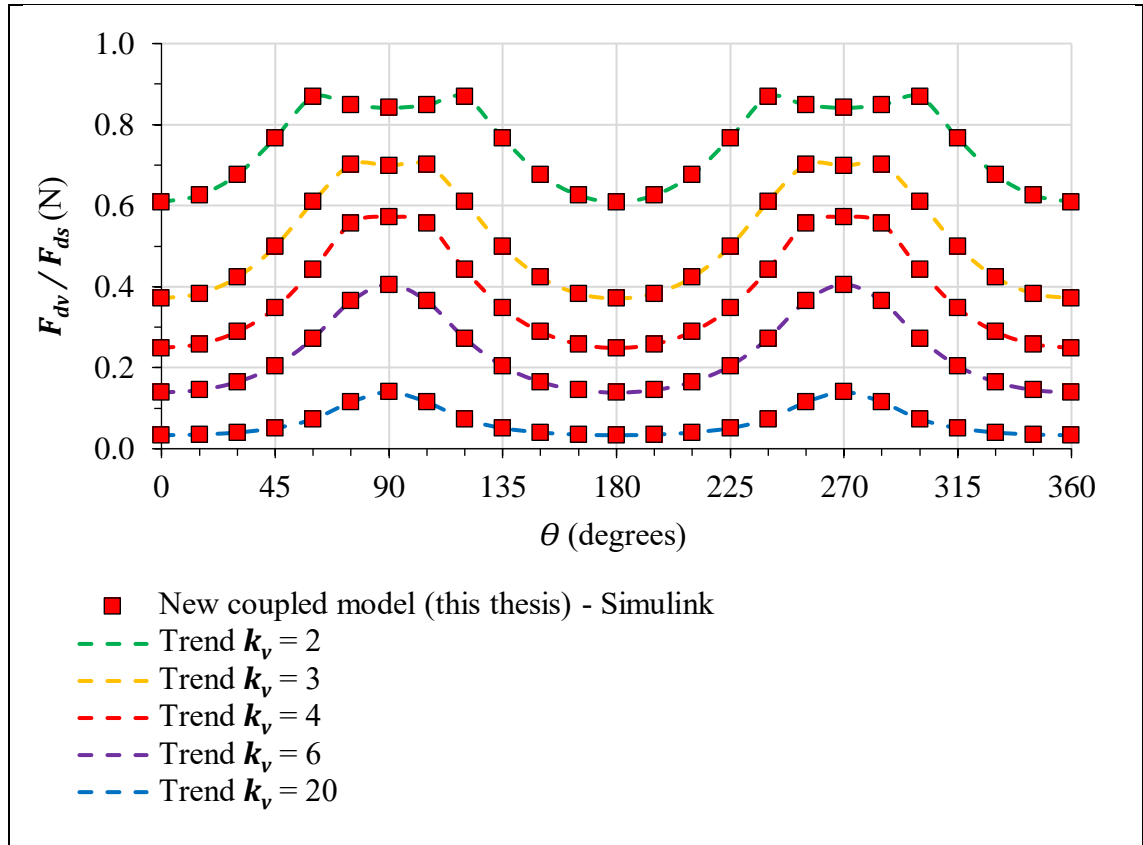


Figure 4.23: Changes in F_{dv}/F_{ds} with θ at selected values of k_v .

4.6. Chapter Discussion and Conclusions

A new analytical model (4.5) has been developed based on two separate pre-existing models (4.3 and 4.4). The new model describes changes in \mathbf{F} and \mathbf{F}_d during sliding motion of a body over a surface vibrating not only in longitudinal or transverse mode, but in any mode $\boldsymbol{\theta}$ of in-plane vibration. The model has been evaluated analytically in Simulink[®] and yields good agreement with the pre-existing models that are already verified against experimental data. This work has further highlighted the importance of using dynamic friction in vibration modelling and demonstrated how friction models can be incorporated into analytical models.

The new coupled model can be used for a three-dimensional planar contact domain (Figure 4.13), where the normal contact pressure is constant. In this case the greatest \mathbf{F}_d reduction is achieved by longitudinal vibration.

To simulate coupled vibration the value of η_y must be known. It is dependent on the combination of f , \mathbf{F}_N , k_t and \mathbf{v}_d so its estimation requires curve fitting against experimental transverse vibration data as per the method described by Gutowski and Leus (2015). It has been assumed that the value of η_y is unaffected by vibration mode $\boldsymbol{\theta}$.

To evaluate more complex contacts such as those of multiple concurrent gear teeth, where normal contact pressures change as teeth enter and exit the gear mesh, one must turn from analytical to numerical methods such as FEA. An advantage of FEA is that the complexity of the domain can be increased simply by modifying the geometry of parts and the way they interact, whereas in analytical modelling this would be difficult to do without having to make significant changes to the formulation. The next chapter thus implements the coupled vibration model of friction into an FEA software tool to check that the same results can be achieved by numerical method.

Chapter 5

Numerical Simulation of Friction Model with Vibration

5.1. Chapter Introduction

A limitation of the new analytical coupled vibration friction model (4.5) is that it can only be used to evaluate contact between three-dimensional planar surfaces where the normal contact pressure does not change. Mathematically describing the time-varying normal contact pressures generated by multiple gear teeth entering and exiting the gear mesh would add significant complexity to the model formulation, hence the need for FEA.

In FEA the contact pressures and contact displacements are calculated based on the defined boundary conditions. The friction model then uses this data to compute the friction force between surfaces in contact. This means the coupled friction model for vibration (4.5) needs implementation into numerical FEA simulations. Abaqus[®] is an FEA simulation tool that allows user defined friction formulation through use of a friction subroutine. This chapter thus introduces contact interactions in FEA, describes the development of the modelling domain and friction subroutine, and presents numerical simulation results in comparison with analytical results from 4.5.4-4.5.6.

5.2. Introduction to Finite Element Contact Interactions

The FEA simulations performed use surfaces to define contacts. A contact pair comprises assignment of a master and a slave surface. Interaction between the master and slave surfaces is defined by the contact interaction properties, namely the contact discretisation method, tracking approach, normal behaviour, and tangential behaviour. They are explained in 5.2.1-5.2.4.

5.2.1. *Discretisation of Contact Pair Surfaces*

The discretisation method of interacting surfaces governs the locations and constraints used to simulate contact conditions. There are two contact discretisation methods: the traditional node-to-surface discretisation or the surface-to-surface discretisation.

Contact conditions with the node-to-surface discretisation are established such that each slave node on the slave surface interacts with a point of projection normal to the master surface (Figure 5.1). Therefore, each contact condition involves a single slave node and a group of nearby master nodes from which values are interpolated to the projection point. The master surface can penetrate the slave surface between the slave nodes, however, the slave surface cannot penetrate the master surface. Therefore, in FEA

analyses the slave surface is typically assigned to the part that has the finer mesh or the softer underlying material (Abaqus®, 2014b).

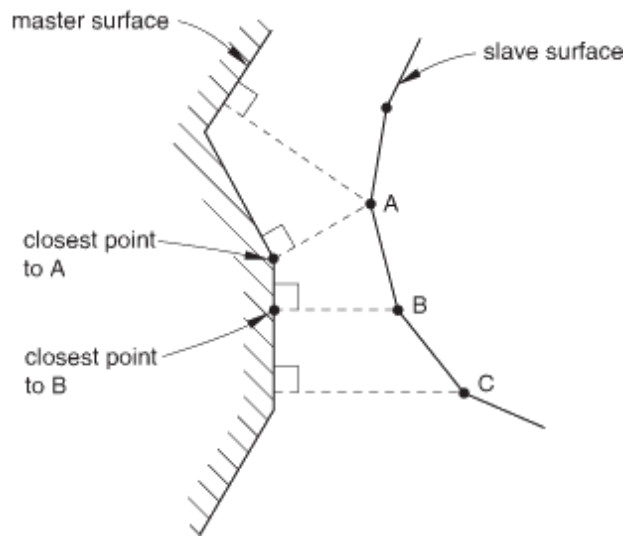


Figure 5.1: Node-to-surface contact discretisation (Abaqus®, 2014c). Each slave node on the slave surface interacts with a point of projection normal to the master surface.

Conversely, surface-to-surface discretisation considers the shape of both the slave and master surfaces in the region of contact. It enforces contact conditions in an average sense over regions nearby the slave nodes rather than only at individual slave nodes. The averaging regions are predominantly centred on one slave node but also consider adjacent slave nodes.

Figure 5.2 shows an example of improved contact pressure accuracy with surface-to-surface contact compared with node-to-surface. Since node-to-surface discretisation simply resists penetrations of slave nodes into the master surface, forces tend to concentrate at these slave nodes, creating spikes and valleys in pressure distribution across the surface. Surface-to-surface discretisation resists penetrations in an average sense, thus having a smoothing effect. As the mesh is refined, the discrepancy between the two methods reduces, but for a given mesh refinement the surface-to-surface method tends to provide more accurate stresses (Abaqus®, 2014c). Surface-to-surface discretisation is thus used for all simulations.

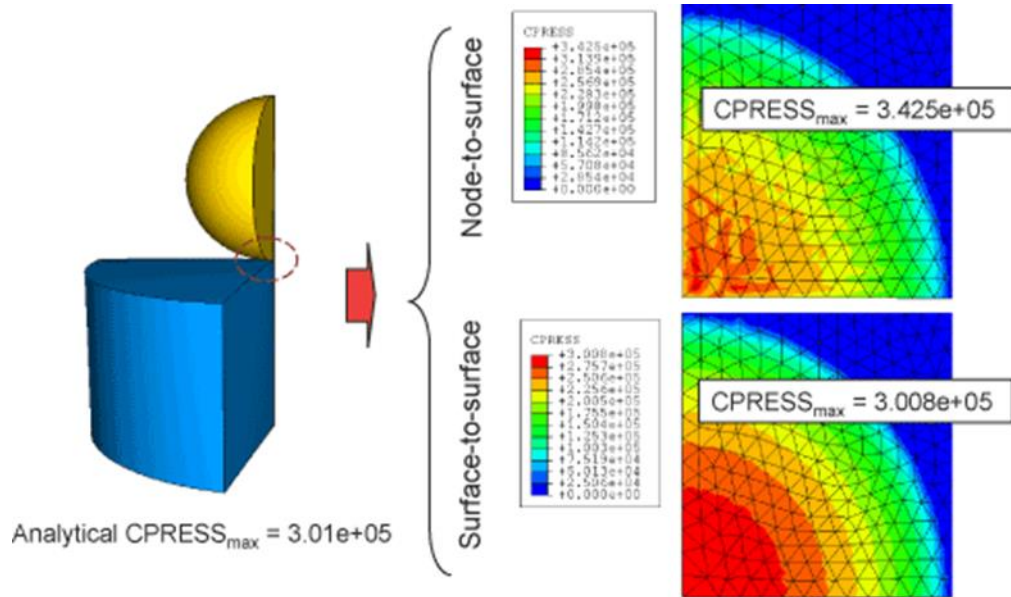


Figure 5.2: Contact pressure accuracy comparison of node-to-surface vs. surface-to-surface contact discretisation (Abaqus[®], 2014c).

5.2.2. Contact Tracking Approaches

There are two tracking approaches for relative motion of contact surfaces: small-sliding and finite-sliding. Small-sliding contact assumes there will be little sliding of one surface against the other such that a slave node will interact with the same local area of the master surface throughout the analysis.

Finite-sliding contact is the most general tracking approach since most contact problems involve relative motion that is greater than the finite element length. Application of drive velocity \mathbf{v}_d (Figure 4.13) means the finite-sliding tracking approach is employed.

5.2.3. Contact Normal Behaviour

Contact behaviour in the normal direction is approximated by a hard pressure-overclosure relationship which minimises the overclosure, or penetration, of the slave surface (in this case the sliding body) into the master surface (the vibrating base). Linear and nonlinear variations of this are available (Figure 5.3). The linear method has a constant normal stiffness, so the pressure-overclosure relationship is linear. With nonlinear method the stiffness increases nonlinearly between regions of constant low initial stiffness and constant high final stiffness (Abaqus[®], 2014d). The simulated contact

pressures are not excessive so nonlinearity normal to the contact is not a concern. Therefore, the default linear method has been used.

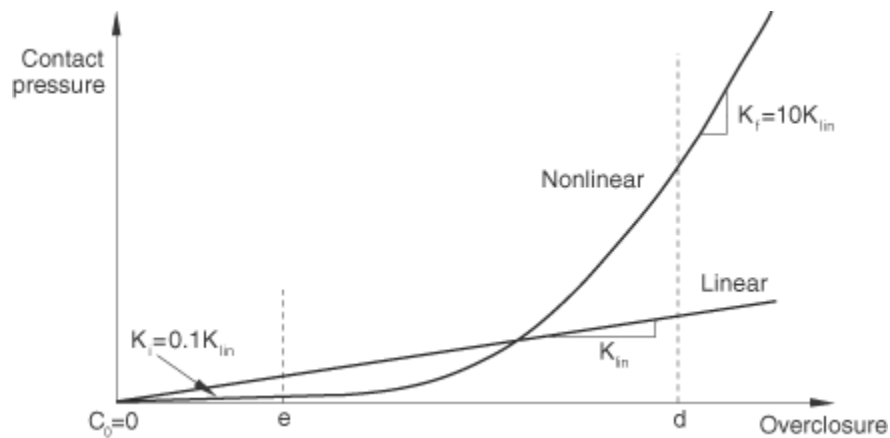


Figure 5.3: Comparison of linear vs. nonlinear pressure-overclosure relationship (Abaqus®, 2014d).

5.2.4. Friction Subroutine for Contact Tangential Behaviour

The desired tangential behaviour is defined by the friction model for coupled longitudinal-transverse vibration (4.5). As this is custom friction behaviour it is not available as standard in Abaqus®, however, the FEA tool enables user defined friction formulation via the use of a friction subroutine. A subroutine is a script, written in Fortran programming language, that implements a user defined friction model into the numerical simulation. A Fortran subroutine included in Appendix D has been written with Intel® Visual Fortran Composer XE 2013, integrated into Microsoft® Visual Studio 2012, to represent the friction model for coupled longitudinal-transverse vibration. Just as the analytical procedure (4.5) is a sequence of equations executed during each time increment, the subroutine is the sequence of equations embedded in Fortran code executed during each iteration of the numerical simulation.

5.3. Finite Element Simulations for Coupled Vibration

Knowledge of finite element simulations involving contact interactions, provided in 5.2, makes it possible to build upon the work from chapter 4. In this section, simulations of a body sliding over a vibrating base are performed numerically using Abaqus®, as an alternative to the analytical implementation of the coupled longitudinal-transverse

vibration model described in 4.5. Results for longitudinal, transverse and coupled vibration modes are compared with previous results from 4.5.4, 4.5.5 and 4.5.6.

5.3.1. Simulation Methodology

Finite element simulations (Figure 5.4) conform to the domain previously used for analytical simulations in Figure 4.13. The deformable sliding body of dimensions $0.04 \times 0.03 \times 0.03$ m is assigned material properties typical of steel; Young's Modulus 209000 MPa and Poisson's Ratio 0.3. Therefore, contact area $A_r = 1.2 \cdot 10^{-3}$ m² is the same as in analytical simulations. The base is a rigid surface of dimensions 0.1×0.1 m. A spring with stiffness $k_d = 96068$ N/m connects points *A* and *B*, conforming to Figure 4.13.

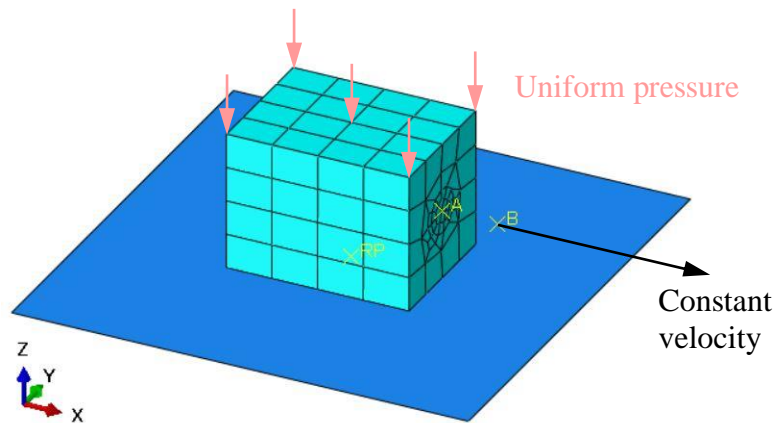


Figure 5.4: FEA simulation domain for coupled longitudinal-transverse vibration.

Simulations consist of sequential analysis steps described by Table 5.1, with a total duration of 0.3 s. This multi-step method is employed to repeat simulations for longitudinal, transverse and coupled vibration modes described in 4.5.4, 4.5.5 and 4.5.6.

Two masses $m = 0.5$ kg and $m = 2$ kg have been used in previous simulations (Table 4.3 and Table 4.4). Due to fixed dimensions of the sliding body, its mass is set by adjusting the material density. Gravity is applied throughout the simulation. The base can be rotated to set positions about axis *Z* to simulate different modes θ of in-plane vibration.

Step no.	Step name	Step duration (s)	Step description
0	Initial	N/A	Body and base boundary conditions are established. The base is static at the start of simulation and the body can move only in direction X (Figure 5.4). Contact conditions between the two parts are also established.
1	Normal pressure	0.05	Uniform pressure is applied to the upper face of the sliding body (Figure 5.4) to generate constant normal force $F_N = 50.8$ N, maintained through all consecutive steps.
2	Sliding	0.09	X direction movement of the sliding body is enabled. Point B is driven at constant velocity $v_d = 0.5 \cdot 10^{-3}$ m/s, to match Table 4.3 and Table 4.4.
4	Base vibration	0.16	Vibration is activated by applying sinusoidal motion to the base.

Table 5.1: Abaqus[®] simulation steps for analysis of two planar contact surfaces.

5.3.2. Simulation Validation for Longitudinal Mode

The simulation described by 5.3.1 has been executed for longitudinal vibration, with parameter values in the friction subroutine defined as per the values used in previous analytical execution of the coupled vibration friction model (Table 4.3).

Figure 5.5 superimposes numerical results from Abaqus[®] onto the previous longitudinal vibration analytical results obtained from Simulink[®] (Figure 4.17). Each data point on the graph corresponds to the result of a single simulation. The Abaqus[®] numerical results at different values of k_v match the expected trend formed by the previous analytical results.

Figure 5.6 and Figure 5.7 superimpose Abaqus[®] numerical results onto previous analytical results of F_d and F_x (Figure 4.18 and Figure 4.19) when $k_v = 6$. The numerical results show subtle differences to analytical results. These differences can be attributed to the Abaqus[®] numerical solver which evaluates the subroutine iteratively in each time increment to compute an approximation while enforcing equilibrium of internal structure forces with externally applied loads, whereas Simulink[®] performs an analytical calculation that outputs the exact solution of the formulation. The subtle differences in

F_x , Figure 5.7, affect the correlation of the Abaqus[®] computed F_d in Figure 5.6, otherwise the numerical implementation of the friction model agrees very well with previous work for longitudinal vibration.

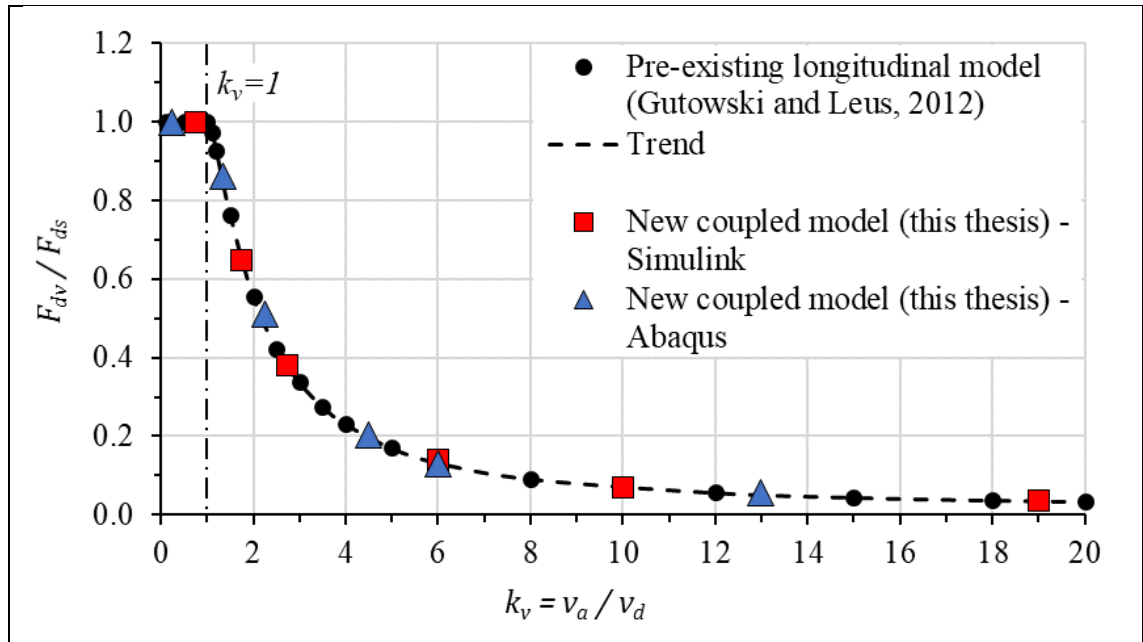


Figure 5.5: Change in F_{dv}/F_{ds} with k_v , longitudinal vibration. Abaqus[®] numerical results superimposed.

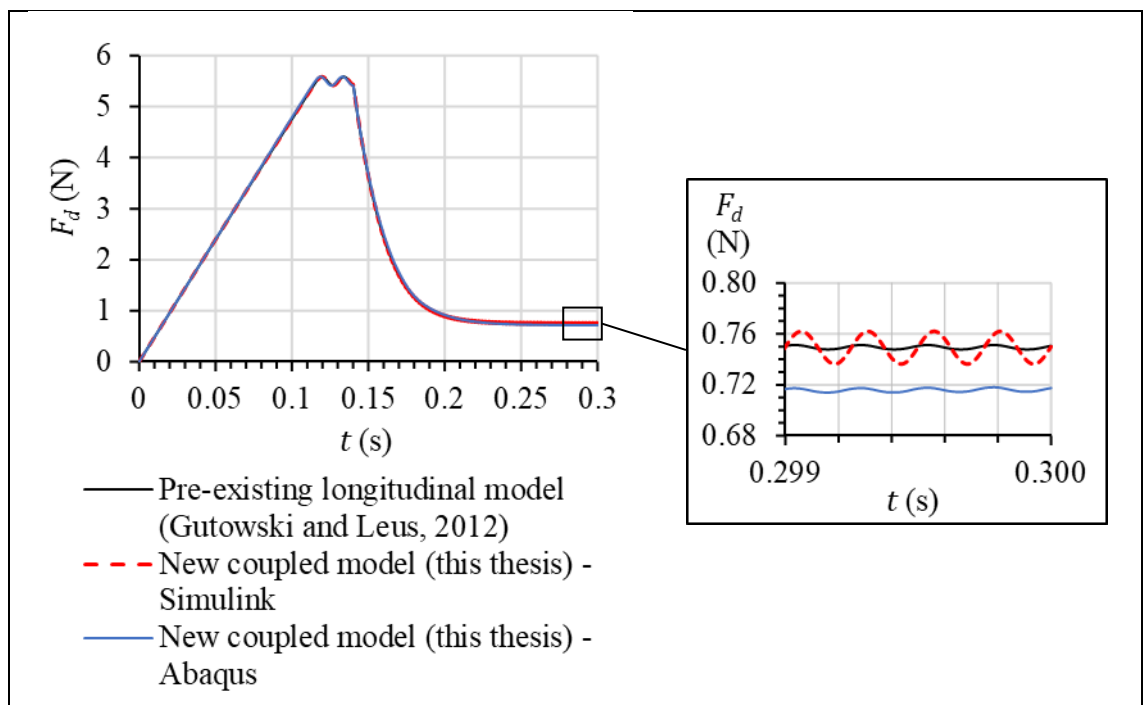


Figure 5.6: Comparison of time varying F_d at $k_v = 6$, longitudinal vibration. Abaqus[®] numerical results superimposed.

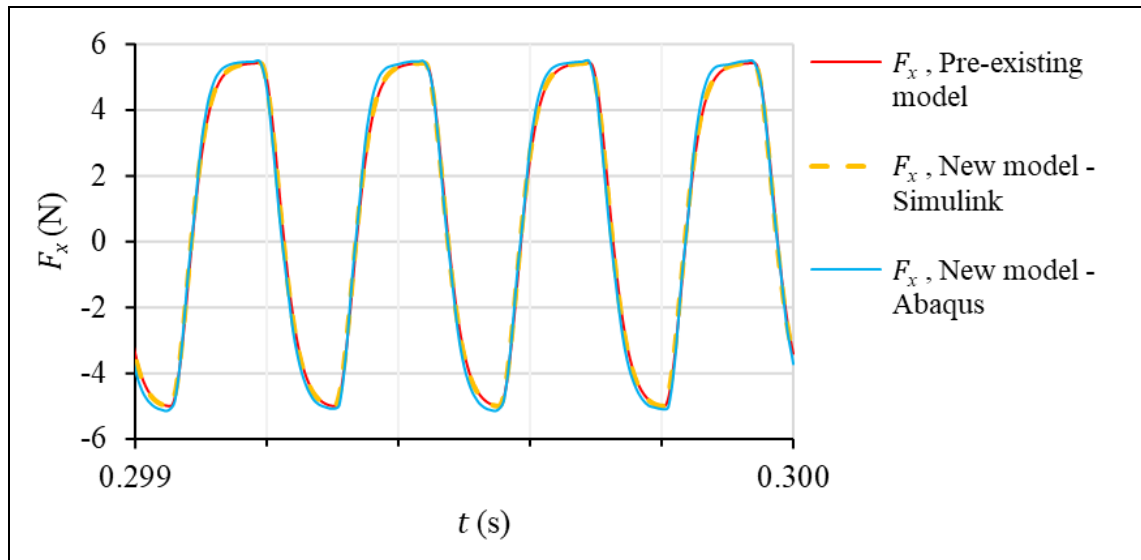


Figure 5.7: Comparison of time varying F_x at $k_v = 6$, longitudinal vibration. Abaqus[®] numerical results superimposed.

5.3.3. Simulation Validation for Transverse Mode

The simulation described by 5.3.1 has been executed for transverse vibration, with parameter values in the friction subroutine defined as per the values used in previous analytical execution of the coupled vibration friction model (Table 4.4).

Figure 5.8 superimposes numerical results from Abaqus[®] onto the previous transverse vibration analytical results obtained from Simulink[®] (Figure 4.20). Each data point on the graph corresponds to the result of a single simulation. The Abaqus[®] numerical results at different values of k_v match the expected trend formed by the previous analytical results.

Figure 5.9 and Figure 5.10 superimpose Abaqus[®] numerical results onto previous analytical results of F_d , F_x and F_y (Figure 4.21 and Figure 4.22) when $k_v = 20$. The numerical results show subtle differences to analytical results. As explained in 5.3.2, these differences can be attributed to the Abaqus[®] numerical solver. The subtle differences in F_x and F_y , Figure 5.10, affect the correlation of the Abaqus[®] computed F_d in Figure 5.9, otherwise the numerical implementation of the friction model agrees very well with previous work for transverse vibration.

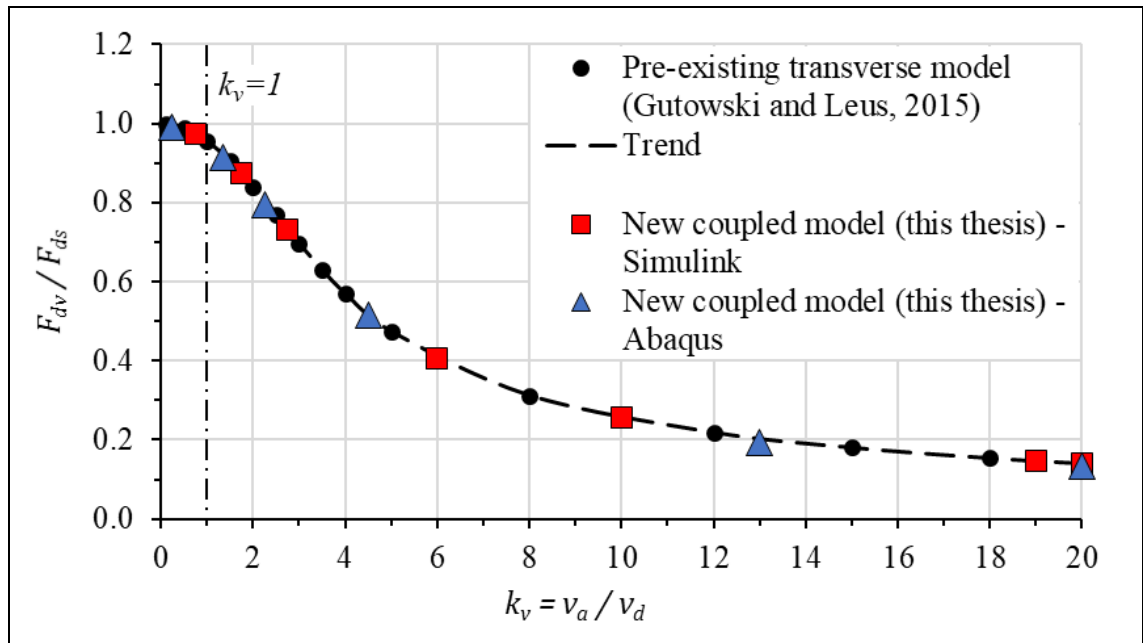


Figure 5.8: Comparison of change in F_{dv}/F_{ds} with k_v , transverse vibration. Abaqus® numerical results superimposed.

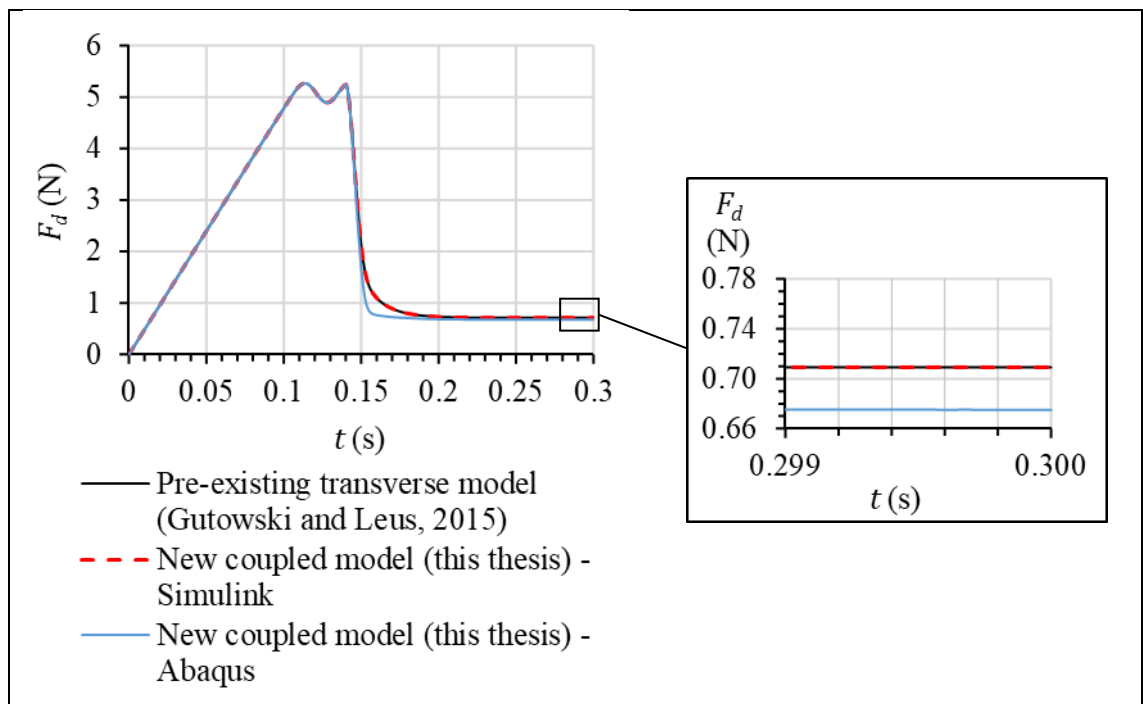


Figure 5.9: Comparison of time varying F_d at $k_v = 20$, transverse vibration. Abaqus® numerical results superimposed.

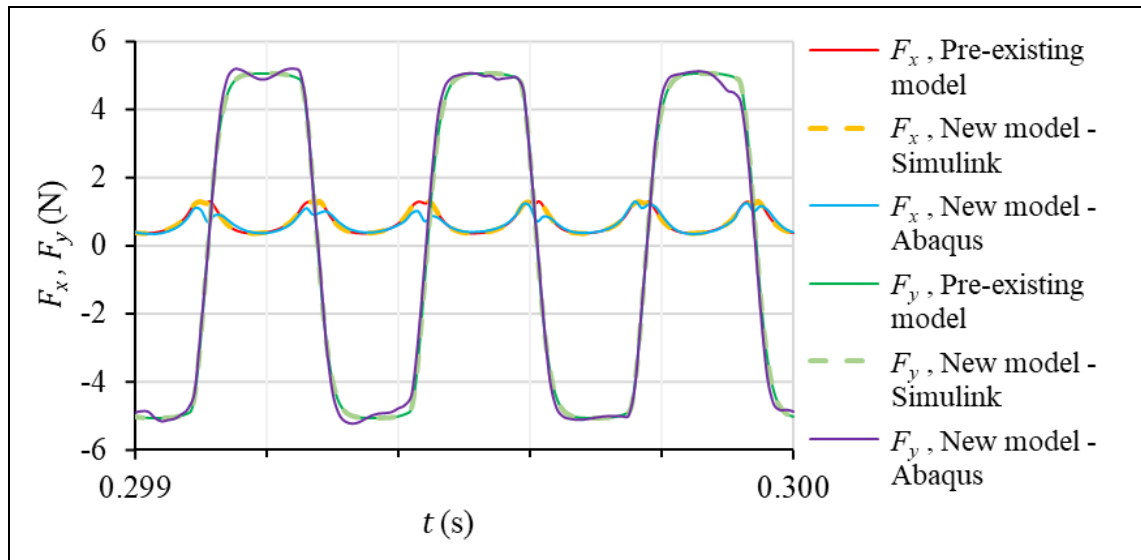


Figure 5.10: Comparison of time varying F_x and F_y at $k_v = 20$, transverse vibration.

Abaqus[®] numerical results superimposed.

5.3.4. Results for Coupled Vibration Modes

The simulation described by 5.3.1 has been executed for coupled longitudinal-transverse vibration modes, using parameter values listed in Table 4.4. At each of the previously selected values of k_v (2, 3, 4, 6, and 20) from 4.5.6, three different coupled vibration modes θ have been numerically simulated in Abaqus[®]. Figure 5.11 superimposes these numerical results onto the previous coupled vibration analytical results from Simulink[®] (Figure 4.23). The numerical and analytical results are in good agreement.

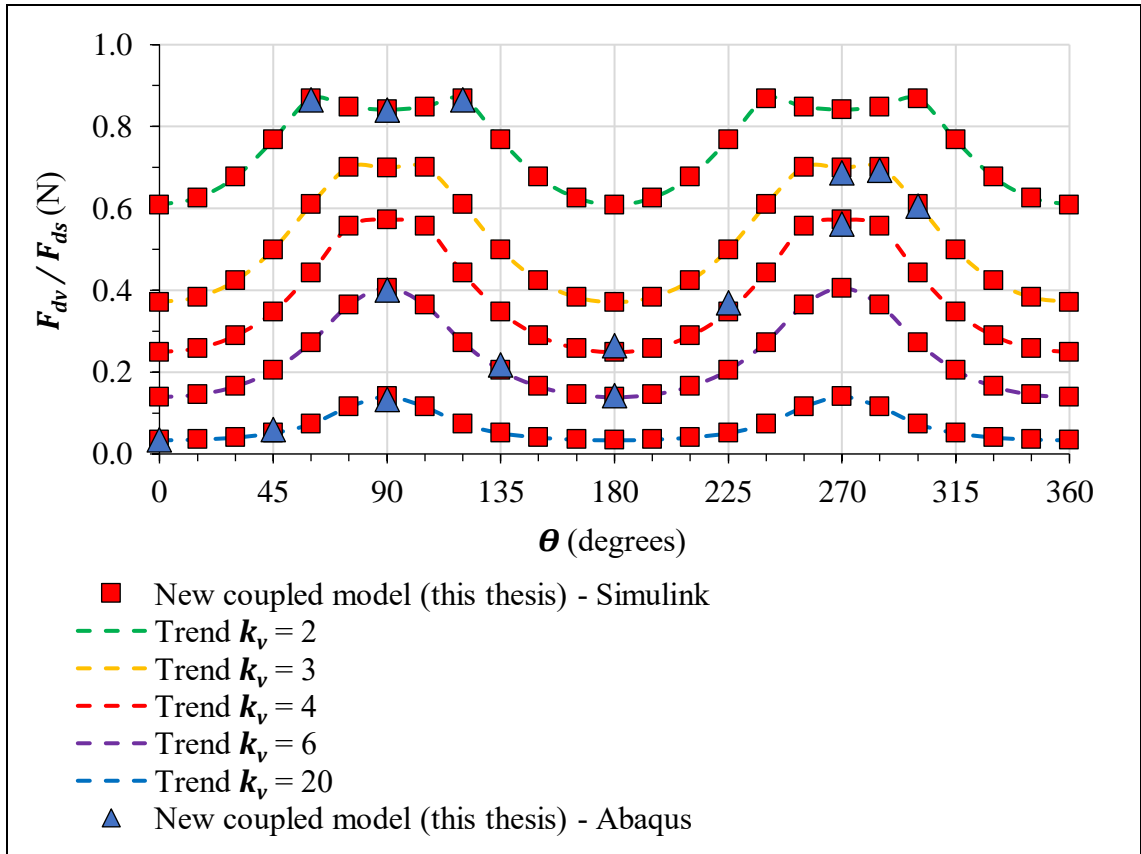


Figure 5.11: Changes in F_{dv}/F_{ds} with θ at selected values of k_v . Abaqus[®] numerical results superimposed.

5.3.5. Limitations of Modelling and Error Mitigation

The mathematical model behind an FEA simulation (5.2.4), the applied boundary conditions (5.3.1), and the contact properties (5.2.1-5.2.45.2.3) are all factors that can affect the accuracy of FEA results regardless of how well they represent reality. Validation of FEA simulations is thus necessary and has been conducted by comparing the FEA results of friction simulations with analytical results. The graphs in Figure 5.6, Figure 5.7, Figure 5.9 and Figure 5.10 show subtle differences between FEA output and analytical results, which may improve with a finer mesh. However, mesh refinement has not been pursued since the normalised results (Figure 5.5, Figure 5.8 and Figure 5.11) agree very well.

5.4. Chapter Discussion and Conclusions

This chapter has described the conduct of numerical FEA contact simulations in Abaqus[®]. To use the new friction model in numerical analyses of coupled longitudinal-transverse vibration, the standard FEA contact behaviour has been modified by embedding the analytical procedure into a Fortran subroutine (Appendix D). The previous analytical simulations of a body sliding over a vibrating base (Figure 4.13, 4.5.4-4.5.6) have then been repeated numerically with FEA. Numerical results from Abaqus[®] superimposed with Simulink[®] analytical results show very good agreement between the two methods of analysis. It has thus been proven that numerical FEA can be used to simulate the friction reduction effect of vibration.

The subroutine uses the time varying contact pressures and contact displacements determined during the numerical analysis, whereas the analytical model would require this information to be mathematically defined. The finite element technique is thus employed in chapter 7 to simulate the effect of vibration on efficiency of a worm gearset.

Chapter 6

Experiments

6.1. Chapter Introduction

Previous experimental studies investigating the influence of vibration on friction (Gutowski and Leus, 2011; Gutowski and Leus, 2012; Gutowski and Leus, 2015), as well as analytical and numerical studies in chapters 4 and 5 which build upon previous work, are based on two planar surfaces in contact with one subjected to vibration. Since gear teeth are non-planar, experimental investigation on non-planar contact surfaces is necessary to give confidence that friction reduction still occurs with imposed vibration.

For reasons explained in 6.2 the decision is made to develop a custom test rig which produces sliding-rolling contact, rather than to test worm gearsets themselves. 6.3 describes the design and initial testing performed on a preliminary disc-on-disc test rig as proof of concept, with learning outcomes applied to develop a more sophisticated disc-on-disc rig in 6.4. Selection of test variables is also explained and results for transverse and longitudinal vibration are evaluated in 6.4.13 and 6.6 respectively, with commentary on wear life impact given in 6.7.

6.2. The Need for a Custom Test Rig

Tribological tests can be performed in an almost endless number of ways, depending on the purpose of the tribological investigation and end application of interest. Choosing the appropriate test is fundamental in being able to attain relevant results, since the outcome of a tribological test is related not only to the test environment and characteristics of the test materials, but also to the way in which the mechanical system makes them interact.

The intention is to imitate conditions of the real application as closely as possible so that test results are meaningful. Worm and wheel gear contacts can experience high sliding speeds. The contact is predominantly sliding, accompanied by a degree of rolling. The slide-roll action is not reciprocated; when the worm gear turns clockwise and anticlockwise its teeth contact opposite flanks of the wheel teeth. Tests using worm and wheel gear pairs would be ideal, however, owing to their process of manufacture the gear teeth themselves are known to have slight variation from one sample to another, which could in turn impact test results. Furthermore, a method of applying in-plane vibration to the contact while the worm and wheel is in motion would have to be developed. From a research project perspective, it increases the risks of being able to achieve the aims of the scientific investigation as it has potential to divert the focus of research onto delivering a

specific method of applying vibration for the application, before fully understanding the slide-roll vibration-friction interactions and attaining meaningful results at a simpler level. For these reasons a simple and consistent test system is necessary to run slide-roll contact experiments under the influence of vibration.

Common tribological tests for which apparatus are already available, such as the pin-on-disc, four ball test, and reciprocating sliding test, do not imitate the worm and wheel contact interaction described above and they do not have a method by which vibration can be induced to the contact. A custom test rig is thus designed and developed. Test specimens in the shape of 8 mm thick discs are chosen. With the outer circumferential surfaces of the two discs maintained in contact, their individual rotational speeds can be adjusted to give the desired slide-roll contact characteristics. Discs can be manufactured easily and repeatedly within set tolerances. Disc-on-disc configuration has been accepted in previous research to test performance of base materials and coatings for helical and worm gearing (Amaro *et al.*, 2005; Fontanari *et al.*, 2013; Fontanari *et al.*, 2016; Benedetti *et al.*, 2017). The disc geometry makes it possible to apply longitudinal and transverse vibration during sliding-rolling interaction, thus opening the relevance of experiments to a wider field of applications beyond gearing alone.

6.3. Preliminary Testing

The need for a custom test rig is identified in 6.2, where the decision to pursue a disc-on-disc test is also justified. Test rig development requires the build of a preliminary rig for an initial assessment of key features. The following sections describe features of the preliminary rig, results of preliminary tests, and useful learning outcomes from this that are applied as design improvements for the final rig. The final disc-on-disc test rig and its features are later described in 6.4.1.

6.3.1. Features of the Preliminary Disc-on-Disc Test Rig

The preliminary test rig, Figure 6.1, comprises an aluminium-bronze disc of material grade CuAl10Ni5Fe4, and diameter $d_a = 95$ mm, mounted in a bracket that is fixed to an aluminium plate, and is loaded against a steel disc of material grade 817M40, and diameter $d_s = 40$ mm, by suspended dead mass off a pulley. This constitutes the normal load F_N . The aluminium platform is mounted on two linear slides, so it is free to slide in the direction of applied load.

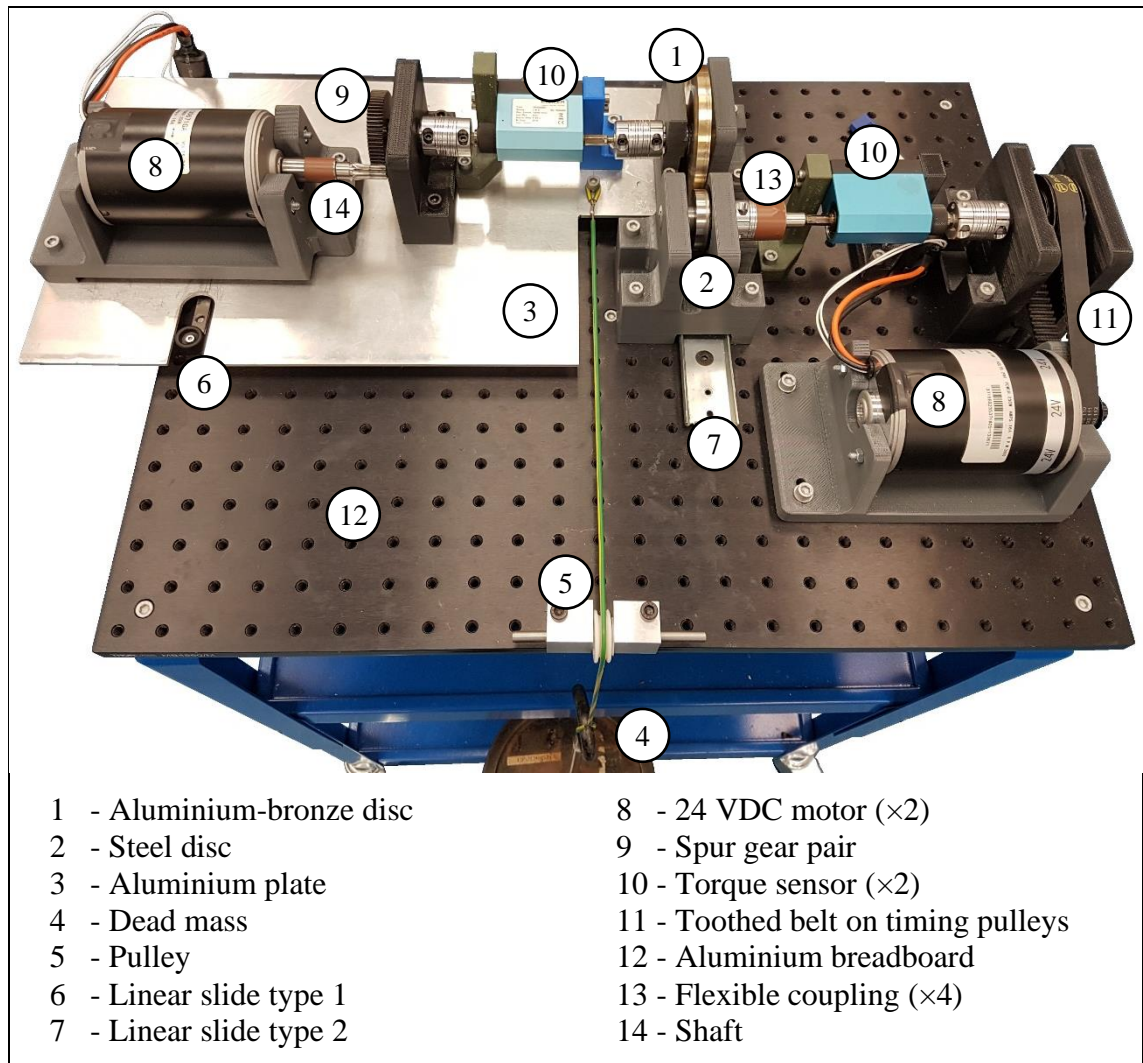


Figure 6.1: Preliminary test rig.

Both discs have thickness 8 mm and are driven individually by two 24 VDC motors rated to 250 W power. The aluminium-bronze disc is driven via a pair of spur gears with speed reduction ratio 68:9, while a torque sensor measures the torque required to turn this disc. The steel disc is driven via a toothed belt on timing pulleys with speed reduction ratio 3:1, while a second torque sensor measures the torque required to turn this disc. Since this is a preliminary rig, to keep costs and development time to a minimum, the mounting brackets for the motors, drive system, torque sensors and discs are all made by rapid prototype 3D printing. A Thorlabs aluminium breadboard with 25 mm spaced M6 tapped holes constitutes the base of the rig.

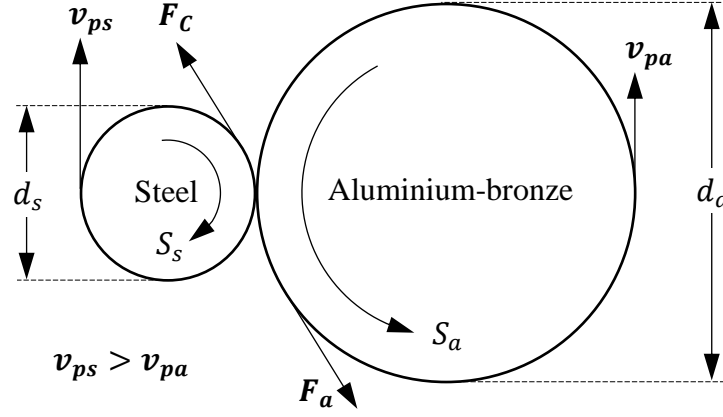


Figure 6.2: Schematic of discs in preliminary test rig. Disc rotational speeds S_s and S_a are selected such that peripheral velocity v_{ps} exceeds v_{pa} , thus the steel disc generates driving force F_a on the aluminium-bronze disc, and an opposite friction force F_C acts on the steel disc.

The selected speed reduction ratios in the drive enable the steel disc to turn faster than the aluminium-bronze such that $v_{ps} > v_{pa}$ in Figure 6.2. The linear peripheral velocities v_{ps} and v_{pa} are determined by:

$$v_{ps} = \frac{\pi d_s S_s}{60} \quad (62)$$

$$v_{pa} = \frac{\pi d_a S_a}{60} \quad (63)$$

Flexible couplings are used to account for any misalignment between shafts. Rotational speed S_s is measured using a calibrated handheld digital laser tachometer on a flexible coupling near the steel disc. Since the aluminium-bronze disc rotates much slower than the steel disc, the time between revolutions is long, causing difficulty in accurately detecting changes in rotational speed S_a . Therefore, S_a is determined from the measured motor output speed S_{ma} and the gear speed reduction ratio:

$$S_a = S_{ma} \left(\frac{9}{68} \right) \quad (64)$$

Since $v_{ps} > v_{pa}$, when the discs are in contact the steel disc generates a driving force F_a on the aluminium-bronze disc (Figure 6.2), and an opposite friction force F_C acts on the steel disc. The discs are affixed on shafts that each run in four flanged plastic bushes, Figure 6.3. These bearings generate torque losses T_{ba} and T_{bs} in the drive. The torque sensors are manufactured by Kistler, model no. 4502A002H, and have a

measurable torque range of ± 2 Nm. T_s and T_a denote the torque measured by these sensors for the steel and aluminium-bronze disc, where in accordance with Figure 6.2 and Figure 6.3:

$$T_s = T_{bs} + F_c \frac{d_s \cdot 10^{-3}}{2} = T_{bs} + \mu F_N \frac{d_s}{2000} \quad (65)$$

$$T_a = T_{ba} - F_a \frac{d_a \cdot 10^{-3}}{2} = T_{ba} - \mu F_N \frac{d_a}{2000} \quad (66)$$

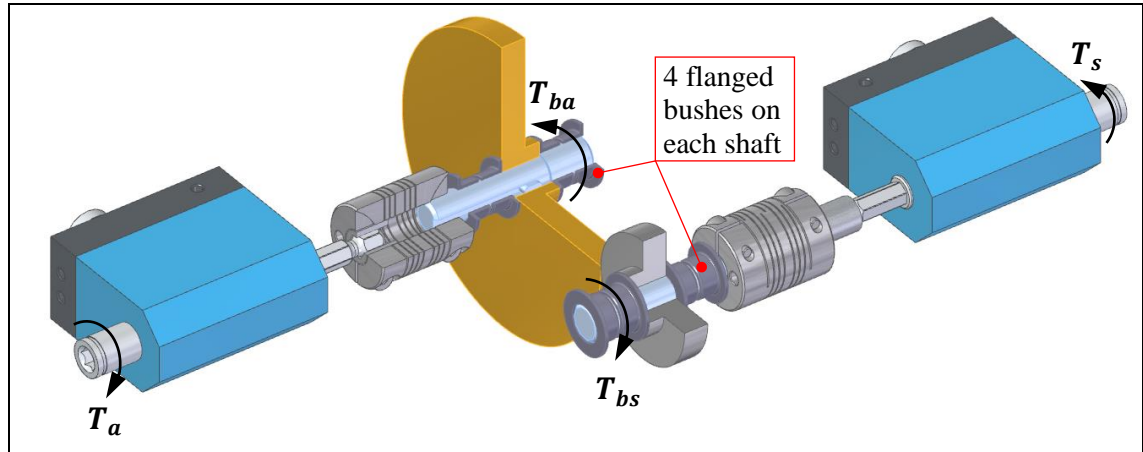


Figure 6.3: Sectioned CAD image of disc and shaft subassemblies in preliminary rig.

6.3.2. Purpose of Preliminary Tests

The purpose of conducting preliminary tests is to develop understanding of whether the different elements of the preliminary test rig work as intended, and if not, how they can be improved for the final rig. The key elements to be assessed are the motors, the drive train, disc specimens, torque sensing and pulley loading system. The specific learning outcomes and design improvements to be carried forward to the final rig are listed in 6.3.6.

6.3.3. Surface Roughness Measurement

Literature review has highlighted that surface finish influences friction between sliding surfaces (Figure 2.17), therefore, it is important to have a measure of surface roughness prior to performing tests. Commonly used in surface texture measurement is a mean line which, as shown in Figure 6.4, is a line that bisects the roughness profile such that the area above and below it is equal. Ra is the universally recognised international parameter for roughness. It is the arithmetic mean of the departures of the profile from the mean line (Taylor Hobson[®], 2004).

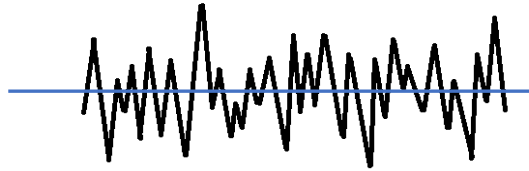


Figure 6.4: Mean line (blue) of surface roughness profile.

Measurements have been taken using a calibrated Taylor Hobson Surtronic 3+ roughness measurer. Figure 6.5 and Figure 6.6 show the setup for measuring the circumferential and lateral surface roughness of the aluminium-bronze disc. The steel disc surface roughness has been measured in a similar manner. The pick-up, Figure 6.7, is a diamond stylus transducer supported on the measuring surface by a pink coloured skid. As the pick-up traverses across the surface, movements of the diamond stylus relative to the skid are detected and converted into a proportional electrical signal. The radius of curvature of the skid enables it to glide the surface unaffected by the roughness.

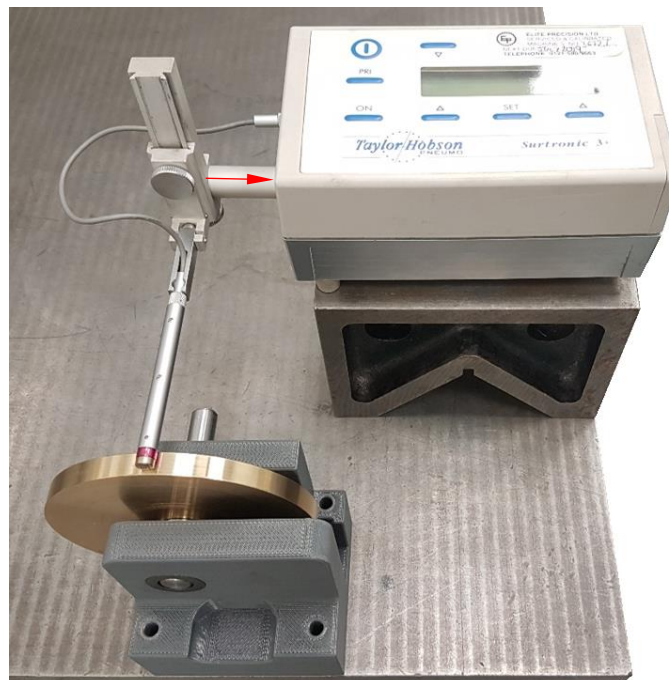


Figure 6.5: Aluminium-bronze disc circumferential surface roughness measurement.

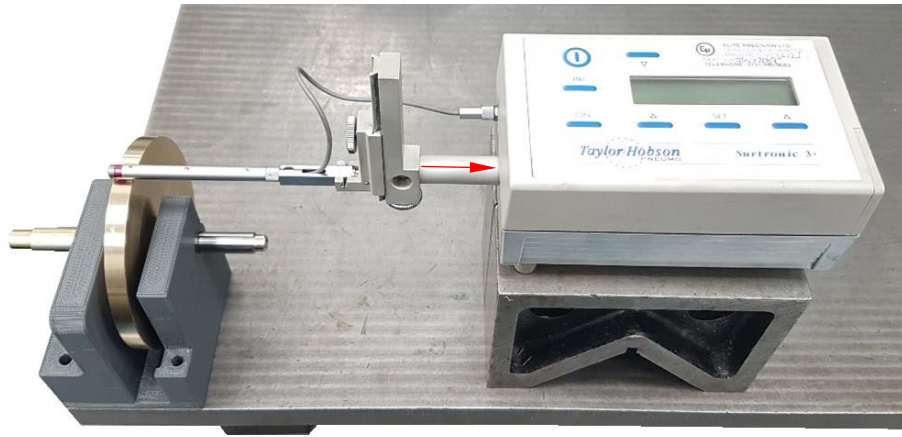


Figure 6.6: Aluminium-bronze disc lateral surface roughness measurement.

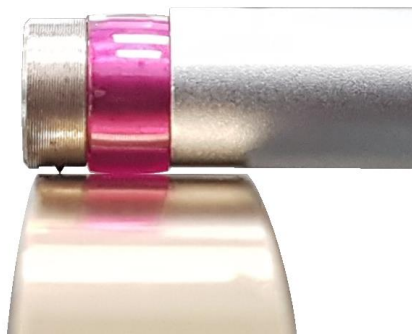


Figure 6.7: Pick-up on aluminium-bronze surface, comprising a diamond stylus transducer supported on the measuring surface by a pink skid.

Both discs are ethanol cleaned to remove surface grease and dust prior to roughness measurement. On each disc, three lateral and three circumferential surface readings are taken at three different locations around the circumference. An overall average roughness R_a is calculated for each direction, see Table 6.1 and Table 6.2. The lateral roughness of discs is greater than the circumferential. This is not surprising given the discs have been machined by turning process.

Disc material	Location	Ra readings			Location average Ra	Overall average Ra
		1	2	3		
Al-Bronze CW307G	1	0.16	0.16	0.16	0.16	0.14
	2	0.14	0.12	0.14	0.13	
	3	0.14	0.12	0.12	0.13	
Steel 817M40	1	0.26	0.26	0.24	0.25	0.26
	2	0.26	0.26	0.26	0.26	
	3	0.26	0.26	0.26	0.26	

Table 6.1: Circumferential surface Ra readings of discs for preliminary test rig.

Disc material	Location	Ra readings			Location average Ra	Overall average Ra
		1	2	3		
Al-Bronze CW307G	1	0.76	0.76	0.76	0.76	0.76
	2	0.74	0.72	0.72	0.73	
	3	0.80	0.80	0.80	0.80	
Steel 817M40	1	0.76	0.76	0.76	0.76	0.81
	2	0.92	0.90	0.92	0.91	
	3	0.78	0.78	0.76	0.77	

Table 6.2: Lateral surface Ra readings of discs for preliminary test rig.

6.3.4. Dry Sliding-Rolling Test and Results

A test without any lubrication applied to the discs is performed first. The purpose of this is to:

- i. check that sliding-rolling action can indeed be produced.
- ii. check if changes in torque and speed can be detected with change in applied normal load F_N .

The steel disc, when unloaded and not in contact with the aluminium-bronze disc, is set to rotational speed of $S_s = 1000$ RPM. At the same time, the aluminium-bronze disc is set to $S_a = 18.7$ RPM. To achieve these rotational speeds the respective motor supply voltages are set to $V_{ms} = 17.1$ V and $V_{ma} = 1$ V. Motor voltage is related to the motor speed; the higher the set voltage, the higher the motor speed for a set normal load F_N .

Motor current draw is related to the torque that the motor produces in response to the set voltage and F_N ; the higher the motor current the higher the torque produced by the

motor to overcome resistances in the drive. In the unloaded condition ($F_N = 0$), the current drawn by the two motors is $i_{ms} = 2.35$ A for the steel disc, and $i_{ma} = 0.8$ A for aluminium-bronze (Table 6.3).

While maintaining the motor supply voltages, Table 6.3 and Figure 6.8 show the effect of increasing F_N on S_s , S_a , i_{ms} and i_{ma} . As F_N increases, S_s reduces and i_{ms} increases. Current draw i_{ms} at $F_N = 5$ N is almost double of that when there is no normal load. This indicates that the motor driving the steel disc must overcome almost twice the frictional resistance.

Conversely, for the aluminium-bronze disc $i_{ma} = 0$ when $F_N \geq 3.6$ N (8 lbs). This means when $F_N \geq 3.6$ N, force F_a alone (Figure 6.2) is large enough to overcome the torque losses T_{ba} (Figure 6.3) such that the motor no longer needs to produce any torque to drive the aluminium-bronze disc.

As F_N increases, S_a also increases. This results in reduced sliding action and increased rolling as shown by Table 6.3 and Figure 6.9. Slide velocity v_{sl} , roll velocity v_{ro} and slide-roll ratio R are calculated by the following equations, where $R = 0$ is pure rolling and $R = 1$ pure sliding (Benedetti *et al.*, 2017):

$$v_{sl} = v_{ps} - v_{pa} = \frac{\pi d_s S_s - \pi d_a S_a}{60} \quad (67)$$

$$v_{ro} = \frac{v_{ps} + v_{pa}}{2} = \frac{\pi d_s S_s + \pi d_a S_a}{120} \quad (68)$$

$$R = \left(\frac{v_{sl}}{2v_{ro}} \right) \quad (69)$$

F_N		Steel		Al-bronze		v_{sl} (mm/s)	v_{ro} (mm/s)	R
(lbs)	(N)	S_s (RPM)	i_{ms} (A)	S_a (RPM)	i_{ma} (A)			
0	0	1000	2.35	18.7	0.8	2001	1094	0.92
2	0.9	990	2.50	20.5	0.5	1971	1088	0.91
4	1.8	975	2.80	21.7	0.4	1934	1075	0.90
8	3.6	942	4.10	96.5	0	1493	1226	0.61
11	5.0	926	4.50	256.6	0	663	1608	0.21

Table 6.3: Table of results for preliminary dry sliding-rolling tests, plotted in Figure 6.8 and Figure 6.9.

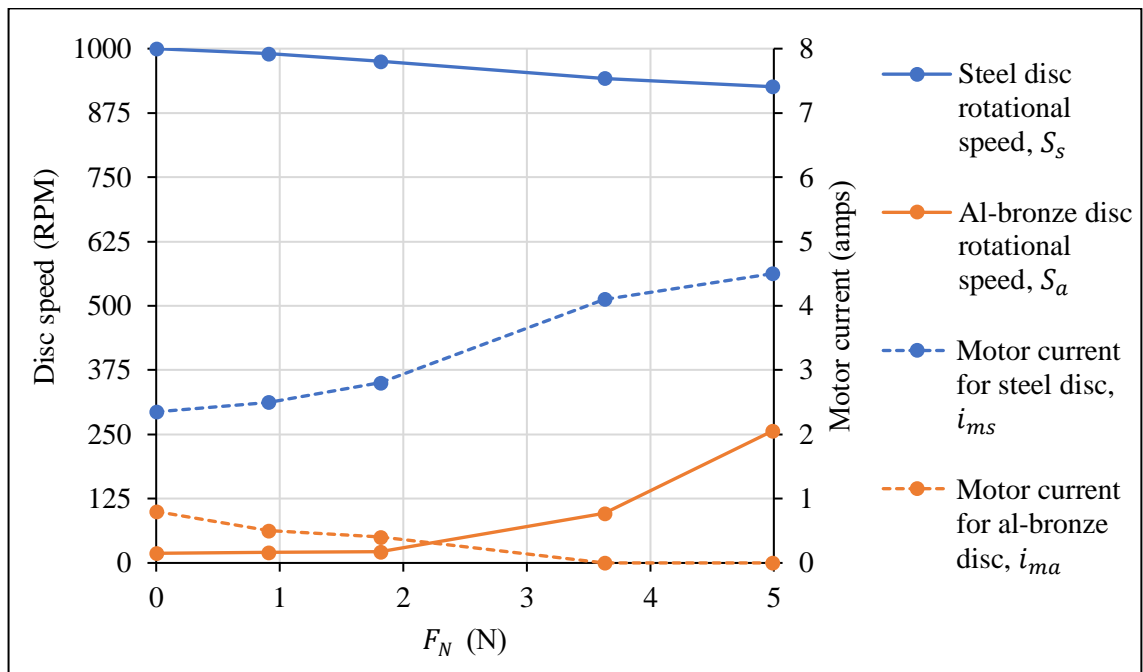


Figure 6.8: Graph showing effect of F_N on S_s , S_a , i_{ms} and i_{ma} . Dry contact.

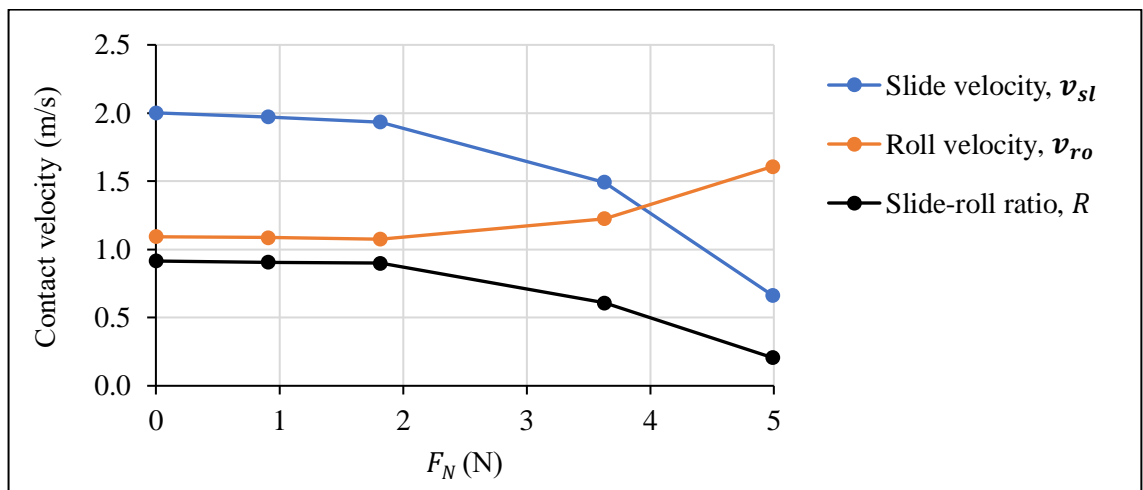


Figure 6.9: Graph showing effect of F_N on v_{sl} , v_{ro} and R . Dry contact.

Material transfer is observed from the aluminium-bronze disc to the steel within just a few minutes of dry running, Figure 6.10. There is evidence of a surface high spot, resulting in wear occurring over a thin portion of the 8 mm thickness. This demonstrates the important role of lubricants in preventing such rapid contact wear.

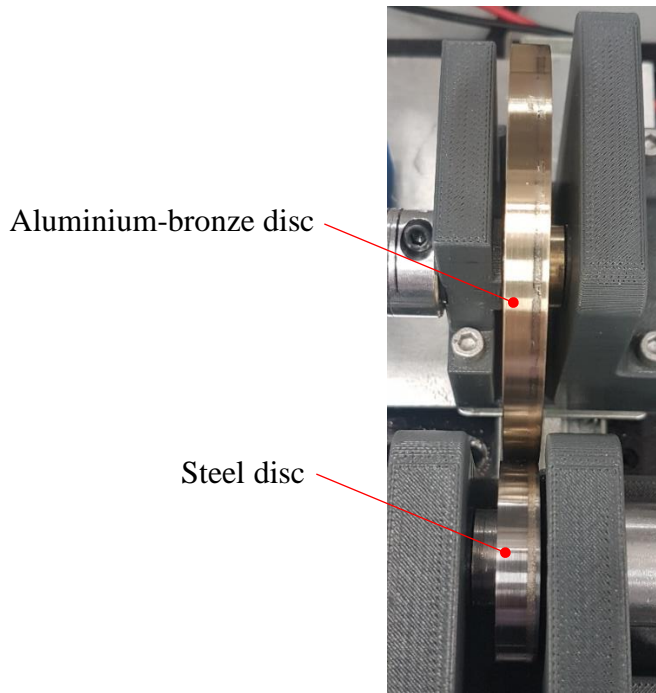


Figure 6.10: Material transfer of aluminium-bronze onto steel disc during dry sliding-rolling test.

Figure 6.11 shows the captured torque profiles at $F_N = 0.9$ N (2 lbs) and 1.8 N (4 lbs). Initially the motors are stationary. Power is applied at 2 s. T_s is larger at larger F_N . This agrees with equation (65). T_a is negative, thus equation (66) suggests that $\mu F_N \frac{d_a}{2000} > T_{ba}$. The T_a reading is noisy at $F_N = 0.9$ N and gets worse at $F_N \geq 1.8$ N. This is attributed to stick-slip behaviour of the dry contact causing large fluctuations in contact friction force, and thus in the measured torque.

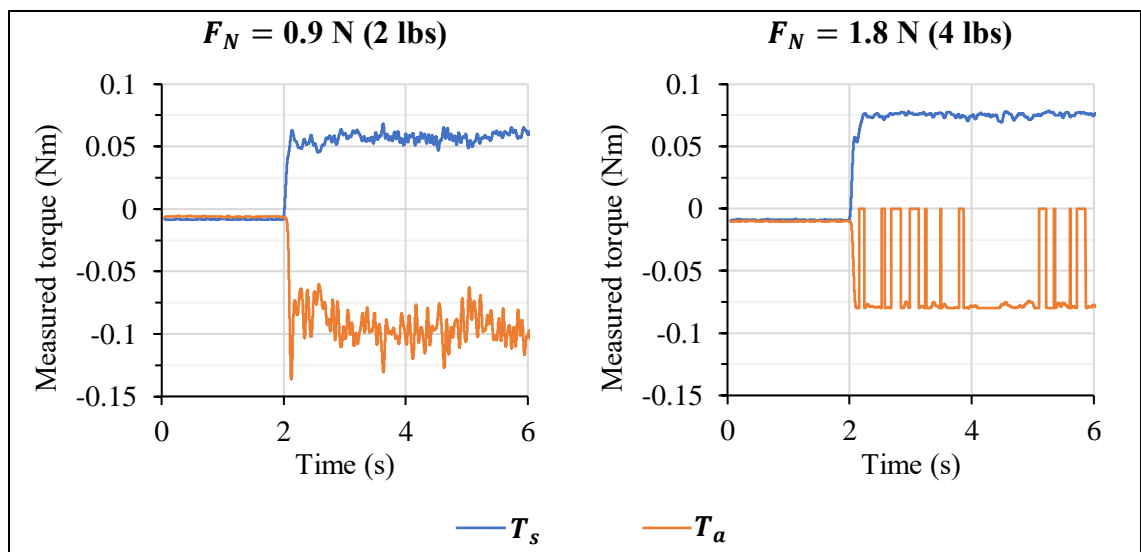


Figure 6.11: Graphs showing effect of F_N on T_s and T_a . Dry contact.

6.3.5. Greased Sliding-Rolling Test and Results

Tests in 6.3.4 are repeated with grease applied to both discs. Properties of the grease, Hydralube WIC Medium Compound, are listed in Table 6.4.

Lubricant property	Description
Appearance	Homogeneous white compound
Flash point	Above 220°C (base oil)
Melting point	Does not melt
Density	0.85-0.95 kg/l
NLGI grade	2
Temperature range	-40°C to +230°C

Table 6.4: Properties of Hydralube WIC Medium Compound grease.

The supply voltages for the motors are the same as for dry sliding-rolling tests in 6.3.4; $V_{ms} = 17.1$ V and $V_{ma} = 1$ V. With these voltages maintained, Table 6.5 shows the effect of increasing F_N , for comparison with Table 6.3.

Figure 6.12 is comparable to Figure 6.8. The overall changes in S_s , i_{ms} and i_{ma} are similar, however, in the case of dry contact these changes occur over an F_N range of just 5 N, whereas with grease applied a higher load of 23.6 N can be achieved. This indicates friction is significantly reduced with grease.

By comparing Figure 6.13 with Figure 6.9 it is evident that application of grease makes it possible to maintain the slide-roll ratio R over a higher F_N range.

F_N		Steel		Al-bronze		v_{sl} (m/s)	v_{ro} (m/s)	R
(lbs)	(N)	S_s (RPM)	i_{ms} (A)	S_a (RPM)	i_{ma} (A)			
0	0.0	1000	2.35	18.7	0.8	2.00	1.09	0.91
2	0.9	996	2.55	18.9	0.75	1.99	1.09	0.91
4	1.8	992	2.66	19.2	0.71	1.98	1.09	0.91
8	3.6	976	3.05	19.8	0.66	1.95	1.07	0.91
11	5.0	970	3.3	20.1	0.63	1.93	1.07	0.91
17	7.7	952	3.59	20.8	0.48	1.89	1.05	0.90
24	10.9	938	3.91	22.6	0.38	1.85	1.04	0.89
36	16.3	930	4.33	23.7	0.21	1.83	1.03	0.89
41	18.6	920	4.61	24.3	0.15	1.81	1.02	0.88
52	23.6	901	5.12	42	0	1.68	1.05	0.80

Table 6.5: Table of results for preliminary greased sliding-rolling tests, plotted in Figure 6.12 and Figure 6.13.

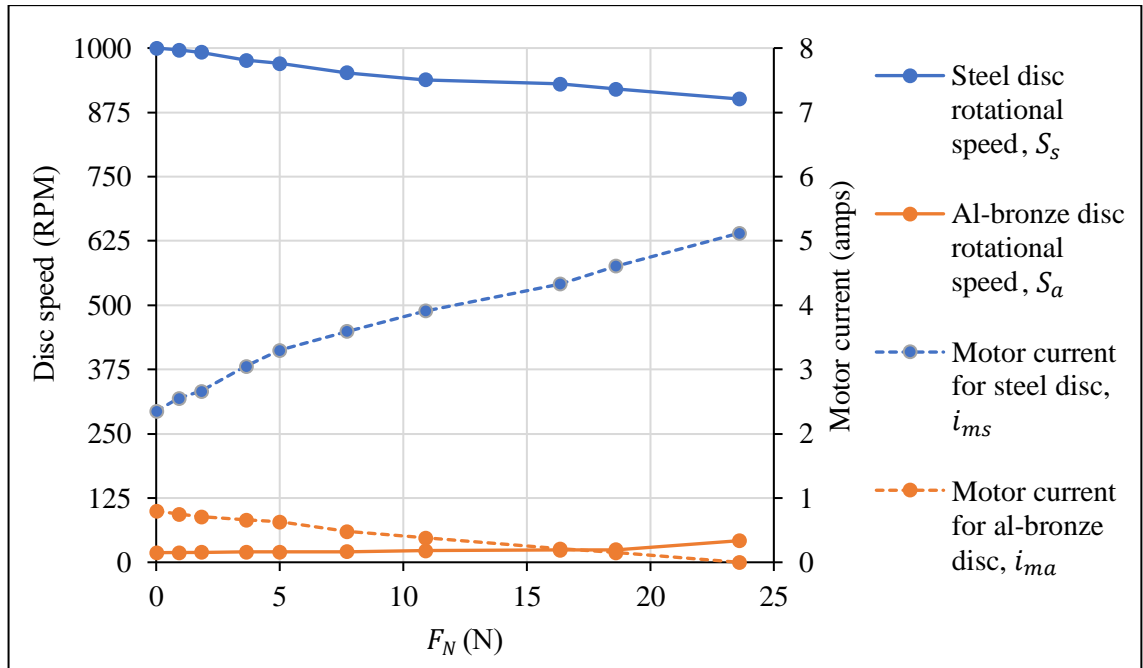


Figure 6.12: Graph showing effect of F_N on S_s , S_a , i_{ms} and i_{ma} . Greased contact.

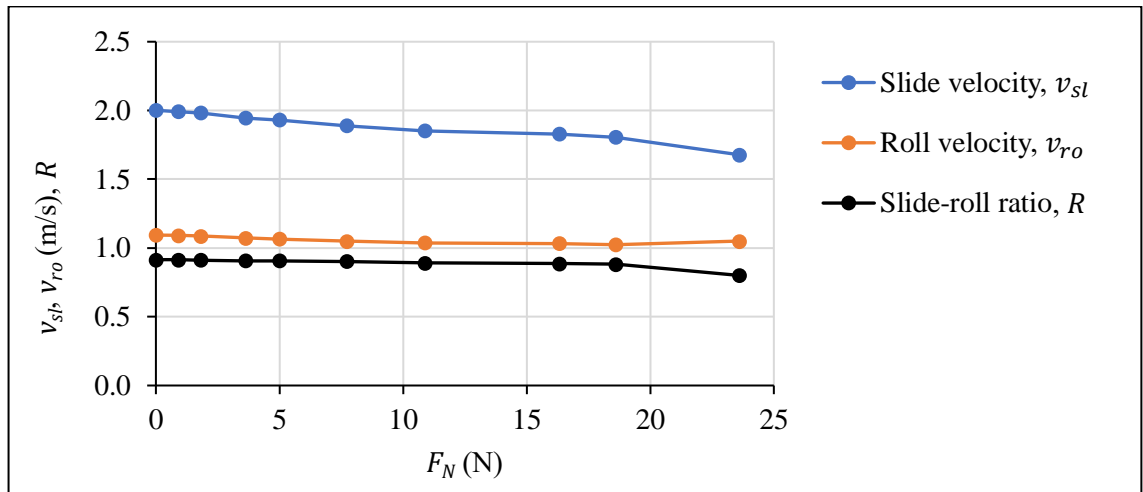


Figure 6.13: Graph showing effect of F_N on v_{sl} , v_{ro} and R . Greased contact.

Figure 6.14 shows the captured torque profiles at selected magnitudes of F_N . Power is applied to the motors at 2 s. As expected, the magnitude of both T_s and T_a increases with F_N . The torque readings become increasingly noisy as F_N increases, however, a greased contact at $F_N = 23.6$ N still produces less noise in the T_a measurement than dry contact does at just $F_N = 1.8$ N (Figure 6.11). This indicates that grease significantly reduces stick-slip behaviour of the contact.

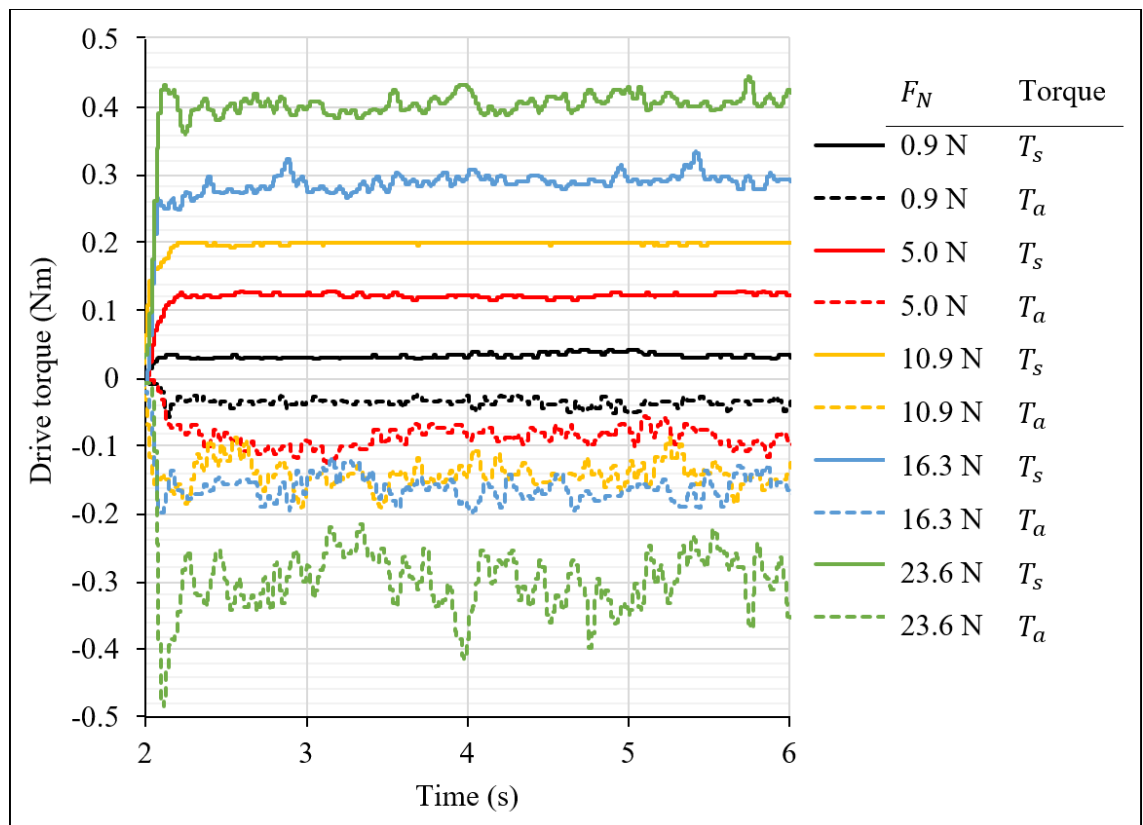


Figure 6.14: Graph showing effect of F_N on T_s and T_a . Greased contact.

Given that d_a is 2.375 times larger than d_s , expectation is that at any given F_N , T_a would also be larger than T_s by the same factor. Figure 6.14 shows this is not the case. This is explained by reference to Figure 6.2; friction torque $F_c \frac{d_s}{2}$ resists rotation of the steel disc, whereas $F_a \frac{d_a}{2}$ aids the aluminium-bronze disc rotation. There are also torque losses T_{bs} and T_{ba} (Figure 6.3) which are unequal due to the difference in bush sizes. The assumption that T_a would be larger than T_s by a factor of 2.375 is therefore erroneous.

6.3.6. Summary and Learning Outcomes

Preliminary testing has enabled an initial assessment of features of the custom disc-on-disc tribological test system. The following learning outcomes are realised and considered in the design of the improved final test rig (6.4.1):

- i. The disc-on-disc configuration can produce the intended sliding-rolling contact action, as demonstrated by Table 6.5 and Figure 6.13.
- ii. The torque sensors detect changes in T_s and T_a with change in F_N . The measurable range of the sensors of ± 2 Nm is adequate for the loads and speeds under test.
- iii. Dry contact produces large fluctuations in torque measurement due to stick-slip interactions. Higher F_N and v_{sl} make these fluctuations more severe while also causing rapid material transfer from the aluminium-bronze disc to the steel. For this reason, it is the norm to employ a lubricant in applications. Metallic gears are also used with some form of lubrication, thus there is no use of conducting further dry sliding tests. All tests henceforth are conducted under lubrication.
- iv. The assumption that $T_a = 2.375T_s$ because $d_a = 2.375d_s$ is erroneous. In fact, magnitude of T_s can be larger than T_a (Figure 6.14). d_s must be increased in the improved rig to obtain larger torque T_s readings.
- v. Torque changes due to vibration would be easier to capture on the disc that requires the larger driving torque. Therefore, changes in torque must be assessed on the steel disc, while the aluminium-bronze disc is subjected to vibration.
- vi. S_a is influenced by S_s . The faster steel disc causes the aluminium-bronze disc to speed up. This happens because the aluminium-bronze disc is driven via spur

- gears, and spur gears by their nature are not self-locking. Replacing spur gears with a high ratio worm gear pair can reduce the influence of S_s on S_a .
- vii. Horizontal loading of the discs by suspended dead-weights is difficult to achieve given that an oil bath to lubricate the discs is also required. Instead, the discs must be vertically loaded such that their interaction can take place in an oil reservoir.

6.4. Experimental Investigation

Considering the learning outcomes in 6.3.6, an upgraded custom disc-on-disc sliding-rolling test rig has been designed and built for experimental investigation. The final test rig and its elements are described in 6.4.1-6.4.11, followed by a test procedure in 6.4.12 for the conduct of transverse and longitudinal vibration experiments. Results from these experiments are presented in 6.4.13 and 6.6.

6.4.1. Features of the Final Disc-on-Disc Test Rig

A photograph of the upgraded custom disc-on-disc test rig which features a method of applying vibration is shown in Figure 6.15, followed by a sectioned CAD image of the rig in Figure 6.16. Both figures show the rig configured to apply transverse vibration, but it can also be configured for longitudinal mode as discussed later in this section.

The test rig (Figure 6.15, Figure 6.16 and Figure 6.21) comprises two 24 VDC motors adopted from the preliminary rig (Figure 6.1), the rotational speeds of which are measured by two Bourns 5 VDC optical speed encoders. The lower motor drives a worm and wheel gear pair with speed reduction ratio 60:1, while a torque sensor measures drive torque T_a for the aluminium-bronze disc. The upper motor drives a 90° gearbox of 30:1 speed reduction ratio, while another torque sensor measures drive torque T_s for the steel disc. The torque sensors, flexible couplings and aluminium breadboard are also adopted from the preliminary rig.

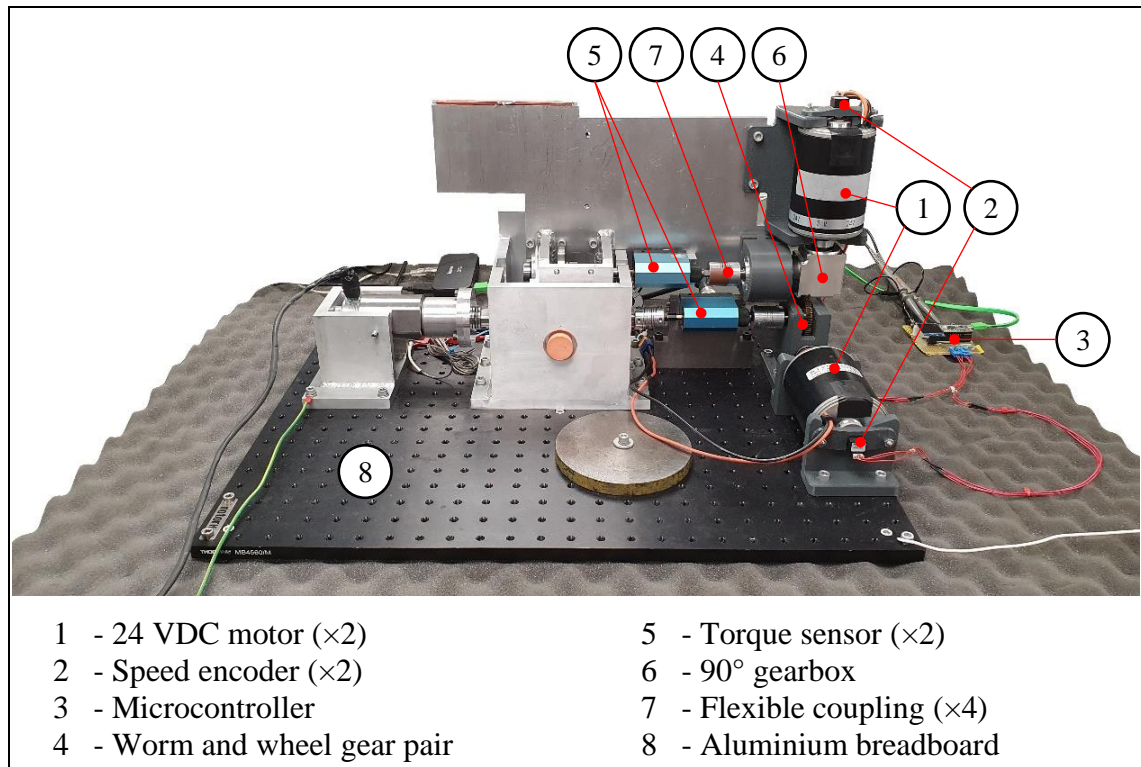


Figure 6.15: Photograph of disc-on-disc rig configured for transverse vibration.

The upper motor, 90° gearbox, upper torque sensor, and shaft on which the steel disc is mounted, are all assembled onto a 10 mm thick aluminium platform (Figure 6.16). The entire platform is mounted to a Schaeffler ball bearing linear guide, such that the platform can traverse only in the vertical direction. Therefore, the platform subassembly mass of $m_r = 5.36$ kg due to gravity acts directly at the contact between the steel and aluminium-bronze discs. Additional dead mass m_w can be placed on the platform as necessary.

The shaft on which the aluminium-bronze disc is mounted, while being rotationally driven by its motor via the worm and wheel gear pair, is also vibrated by a sonotrode. The aluminium casing not only supports the shaft for the aluminium-bronze disc, but it also provides a mounting face for the vertical linear guide and forms an oil reservoir. 0.7 litres of oil is necessary to dip lubricate the aluminium-bronze disc (Figure 6.31). Lubrication is further discussed in 6.4.9.

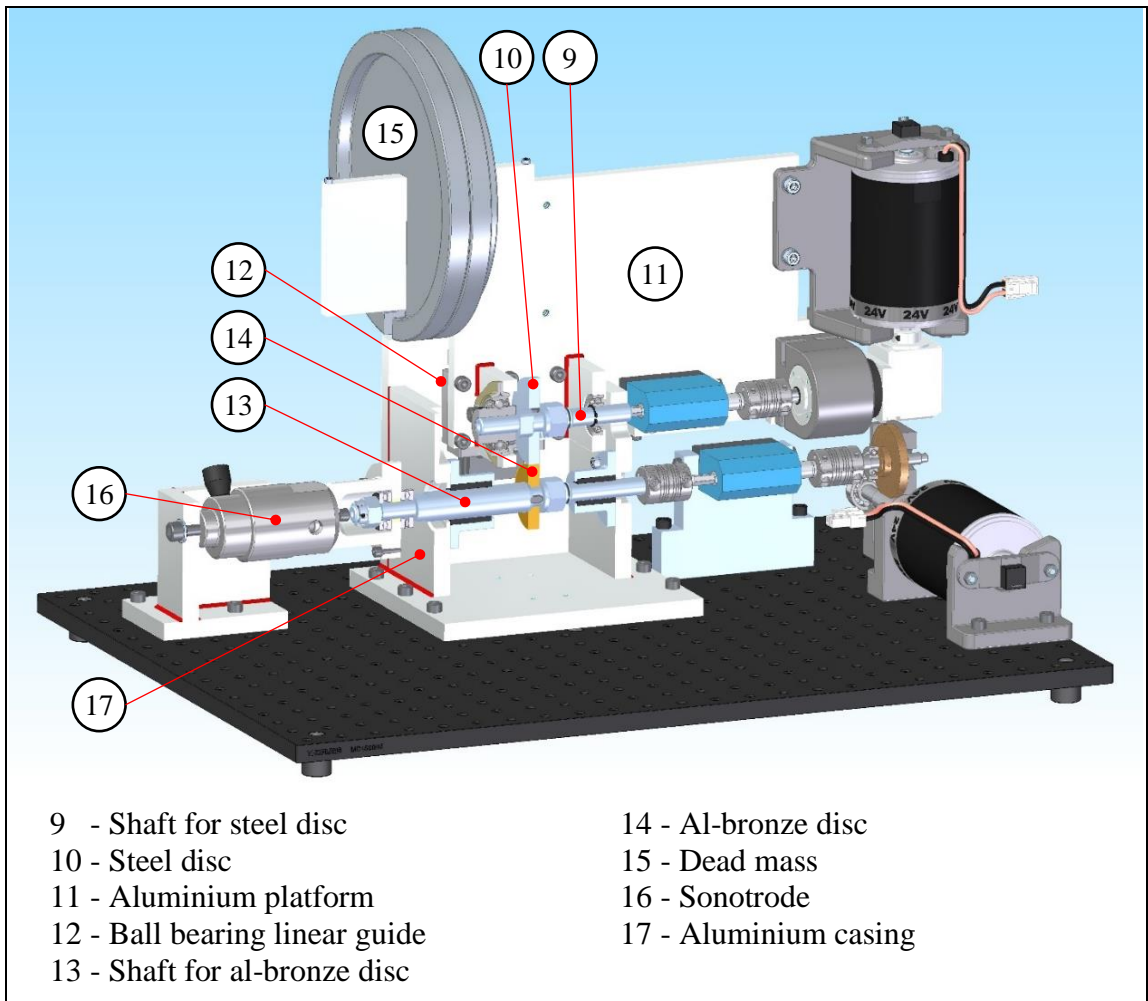


Figure 6.16: Sectioned CAD image of rig in transverse vibration configuration.

Figure 6.17 shows a detail sectioned view of the disc and shaft subassemblies. An aluminium-bronze disc, material grade BS EN 1982 CC333G-GC, of diameter $d_a = 45$ mm is loaded vertically against a steel disc, material grade BS EN 10084 15NiCr13, of diameter $d_s = 60$ mm. The steel disc is hardened to 620-708 VP. Both discs are mounted against a shoulder on their respective shafts by an M14 nut and spring washer. A square section key between each disc and respective shaft couples their rotation.

The lower shaft is supported by two linear-rotary ball bearings. The upper shaft is supported by an oval flanged ball bearing on one end, and a deep groove ball bearing on the other. Axial movement of the upper shaft is restricted by grub screws on the flanged ball bearing.

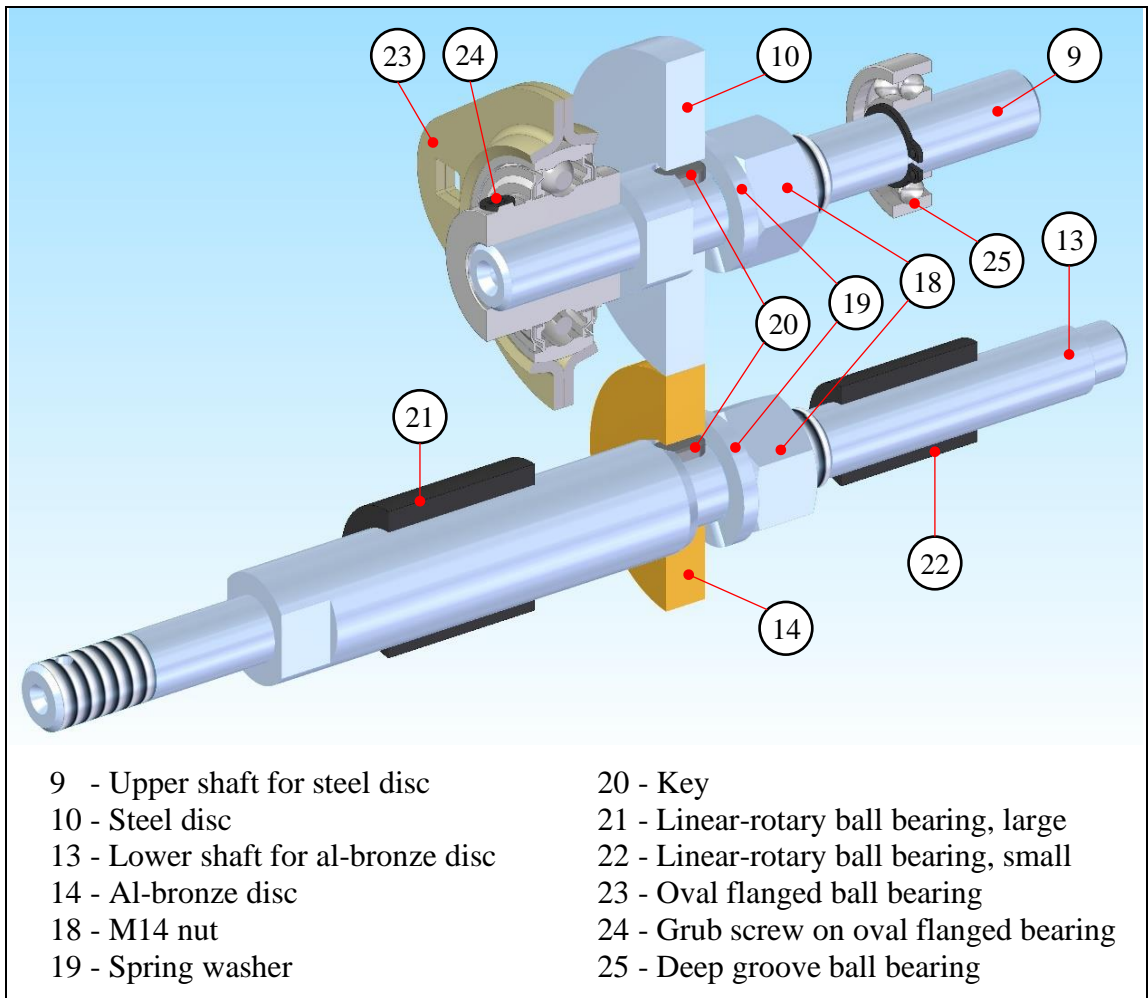


Figure 6.17: Sectioned CAD image of disc and shaft subassemblies in transverse vibration configuration.

The sonotrode, Figure 6.18, comprises a rear steel housing in which a Physik Instrumente piezo actuator model P-887.91 (Figure 6.19) is centre positioned by a polymer bush. The piezo actuator has dimensions $7 \times 7 \times 36$ mm, and travel range of 32 μm at operating voltage range -20 to $+120$ V. It has a blocking force of 1850 N; this is the force above which it will not actuate. The piezo is highly responsive to changes in operating voltage, thus applying a high frequency periodic voltage to it generates vibration.

During a single vibration cycle, as supply voltage increases the piezo actuator extends and pushes a steel output pin, compressing two parallel stacked disc springs. The compressive force is registered on a load cell, located between two steel spacers. Subsequently, as supply voltage decreases during the vibration cycle, the piezo actuator retracts and the disc springs return the steel pin to its start position. For the disc springs to provide adequate returning force at high frequency, these springs must be appropriately

preloaded, noting that the preload must also be a good margin below the blocking force of 1850 N. The rear housing has an external thread. Preload is set by screwing the front housing onto the rear housing and locking the set position. 6.4.3 explains selection of the preload level.

While the shaft for the aluminium-bronze disc must be free to rotate and vibrate concurrently, the output pin must be isolated from this rotation to avoid risk of damaging the piezo actuator. A special coupling has been designed for this purpose, comprising a 7 mm thick aluminium circular plate on an IGUS Iglidur[®] polymer sleeve bearing, mounted between two thrust ball bearings. The locked castle nut, adjacent disc spring and thrust bearing are enclosed in an aluminium housing, one side of which is fixed to the circular plate and the other to the output pin. The thrust bearings decouple the shaft rotation from the aluminium plate. The output pin transfers vibration to the coupling and hence the shaft.

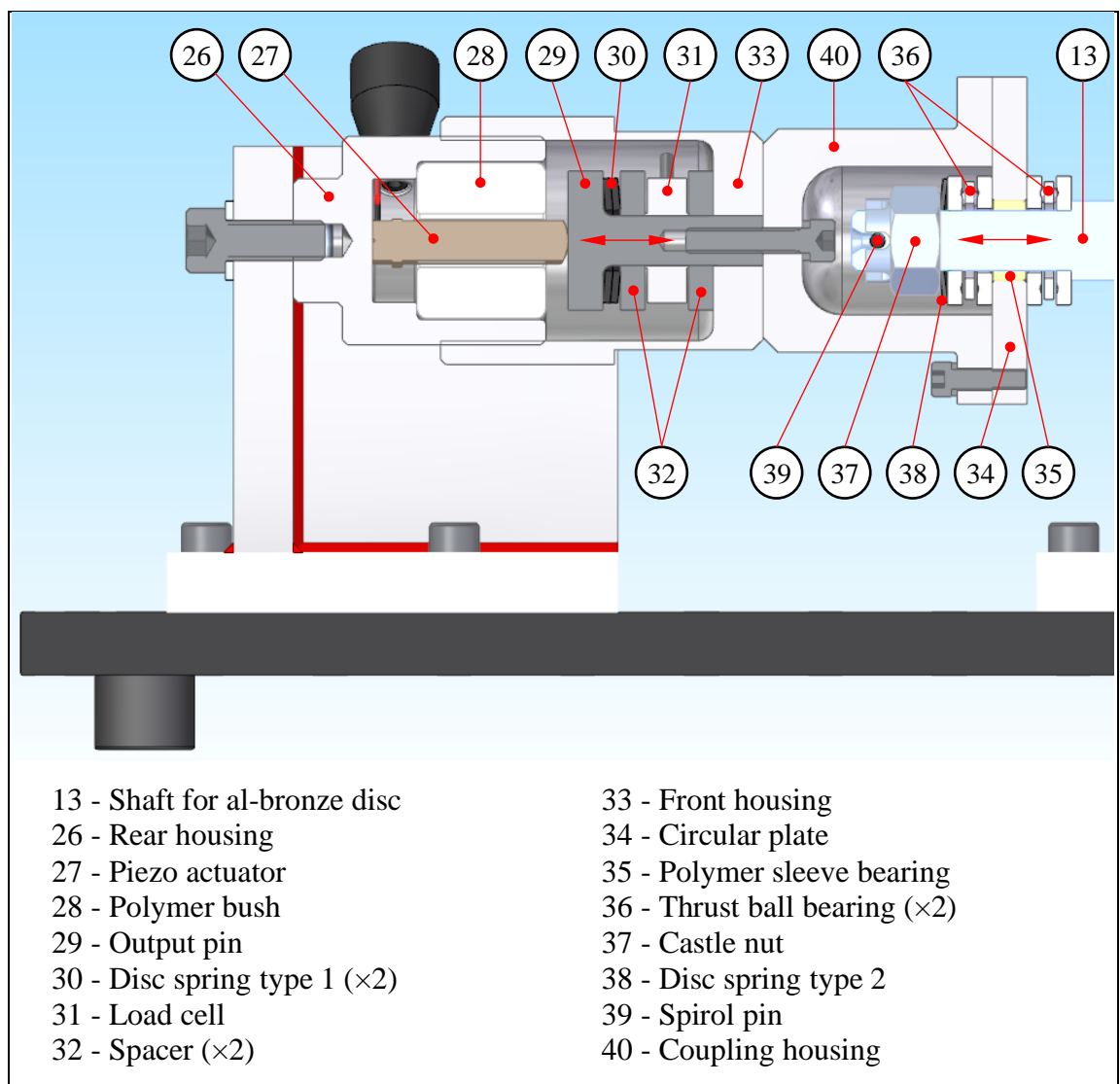


Figure 6.18: Sectioned CAD image of sonotrode.

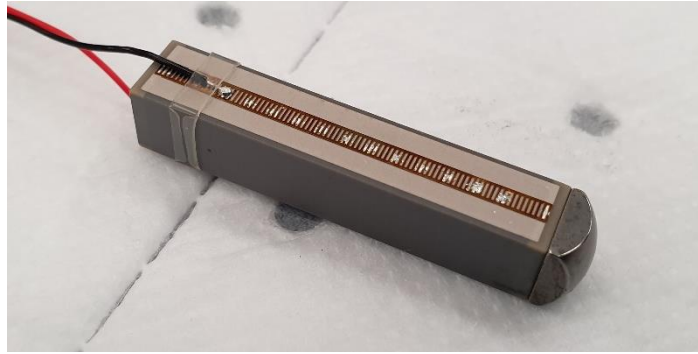


Figure 6.19: Physik Instrumente piezo actuator model P-887.91.

An electronic control box and voltage amplifier (Figure 6.20) operate the piezo actuator in the sonotrode. The user interacts with the USB powered Mbed Microcontroller (Figure 6.21) via a PuTTY command terminal. The Mbed controls a dedicated signal generator chip on an evaluation board to produce a periodic wave. Sinusoidal or triangular wave type can be selected from the PuTTY terminal (Figure 6.25). The signal generator output is then passed through analogue circuitry powered by a DC dual power supply to amplify, level shift, and filter the output to the Picoscope[®] and the voltage amplifier. The periodic voltage signal is amplified $\times 10$ to the range -20 to $+120$ V which is then applied to the piezo actuator. The load cell signal into the Picoscope[®] is used to set the sonotrode preload in 6.4.2.

The speed encoders are powered by a Teensy LC microcontroller. The encoders each send 32 pulses per revolution to the microcontroller. The microcontroller computes the pulse counts into RPM values which are scaled and filtered to give proportional voltage outputs registered by the Picoscope[®].

The torque sensors and battery powered current clamps also feed into the Picoscope[®]. All 8 channels of data are recorded on a laptop with Picoscope[®] oscilloscope software, further explained in 6.4.11.

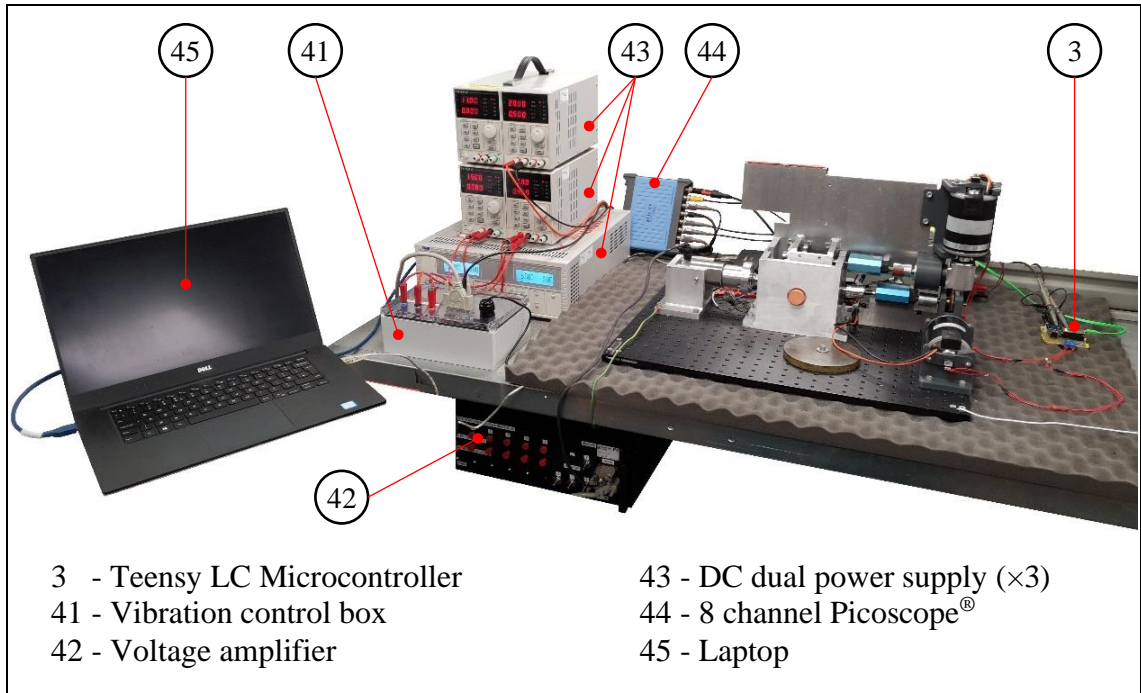


Figure 6.20: Photograph of ancillary equipment for disc-on-disc rig.

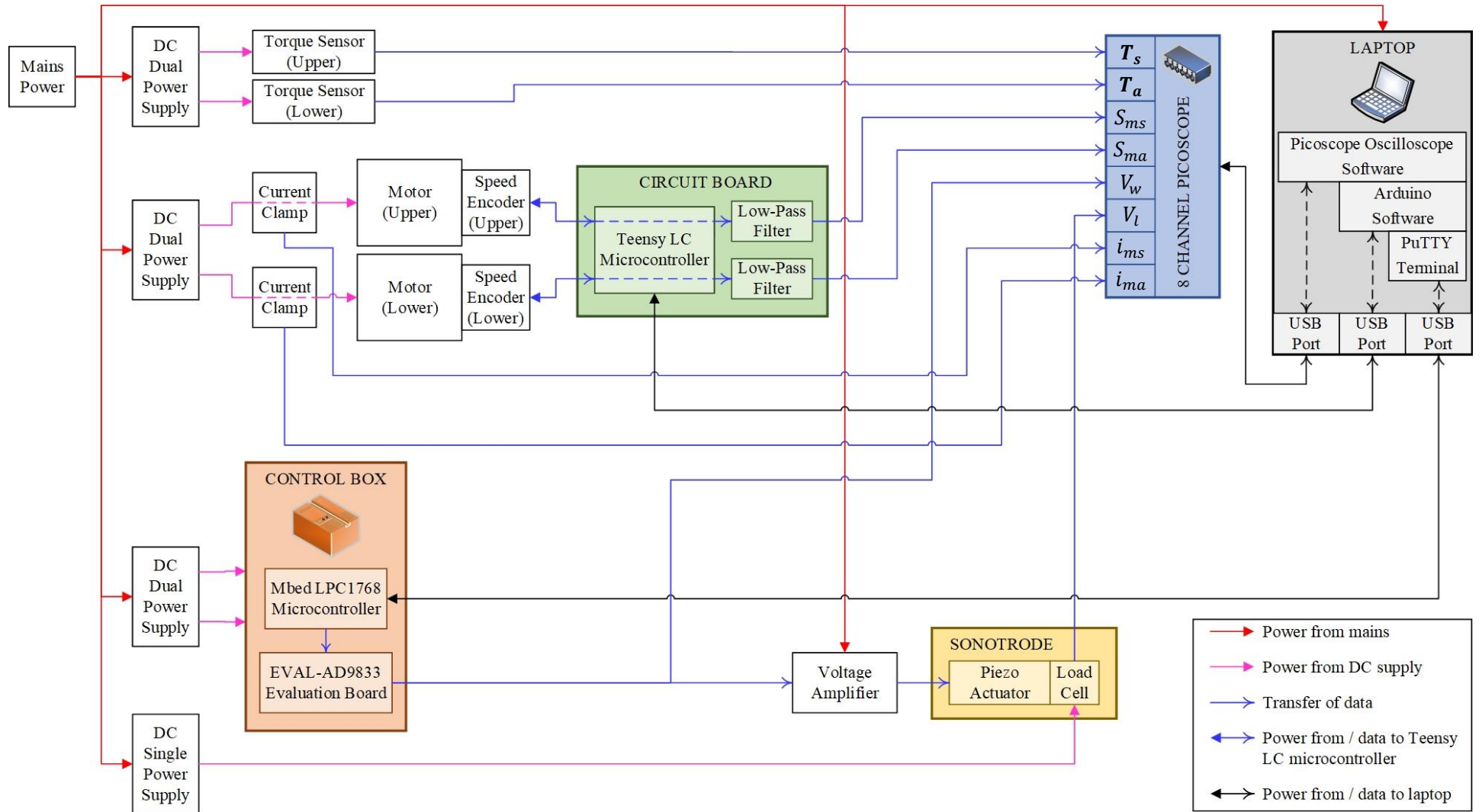


Figure 6.21: Test rig equipment interface map.

To configure the rig for longitudinal vibration the sonotrode location is changed as per Figure 6.22. Vibration is now applied via a stub shaft, fastened to a bracket which is mounted on a second Schaeffler four-row ball bearing linear guide, model KUV6.

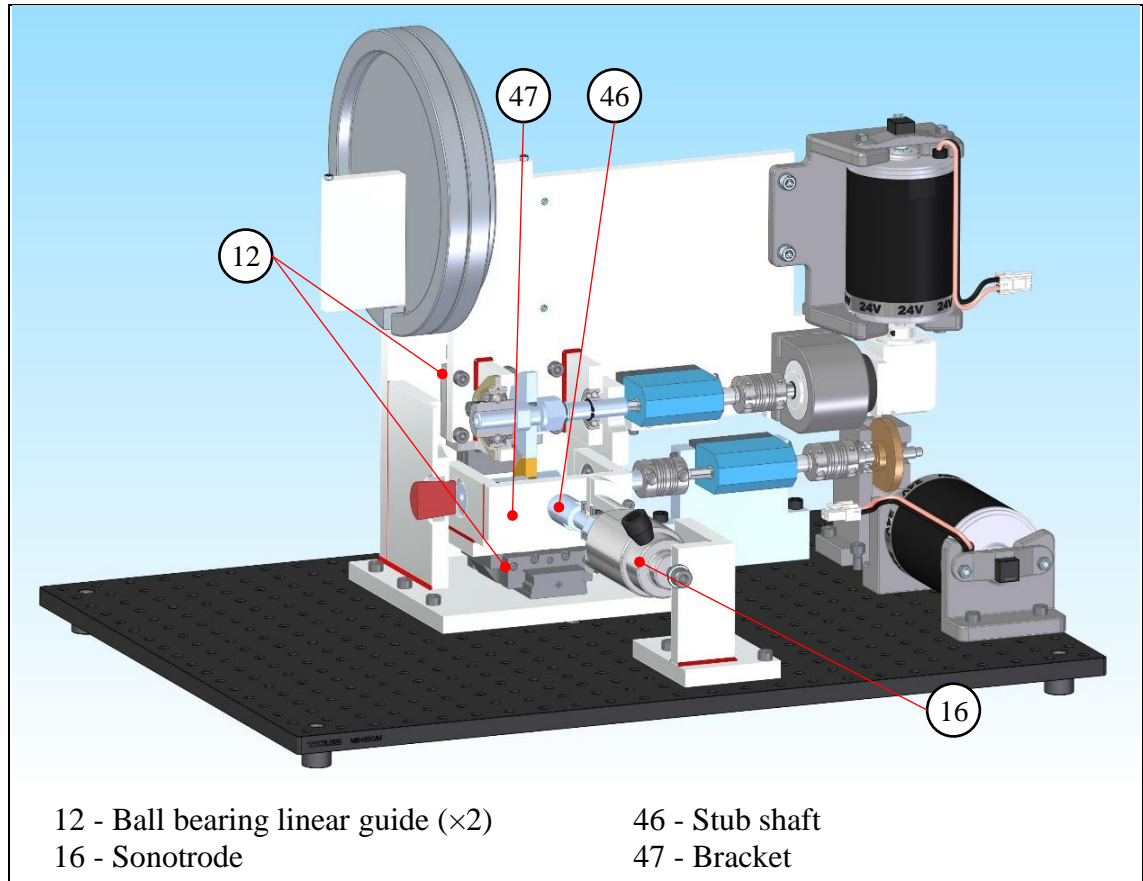


Figure 6.22: Sectioned CAD image of disc-on-disc rig configured for longitudinal vibration.

In comparison to Figure 6.17, the lower shaft assembly for the longitudinal vibration configuration is shown in Figure 6.23. The bracket, which has been sectioned for clarity, holds two different press-fitted deep groove ball bearings. These bearings support a new shaft onto which the aluminium-bronze disc is mounted. The method of mounting the discs onto their respective shafts is unchanged.

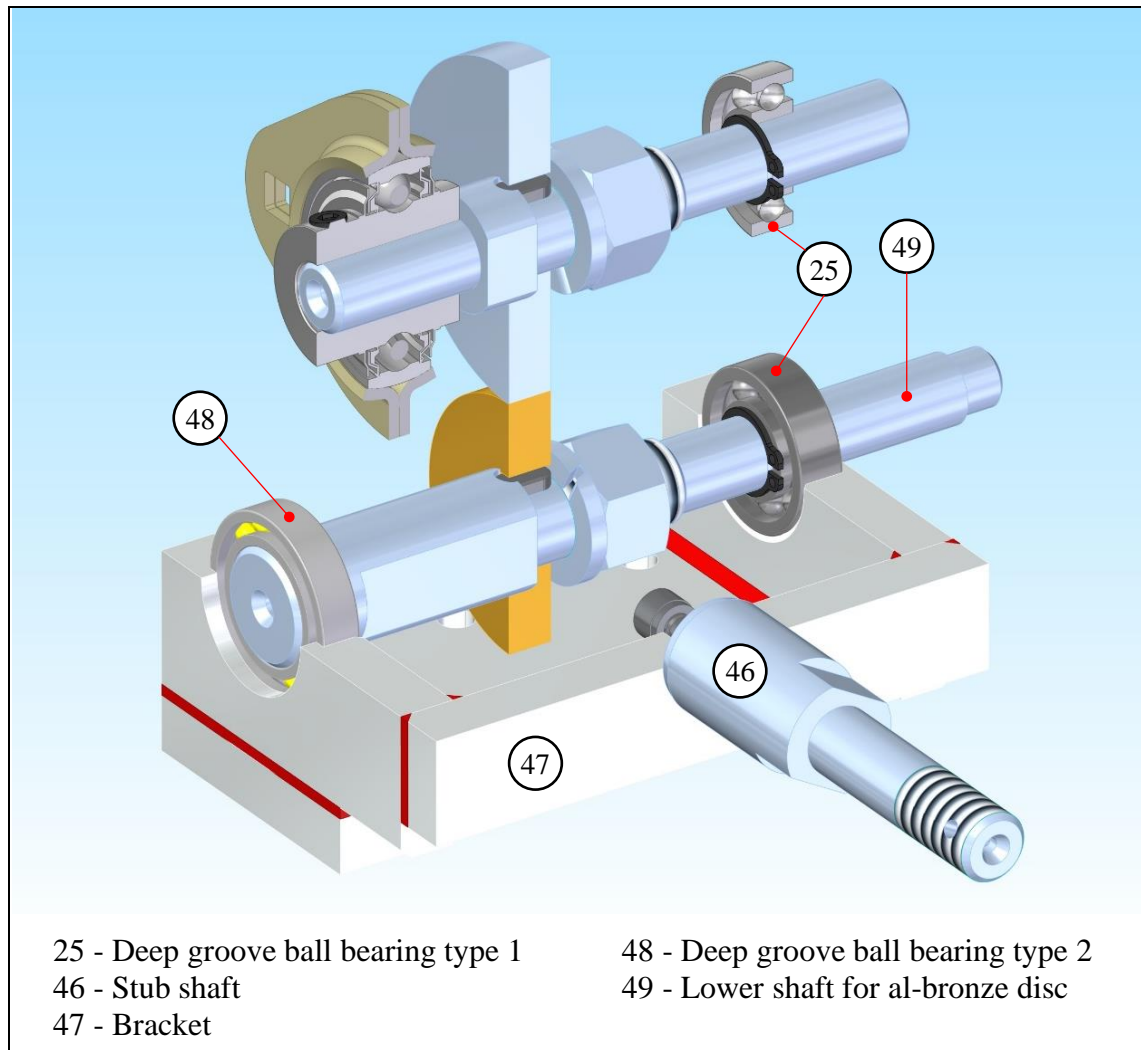


Figure 6.23: Sectioned CAD image of disc and shaft subassemblies in longitudinal vibration configuration.

6.4.2. *Vibration Mode, Frequency, and Waveform*

The test rig can be configured to apply transverse (Figure 6.15 and Figure 6.16) or longitudinal (Figure 6.22) mode of vibration. Vibration frequencies selected for test are 250, 500, 750, 1000, 2000 and 3000 Hz. These frequencies are within the range previously studied by Gutowski and Leus (2011; 2012; 2015).

Current literature and models including those in chapters 4 and 5 assume vibration is harmonic where the displacement \mathbf{u} is sinusoid. Other waveforms have not previously been experimented. The effect of triangular wave vibration in comparison to sinusoidal is tested as part of this research. Figure 6.24 illustrates the two waveforms when $f = 750$ Hz and $u_a = 16 \mu\text{m}$.

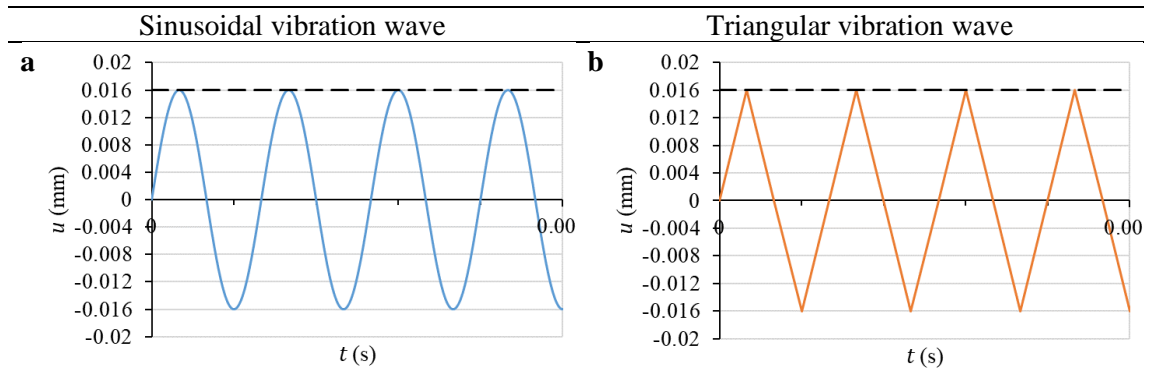


Figure 6.24: Vibration waveforms at $f = 750$ Hz, $u_a = 0.016$ mm (a) sinusoidal (b) triangular.

The control box (Figure 6.21) can generate sinusoidal and triangular type vibration waves. The wave type and frequency are selected via the PuTTY command terminal, Figure 6.25.

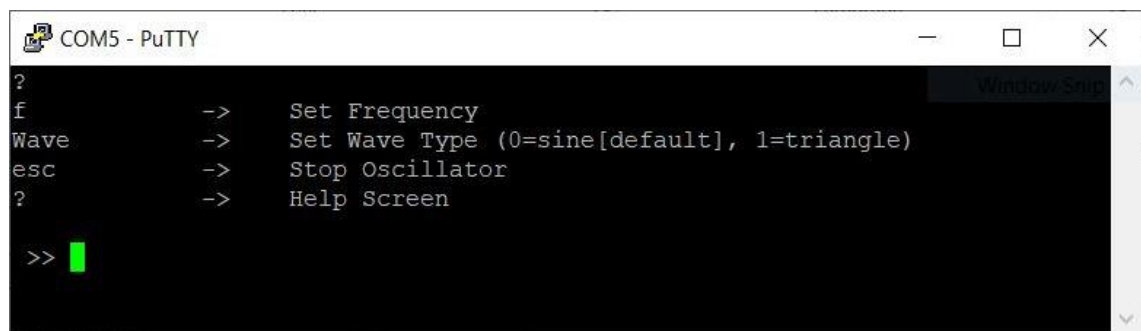


Figure 6.25: PuTTY command terminal for vibration control.

6.4.3. Sonotrode Preload Selection

Output V_l from the load cell (Figure 6.21) can be used to set the desired compression preload on the piezo actuator. To do this, V_l must first be calibrated against known loads. The setup in Figure 6.26 is used for this. The sonotrode is clamped to the edge of a work bench and dead mass suspended off its output pin (Figure 6.26). Figure 6.27 shows an almost perfectly linear relationship between applied load and V_l .

Considering the piezo actuator has blocking force of 1850 N, the preload must be sufficiently large such that the sonotrode is responsive at the higher test frequencies selected (6.4.2), yet small enough to allow margin for inertia force generated by the vibrating components. Operating the sonotrode while attached to the test rig at three different preload settings, 10, 12 and 14 mV, does not affect the output voltage V_l

measured during vibration. 14 mV preload setting is chosen, equivalent to $\approx 1/4$ of the blocking force.



Figure 6.26: Setup for measuring voltage output V_l from load cell at different loads.

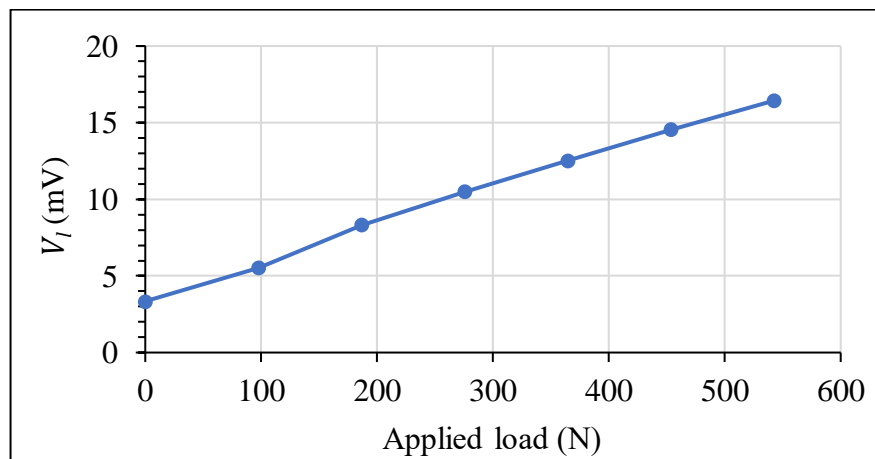


Figure 6.27: Graph of measured voltage output V_l from load cell at different loads.

6.4.4. Sonotrode Travel Range

The selected preload setting must not compromise the piezo actuator's ability to achieve its 32 μm displacement range when attached to the test rig. A check for displacement range confirms there are no pinch points or misalignments in the assembly that could inhibit vibration of the aluminium-bronze disc.

With the sonotrode initially detached from the rig, and 14 mV preload set, the displacement output from the sonotrode at its rated voltage limits -20 to $+120$ V can be checked with a clock dial displacement transducer. Figure 6.28 shows that at application of steady state voltage -20 V the piezo actuator detracts by ≈ 7 μm , and at $+120$ V it extends by ≈ 25 μm , meaning total travel of 32 μm . This confirms the test rig assembly and selected preload do not compromise displacement output of the sonotrode.

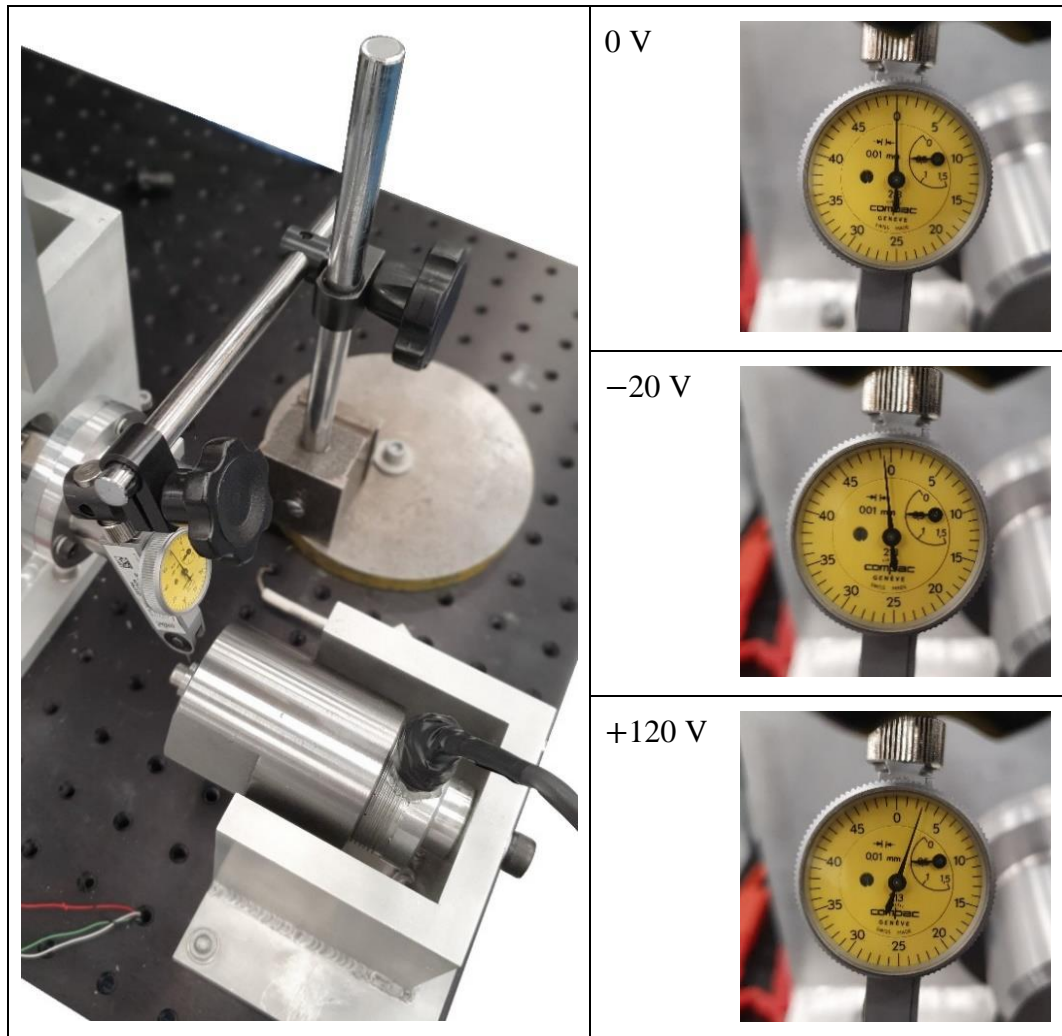


Figure 6.28: Sonotrode displacement response to steady voltage measured with clock dial displacement transducer clamped to magnetic stand. Sonotrode detached from rig.

The sonotrode output displacement check is also performed with the sonotrode attached to the test rig and steady state voltages reapplied. The displacement is measured on the circular plate of the special coupling, and at the opposite end of the lower shaft which interfaces with the torque sensor, Figure 6.29. At 120 V a displacement response of ≈ 25 μm is again measured at both locations. This concludes that attaching the sonotrode to the rig does not compromise its displacement response, and that the

displacement is fully transferred through to the lower shaft on which the aluminium-bronze disc is mounted. Adding 40 lbs (178 N) of dead mass has no impact on the displacement result. The same checks have also been completed in the longitudinal rig configuration.

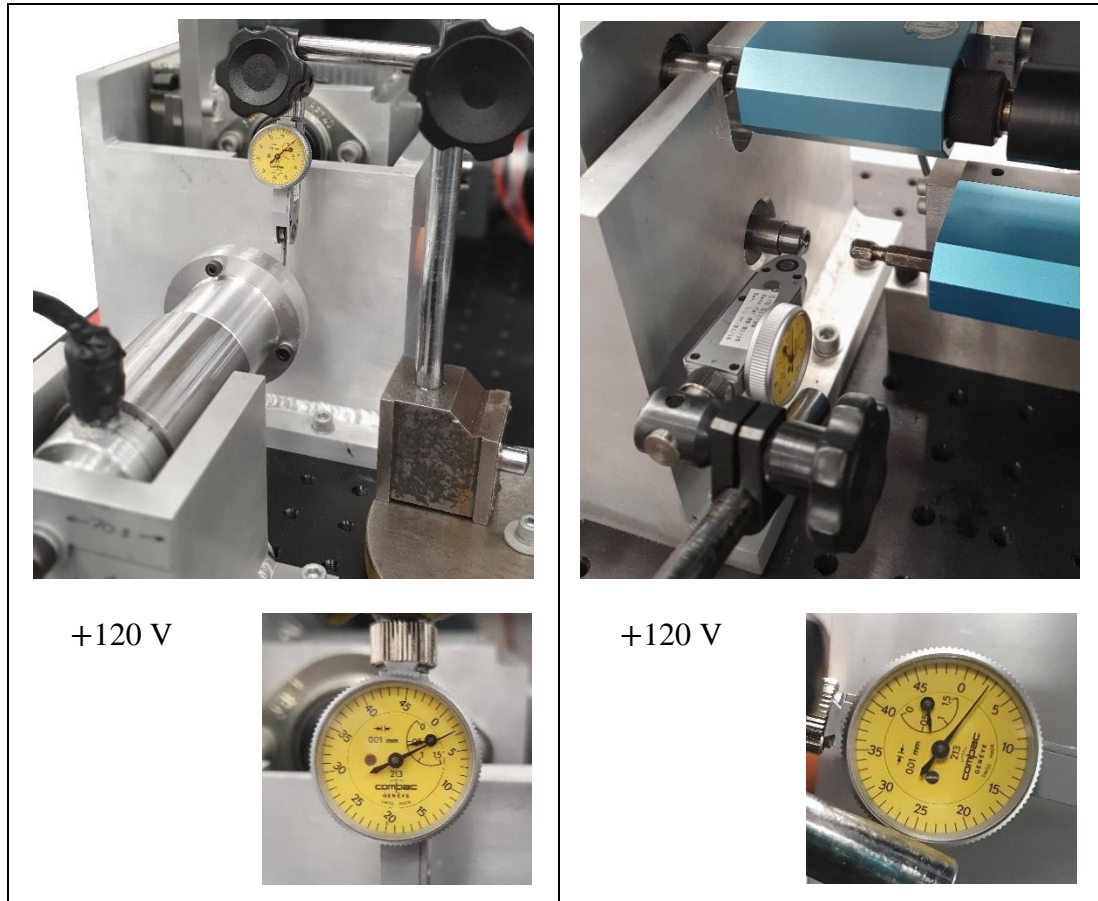


Figure 6.29: Sonotrode displacement response to steady voltage measured with clock dial displacement transducer clamped to magnetic stand. Sonotrode attached to rig.

6.4.5. Noise Isolation

Vibration frequencies above 500 Hz are boisterous. For noise isolation the entire test rig is placed on convoluted acoustic foam (Figure 6.15, Figure 6.20). Also, a noise isolation box large enough to enclose the entire rig has been made by affixing convoluted acoustic foam to all internal faces of a corrugated cardboard box.



Figure 6.30: Noise isolation box.

6.4.6. *Surface Roughness*

Due to learning outcome 6.3.6, iv, from preliminary testing, the test disc diameters d_s and d_a have been changed for the final rig. Therefore, a new batch of discs are manufactured, and surface roughness measurement repeated per 6.3.3 on two aluminium-bronze and two steel discs. For each disc, three circumferential and three lateral readings of Ra are taken at three different locations around the circumference, see Table 6.6 and Table 6.7. Both tables show that the location average Ra between two identical discs is very similar. This indicates manufacturing consistency. An overall average Ra is also calculated for each material. The overall circumferential average Ra (Table 6.6) is similar regardless of material.

Disc material	Disc no.	Location	Ra readings			Location average Ra	Overall average Ra
			1	2	3		
Al-Bronze CC333G- GC	1	1	0.39	0.40	0.40	0.40	0.40
		2	0.40	0.40	0.41	0.40	
		3	0.40	0.40	0.41	0.40	
	2	1	0.40	0.39	0.40	0.40	
		2	0.41	0.40	0.40	0.40	
		3	0.40	0.40	0.40	0.40	
Steel 15NiCr13	1	1	0.44	0.44	0.44	0.44	0.43
		2	0.44	0.45	0.44	0.44	
		3	0.45	0.44	0.44	0.44	
	2	1	0.42	0.41	0.42	0.42	
		2	0.42	0.42	0.42	0.42	
		3	0.42	0.42	0.42	0.42	

Table 6.6: Circumferential surface Ra readings of discs, final rig.

Disc material	Disc no.	Location	Ra readings			Location average Ra	Overall average Ra
			1	2	3		
Al-Bronze CC333G- GC	1	1	0.78	0.78	0.77	0.78	0.79
		2	0.77	0.77	0.77	0.77	
		3	0.76	0.79	0.76	0.77	
	2	1	0.81	0.80	0.80	0.80	
		2	0.80	0.80	0.80	0.80	
		3	0.80	0.81	0.80	0.80	
Steel 15NiCr13	1	1	0.32	0.32	0.31	0.32	0.34
		2	0.32	0.32	0.32	0.32	
		3	0.32	0.32	0.32	0.32	
	2	1	0.36	0.37	0.36	0.36	
		2	0.37	0.38	0.38	0.38	
		3	0.36	0.36	0.36	0.36	

Table 6.7: Lateral surface Ra readings of discs, final rig.

6.4.7. Sliding Velocity

Selection of sliding velocity v_{sl} , as well as normal load F_N (6.4.8) and lubricant type (6.4.9), requires consideration of in-application worm gearing contact characteristics. v_g and v_{sl} are both contact sliding velocities but in different domains, the former for worm gearing as in Table 3.5, and the latter for contact between two discs as per equation (67). Table 3.5 shows a range $1.05 \leq v_g \leq 2.40$ m/s for the worm gearsets selected. v_{sl} for a representative test should ideally be within the range of v_g .

In previous studies of in-plane vibration (Littmann, Storck and Wallaschek, 2001; Gutowski and Leus, 2011; Gutowski and Leus, 2012; Gutowski and Leus, 2015; Gutowski and Leus, 2020), which experiment only with contact of planar surfaces, drive velocities v_d up to only 5 mm/s have been tested. A jump from such slow sliding to velocities above 1 m/s pose risk of obtaining null results. Therefore, a progressive approach has been taken where intermediate values of sliding velocity v_{sl} have been selected for disc-on-disc experiments.

Three motor speed settings have been selected for tests. They are applied by setting the DC voltage supply of the upper motor (Figure 6.21) to $V_{ms} = 1, 3$ and 5.5 V, while supply voltage to the aluminium-bronze disc's drive motor is maintained at a constant $V_{ma} = 0.9$ V. This produces average slide-roll ratios $R = 0.44, 0.88$ and 0.94 respectively with sliding velocities in the range $2 \leq v_{sl} \leq 90$ mm/s. This is still faster than any sliding velocity previously tested for vibration induced friction reduction in a sliding-rolling lubricated contact.

6.4.8. Normal Load Selection

Using Hertzian contact relationship (70) the contact pressure p_{max} between the two discs can be calculated (Budynas and Nisbett, 2011), where the Hertzian contact area half-width b is given by (71), and F_N by (72). Values used for the p_{max} calculation are listed in Table 6.8, in which the results of (70)-(72) are coloured grey. The table shows that additional mass $m_w = 9.1$ kg (20 lbs) causes $p_{max} = 194.3$ N/mm² between the discs. In the interest of sustaining the rig the dead mass $m_w = 9.1$ kg is not exceeded and remains constant for all tests.

$$p_{max} = \frac{2F_N}{\pi bD} \tag{70}$$

$$b = \sqrt{\frac{2F_N (1 - \epsilon_s^2)/E_s + (1 - \epsilon_a^2)/E_a}{\pi D (1/d_s + 1/d_a)}} \quad (71)$$

$$F_N = (m_r + m_w) \times 9.81 \quad (72)$$

Description	Symbol	Units	Steel disc	Al-bronze disc
Poisson's ratio	ϵ_s, ϵ_a		0.291	0.320
Modulus of elasticity	E_s, E_a	N/mm ²	207,000	125,000
Disc diameter	d_s, d_a	mm	60	45
Disc thickness	D	mm	8	
Mass of rig platform subassembly	m_r	kg	5.36	
Dead mass	m_w	kg	9.07	
Normal force	F_N	N	141.6	
Contact area half-width	b	mm	0.058	
Max Hertzian contact pressure	p_{max}	N/mm ²	194.3	

Table 6.8: Parameters used for calculation of Hertzian contact pressure.

6.4.9. Lubricant Selection

Due to learning outcome 6.3.6, iii, from preliminary testing, all tests are conducted in the presence of lubricant. In application (Figure 1.1) the worm gearset is fully submerged in mineral oil Fuchs Titan Gear MP SAE 80. However, the evasion of seals from the test rig to reduce drag make it impossible to fully submerge both discs in oil. Dip lubrication is thus used instead, Figure 6.31.

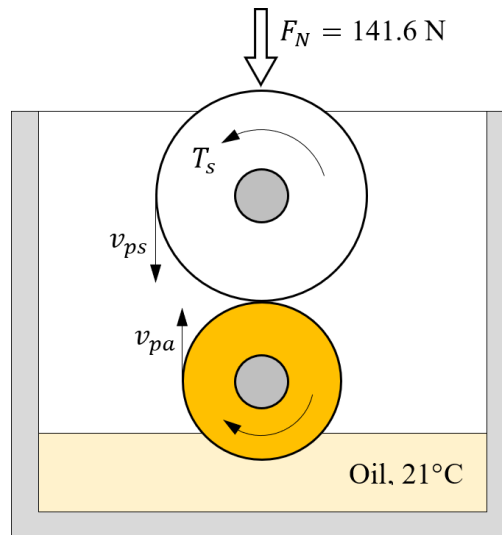


Figure 6.31: Schematic showing dip lubrication of aluminium-bronze disc, peripheral disc velocities and normal load.

Tests are first conducted with WIC Medium Compound grease (Table 6.4) brushed onto the discs. Then, unused clean disc specimens are tested in 0.7 litres of SAE 80 oil (Table 6.9) filled into the casing to dip lubricate the aluminium-bronze disc. Refer to Table 6.10 for a matrix of test combinations.

Lubricant property	Description
Appearance	Brown liquid
Flash point	215°C
Density	0.893 kg/l
v_{40}	92 mm ² /s
v_{100}	10 mm ² /s
Viscosity index	96

Table 6.9: Properties of Fuchs Titan Gear MP SAE 80 mineral oil (Fuchs, 2011).

6.4.10. Test Matrix

Information from 6.4.2, 6.4.7 and 6.4.9 is assembled into test matrix Table 6.10 to summarise the combinations of tests conducted (✓), and those that have been excluded (✗). Two parameters remain constant across all tests, as per 6.4.7 and 6.4.8; $V_{ma} = 0.9$ V, $F_N = 141.6$ N.

Mode:		Transverse						Longitudinal					
Lubricant:		Grease			Oil			Grease			Oil		
V_{ms} :		1	3	5.5	1	3	5.5	1	3	5.5	1	3	5.5
Sinusoidal wave	250 Hz	✓	✓	✓	✓	✓	✓	✗	✗	✗	✓	✓	✓
	500 Hz	✓	✓	✓	✓	✓	✓	✗	✗	✗	✓	✓	✓
	750 Hz	✓	✓	✓	✓	✓	✓	✗	✗	✗	✓	✓	✓
	1000 Hz	✓	✓	✓	✓	✓	✓	✗	✗	✗	✓	✓	✓
	2000 Hz	✓	✓	✓	✓	✓	✓	✗	✗	✗	✓	✓	✓
	3000 Hz	✓	✓	✓	✓	✓	✓	✗	✗	✗	✓	✓	✓
Triangular wave	250 Hz	✗	✗	✗	✓	✓	✓	✗	✗	✗	✓	✓	✓
	500 Hz	✗	✗	✗	✓	✓	✓	✗	✗	✗	✓	✓	✓
	750 Hz	✗	✗	✗	✓	✓	✓	✗	✗	✗	✓	✓	✓
	1000 Hz	✗	✗	✗	✓	✓	✓	✗	✗	✗	✓	✓	✓
	2000 Hz	✗	✗	✗	✓	✓	✓	✗	✗	✗	✓	✓	✓
	3000 Hz	✗	✗	✗	✓	✓	✓	✗	✗	✗	✓	✓	✓

Table 6.10: Test matrix.

6.4.11. Data Capture

Figure 6.21 lists the test data captured by an 8 channel Picoscope[®]. The Picoscope[®] software is configured such that all 8 channels concurrently display torques (T_s and T_a), disc speeds (S_{ms} and S_{ma}), voltages (V_w and V_l) and motor currents (i_{ms} and i_{ma}).

The aluminium-bronze disc is used as control; it has a fixed supply $V_{ma} = 0.9$ V throughout the tests, and vibration test frequencies applied to it are for analysing the effect on the steel disc. Data regarding the aluminium-bronze disc is thus captured for information only. Of greater interest is what happens with the steel disc.

Table 6.11 summarises test data for the steel disc before and after application of 750 Hz transverse sinusoidal vibration with oil lubrication when $V_{ms} = 1$ V. Before applying vibration $\bar{T}_s = 0.6448$ Nm. After applying vibration $\bar{T}_s = 0.0925$ Nm. Changes also occur to the motor speed and motor current for the steel disc due to vibration (Table 6.11).

\vec{T}_s	\vec{T}_s	\vec{S}_{ms}	\vec{S}_{ms}	\vec{i}_{ms}	\vec{i}_{ms}
(Nm)	(Nm)	(RPM)	(RPM)	(amps)	(amps)
0.6448	0.0925	70.54	95.51	1.4020	0.9653

Table 6.11: Test data for steel disc at 750 Hz transverse sinusoidal vibration, oil lubrication, $V_{ms} = 1$ V.

Relationships (73)-(75) are applied to quantify the influence of vibration on drive torque, power loss and efficiency of the steel disc's drive. Likewise, test data for all test combinations (Table 6.10) is processed for graphical representation and discussion in 6.4.13 and 6.6.

$$\% \text{ change in } T_s = \left(\frac{\vec{T}_s - \vec{T}_s}{\vec{T}_s} \right) 100 \quad (73)$$

$$\% \text{ change in } P_{loss_s} = \left(\frac{\vec{T}_s \vec{S}_{ms} - \vec{T}_s \vec{S}_{ms}}{\vec{T}_s \vec{S}_{ms}} \right) 100 \quad (74)$$

$$\Delta \eta_s = \left[\left(\frac{V_{ms} \vec{i}_{ms} - \frac{\pi \vec{T}_s \vec{S}_{ms}}{960}}{V_{ms} \vec{i}_{ms}} \right) - \left(\frac{V_{ms} \vec{i}_{ms} - \frac{\pi \vec{T}_s \vec{S}_{ms}}{960}}{V_{ms} \vec{i}_{ms}} \right) \right] 100 \quad (75)$$

6.4.12. Test Procedure

The test procedure describes the sequential steps taken to collect results for tests identified in Table 6.10.

1. Wipe the steel and aluminium-bronze test discs clean with isopropyl alcohol.
2. Measure and record the weight of both discs.
3. Configure the test rig for transverse vibration (Figure 6.15 and Figure 6.16). Install discs onto their respective shafts.
4. Place dead mass $m_w = 9.1$ kg (20 lbs) on rig (Figure 6.16).
5. Switch on mains power and DC power supplies for the torque sensors, vibration control box and sonotrode load cell (Figure 6.21).
6. Switch on the two current clamps and laptop (Figure 6.21).
7. Connect USB devices to laptop (Figure 6.21). Load PuTTY, Arduino[®] and Picoscope[®] software.
8. Using Picoscope[®] data capture set the sonotrode preload to $V_l = 14$ mV (6.4.3).
9. With PuTTY set the vibration waveform to sinusoidal (Figure 6.25).

10. If lubricant is grease, brush grease onto outer diameter of both discs. If lubricant is oil, fill the aluminium casing (Figure 6.16) with 0.7 litres of SAE 80 oil (Table 6.9) to dip lubricate the aluminium-bronze disc.
11. Cover test rig with noise isolation box (Figure 6.30).
12. Set voltage supply to the motors $V_{ma} = 0.9$ V and $V_{ms} = 1$ V.
13. Perform trial run; start Picoscope[®] data logger and energise motors temporarily.
14. De-energise the motors and stop Picoscope[®] data logger. Check plots to ensure the current clamps are zeroed when motors are unpowered. If not, zero the current clamps and go back to step 13.
15. Check that the torques, speeds and motor currents change at the time when the motors are energised. If not, check power and cabling for the sensors and go back to step 13.
16. Re-energise motors temporarily to manually measure their speeds using a calibrated handheld digital laser tachometer. Check that the manually measured motor speeds match the sensor detected speeds from step 15. If not, check the sensor voltage to RPM scaling values then go back to step 13.
17. Perform actual test run; energise the motors and start Picoscope[®] data logger. Allow the discs to slide-roll for 10 seconds minimum.
18. With PuTTY (Figure 6.25) apply vibration frequency command $f = 250$ Hz and allow to run for another 10 seconds minimum.
19. De-energise the motors and apply PuTTY command to stop vibration. Wait 10 seconds at idle.
20. Re-energise the motors for another 10 seconds minimum.
21. Repeat steps 18-20 until all vibration test frequencies have been applied (Table 6.10).
22. Stop Picoscope[®] data logger and save the data file.
23. Repeat steps 17-22 to obtain a second set of data.
24. Repeat steps 10-23 at $V_{ms} = 3$ V and 5.5 V for intended coverage of transverse sinusoidal vibration tests, per Table 6.10.
25. Remove disc test specimens.
26. Repeat steps 1-2. Store the tested discs.
27. If lubricant is oil, extract the used oil out of the aluminium casing with a vacuum fluid extractor.

28. With new test discs repeat steps 1-27 for intended coverage of transverse triangular vibration tests, per Table 6.10.
29. Reconfigure the test rig for longitudinal vibration (Figure 6.22).
30. With new test discs repeat steps 1-27 for intended coverage of longitudinal sinusoidal vibration tests, per Table 6.10.
31. With new test discs repeat steps 1-27 for intended coverage of longitudinal triangular vibration tests, per Table 6.10.
32. Assemble test data and analyse.

6.4.13. *Limitations of Experiments and Error Mitigation*

One of the limitations of experimentation is that it is a time-consuming process. To do it correctly, each variable has been isolated for tests, and combinations of variables have also been considered (6.4.10). The process of setting up and conducting these tests is lengthy, and a significant amount of time has been required to evaluate the test data.

For experimental research to be effective, a single set of data cannot be trusted, and the results must be reproduced consistently. Each combination in the test matrix (Table 6.10) has been tested twice to remove any doubt over test validity and evaluation of results.

Experimentation should aim to imitate real application conditions as closely as possible. However, worm and wheel gear teeth are known to have slight variation from one sample to another until bedding-in of the gearset. To mitigate from experimental inconsistencies caused by this, while expanding the relevance of experimentation beyond gearing alone, an easily repeatable test specimen geometry in the form of metallic discs has been pursued.

Other measures taken to mitigate errors in experimentation include the use of flexible couplings to account for any shaft misalignments. Measuring equipment such as torque sensors and speed encoders are calibrated before use. The test procedure includes checks before each run to ensure test data is being correctly captured (6.4.12, steps 13-16).

6.5. Transverse Vibration Test Results

The test matrix (Table 6.10) shows the combinations of transverse vibration tests conducted, each performed twice as per the test procedure (6.4.12) for collection of two datasets to assess consistency of results. Transverse vibration test data is evaluated in 6.5.1-6.5.5.

6.5.1. *Torque Reduction due to Transverse Vibration*

Graphs in Figure 6.32-Figure 6.34 show percentage reduction of T_s plotted against f , for each V_{ms} setting. The corresponding average slide velocity \tilde{v}_{sl} is also listed. The graphs show good consistency in \tilde{v}_{sl} between the first and second datasets. However, in terms of % reduction of T_s the two datasets are more consistent only when oil is used as lubricant (Figure 6.33 and Figure 6.34). Evidently, regardless of lubricant type or vibration wave type, at any \tilde{v}_{sl} the largest % reduction of T_s occurs when $f = 750$ Hz. The second most influential frequency is 2000 Hz, and the least influential is 3000 Hz. This proves that a higher vibration frequency does not necessarily mean a greater reduction of T_s . To understand why, further tests are conducted using accelerometers to measure the vibration directly at the lower shaft, detailed in 6.5.2.

Tests using oil lubrication (Figure 6.33 and Figure 6.34) show that at any vibration frequency f , the higher the average sliding velocity \tilde{v}_{sl} the smaller the % reduction of T_s . The same is true for the greased tests (Figure 6.32) except at 500 Hz.

Comparing Figure 6.33 and Figure 6.34, generally a larger % reduction of T_s is achieved by sinusoidal vibration. A noticeable difference is again at 500 Hz, where the triangular waveform has much less impact compared to sinusoidal.

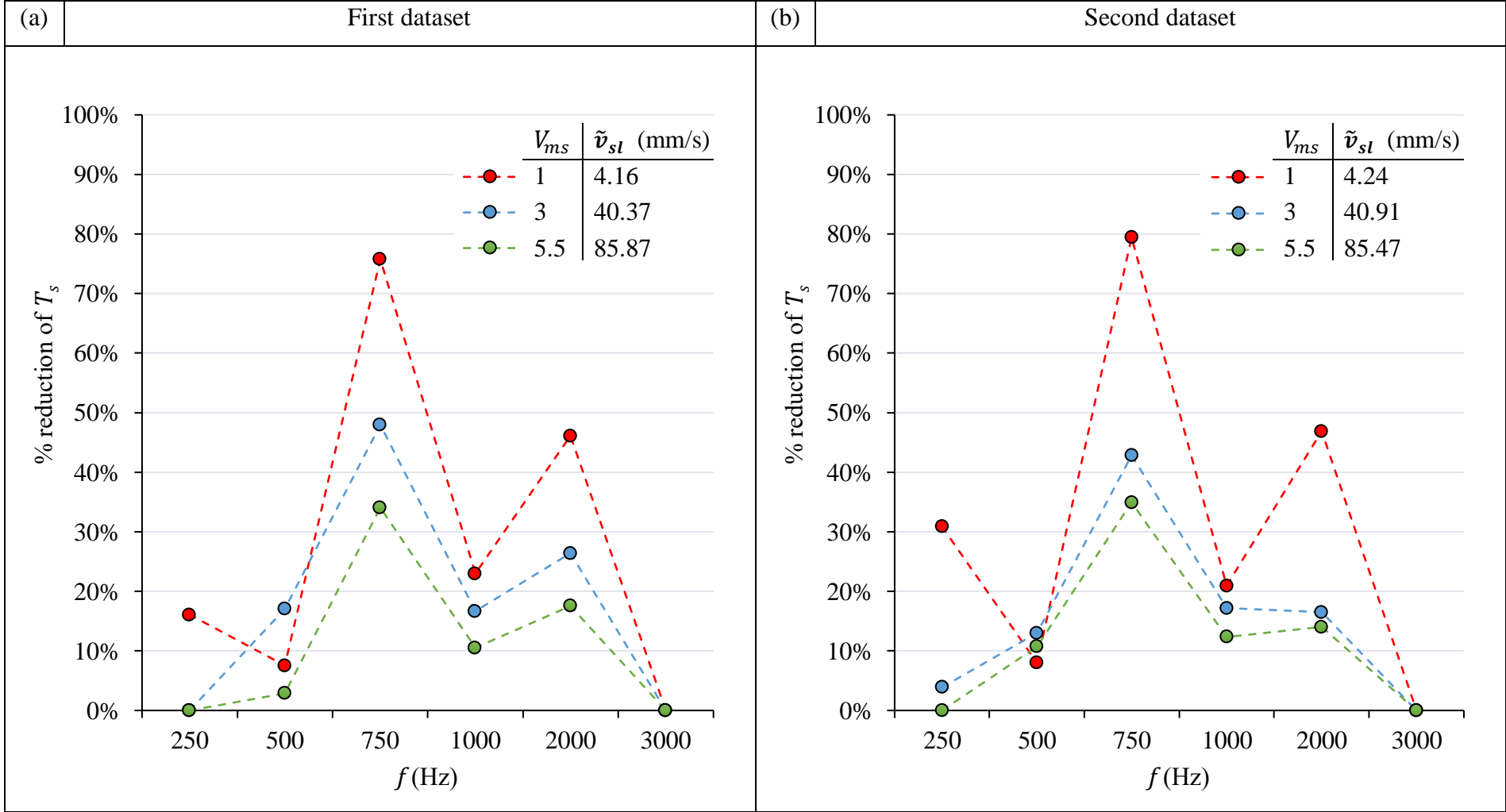


Figure 6.32: Effect of f on T_s . Transverse sinusoidal vibration, greased contact.

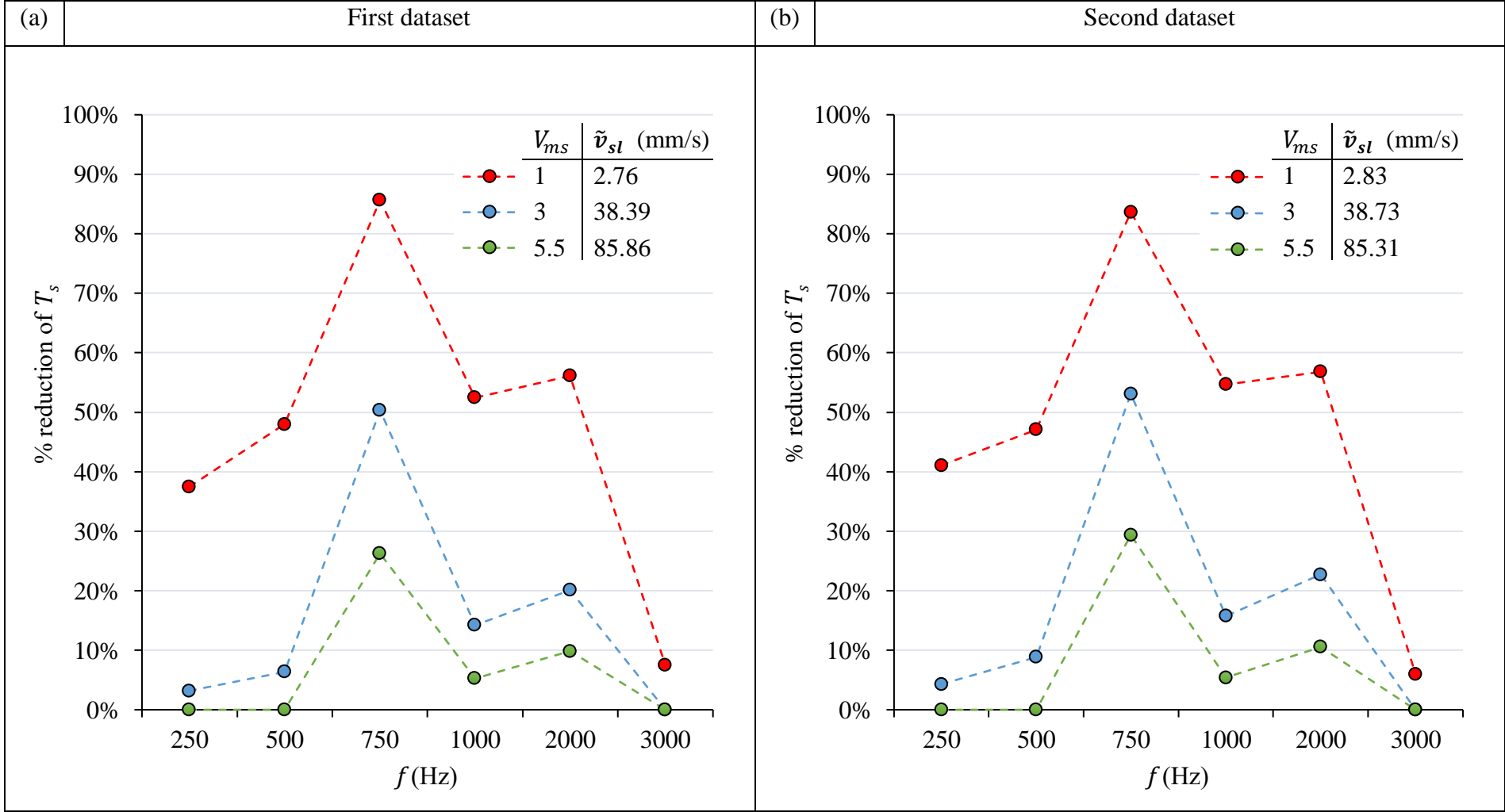
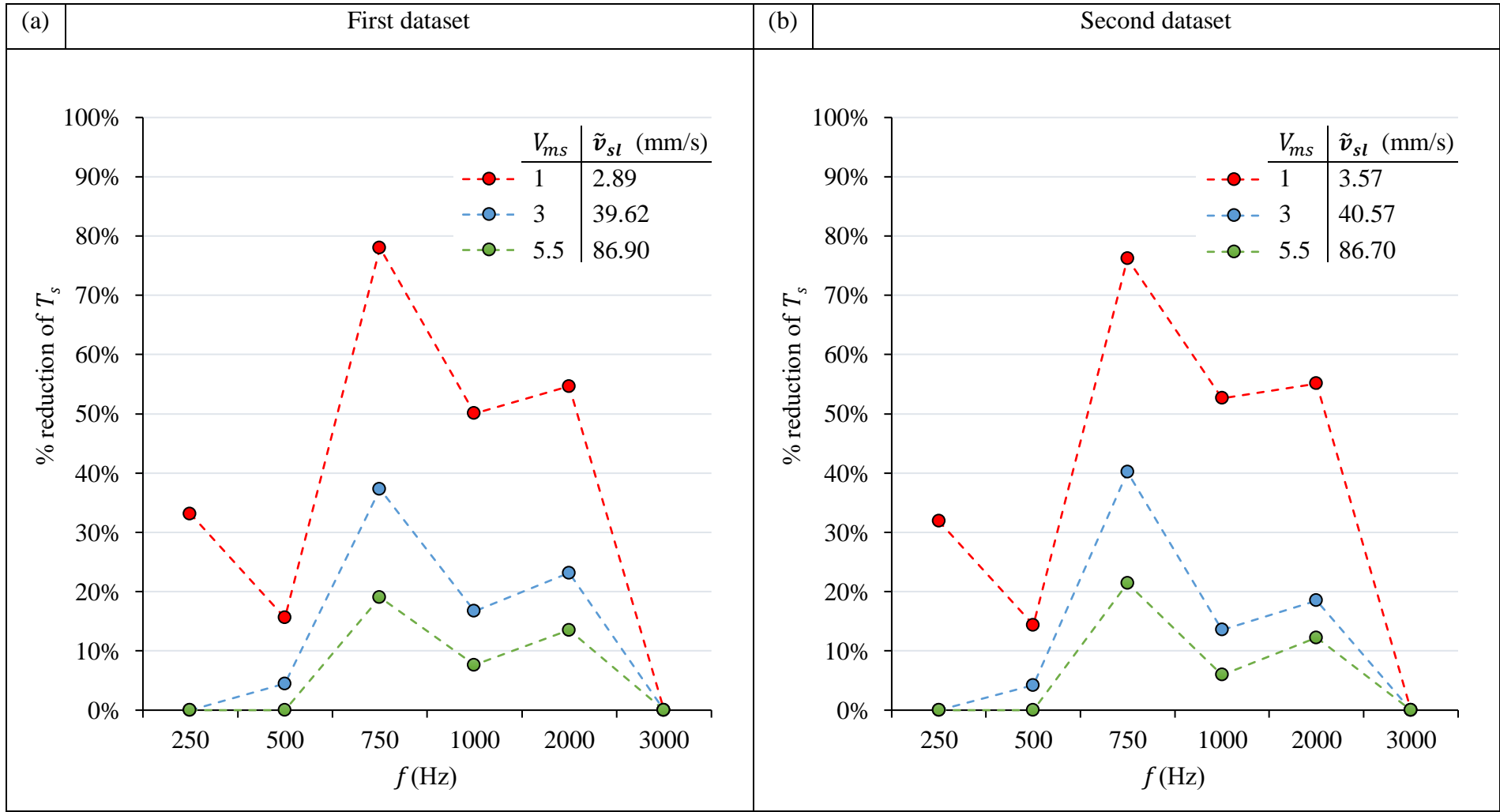


Figure 6.33: Effect of f on T_s . Transverse sinusoidal vibration, oil dip lubrication.



6.5.2. Correlation of Torque Reduction with Accelerometer Data

Figure 6.32-Figure 6.34 show profiles in which $f = 750$ Hz distinctly causes the largest, and 2000 Hz the second largest reduction in T_s . An investigation is conducted to justify the profile in Figure 6.33.

An accelerometer mounted on the flexible coupling (Figure 6.35) measures the vibration frequency f and acceleration a of the lower shaft, and therefore of the aluminium-bronze disc rigidly affixed to it. Knowing f and a it is possible to calculate the vibration velocity amplitude v_a applied to the aluminium-bronze disc:

$$v_a = \frac{a}{2\pi f} \quad (76)$$

Vibration measurement is repeated to collect two sets of accelerometer data. Results are plotted in Figure 6.36, showing close correlation of v_a between both datasets, and that the aluminium-bronze disc experiences the fastest vibration velocity of $v_a = 59$ mm/s at $f = 750$ Hz.

Test conditions are identical to those used for obtaining results in Figure 6.33; transverse vibration with sinusoidal waveform, oil dip lubrication, and $F_N = 141.6$ N. However, in this case the lower shaft cannot be rotationally driven as that would cause the accelerometer wire to wind around the rotating components, risking damage to equipment.

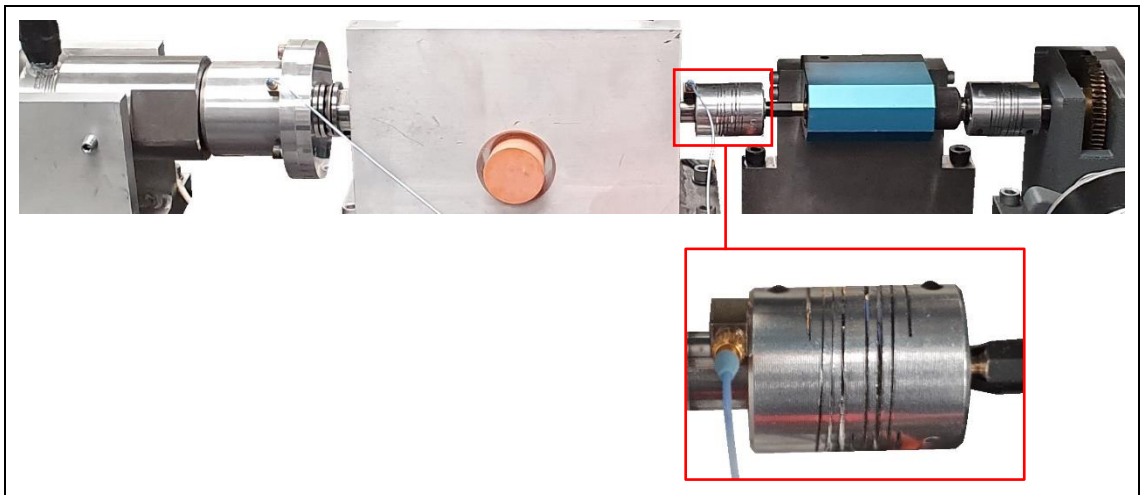


Figure 6.35: Accelerometer position for transverse vibration measurements.

Figure 6.36 compares measured v_a with % reduction of T_s at $V_{ms} = 1$ from Figure 6.33a. v_a evidently correlates with % reduction of T_s . Maximum v_a at 750 Hz

coincides with the maximum reduction of T_s . This work shows that v_a and thus the % reduction of T_s , depend on the vibration characteristics of the test system.

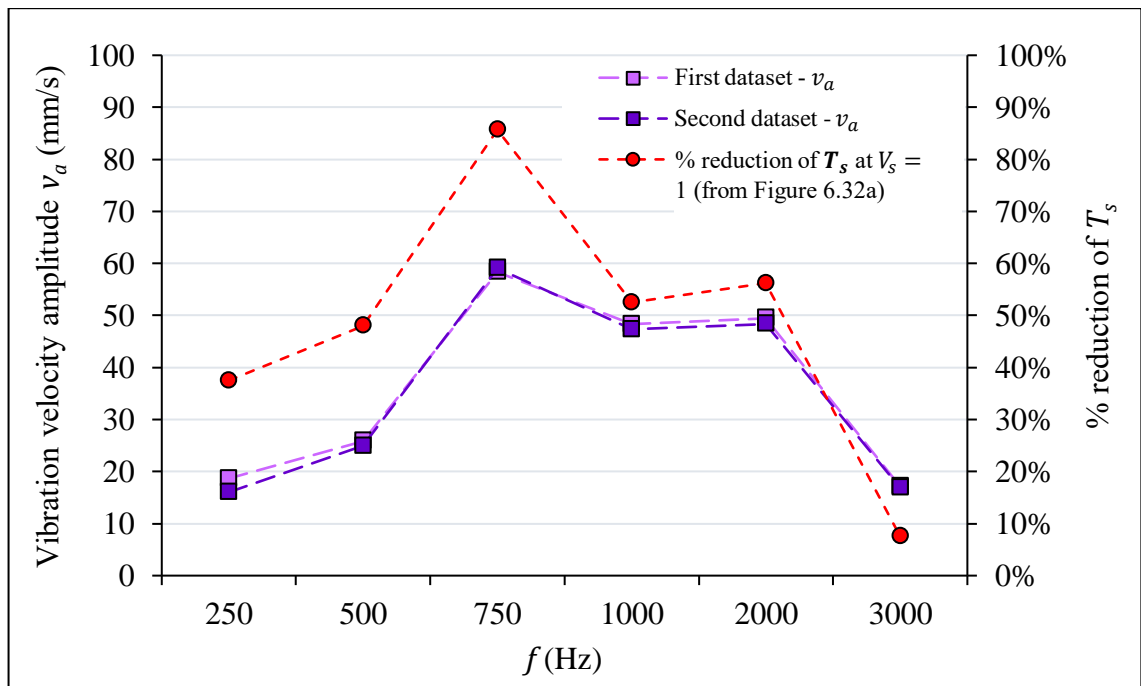


Figure 6.36: Influence of v_a on T_s reduction at applied transverse test frequencies.

6.5.3. Normalised Torque vs. Previous Simulation

Figure 6.37 shows normalised drive torque T_{sv}/T_{ss} from transverse vibration disc-on-disc test at $f = 750$ Hz, in a form that can be compared with previous planar contact simulation results in Figure 5.8. A similarity between disc-on-disc test results and previous simulation results is that reduction of T_{sv}/T_{ss} occurs when $k_v \leq 1$. Figure 6.37 and Figure 5.8 results are not a perfect match owing to the different systems being evaluated.

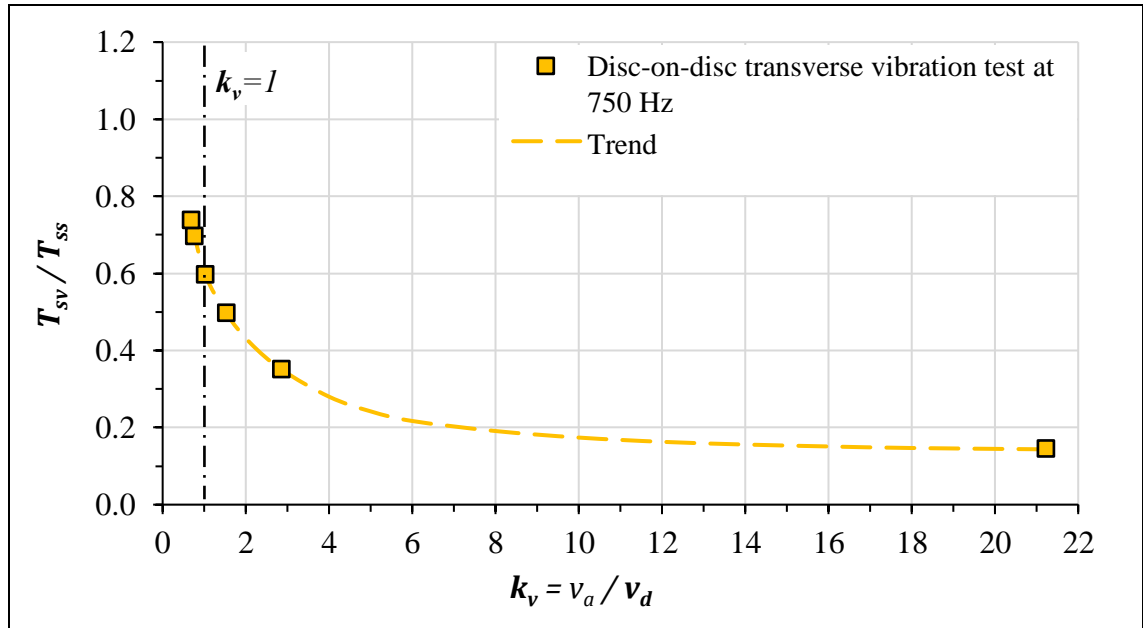


Figure 6.37: Disc-on-disc transverse vibration test, change in T_{sv}/T_{ss} with k_v .

6.5.4. Power loss Reduction due to Transverse Vibration

6.5.1-6.5.3 are concerned with changes in T_s only. Friction reduction due to vibration also results in reduced power loss P_{loss_s} , equation (74). Reduction in P_{loss_s} due to sinusoidal and triangular transverse vibration with oil dip lubrication is plotted in Figure 6.38 and Figure 6.39 respectively. The figures show similar trends to Figure 6.33 and Figure 6.34. This is because speed changes are small in comparison to torque changes, thus T_s is the influencing factor for P_{loss_s} . Test data shows that the higher the average sliding velocity \tilde{v}_{sl} , the smaller the reduction of P_{loss_s} . Since reduction in T_s is larger with sinusoidal vibration (6.5.1), % reduction in P_{loss_s} is also larger with sinusoidal vibration.

6.5.5. Efficiency Improvement due to Transverse Vibration

The improvement in efficiency $\Delta\eta_s$, determined by (75), due to sinusoidal and triangular transverse vibration with oil dip lubrication is plotted in Figure 6.40 and Figure 6.41 respectively. Sinusoidal vibration allows a greater improvement of η_s at the optimum frequency 750 Hz.

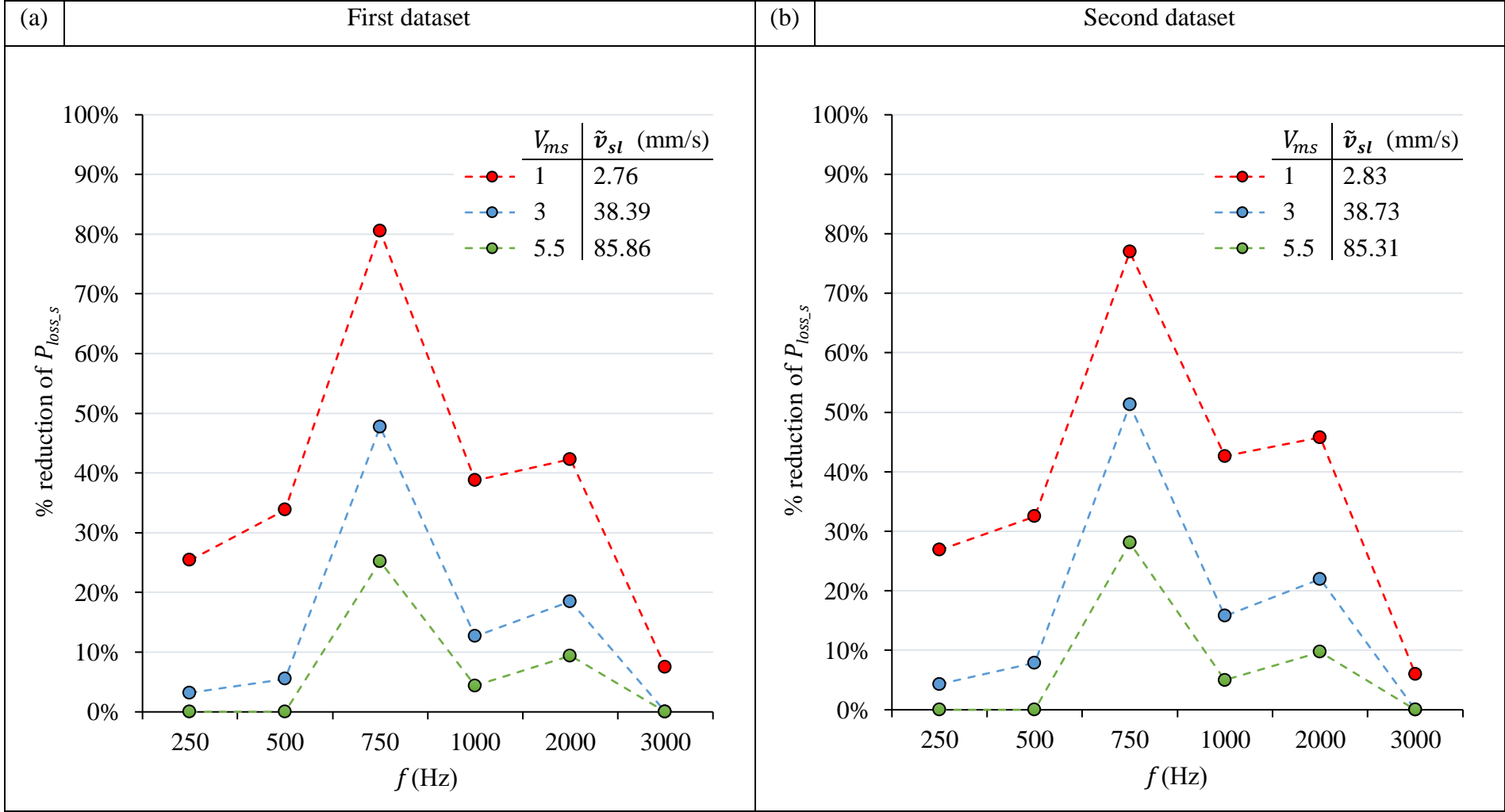
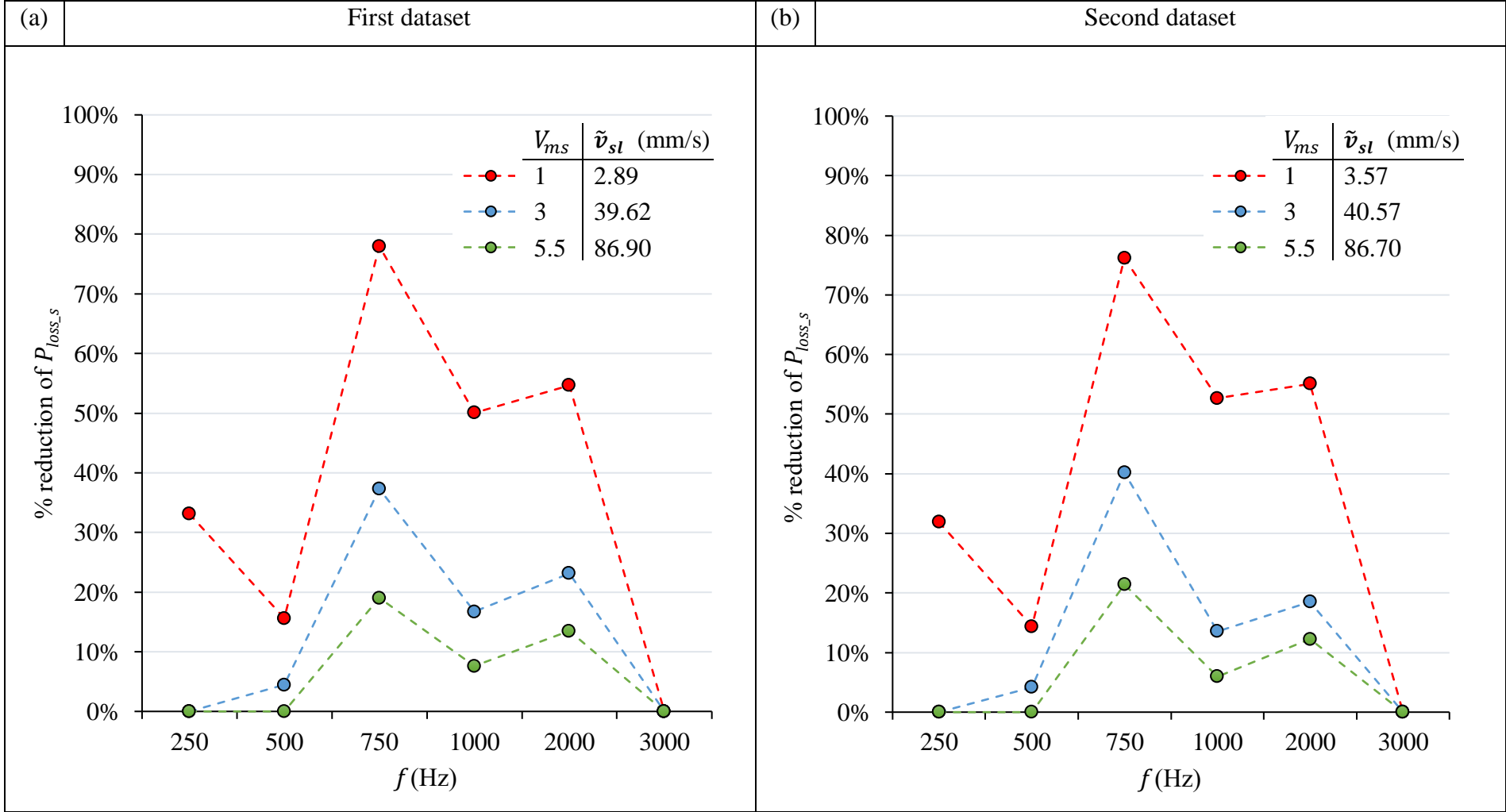


Figure 6.38: Effect of f on $P_{loss,s}$. Transverse sinusoidal vibration, oil dip lubrication.



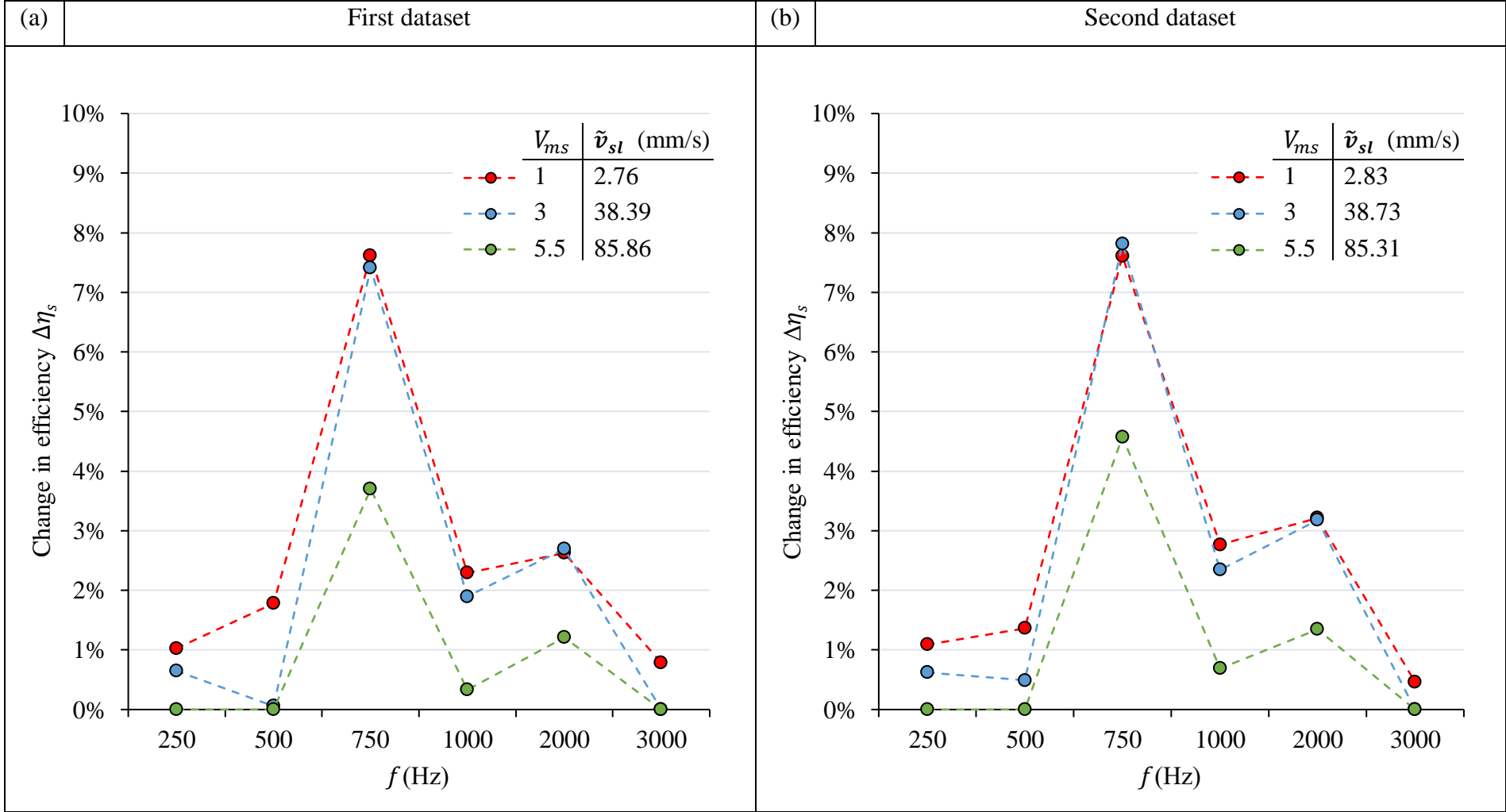
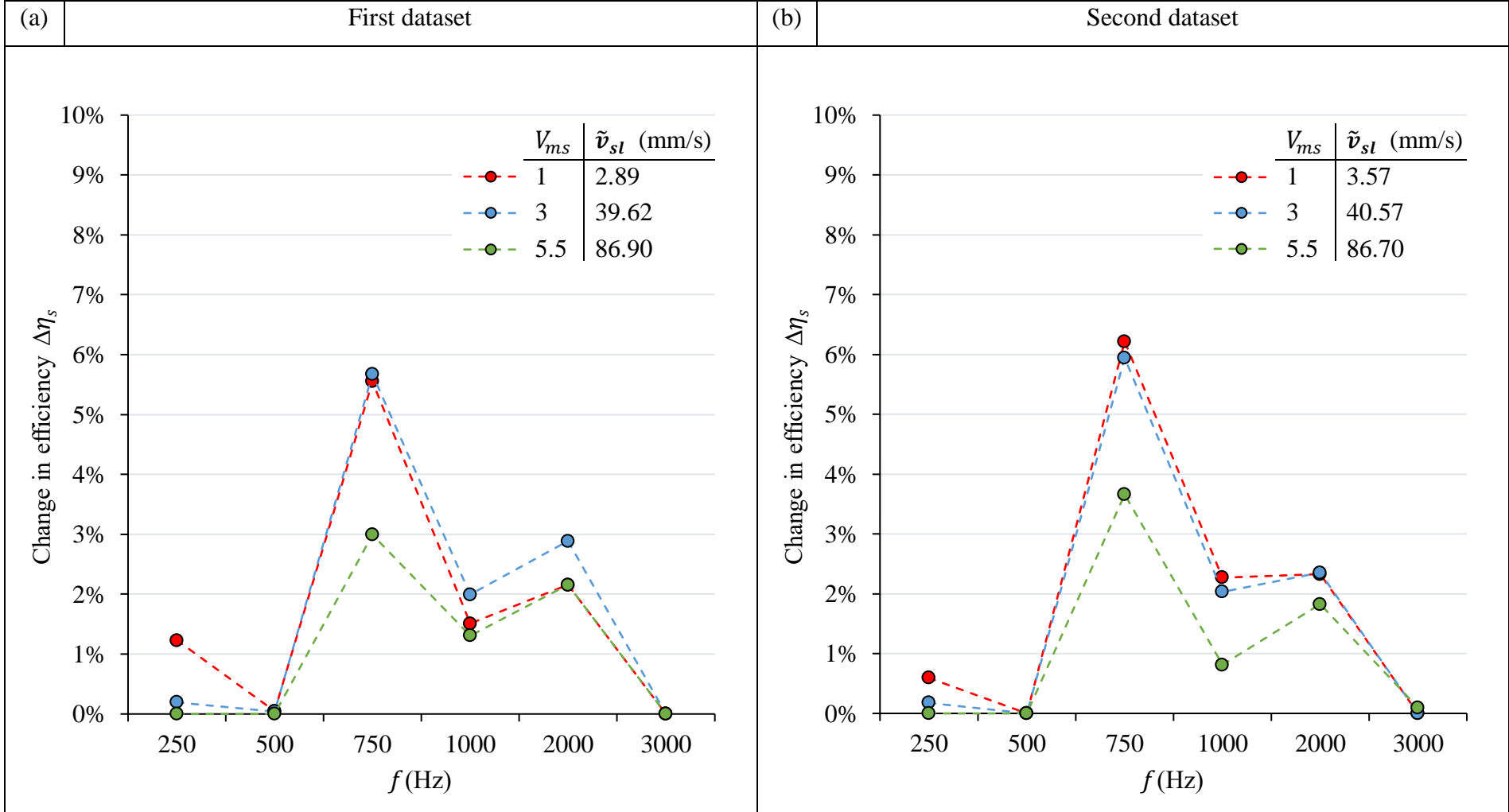


Figure 6.40: Effect of f on $\Delta\eta_s$. Transverse sinusoidal vibration, oil dip lubrication.



6.6. Longitudinal Vibration Test Results

This section follows a similar format to 6.4.13. The test matrix (Table 6.10) shows the combinations of longitudinal vibration tests conducted, each performed twice as per the test procedure (6.4.12) for collection of two datasets to assess consistency of results. Longitudinal vibration test data is evaluated in 6.6.1-6.6.5.

6.6.1. *Torque Reduction due to Longitudinal Vibration*

In similarity to transverse vibration results (6.5.1), it is evident from Figure 6.42 and Figure 6.43 that at any \tilde{v}_{sl} the largest % reduction of T_s occurs when $f = 750$ Hz, regardless of the vibration wave type. The secondary peak present at 2000 Hz with transverse vibration (Figure 6.33 and Figure 6.34) is no longer present in longitudinal mode.

Comparing Figure 6.42 with Figure 6.43, maximum % reduction of T_s is again achieved by sinusoidal vibration. However, in longitudinal mode the triangular wave is more effective when $f \geq 2000$ Hz, at slower sliding speeds.

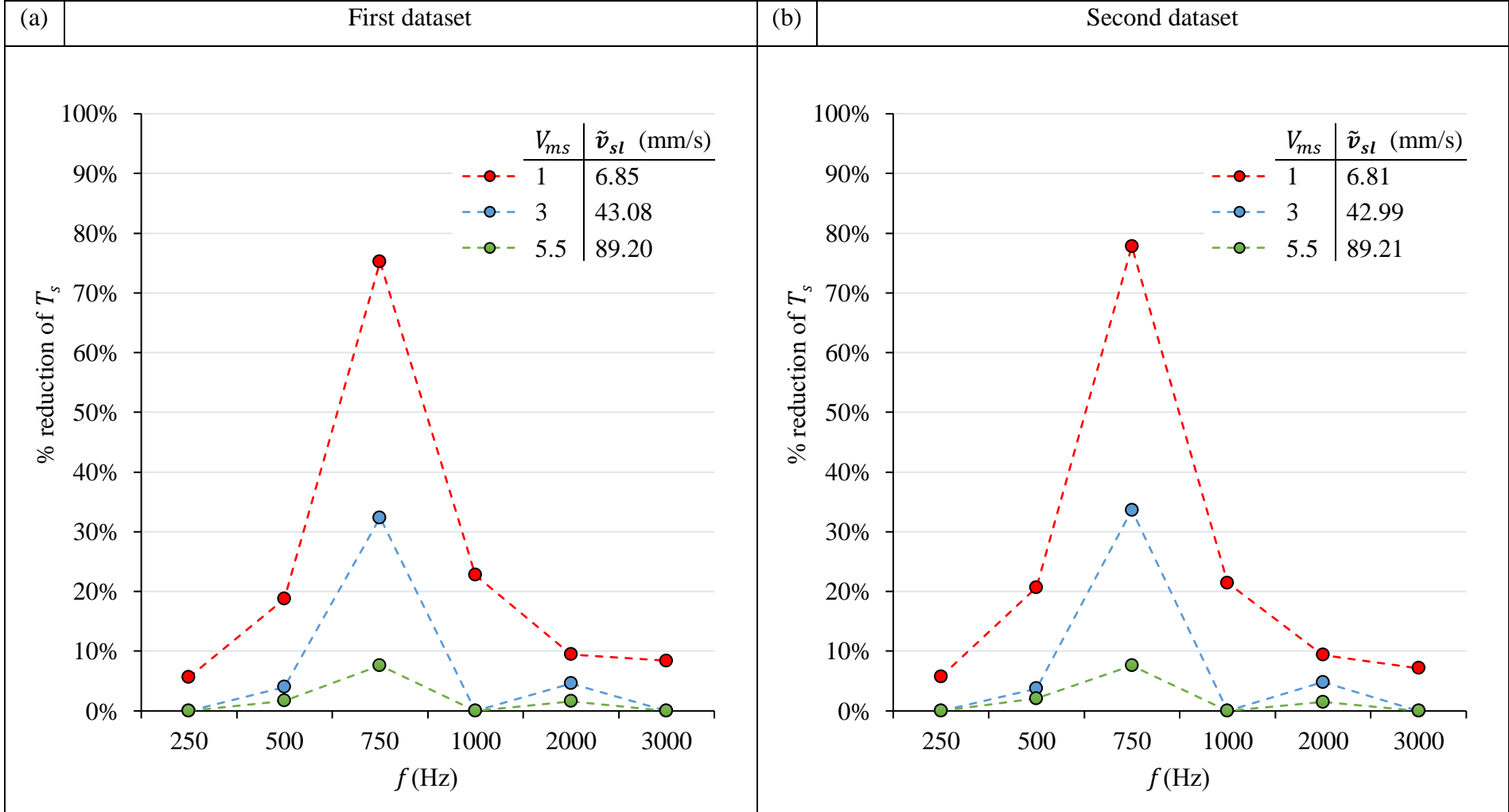
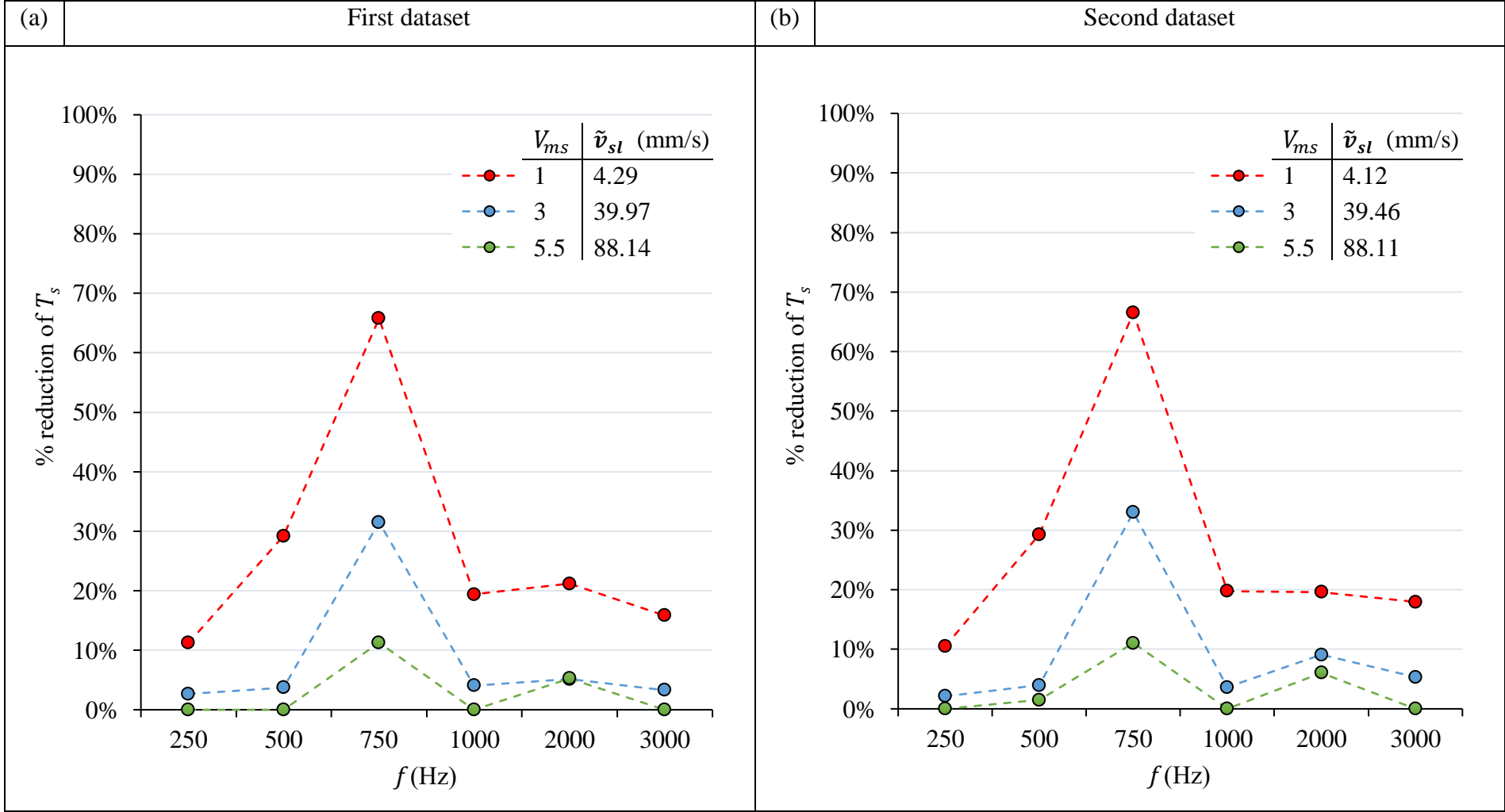


Figure 6.42: Effect of f on T_s . Longitudinal sinusoidal vibration, oil dip lubrication.



6.6.2. Correlation of Torque Reduction with Accelerometer Data

In similarity to 6.5.2, the longitudinal vibration results in Figure 6.42 are investigated using an accelerometer (Figure 6.44) mounted on a flat face of the lower shaft (Figure 6.23), to measure the vibration frequency f and acceleration a to which the aluminium-bronze disc is subjected. Knowing f and a , equation (76) calculates the vibration velocity amplitude v_a applied to the aluminium-bronze disc:

Figure 6.45 shows close correlation of v_a between the first and second datasets collected. The aluminium-bronze disc experiences the fastest vibration velocity of $v_a = 87$ mm/s at $f = 750$ Hz.

Test conditions are identical to those used for obtaining results in Figure 6.42; longitudinal vibration with sinusoidal waveform, oil dip lubrication, and $F_N = 141.6$ N. However, as is the case in 6.5.2 the lower shaft cannot be rotationally driven as that would cause the accelerometer wire to wind around the rotating components, risking damage to equipment.

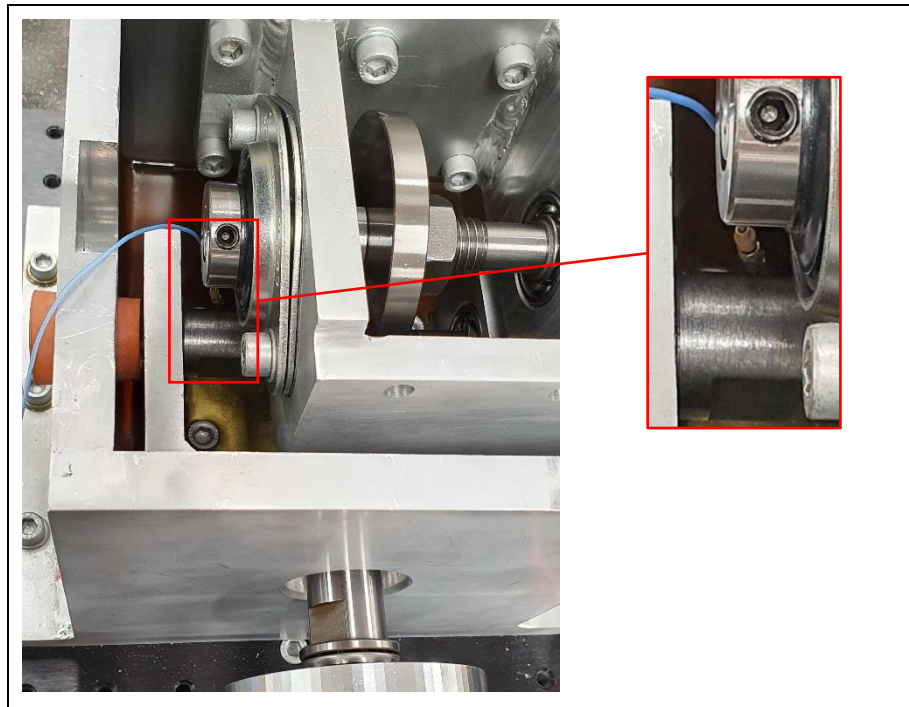


Figure 6.44: Accelerometer position for longitudinal vibration measurements.

Figure 6.45 compares measured v_a with % reduction of T_s at $V_{ms} = 1$ from Figure 6.42a. Maximum v_a at 750 Hz coincides with the maximum reduction of T_s . This work supports 6.5.2 in showing that v_a and thus the % reduction of T_s , depend on the vibration characteristics of the test system.

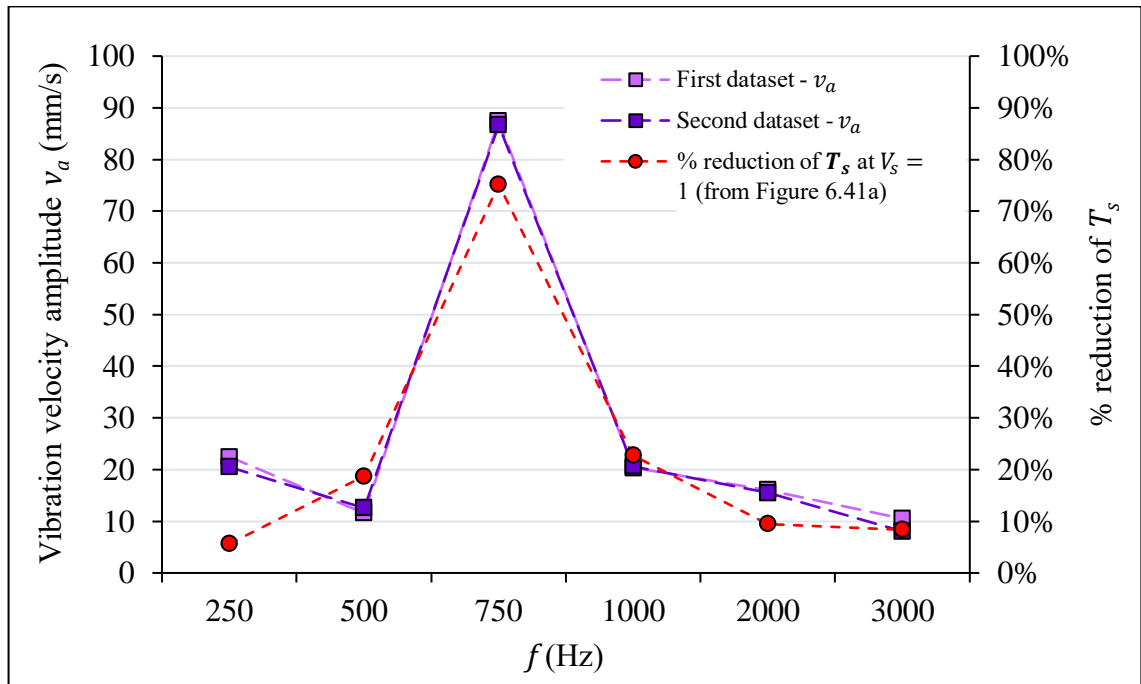


Figure 6.45: Influence of v_a on T_s reduction at applied longitudinal test frequencies.

6.6.3. Normalised Torque vs. Previous Simulation

Figure 6.46 shows normalised drive torque T_{sv}/T_{ss} from longitudinal vibration disc-on-disc test at $f = 750$ Hz, in a form that can be compared with previous planar contact simulation results in Figure 5.5. Disc-on-disc test results are similar to previous simulation results in that T_{sv}/T_{ss} approaches 1 when k_v approaches 1. Tests at $k_v < 1$ cannot be performed in longitudinal mode since v_a in this mode (Figure 6.45) is much greater than in transverse mode (Figure 6.36), while the drive velocity of the rig cannot be increased further. Figure 6.46 and Figure 5.5 results are not a perfect match owing to the different systems being evaluated.

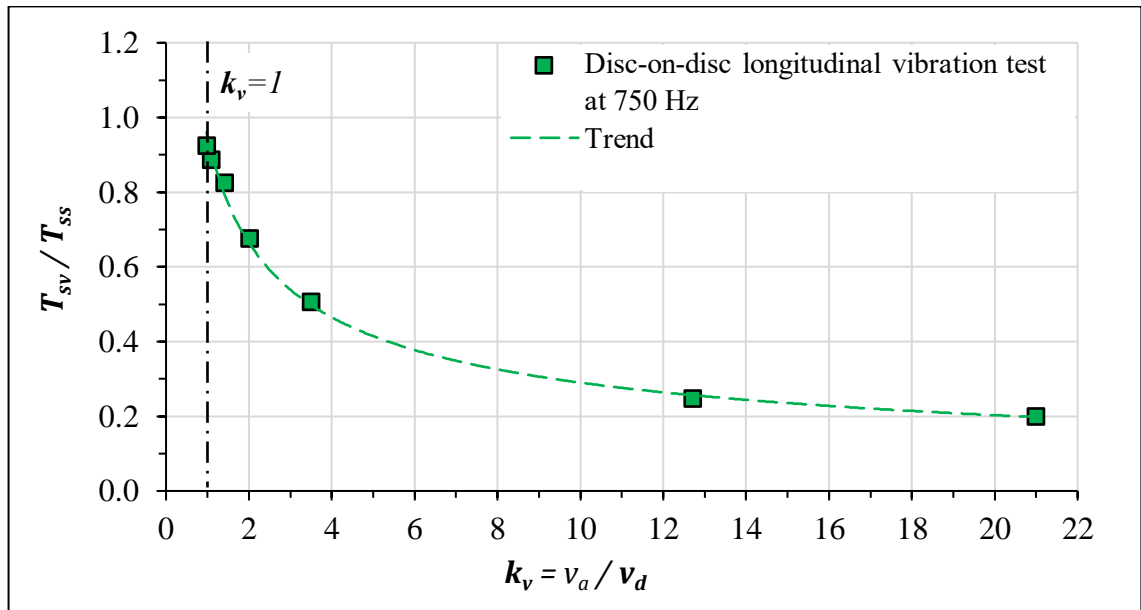


Figure 6.46: Disc-on-disc longitudinal vibration test, change in T_{sv}/T_{ss} with k_v .

6.6.4. Power loss Reduction due to Longitudinal Vibration

In similarity to 6.5.4, reduction in P_{loss_s} due to sinusoidal and triangular longitudinal vibration with oil dip lubrication is plotted in Figure 6.47 and Figure 6.48 respectively. The figures show similar trends as Figure 6.42 and Figure 6.43. This is because speed changes are small in comparison to torque changes, thus T_s is the influencing factor for P_{loss_s} . As with transverse vibration, the higher the average sliding velocity \tilde{v}_{sl} , the smaller the reduction of P_{loss_s} .

6.6.5. Efficiency Improvement due to Longitudinal Vibration

The improvement in efficiency $\Delta\eta_s$, determined by (75), due to sinusoidal and triangular longitudinal vibration with oil dip lubrication is plotted in Figure 6.49 and Figure 6.50 respectively. Sinusoidal vibration allows a greater improvement of η_s at the optimum frequency 750 Hz. This is in line with the finding from transverse vibration tests (6.5.5).

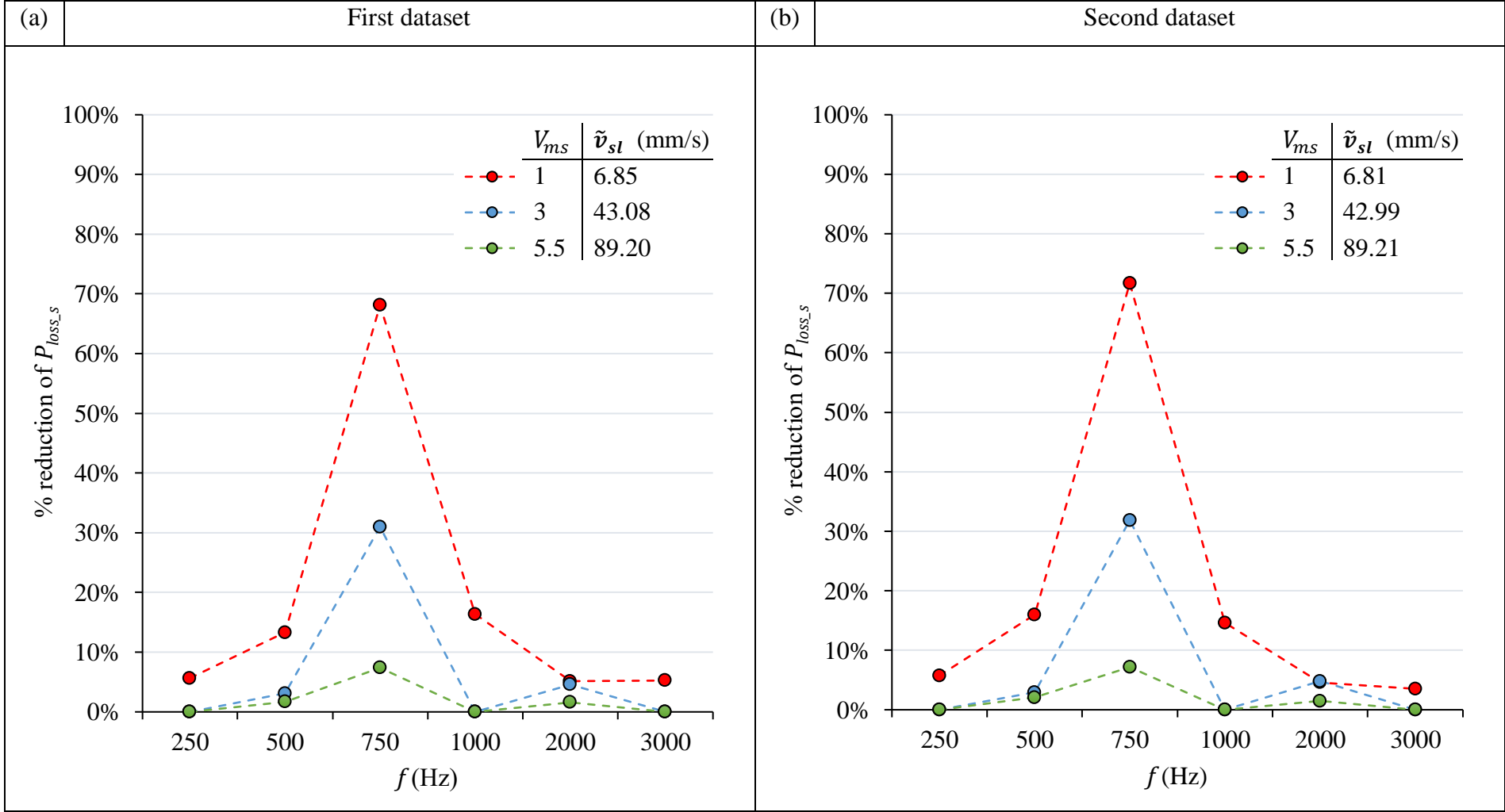
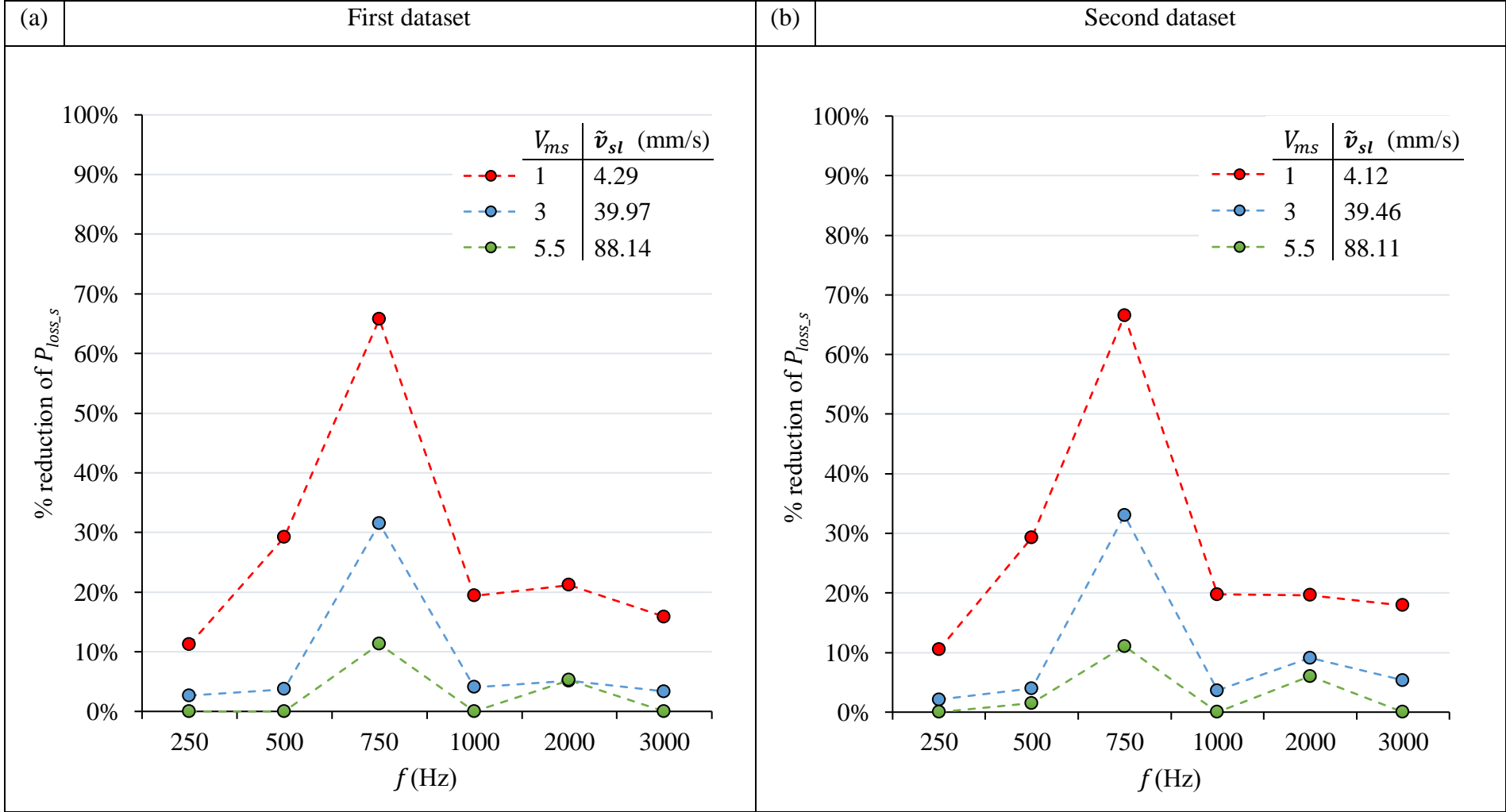


Figure 6.47: Effect of f on $P_{loss,s}$. Longitudinal sinusoidal vibration, oil dip lubrication.



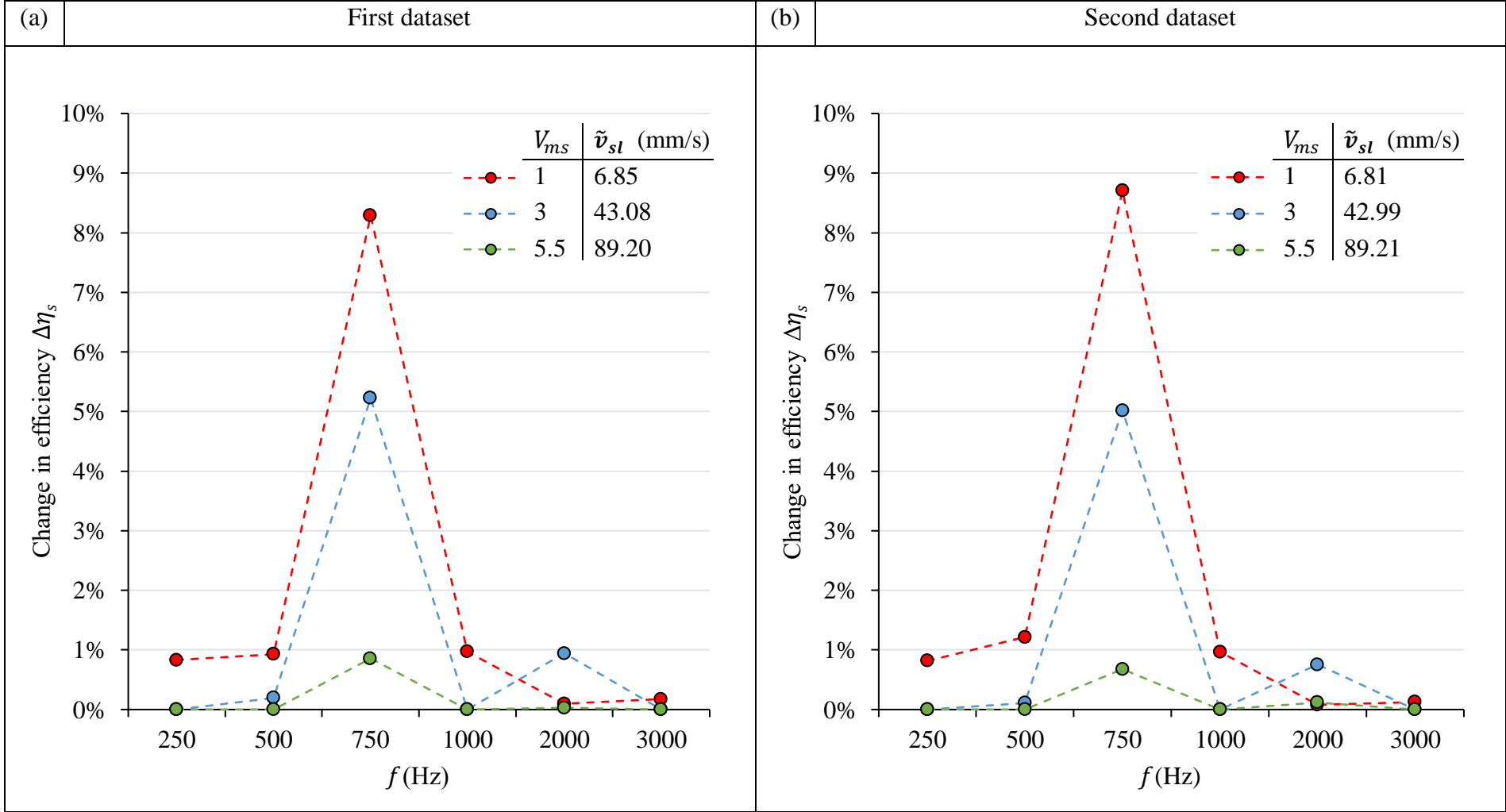
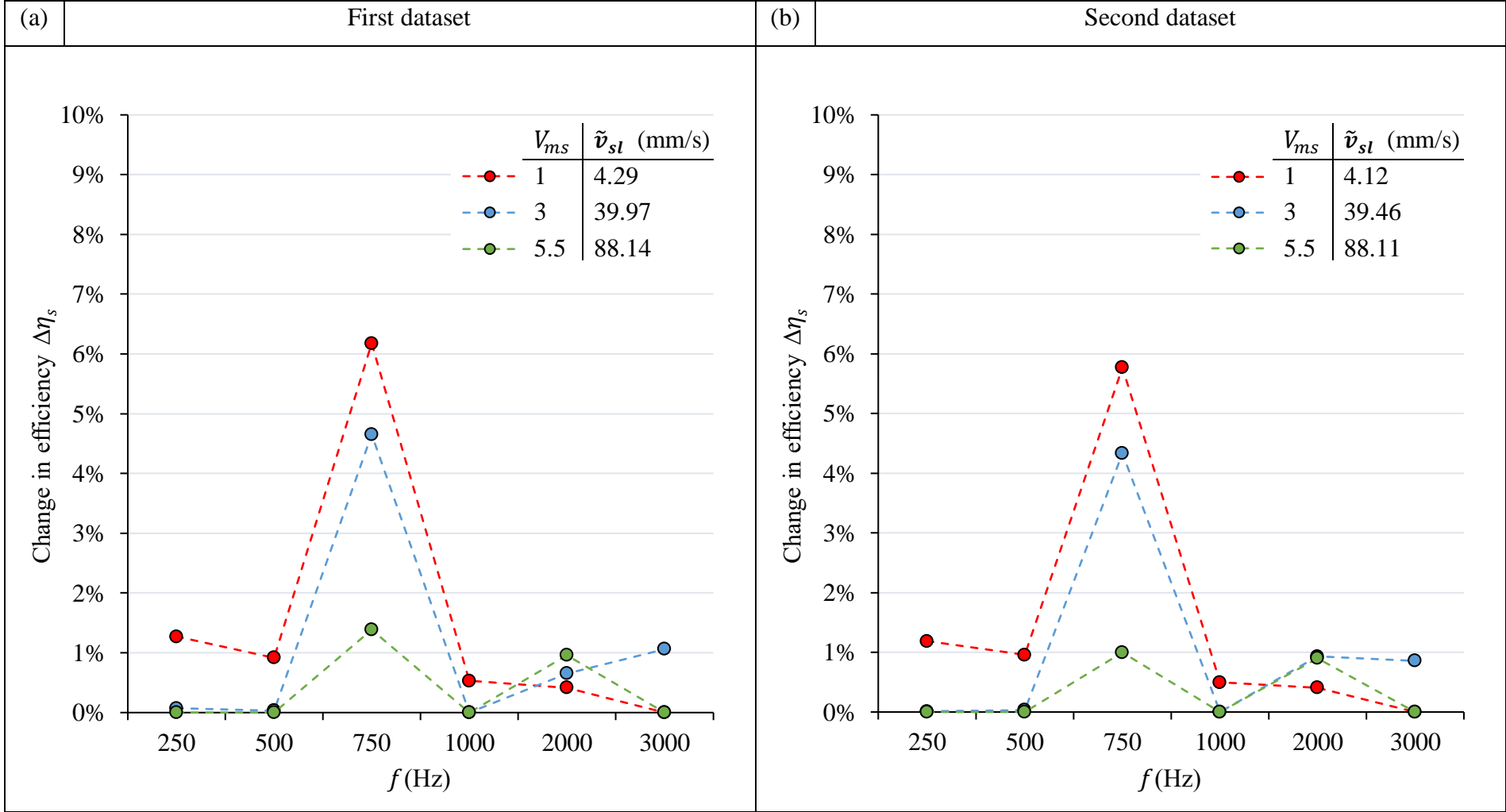


Figure 6.49: Effect of f on $\Delta\eta_s$. Longitudinal sinusoidal vibration, oil dip lubrication.



6.7. Wear Life Consideration

In section 2.7.1 of the literature review a study by Chowdhury and Helali (2007) is identified where the wear rate of steel-steel contact is shown to reduce with application of normal vibration. No studies have been reported to support whether the same applies with in-plane vibration. Therefore, a wear test is performed to give an indication of the influence of longitudinal vibration on wear. A transverse vibration wear test has not been performed.

The test consists of two runs; one without vibration applied and one with longitudinal vibration applied. Vibration frequency $f = 750$ Hz is used since this is found to produce the highest vibration velocity v_a and consequently the greatest reduction in torque T_s (Figure 6.45). For maximum wear rate the fastest sliding speed setting is used for both runs, $V_{ms} = 5.5$ V and $V_{ma} = 0.9$ V. Normal force is set to $F_N = 141.6$ N as per Table 6.8, and dip lubrication with SAE 80 oil is used as per 6.4.9. Monitoring S_{ma} and S_{ms} throughout the wear test allows the total sliding distance to be recorded for both runs. Both wear test runs have completed a minimum of 1800 metres of total sliding in under 6 hours. The weight loss of the test disc specimens after the runs is given in Table 6.12. Results indicate that in-plane vibration increases wear.

Wear test	Duration (hh:mm)	Sliding distance (m)	Disc weight before (g)		Disc weight after (g)		Percentage weight loss	
			St	Al-Br	St	Al-Br	St	Al-Br
Without vibration	05:57	1805	165.8	85.022	165.8	84.982	0%	0.05%
With longitudinal vibration	05:53	1801	166.3	84.932	166.3	84.824	0%	0.13%

Table 6.12: Effect of longitudinal vibration on weight loss of steel and aluminium-bronze discs.

6.8. Chapter Discussion and Conclusions

This chapter has identified the need for a custom disc-on-disc test rig to imitate the sliding-rolling contact interaction typical of worm gearing, while allowing vibration to be applied to one of the discs. A preliminary test system has been useful for understanding the dynamics and feasibility of an initial design. Learning outcomes (6.3.6) from preliminary testing have been applied to develop an improved disc-on-disc test rig. Features of the rig, interfaces with other equipment, the test conditions and procedure have been given a detailed account.

Test results have been collected to analyse the influence of lubricant type, vibration mode, vibration waveform, vibration frequency f , and sliding speed \tilde{v}_{sl} on disc drive torque T_s , disc rotational speed S_s and motor current draw i_{ms} . Test data has enabled a study of the influence of vibration frequency f on reduction of T_s , reduction of frictional power loss P_{loss_s} and improvement in efficiency. Results show better consistency of data with oil dip lubrication compared to grease. The most favourable results in both vibration modes are achieved in oil at $f = 750$ Hz with sinusoidal waveform. T_s reduces by up to 86% under transverse vibration (Figure 6.33), and up to 78% under longitudinal vibration (Figure 6.42). This marries well with accelerometer data showing the highest vibration velocity v_a at $f = 750$ Hz. Vibration velocity imposed on the test specimen is influenced by the transmissibility of the mechanical system. For example, v_a is much greater in longitudinal mode (Figure 6.45) than in transverse (Figure 6.36).

Superimposition of transverse and longitudinal normalised torque results at $f = 750$ Hz (Figure 6.51) show greater friction reduction effect from transverse vibration. This is contrary to previous experiments by Gutowski and Leus (2015) of two planar contact surfaces where transverse vibration produces less reduction of friction. A possible explanation is that in these previous experiments, movement of the sliding body in the transverse direction has not been restricted, thus there is partial transfer of transverse motion from the base to the sliding body. In the disc-on-disc rig the position of the steel disc is fixed in the transverse direction. This maximises the relative transverse vibration velocity at the contact, and thus maximises the effectiveness of transverse vibration.

Although friction is reduced by vibration, wear test indicates that wear life also reduces, and this must be considered in the design of any system involving vibration.

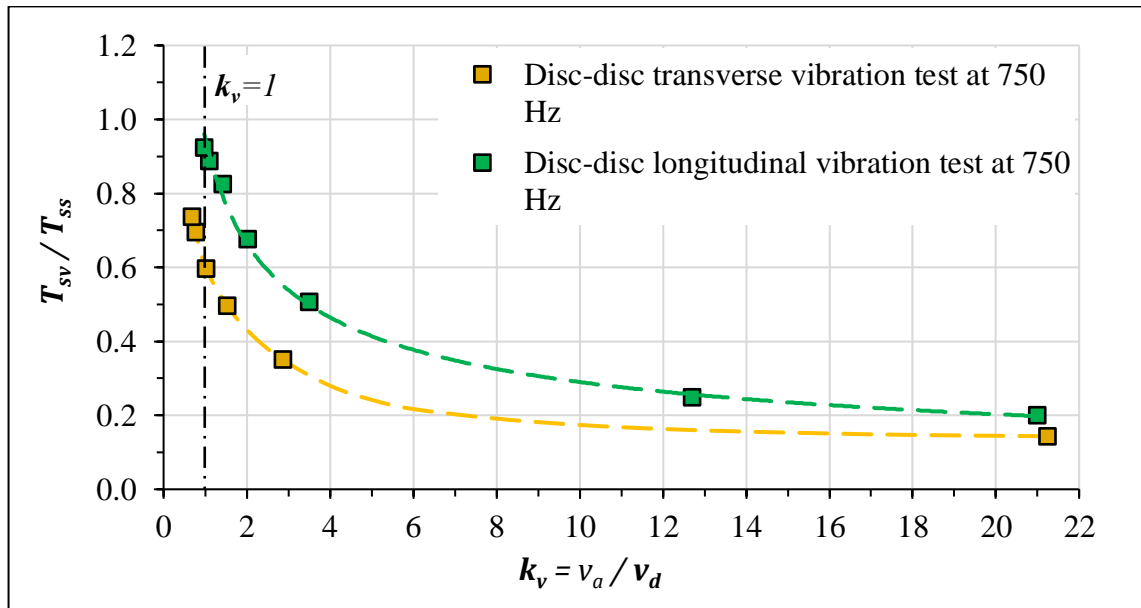


Figure 6.51: Comparison of transverse and longitudinal disc-on-disc normalised torque results. Superimposition of Figure 6.37 and Figure 6.46.

Chapter 4 comprises analytical investigations of vibration with a test system unrelated to worm gearing. Chapter 5 uses the same system and lays the foundations for FEA simulations by demonstrating that numerical analysis achieves the same results as analytical method. Chapter 6 has developed and tested a system more relevant to worm gearing by introducing sliding-rolling contact interaction and use of lubricant to pre-existing investigations. The next chapter further advances towards the intended application by building upon the foundations of Chapter 5 to numerically analyse the effect of vibration on worm gearing efficiency, and to compare results with empirical results from chapter 6.

Chapter 7

Worm and Wheel Simulation

7.1. Chapter Introduction

Having developed knowledge of friction modelling for vibration in chapter 4, followed by establishing a technique for 3D simulations of planar contact surfaces under vibration in chapter 5, and having proven the friction reduction benefit of imposed vibration for sliding-rolling contact in chapter 6, the foundations have been set for evaluating the effect of vibration on worm gearing efficiency. A CAD model of worm gearset 3 (Table 3.5) is used for conducting numerical simulations in this chapter.

7.2 contains the simulation methodology, describing the simulation domain, simulation sequence, boundary conditions and measures taken to simplify the finite element mesh. Subroutine development for the worm gearset simulation is explained in 7.3.

7.4 evaluates the simulation results. To initially validate the simulation, worm gearset efficiency without vibration is compared with theoretically calculated efficiency η_{z1-2} from Table 3.5. A mesh density study then allows selection of the appropriate mesh size, followed by simulations studying the effect of vibration on input gearset torque, mechanical advantage, and efficiency.

7.2. Worm Gearing Simulation Methodology

Importing worm and wheel CAD models straight into Abaqus[®] for FEA makes the conduct of simulations difficult for two reasons. The first is that to achieve an adequately fine mesh at the gear teeth, a large bulk of material in the two parts also must be finely meshed. This creates an exorbitant number of finite elements, requiring significant computer processing power. Secondly, generating accurate CAD gear tooth geometries requires simulation of material removal by the manufacturing process. Machine tool cutting paths create faceted faces on the tooth flanks (Figure 7.1) which, although realistic, cause further meshing difficulties. Section 7.2.1 explains the steps taken to resolve these issues.

Setup and conduct of a simulation of material removal to generate accurate CAD gear tooth geometries is a lengthy process. An accurate CAD model of gearset 3, identified in Table 3.5, has already previously been produced and is available for use. CAD models for the other gearsets do not exist, so in the interest of time, simulations studying the influence of vibration on worm gearing efficiency have been conducted using the pre-existing gearset 3 CAD model (Figure 7.1).

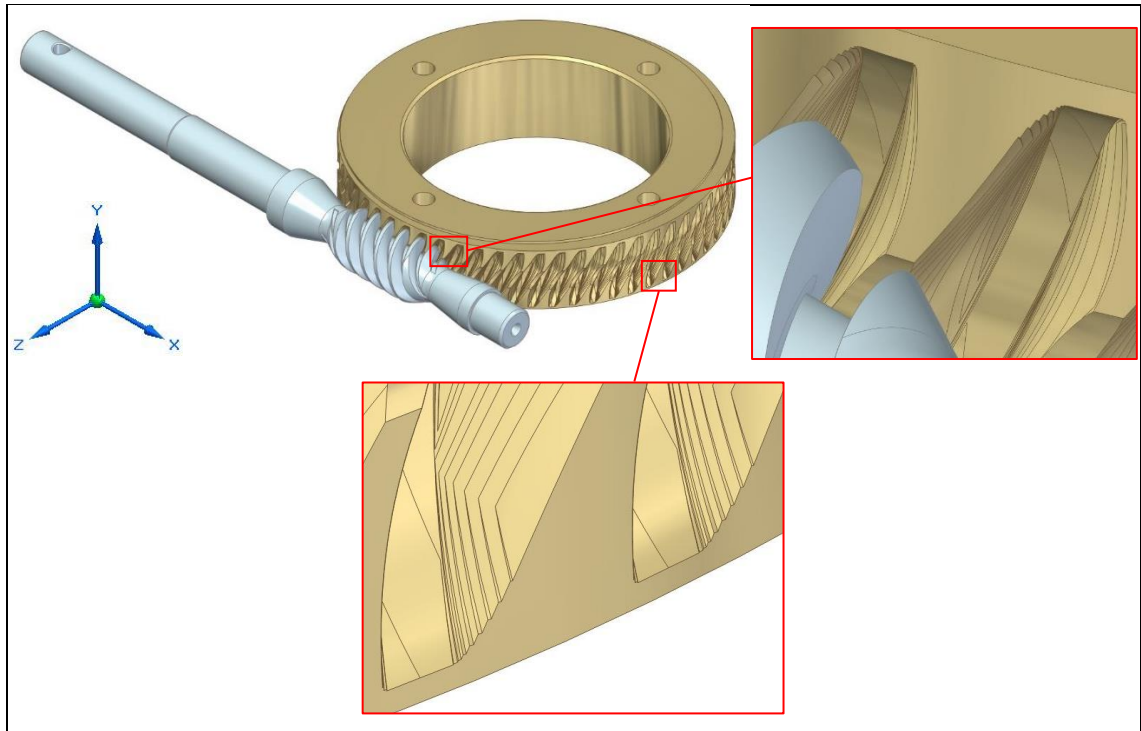


Figure 7.1: CAD model of worm gearset 3. Facets on tooth flanks of wheel gear caused by machining simulation.

Gear simulations are performed in Abaqus[®] with contact pressure 194.3 N/mm^2 and vibration frequency 750 Hz to match the contact pressure (Table 6.8) and optimum frequency (Figure 6.36 and Figure 6.45) during disc-on-disc experiments. Sinusoidal vibration waveform is used since chapter 6 concludes better results when compared to the triangular wave.

Simulations are also performed at the gearset's rated torque $T_R = 366 \text{ Nm}$ and speed $n_1 = 1440 \text{ RPM}$, which constitute to load and speed significantly beyond the levels used in experiments. This is done in the interest of predicting the level of vibration that would have to be applied to get an efficiency benefit under real application conditions.

The previously developed friction subroutine (5.2.4) which has been used for numerical FEA simulations of coupled longitudinal-transverse vibration (5.3) are found to cause errors when applied to the analysis of worm gearing. Section 7.3 explains subroutine modifications implemented to resolve this.

7.2.1. Geometry and Topology Adjustment

To reduce computational effort and thus minimise simulation durations, it is necessary to exclude component features that are away from the gear teeth. The CAD

models are therefore simplified from Figure 7.1 to Figure 7.2. The worm and wheel are then imported into Abaqus® as two separate parts.



Figure 7.2: CAD model of worm gearset 3 simplified for import into Abaqus®.

To further reduce computational effort the worm gear, after imported to Abaqus®, is changed to an analytical rigid shell (Figure 7.3).

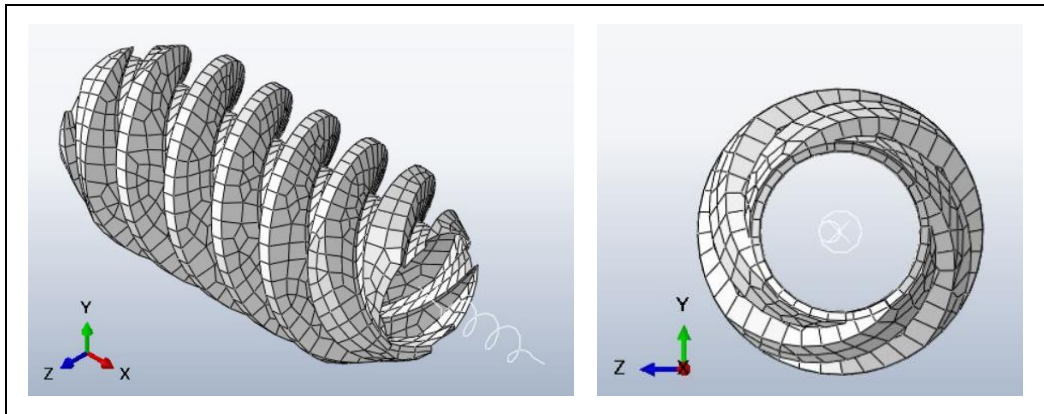


Figure 7.3: Worm gear as analytical rigid shell in Abaqus®.

The wheel gear teeth are created in a CAD program by modelling material removal using mathematical relationships that define the sweeps of the cutting hob during manufacture. The resultant step-like features, referred to as facets, on the tooth flanks (Figure 7.1) create meshing difficulties. Geometry editing options within Abaqus® are employed to remove faceted edges and blend adjacent faces to create a single flank face on each side of the wheel tooth (Figure 7.4). Initial contact checks reveal that the worm teeth make centre contact with wheel teeth (refer to section 2.6 for an explanation of centre contact). Since the facets are located at the edges of wheel teeth, topology

adjustment is assumed to have minimal impact on flank geometry at the centre of teeth where contact occurs. A mesh study is performed (7.4.2) to select the appropriate mesh density for simulations.

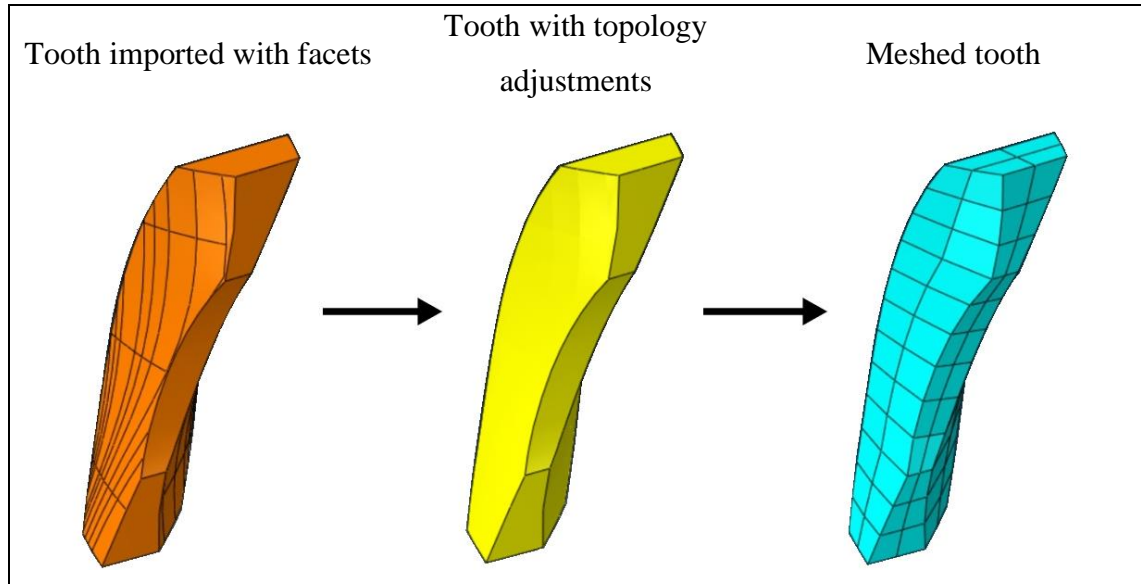


Figure 7.4: Wheel gear tooth topology adjustment and mesh in Abaqus®.

7.2.2. Simulation Domain

The worm is an analytical rigid shell (Figure 7.3, Figure 7.6) of which the tooth flanks constitute the master surface of the contact pair. The wheel gear is a revolution of 60 deformable meshed teeth (Figure 7.6), the flanks of which are assigned slave surfaces. The wheel teeth have material properties typical of aluminium-bronze; Young's Modulus 120000 N/mm^2 and Poisson's Ratio 0.3.

The inside faces of the 60 revolved wheel teeth are constrained to the centre point of the wheel gear (Figure 7.5) using a kinematic coupling constraint. This constrains all degrees of freedom of the selected faces to the centre point of the wheel. In this manner the torque applied on the wheel gear can be measured at the single centre point.



Figure 7.5: Inside faces of wheel teeth constrained to centre point of wheel gear.

A torsional spring on the rotation axis of the worm (Figure 7.6), with one end fixed to the worm at point A and the other to a reference point B in space, represents the torsional stiffness of the shaft. Torsional stiffness k_D of the worm shaft is estimated as follows (Budynas and Nisbett, 2011):

$$\begin{aligned}
 k_D &= \frac{\pi G_s d^4}{32l} = \frac{\pi E_s d^4}{64l(1 + \epsilon_s)} \\
 &= \frac{\pi \cdot 209000 \cdot 17^4}{64 \cdot 150 \cdot (1 + 0.3)} = 4394 \cdot 10^{-3} \text{ Nmm/rad} = 4394 \text{ Nm/rad}
 \end{aligned}$$

Rotational velocity to the worm is applied at point B (Figure 7.6). This is like the previous application of linear velocity in Figure 4.13 and Figure 5.4 via a linear stiffness between points A and B .

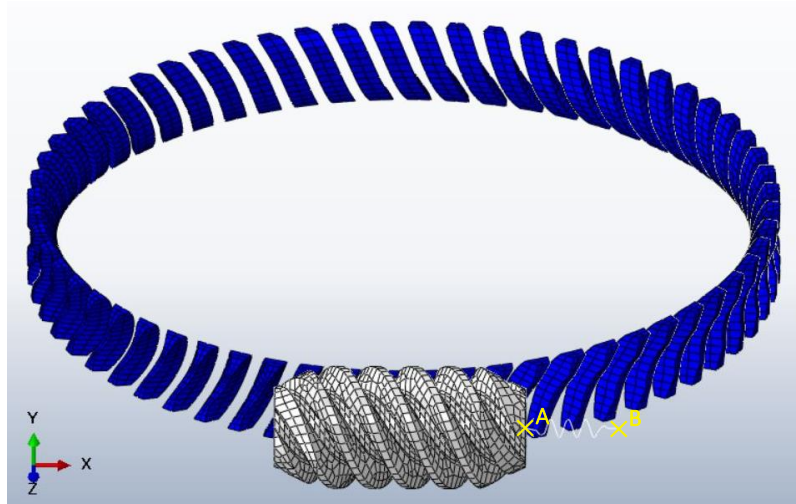


Figure 7.6: Worm and wheel finite element mesh with torsional stiffness AB .

7.2.3. Simulation Steps and Boundary Conditions

Worm gearing simulations consist of the analysis steps and boundary conditions described in Table 7.1.

Step no.	Step name	Step duration (s)	Step description and boundary conditions
0	Initial	N/A	The ‘velocity/angular velocity’ type boundary condition is applied to the worm point <i>A</i> and point <i>B</i> (Figure 7.6), and wheel centre point (Figure 7.5). Point <i>A</i> can only rotate about axis <i>X</i> (Figure 7.6) for the entire simulation. The wheel centre point, which is coupled to the wheel teeth (Figure 7.5), can only rotate about axis <i>Y</i> for the entire simulation. Point <i>B</i> is free to rotate about axis <i>X</i> until step 1. Worm and wheel teeth are out of contact until completion of step 1.
1	Make contact	0.04	Angular velocity of 60 RPM is applied to Point <i>B</i> . This initially slow velocity maintains a stable simulation while the worm teeth establish contact with the wheel teeth during this step.
2	Apply wheel load	0.005	Having established contact in step 1, a constant resistive torque in step 2 is applied at the wheel centre point, the magnitude of which is based on the desired contact pressure for the simulation. 3 sets of gear simulations are performed with varying contact pressures as per Table 7.2. The resistive torque is maintained in subsequent steps.
3	Drive worm	Up to 0.4	Rotational velocity applied to point <i>B</i> is increased to achieve the desired contact sliding velocity v_g . 3 sets of gear simulations are performed with varying v_g as per Table 7.2. Rotational velocity is maintained in the subsequent step.

Step no.	Step name	Step duration (s)	Step description and boundary conditions
4	Vibrate worm	Up to 0.07	The rotational velocity applied to point <i>B</i> in step 3 is propagated into this step. Meanwhile, vibration is activated by applying sinusoidal motion to point <i>A</i> such that the worm oscillates parallel to axis <i>X</i> . The time increments during this simulation step are small, allowing fine resolution of data during vibration.

Table 7.1: Sequential steps and boundary conditions for worm gearing numerical simulation with vibration applied.

7.2.4. Simulation Sets

Table 7.2 lists the conditions for 3 sets of simulations performed. For each set, the effect on gear efficiency is studied when applying vibration to the worm parallel to axis direction *X* (Figure 7.6). The 33 rows of conditions in Table 7.2 constitute to the total number of simulations performed.

Movement of the worm shaft parallel to axis directions *Y* and *Z* is restricted by design with use of bearings to locate the shaft. Therefore, in real applications it is not easily feasible to apply vibration in these two directions.

$\mu = 0.1344$ is used for all simulations of worm gearset 3 to match the calculated mean tooth coefficient of friction μ_{zm} for this gearset (Table 3.5). The maximum elastic contact deformation is assumed $s_{max} = 7 \cdot 10^{-8}$ m, an intermediate value between those previously used in longitudinal (Table 4.3) and transverse (Table 4.4) vibration simulations.

The first set of simulations (Table 7.2) apply 750 Hz vibration at $v_a = 59$ mm/s, matching the peak v_a measured in transverse vibration disc-on-disc tests (Figure 6.36). A second set of simulations apply $v_a = 87$ mm/s, matching peak v_a from longitudinal vibration tests (Figure 6.45). u_a in Table 7.2 is calculated from relationship (12). v_g is selected such that k_w ranges between 0.1 to 20, so a graph similar to Figure 6.51 can be produced. Simulated worm speed n_1 necessary to achieve v_g is calculated using the worm gearset 3 calculation sheet (Appendix C). Likewise, the wheel output torque for simulation is selected such that the wheel contact stress σ_c equals the Hertzian contact

pressure 194.3 N/mm^2 from disc-on-disc experiments (Table 6.8). Theory suggests the gearset must produce output wheel torque of 23 Nm to generate $\sigma_c = 194.3 \text{ N/mm}^2$. A resistive constant torque of 23 Nm is thus applied to the wheel gear for all simulations in set 1 and 2, while the worm rotates at speed n_1 .

Simulation set 3 resembles the in-application gearset torque and speed, $T_R = 366 \text{ Nm}$ resulting in $\sigma_c = 778 \text{ N/mm}^2$, and $n_1 = 1440 \text{ RPM}$. Since n_1 is constant, sliding speed \mathbf{v}_g is also a constant 1510.8 mm/s . Therefore, to achieve the desired range of \mathbf{k}_w the magnitude of v_a must change. The clearance between worm and wheel teeth in the gear mesh allows for a maximum vibration displacement amplitude of $u_a = 0.16 \text{ mm}$. In accordance with (12), change to v_a with constant u_a through simulation set 3 requires that f must change. For this reason, simulation set 3 is the only set in which f and v_a change value while n_1 and \mathbf{v}_g do not.

Simulation set	Simulation reference	f (Hz)	v_a (mm/s)	u_a (mm)	v_g (mm/s)	$k_w = v_a / v_g$	n_1 (RPM)	σ_c (N/mm ²)
1	1	750	59	0.0125	590.0	0.1	562.4	194.3
	2				86.8	0.68	82.7	
	3				76.6	0.77	73	
	4				57.8	1.02	55.1	
	5				38.6	1.53	36.8	
	6				20.6	2.86	19.6	
	7				11.8	5	11.2	
	8				7.4	8	7.1	
	9				4.9	12	4.7	
	10				3.7	16	3.5	
	11				3.0	20	2.9	
2	12	750	87	0.0185	873.9	0.1	833	194.3
	13				128.5	0.68	122.5	
	14				113.5	0.77	108.2	
	15				85.7	1.02	81.7	
	16				57.1	1.53	54.4	
	17				30.6	2.86	29.2	
	18				17.5	5	16.7	
	19				10.9	8	10.4	
	20				7.3	12	7	
	21				5.5	16	5.2	
	22				4.4	20	4.2	
3	23	150	151.1	0.1600	1510.8	0.1	1440	778
	24	1022	1027.3			0.68		
	25	1157	1163.3			0.77		
	26	1533	1541.0			1.02		
	27	2299	2311.5			1.53		
	28	4298	4320.8			2.86		
	29	7514	7553.8			5		
	30	12022	12086.0			8		
	31	18033	18129.0			12		
	32	24044	24172.0			16		
	33	30055	30215.0			20		

Table 7.2: Conditions for vibration simulations of gearset 3.

7.3. Friction Model and Subroutine Modification

In earlier work, depicted by Figure 4.13, vibration is applied to the base on which another body slides. This causes partial transfer of vibration from the base to the sliding body. In worm gearset simulations (Figure 7.6), the worm is the sliding body and vibration is applied directly to it. Therefore, the previously developed friction model for coupled longitudinal-transverse vibration (4.5) incorporated into a friction subroutine (5.2.4) are no longer valid. The mathematical model is modified, and the subroutine updated for worm gearset vibration simulations. Simulation results using the modified subroutine are discussed in 7.4. The modified subroutine is in Appendix E and includes descriptions of changes made in comparison to the previous subroutine in Appendix D.

Sections 7.3.1-7.3.5 describe the modified friction model. As a starting point consider Figure 4.13 in which vibration is applied to the base. Since vibration now acts directly on the sliding worm gear, $\mathbf{x}_b = \mathbf{y}_b = 0$. Change in magnitude and direction of elastic deformation during a single time increment Δt are now described by Figure 7.7 instead of Figure 4.15.

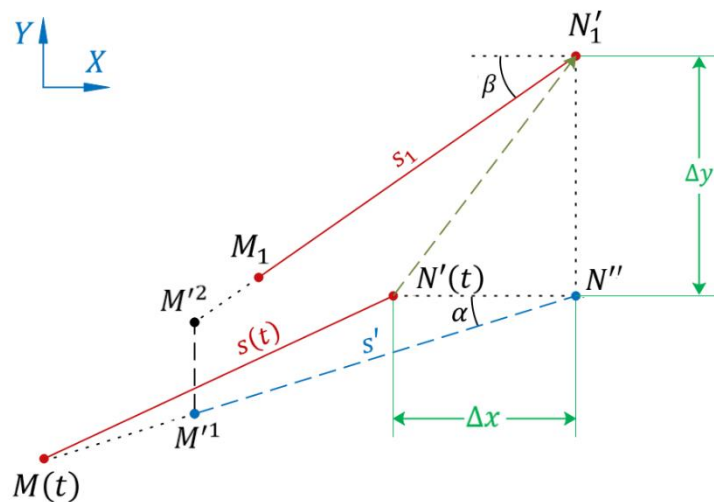


Figure 7.7: Change in magnitude and direction of deformation from \mathbf{s} to \mathbf{s}_1 during a time increment Δt , due to incremental displacements $\Delta \mathbf{x}$ and $\Delta \mathbf{y}$ as vibration is applied directly to the sliding body during sliding motion.

During a consecutive time increment Δt , M and N' change their relative positions thus \mathbf{s} undergoes a change in its magnitude and direction from $\mathbf{s}(t)$ at the beginning of the time increment to $\mathbf{s}_1(t + \Delta t)$ at the end of the increment (Figure 7.7). Coordinates of

M and N' , and magnitude of $\mathbf{s}(t)$ at the start of the increment are still given by (38)-(40), and at the end of the increment by (24) and (25).

The change from \mathbf{s} to \mathbf{s}_1 is separated into two phases. In the first phase the intermediate deformation \mathbf{s}' is analysed as a result of $\Delta\mathbf{x}$ motion of the body which moves point N' to an intermediate N'' . In the second phase the final deformation \mathbf{s}_1 is analysed as a result of $\Delta\mathbf{y}$ motion which moves intermediate point N'' to the final N'_1 . $\Delta\mathbf{x}$ and $\Delta\mathbf{y}$ are computed at every time increment of the FEA simulation based on relative motion at the contacts between gear teeth. Therefore, it simply follows that:

$$\mathbf{x} = \boxed{\mathbf{x}} + \Delta\mathbf{x} \quad (77)$$

$$\mathbf{y} = \boxed{\mathbf{y}} + \Delta\mathbf{y} \quad (78)$$

7.3.1. First Phase of Motion

In the first phase of motion, as N' moves to an intermediate position N'' , M moves along the path $\overline{MN''}$ to intermediate position M'^1 . Consequently, deformation \mathbf{s} changes to an intermediate \mathbf{s}' with a new instantaneous direction determined by angle α , whilst the change in its magnitude is determined by an increment $\Delta\mathbf{s}$ evaluated using (17). Therefore, the magnitude of deformation \mathbf{s}' after this first phase of motion is calculated by a simplification of (44) due to substitution of (18):

$$\mathbf{s}' = \boxed{\mathbf{s}_1} + \mathbf{v}_{r1} \left[1 - \frac{\boxed{\mathbf{s}_1} \text{sgn}(\mathbf{v}_{r1})}{s_{max}} \right]^i \Delta t \quad (79)$$

Relative velocity \mathbf{v}_{r1} along the line of action of the lumped elastic asperity is determined by:

$$\mathbf{v}_{r1} = \frac{\overline{MN''} - \overline{MN'}}{\Delta t} = \frac{\overline{MN''} - \mathbf{s}}{\Delta t} = \frac{\overline{MN''} - \boxed{\mathbf{s}_1}}{\Delta t} \quad (80)$$

where:

$$\begin{aligned} \overline{MN''} &= \sqrt{[N''_x - M_x(t)]^2 + [N''_y - M_y(t)]^2} \\ &= \sqrt{[N'_{1x} - M_x(t)]^2 + [N'_y(t) - M_y(t)]^2} \\ &= \sqrt{[\mathbf{x} - \boxed{M_{1x}}]^2 + [\mathbf{y} - \boxed{M_{1y}}]^2} \end{aligned} \quad (81)$$

Direction of \mathbf{v}_{r1} in relation to axis X is determined by angle α (Figure 7.7) where:

$$\sin \alpha = \frac{\boxed{y} - \boxed{M_{1y}}}{\overline{MN''}} \quad (82)$$

$$\cos \alpha = \frac{x - \boxed{M_{1x}}}{\overline{MN''}} \quad (83)$$

Note that $\sin \alpha$ and $\cos \alpha$ in (47) and (48) require ‘if’ conditions to avoid errors in the formulation when dividing by zero. This is not required in the friction subroutine (Appendix E).

7.3.2. Second Phase of Motion

Within the same time increment Δt , in the second phase of motion, as $\Delta \mathbf{y}$ moves N'' to the final position N'_1 (Figure 7.7) a proportion of $\Delta \mathbf{y}$ moves M^{11} to position M'^2 , where:

$$\overline{M^{11}M'^2} = \eta_y^* \Delta \mathbf{y} \quad (84)$$

and:

$$\eta_y^* = 1 - \eta_y \quad (85)$$

M'^2 then moves along the path $\overline{M'^2N'_1}$ to final position M_1 . Consequently, deformation \mathbf{s}' changes to a final \mathbf{s}_1 with a new instantaneous direction determined by angle β , whilst the change in its magnitude is determined by an increment $\Delta \mathbf{s}'$. Therefore, the magnitude of deformation \mathbf{s}_1 after this second phase of motion is calculated by a simplification of (33) due to substitution of (18):

$$\mathbf{s}_1 = \mathbf{s}' + \mathbf{v}_{r2} \left[1 - \frac{\mathbf{s}' \cdot \text{sgn}(\mathbf{v}_{r2})}{s_{max}} \right]^i \Delta t \quad (86)$$

Relative velocity \mathbf{v}_{r2} along the line of action of the lumped elastic asperity is determined by:

$$\mathbf{v}_{r2} = \frac{\overline{M'^2N'_1} - \overline{M^{11}N''}}{\Delta t} = \frac{\overline{M'^2N'_1} - \mathbf{s}'}{\Delta t} \quad (87)$$

where:

$$\begin{aligned}
 \overline{M'^2 N'_1} &= \sqrt{[N'_{1x} - M'_x{}^2]^2 + [N'_{1y} - M'_y{}^2]^2} \\
 &= \sqrt{[x - (x - s' \cos \alpha)]^2 + [y - (N'_y - s' \sin \alpha + \overline{M'^1 M'^2})]^2} \\
 &= \sqrt{[s' \cos \alpha]^2 + [y - \boxed{y}] + s' \sin \alpha - \eta_y^* \Delta y]^2}
 \end{aligned} \tag{88}$$

Direction of \mathbf{v}_{r2} in relation to axis X is determined by angle β (Figure 7.7) where:

$$\sin \beta = \frac{y - \boxed{y} + s' \sin \alpha - \eta_y^* \Delta y}{\overline{M'^2 N'_1}} \tag{89}$$

$$\cos \beta = \frac{s' \cos \alpha}{\overline{M'^2 N'_1}} \tag{90}$$

Coordinates of point M_1 after lapse of Δt are then determined by (34) and (91), and friction force components \mathbf{F}_x and \mathbf{F}_y based on Dahl friction by (36) and (37).

$$M_{1y} = M_y(t + \Delta t) = y - s_1 \sin \beta \tag{91}$$

7.3.3. Partial Derivatives

To avoid simulation errors the friction subroutine (Appendix E) must also define the partial derivatives of friction stress components τ_x and τ_y with respect to \mathbf{x} , \mathbf{y} and p , where:

$$\tau_x = \frac{\tau_{crit}}{s_{max}} s_1 \cos \beta \tag{92}$$

$$\tau_y = \frac{\tau_{crit}}{s_{max}} s_1 \sin \beta \tag{93}$$

and:

$$k_t = \frac{\tau_{crit}}{s_{max}} = \frac{\mu p}{s_{max}} \tag{94}$$

(94) is the stress form of equation (18). (92) and (93) are true if $\tau_{eqv} \leq \tau_{crit}$, where the equivalent friction stress is:

$$\tau_{eqv} = \sqrt{\tau_x^2 + \tau_y^2} \tag{95}$$

If $\tau_{eqv} > \tau_{crit}$ then the friction stresses are given by:

$$\boldsymbol{\tau}_x = \tau_{crit} \cos \boldsymbol{\beta} \quad (96)$$

$$\boldsymbol{\tau}_y = \tau_{crit} \sin \boldsymbol{\beta} \quad (97)$$

The partial derivatives of $\boldsymbol{\tau}_x$ and $\boldsymbol{\tau}_y$ that need to be determined are:

$$\frac{\partial \boldsymbol{\tau}_x}{\partial \boldsymbol{x}}, \frac{\partial \boldsymbol{\tau}_x}{\partial \boldsymbol{y}}, \frac{\partial \boldsymbol{\tau}_x}{\partial p}, \frac{\partial \boldsymbol{\tau}_y}{\partial \boldsymbol{x}}, \frac{\partial \boldsymbol{\tau}_y}{\partial \boldsymbol{y}}, \frac{\partial \boldsymbol{\tau}_y}{\partial p}$$

This requires partial differentiation of (92) and (93) for the condition $\tau_{eqv} \leq \tau_{crit}$, and (96) and (97) for the condition $\tau_{eqv} > \tau_{crit}$. Since these four equations are derived from a series of other equations containing the terms $\overline{MN''}$, \boldsymbol{v}_{r1} , $\Delta \boldsymbol{s}$, \boldsymbol{s}' , $\cos \boldsymbol{\alpha}$, $\sin \boldsymbol{\alpha}$, $\overline{M'^2 N'_1}$, \boldsymbol{v}_{r2} , $\Delta \boldsymbol{s}'$, \boldsymbol{s}_1 , $\cos \boldsymbol{\beta}$ and $\sin \boldsymbol{\beta}$, the terms have to be partially differentiated too with respect to \boldsymbol{x} , \boldsymbol{y} and p . Therefore, only after computing partial derivatives of these terms using (98)-(135) can the partial derivatives of $\boldsymbol{\tau}_x$ and $\boldsymbol{\tau}_y$ be determined by (136)-(141).

Partial derivatives of $\overline{MN''}$ with respect to \boldsymbol{x} , \boldsymbol{y} and p :

$$\frac{\partial(\overline{MN''})}{\partial \boldsymbol{x}} = \frac{\boldsymbol{x} - \boxed{M_{1x}}}{\overline{MN''}} \quad (98)$$

$$\frac{\partial(\overline{MN''})}{\partial \boldsymbol{y}} = \frac{\partial(\overline{MN''})}{\partial p} = 0 \quad (99)$$

Partial derivatives of \boldsymbol{v}_{r1} with respect to \boldsymbol{x} , \boldsymbol{y} and p :

$$\frac{\partial(\boldsymbol{v}_{r1})}{\partial \boldsymbol{x}} = \frac{\partial(\overline{MN''})}{\partial \boldsymbol{x}} \quad (100)$$

$$\frac{\partial(\boldsymbol{v}_{r1})}{\partial \boldsymbol{y}} = \frac{\partial(\boldsymbol{v}_{r1})}{\partial p} = 0 \quad (101)$$

Partial derivatives of $\Delta \boldsymbol{s}$ with respect to \boldsymbol{x} , \boldsymbol{y} and p :

$$\frac{\partial(\Delta \boldsymbol{s})}{\partial \boldsymbol{x}} = \frac{\partial(\boldsymbol{v}_{r1})}{\partial \boldsymbol{x}} \left[1 - \frac{\boxed{\boldsymbol{s}_1} \operatorname{sgn}(\boldsymbol{v}_{r1})}{s_{max}} \right]^i \quad (102)$$

$$\frac{\partial(\Delta \boldsymbol{s})}{\partial \boldsymbol{y}} = \frac{\partial(\Delta \boldsymbol{s})}{\partial p} = 0 \quad (103)$$

Partial derivatives of s' and $(s')^2$ with respect to x , y and p :

$$\frac{\partial(s')}{\partial x} = \frac{\partial(\Delta s)}{\partial x} \quad (104)$$

$$\frac{\partial(s')^2}{\partial x} = 2s' \frac{\partial(s')}{\partial x} \quad (105)$$

$$\frac{\partial(s')}{\partial y} = \frac{\partial(s')^2}{\partial y} = \frac{\partial(s')}{\partial p} = \frac{\partial(s')^2}{\partial p} = 0 \quad (106)$$

Partial derivatives of $\cos \alpha$ and $\cos^2 \alpha$ with respect to x , y and p :

$$\frac{\partial(\cos \alpha)}{\partial x} = \frac{\overline{MN''} - (x - \boxed{M_{1x}}) \frac{\partial(\overline{MN''})}{\partial x}}{(\overline{MN''})^2} \quad (107)$$

$$\frac{\partial(\cos^2 \alpha)}{\partial x} = \frac{2(x - \boxed{M_{1x}}) \left((\overline{MN''})^2 - (x - \boxed{M_{1x}})^2 \right)}{(\overline{MN''})^4} \quad (108)$$

$$\frac{\partial(\cos \alpha)}{\partial y} = \frac{\partial(\cos^2 \alpha)}{\partial y} = \frac{\partial(\cos \alpha)}{\partial p} = \frac{\partial(\cos^2 \alpha)}{\partial p} = 0 \quad (109)$$

Partial derivatives of $\sin \alpha$ and $\sin^2 \alpha$ with respect to x , y and p :

$$\frac{\partial(\sin \alpha)}{\partial x} = \frac{-\left(\boxed{y} - \boxed{M_{1y}}\right) \frac{\partial(\overline{MN''})}{\partial x}}{(\overline{MN''})^2} \quad (110)$$

$$\frac{\partial(\sin^2 \alpha)}{\partial x} = \frac{-2(x - \boxed{M_{1x}}) \left(\boxed{y} - \boxed{M_{1y}}\right)^2}{(\overline{MN''})^4} \quad (111)$$

$$\frac{\partial(\sin \alpha)}{\partial y} = \frac{\partial(\sin^2 \alpha)}{\partial y} = \frac{\partial(\sin \alpha)}{\partial p} = \frac{\partial(\sin^2 \alpha)}{\partial p} = 0 \quad (112)$$

Partial derivatives of $\overline{M'^2 N'_1}$ with respect to x , y and p :

$$\begin{aligned} \frac{\partial(\overline{M'^2 N'_1})}{\partial x} = & \frac{0.5}{\overline{M'^2 N'_1}} \left(\frac{\partial(s' \cos \alpha)^2}{\partial x} + \frac{\partial(2ys' \sin \alpha)}{\partial x} - \frac{\partial(2\boxed{y}s' \sin \alpha)}{\partial x} \right. \\ & \left. + \frac{\partial(s' \sin \alpha)^2}{\partial x} - \frac{\partial(2s'\eta_y^* \Delta y \sin \alpha)^2}{\partial x} \right) \end{aligned} \quad (113)$$

$$\frac{\partial(\overline{M'^2 N'_1})}{\partial y} = \frac{0.5}{\overline{M'^2 N'_1}} \left(2y - 2\boxed{y} + 2s' \sin \alpha + 2\eta_y^* (\boxed{y} + \eta_y^* \Delta y - y - \Delta y) \right) \quad (114)$$

$$\frac{\partial(\overline{M'^2 N'_1})}{\partial p} = 0 \quad (115)$$

Partial derivatives of \mathbf{v}_{r2} with respect to \mathbf{x} , \mathbf{y} and p :

$$\frac{\partial(\mathbf{v}_{r2})}{\partial \mathbf{x}} = \frac{\partial(\overline{\mathbf{M}'^2 \mathbf{N}'_1})}{\partial \mathbf{x}} - \frac{\partial(\mathbf{s}')}{\partial \mathbf{x}} \quad (116)$$

$$\frac{\partial(\mathbf{v}_{r2})}{\partial \mathbf{y}} = \frac{\partial(\overline{\mathbf{M}'^2 \mathbf{N}'_1})}{\partial \mathbf{y}} \quad (117)$$

$$\frac{\partial(\mathbf{v}_{r2})}{\partial p} = 0 \quad (118)$$

Partial derivatives of $\Delta \mathbf{s}'$ with respect to \mathbf{x} , \mathbf{y} and p :

$$\begin{aligned} \frac{\partial(\Delta \mathbf{s}')}{\partial \mathbf{x}} = \frac{\partial(\mathbf{v}_{r2})}{\partial \mathbf{x}} \left[1 - \frac{\mathbf{s}' \operatorname{sgn}(\mathbf{v}_{r2})}{s_{max}} \right]^i \\ - \frac{\partial(\mathbf{s}')}{\partial \mathbf{x}} \left[1 - \frac{\mathbf{s}' \operatorname{sgn}(\mathbf{v}_{r2})}{s_{max}} \right]^{i-1} \left(\frac{\mathbf{v}_{r2} i \operatorname{sgn}(\mathbf{v}_{r2})}{s_{max}} \right) \end{aligned} \quad (119)$$

$$\frac{\partial(\Delta \mathbf{s}')}{\partial \mathbf{y}} = \frac{\partial(\mathbf{v}_{r2})}{\partial \mathbf{y}} \left[1 - \frac{\mathbf{s}' \operatorname{sgn}(\mathbf{v}_{r2})}{s_{max}} \right]^i \quad (120)$$

$$\frac{\partial(\Delta \mathbf{s}')}{\partial p} = 0 \quad (121)$$

Partial derivatives of \mathbf{s}_1 with respect to \mathbf{x} , \mathbf{y} and p :

$$\frac{\partial(\mathbf{s}_1)}{\partial \mathbf{x}} = \frac{\partial(\mathbf{s}')}{\partial \mathbf{x}} + \frac{\partial(\Delta \mathbf{s}')}{\partial \mathbf{x}} \quad (122)$$

$$\frac{\partial(\mathbf{s}_1)}{\partial \mathbf{y}} = \frac{\partial(\Delta \mathbf{s}')}{\partial \mathbf{y}} \quad (123)$$

$$\frac{\partial(\mathbf{s}_1)}{\partial p} = 0 \quad (124)$$

Partial derivatives of $\cos \beta$ with respect to \mathbf{x} , \mathbf{y} and p :

$$\frac{\partial(\cos \beta)}{\partial \mathbf{x}} = \frac{\overline{\mathbf{M}'^2 \mathbf{N}'_1} \left(\cos \alpha \left(\frac{\partial(\mathbf{s}')}{\partial \mathbf{x}} \right) + \mathbf{s}' \left(\frac{\partial(\cos \alpha)}{\partial \mathbf{x}} \right) \right) - \mathbf{s}' \cos \alpha \left(\frac{\partial(\overline{\mathbf{M}' \mathbf{N}'_1})}{\partial \mathbf{x}} \right)}{(\overline{\mathbf{M}'^2 \mathbf{N}'_1})^2} \quad (125)$$

$$\frac{\partial(\cos \beta)}{\partial \mathbf{y}} = - \frac{\mathbf{s}' \cos \alpha \left(\frac{\partial(\overline{\mathbf{M}' \mathbf{N}'_1})}{\partial \mathbf{y}} \right)}{(\overline{\mathbf{M}'^2 \mathbf{N}'_1})^2} \quad (126)$$

$$\frac{\partial(\cos \beta)}{\partial p} = 0 \quad (127)$$

Partial derivatives of $\sin \beta$ with respect to \mathbf{x} , \mathbf{y} and p :

$$\begin{aligned} & \frac{\partial(\sin \beta)}{\partial \mathbf{x}} \\ &= \frac{\overline{M'^2 N'_1} \left(\sin \alpha \left(\frac{\partial(s')}{\partial \mathbf{x}} \right) + s' \left(\frac{\partial(\sin \alpha)}{\partial \mathbf{x}} \right) \right) - (\mathbf{y} - \boxed{\mathbf{y}} + s' \sin \alpha - \eta_y^* \Delta \mathbf{y}) \left(\frac{\partial(\overline{M'^2 N'_1})}{\partial \mathbf{x}} \right)}{(\overline{M'^2 N'_1})^2} \end{aligned} \quad (128)$$

$$\frac{\partial(\sin \beta)}{\partial \mathbf{y}} = \frac{\overline{M'^2 N'_1} (1 - \eta_y^*) - (\mathbf{y} - \boxed{\mathbf{y}} + s' \sin \alpha - \eta_y^* \Delta \mathbf{y}) \left(\frac{\partial(\overline{M'^2 N'_1})}{\partial \mathbf{y}} \right)}{(\overline{M'^2 N'_1})^2} \quad (129)$$

$$\frac{\partial(\sin \beta)}{\partial p} = 0 \quad (130)$$

Other partial derivatives required due to the friction model formulation:

$$\frac{\partial(s' \cos \alpha)^2}{\partial \mathbf{x}} = \cos^2 \alpha \left(\frac{\partial(s')^2}{\partial \mathbf{x}} \right) + (s')^2 \left(\frac{\partial(\cos^2 \alpha)}{\partial \mathbf{x}} \right) \quad (131)$$

$$\frac{\partial(s' \sin \alpha)^2}{\partial \mathbf{x}} = \sin^2 \alpha \left(\frac{\partial(s')^2}{\partial \mathbf{x}} \right) + (s')^2 \left(\frac{\partial(\sin^2 \alpha)}{\partial \mathbf{x}} \right) \quad (132)$$

$$\frac{\partial(2\mathbf{y}s' \sin \alpha)}{\partial \mathbf{x}} = \left(2\mathbf{y} \sin \alpha \left(\frac{\partial(s')}{\partial \mathbf{x}} \right) \right) + \left(2\mathbf{y}s' \left(\frac{\partial(\sin \alpha)}{\partial \mathbf{x}} \right) \right) \quad (133)$$

$$\frac{\partial(2\boxed{\mathbf{y}}s' \sin \alpha)}{\partial \mathbf{x}} = \left(2\boxed{\mathbf{y}} \sin \alpha \left(\frac{\partial(s')}{\partial \mathbf{x}} \right) \right) + \left(2\boxed{\mathbf{y}}s' \left(\frac{\partial(\sin \alpha)}{\partial \mathbf{x}} \right) \right) \quad (134)$$

$$\frac{\partial(2s'\eta_y^* \Delta \mathbf{y} \sin \alpha)^2}{\partial \mathbf{x}} = 2\eta_y^* \Delta \mathbf{y} \left(\sin \alpha \left(\frac{\partial(s')}{\partial \mathbf{x}} \right) + s' \left(\frac{\partial(\sin \alpha)}{\partial \mathbf{x}} \right) \right) \quad (135)$$

Partial derivatives of τ_x with respect to \mathbf{x} , \mathbf{y} and p :

$$\frac{\partial \tau_x}{\partial \mathbf{x}} = \begin{cases} \frac{\mu p}{s_{max}} \left(\cos \beta \left(\frac{\partial(s_1)}{\partial \mathbf{x}} \right) + s_1 \left(\frac{\partial(\cos \beta)}{\partial \mathbf{x}} \right) \right) & \text{if } \tau_{eqv} \leq \tau_{crit} \\ \mu p \left(\frac{\partial(\cos \beta)}{\partial \mathbf{x}} \right) & \text{if } \tau_{eqv} > \tau_{crit} \end{cases} \quad (136)$$

$$\frac{\partial \tau_x}{\partial \mathbf{y}} = \begin{cases} \frac{\mu p}{s_{max}} \left(\cos \beta \left(\frac{\partial(s_1)}{\partial \mathbf{y}} \right) + s_1 \left(\frac{\partial(\cos \beta)}{\partial \mathbf{y}} \right) \right) & \text{if } \tau_{eqv} \leq \tau_{crit} \\ \mu p \left(\frac{\partial(\cos \beta)}{\partial \mathbf{y}} \right) & \text{if } \tau_{eqv} > \tau_{crit} \end{cases} \quad (137)$$

$$\frac{\partial \tau_x}{\partial p} = \begin{cases} s_1 \cos \beta \frac{\mu}{s_{max}} & \text{if } \tau_{eqv} \leq \tau_{crit} \\ \mu \cos \beta & \text{if } \tau_{eqv} > \tau_{crit} \end{cases} \quad (138)$$

Partial derivatives of τ_y with respect to x , y and p :

$$\frac{\partial \tau_y}{\partial x} = \begin{cases} \frac{\mu p}{s_{max}} \left(\sin \beta \left(\frac{\partial(s_1)}{\partial x} \right) + s_1 \left(\frac{\partial(\sin \beta)}{\partial x} \right) \right) & \text{if } \tau_{eqv} \leq \tau_{crit} \\ \mu p \left(\frac{\partial(\sin \beta)}{\partial x} \right) & \text{if } \tau_{eqv} > \tau_{crit} \end{cases} \quad (139)$$

$$\frac{\partial \tau_y}{\partial y} = \begin{cases} \frac{\mu p}{s_{max}} \left(\sin \beta \left(\frac{\partial(s_1)}{\partial y} \right) + s_1 \left(\frac{\partial(\sin \beta)}{\partial y} \right) \right) & \text{if } \tau_{eqv} \leq \tau_{crit} \\ \mu p \left(\frac{\partial(\sin \beta)}{\partial y} \right) & \text{if } \tau_{eqv} > \tau_{crit} \end{cases} \quad (140)$$

$$\frac{\partial \tau_y}{\partial p} = \begin{cases} s_1 \sin \beta \frac{\mu}{s_{max}} & \text{if } \tau_{eqv} \leq \tau_{crit} \\ \mu \sin \beta & \text{if } \tau_{eqv} > \tau_{crit} \end{cases} \quad (141)$$

7.3.4. Consecutive Time Increments

The values of state-dependant variables listed in Table 7.3 computed during Δt are carried forward to the next consecutive time increment $2\Delta t$. At consecutive increments ($3\Delta t$, $4\Delta t$, ..., $n\Delta t$) the sequence of equations (38)-(40), (77)-(90), (34) and (91)-(141) is repeated.

State-dependant variable	Computed during Δt by	Carried forward to $2\Delta t$ for use as
x	(77)	\boxed{x} in (77)
y	(78)	\boxed{y} in (78), (81), (82), (88), (89), (110), (111), (113), (114), (128), (129) and (134)
M_{1x}	(34)	$\boxed{M_{1x}}$ in (81), (83), (98), (107), (108) and (111)
M_{1y}	(91)	$\boxed{M_{1y}}$ in (81), (82), (110) and (111)
s_1	(86)	$\boxed{s_1}$ in (79), (80) and (102)

Table 7.3: State-dependant variables for modified friction model.

7.3.5. Subroutine Validation

The new friction model for direct application of vibration to the sliding body, scripted into the subroutine in Appendix E, is validated by repeating the longitudinal and transverse vibration FEA simulations described in 5.3.1-5.3.3. Figure 7.8 and Figure 7.9 show the results superimposed onto previous graphs Figure 5.8 and Figure 5.5 respectively. All results follow the same trend, indicating that the friction reduction effect under longitudinal and transverse vibration is the same regardless of whether vibration is applied to the base or to the sliding body. This is because both methods create the same relative velocity.

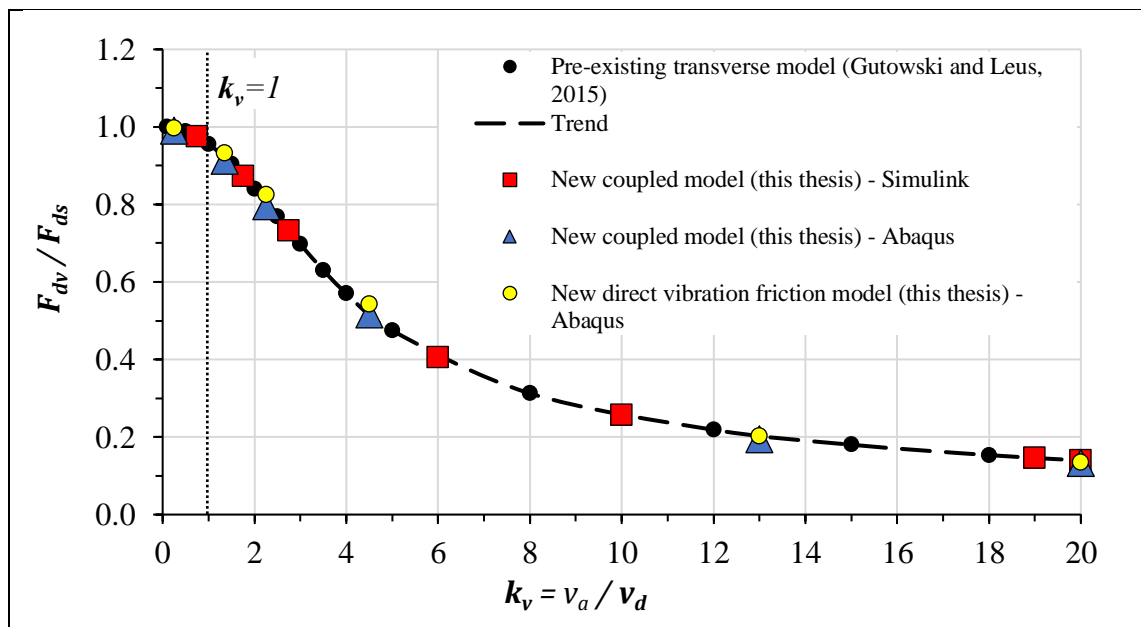


Figure 7.8: Comparison of change in F_{dv}/F_{ds} with k_v , new direct vibration friction model transverse results superimposed.

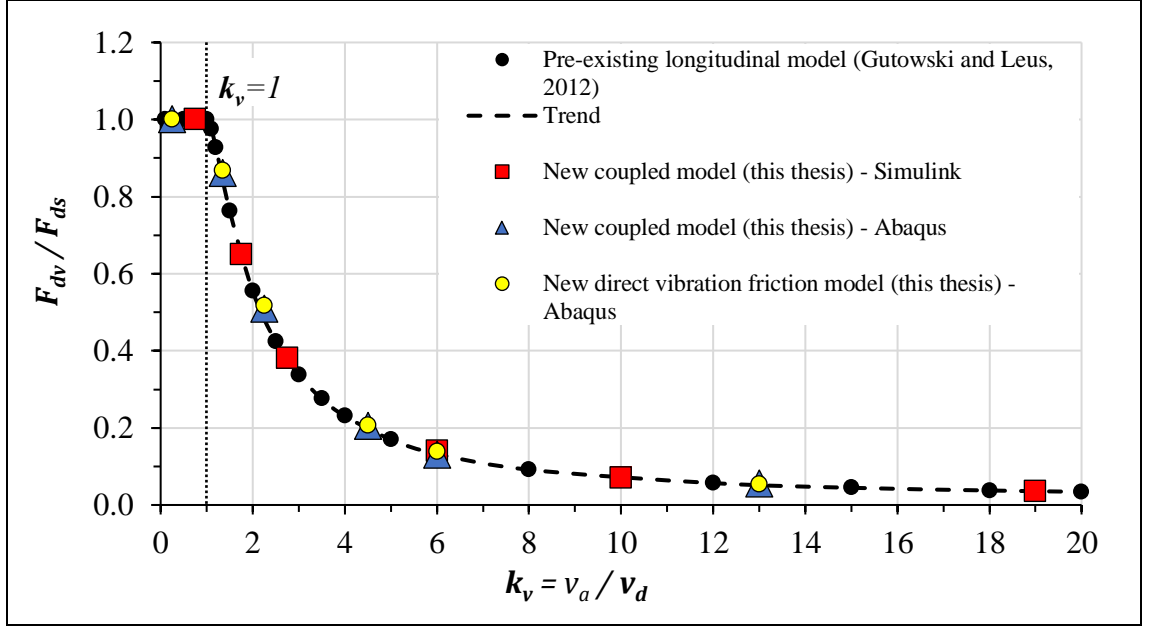


Figure 7.9: Comparison of change in F_{dv}/F_{ds} with k_v , new direct vibration friction model longitudinal results superimposed.

7.4. Worm Gearing Simulation Results

The new direct vibration friction model described in 7.3 is employed in a friction subroutine (Appendix E) to perform worm gearset vibration numerical simulations per the methodology described in 7.2. Results are evaluated in 7.4.1-7.4.6.

7.4.1. Comparison of Simulated vs. Theoretical Efficiency

Figure 7.10 is the input torque T_B to the worm gear, measured at point B (Figure 7.6), for simulation reference 33 in Table 7.2. The black dashed horizontal line shows that worm input torque in the absence of vibration is $T_{Bs} = 33.8$ Nm when $T_R = 366$ Nm. The simulated gear efficiency η_{z1-2} before activation of vibration in step 4 is determined by:

$$\begin{aligned}
 \eta_{z1-2} &= \left(\frac{\text{kW power out from wheel}}{\text{kW power into worm}} \right) 100 \\
 &= \left(\frac{T_R n_2 / 9550}{T_B n_1 / 9550} \right) 100 \\
 &= \left(\frac{366 \times 96 / 9550}{33.8 \times 1440 / 9550} \right) 100 \\
 &= 72\%
 \end{aligned} \tag{142}$$

The theoretical efficiency calculated for gearset 3 (Appendix C) is $\eta_{z1-2} = 73\%$. Simulated efficiency differs against theoretical by only 1%. Therefore, this validates the CAD geometry, simulation methodology and the friction model to set the foundation for evaluating the effect of imposed vibration on the efficiency of the gearset.

Section 7.4.3 explains the fluctuation of worm input torque when vibration is applied in simulation step 4.

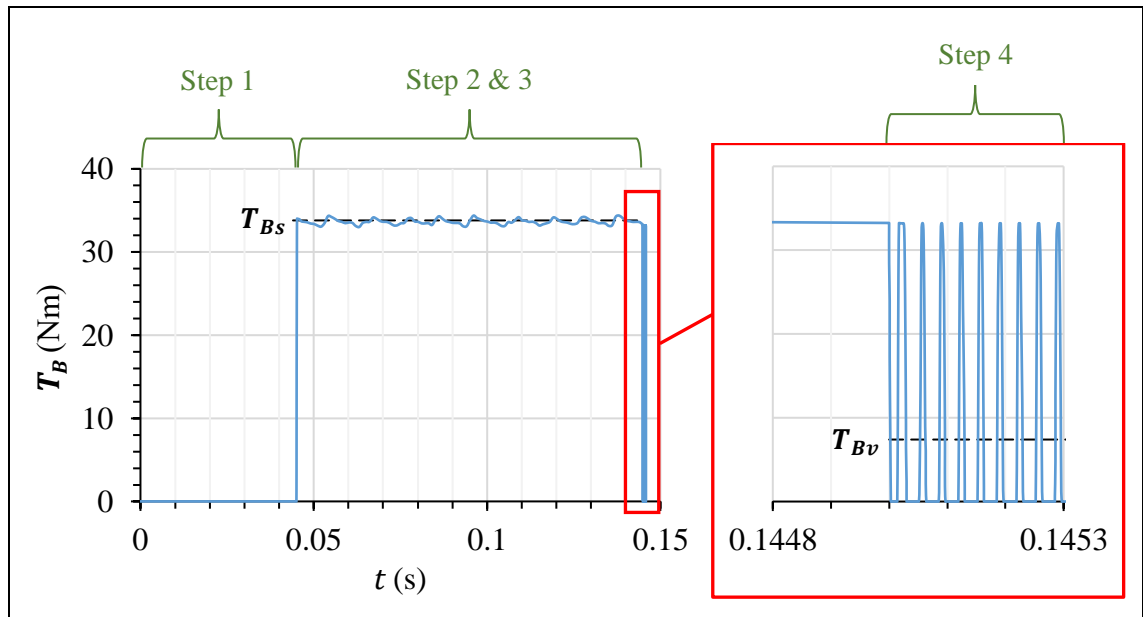


Figure 7.10: Input torque profile T_B for simulation reference 33 in Table 7.2, per simulation steps in 7.2.3.

7.4.2. Mesh Density and Element Types

A study is performed to assess the influence of mesh density on simulation results to thereby select the appropriate mesh. Three mesh densities are used in the study, as per Figure 7.11.

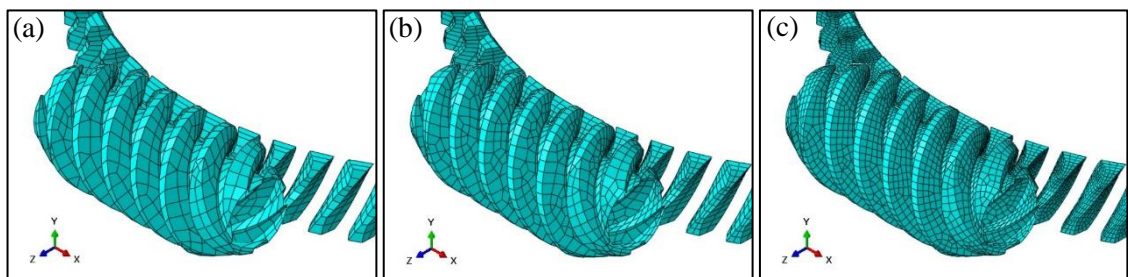


Figure 7.11: Worm gearing mesh densities a) coarse b) intermediate c) fine.

The three mesh densities are applied by assigning values for the global element size. The global element sizes used for the worm and the wheel for each mesh density are

provided in Table 7.4. The intermediate and fine mesh densities are 25% and 50% element size reductions of the coarse density settings.

Mesh density	Worm gear global element size setting	Wheel gear global element size setting
Coarse	2.5	2
Intermediate	1.875	1.5
Fine	1.25	1

Table 7.4: Worm gear and wheel gear global element sizes for the three simulated mesh densities.

The worm mesh is made of standard linear discrete rigid elements of quadrilateral shape, element type reference R3D4. The only other shape option available for discrete rigid elements is triangular, however, Abaqus[®] (2014a) discourages their use as they can exhibit slow convergence.

The wheel mesh is made of standard linear 3D stress elements of hexahedral shape with reduced integration, element type reference C3D8R. 3D stress elements can be wedge shaped or tetrahedrons, however, Abaqus (2014a) recommends that these be used only when necessary for filling in regions to complete a mesh, when the geometry precludes the use of C3D8R elements throughout the model. Wedge and tetrahedral elements exhibit slow convergence and require very fine meshing to obtain accuracy. The choice of reduced integration instead of full integration elements is made to reduce running time. Reduced integration constitutes elements with less integration points so lower order integration is computed to form the element stiffness matrix (Abaqus, 2014a).

As shown in Figure 7.10, vibration activation in step 4 causes fluctuation of worm input torque \mathbf{T}_B . This fluctuation due to vibration causes an average reduction of input torque, termed \mathbf{T}_{Bv} . Therefore, in a similar manner to (60), \mathbf{T}_{Bv} is determined by averaging its magnitude within a single cycle:

$$\mathbf{T}_{Bv} = \frac{1}{n} \sum_{n=1}^n \mathbf{T}_{Bv_n}(t + \Delta t_n) \quad (143)$$

where n is given by (61). $\mathbf{T}_{Bv} = 7.4$ Nm in Figure 7.10. The simulated variability of input torque \mathbf{T}_{Bv} under the influence of vibration in relation to the magnitude \mathbf{T}_{Bs} of this force without vibration is:

$$\begin{aligned} T_{Bv}/T_{Bs} &= 7.4/33.8 \\ &= 0.22 \end{aligned}$$

Simulation set 3 (Table 7.2) has been executed with the three mesh density settings and the results of T_{Bv}/T_{Bs} plotted against dimensionless coefficient $k_w = v_a/v_g$ are displayed in Figure 7.12. There is a clear difference between results of the coarse and intermediate meshes, but there is minimal difference between results of the intermediate and fine meshes. The intermediate and fine mesh produce very similar results, although the intermediate mesh halves the simulation time compared to the fine mesh. Therefore, the intermediate mesh density is selected for all worm gearing simulations.

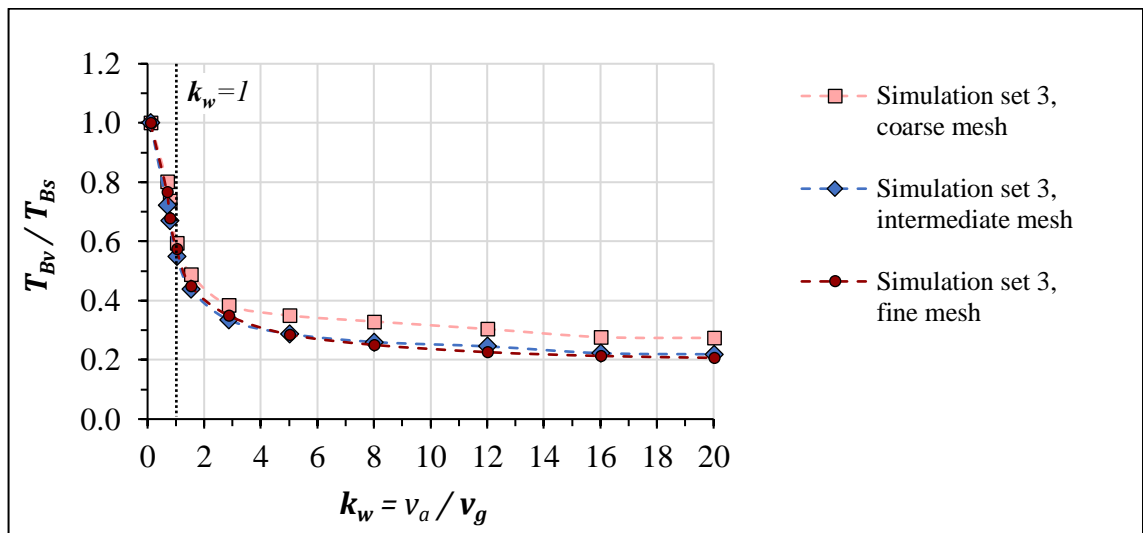


Figure 7.12: Change in T_{Bv}/T_{Bs} with k_w for simulation set 3 at different mesh densities.

7.4.3. Effect of Vibration on Input Torque

In a similar manner to the execution of simulation set 3, the normalised input torque T_{Bv}/T_{Bs} for the remaining 32 simulations listed in Table 7.2 has also been determined. Figure 7.13 shows the normalised input torque T_{Bv}/T_{Bs} as a function of dimensionless coefficient $k_w = v_a/v_g$ for simulation sets 1 and 2. These are plotted on the same figure since in both sets of simulations f , σ_c and the range of k_w are the same. Both sets of simulations produced the same normalised plots.

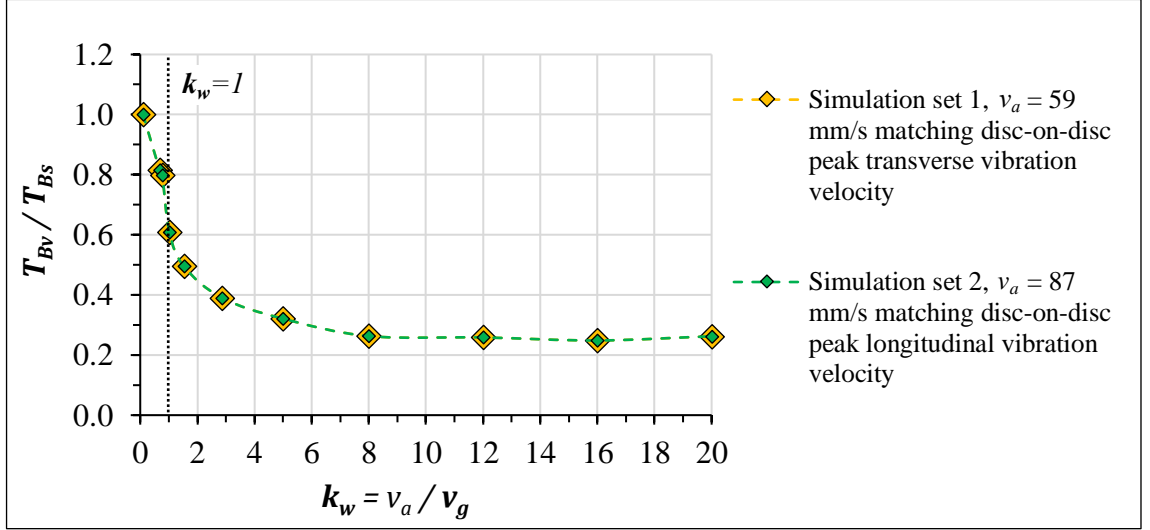


Figure 7.13: Comparison of change in T_{Bv}/T_{Bs} with k_w for simulation set 1 and 2.

Simulation set 3 is plotted on a different graph, Figure 7.12, as that employs a different magnitude of σ_c , a higher sliding velocity v_g representing in-application conditions, and a varying v_a effected by varying the frequency f of vibration. As stated in 7.4.2, simulation set 3 has been executed using three mesh densities and the intermediate mesh density is used for all worm gearing simulations described in this chapter.

Despite the differing conditions applied across the simulations sets (Table 7.2), the shape of the normalised plots in Figure 7.12 and Figure 7.13 are very similar. This means that the relationship between T_{Bv}/T_{Bs} and k_w is similar across the different conditions simulated.

7.4.4. Coulomb Model Comparison

To compare with results in Figure 7.12, simulation set 3 with intermediate mesh has also been executed using Coulomb friction. Figure 7.14 superimposes Coulomb friction results onto the intermediate mesh results from Figure 7.12. Coulomb friction overestimates the normalised worm input torque T_{Bv}/T_{Bs} when $k_w > 1$.

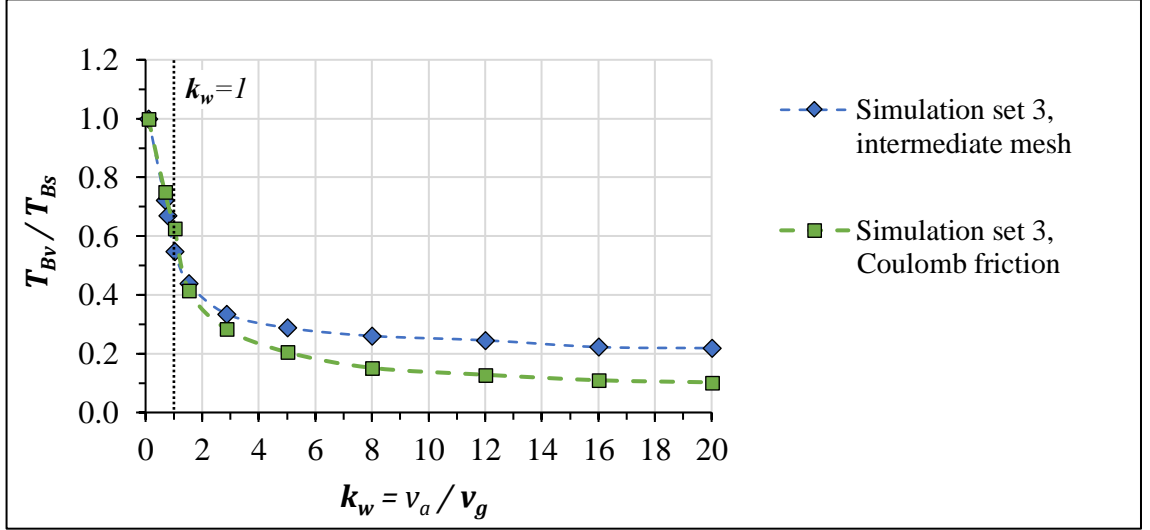


Figure 7.14: Change in T_{Bv}/T_{Bs} with k_w , simulation set 3. Comparison of direct vibration friction model vs. Coulomb friction.

7.4.5. Effect of Vibration on Mechanical Advantage

Simulated mechanical advantage M_a of the worm gearset at each value of k_w (Table 7.2) is given by:

$$M_a = \frac{T_R}{T_B} \quad (144)$$

At $k_w = 20$, reduction of worm torque from $T_{Bs} = 33.8$ Nm to $T_{Bv} = 7.4$ Nm (Figure 7.10) constitutes an improvement in mechanical advantage from $M_a = 10.8$ without vibration to $M_a = 49.5$ with vibration.

Figure 7.15a combines the intermediate mesh results from Figure 7.12 with the corresponding effect on mechanical advantage M_a . Dashed trend lines connect the plotted data points. Vibration reduces worm torque by up to 80% to achieve the same wheel output torque, while increasing M_a by a factor of up to 5.

In comparison, Figure 7.15b superimposes Figure 6.37 and Figure 6.46 to illustrate the normalised steel disc drive torque T_{sv}/T_{ss} under the influence of sinusoidal 750 Hz vibration as a function of dimensionless coefficient k_v from disc-on-disc experiments. Simulated T_{Bv}/T_{Bs} (Figure 7.15a) of the worm gearset matches closely

with disc-on-disc transverse vibration test results only in the range $k_w \leq 3$. The differences in the two plots are due to two different systems being compared. Furthermore, worm rotational velocity $n_1 = 1440$ RPM and wheel output torque 366 Nm constitute to contact sliding speed and contact pressure significantly beyond the levels used in disc-on-disc experiments.

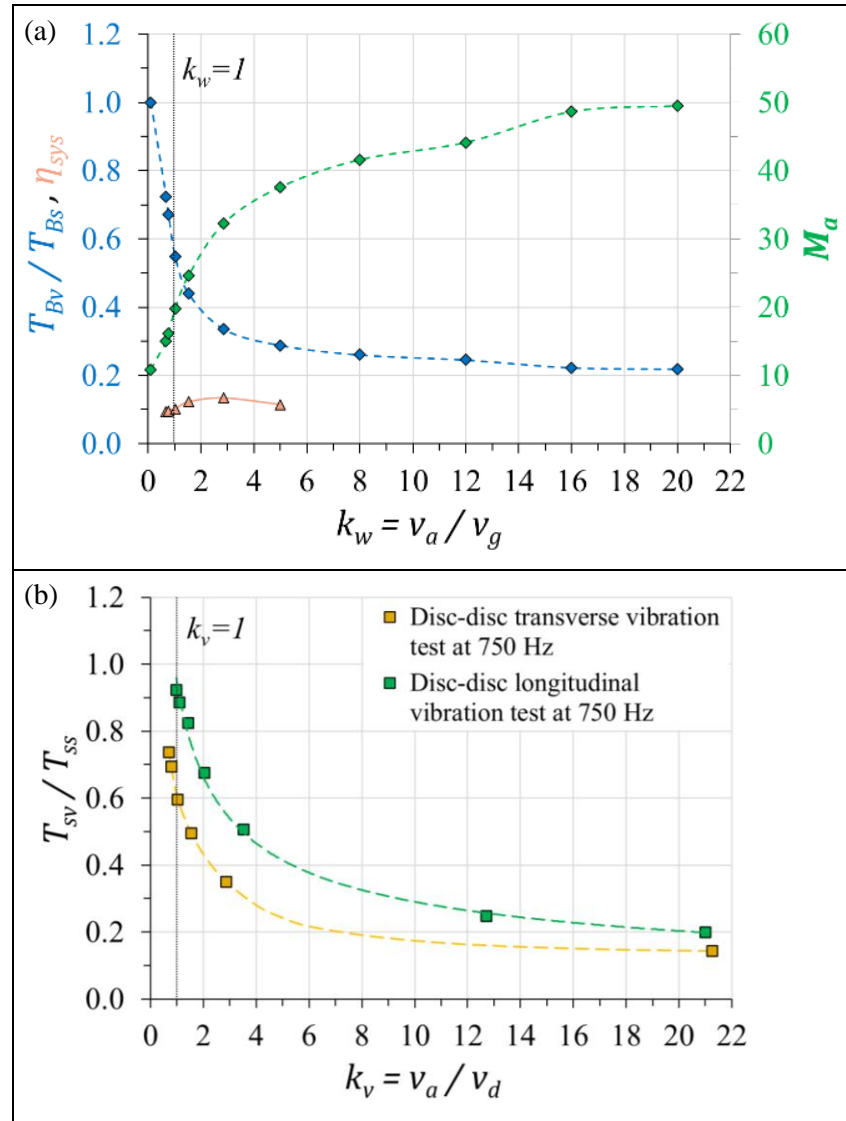


Figure 7.15: (a) Simulated influence of k_w on T_{Bv}/T_{Bs} , M_a and η_{sys} of a worm gearset compared to (b) empirical influence of k_v on T_{sv}/T_{ss} in disc-on-disc experiments.

7.4.6. Effect of Vibration on Efficiency

Mechanical advantage is related to η_{z1-2} by the relationship:

$$\eta_{z1-2} = \left(\frac{M_a}{U} \right) 100 \quad (145)$$

Since the worm gearset simulated has ratio $U = 15$, an increase of M_a beyond 15, as shown by Figure 7.15a, would increase η_{z1-2} beyond 100%. This is incorrect from an energy conservation standpoint as it means output power generated exceeds input power supplied. For this reason, efficiency must be considered as a system efficiency η_{sys} which also includes power supplied into the sonotrode to create the vibration.

As stated in 6.4.4 and illustrated by Figure 6.24, the sonotrode utilised in disc-on-disc experiments generates vibration displacement amplitude $u_a = 0.016$ mm. The amplitude used in gear vibration simulations is 10 times this. The energy law of simple harmonic motion (Earl and Nicholson, 2021) says that the total energy ε of a simple harmonic is related to the maximum velocity v_a by:

$$\varepsilon = \frac{1}{2}mv_a^2 = \frac{1}{2}m(u_a 2\pi f)^2 \quad (146)$$

If u_a is increased by a factor of 10, energy ε of vibration increases by a factor of 100. On this basis, it is assumed that power consumption also multiplies by 100. Therefore, by measuring power consumption of the sonotrode utilised in disc-on-disc experiments it is possible to estimate the power required to generate the higher amplitude vibration used in gear simulations. Equation (147) then allows system efficiency η_{sys} to be plotted against k_w , shown up to $k_w = 5$ in Figure 7.15a.

$$\begin{aligned} \eta_{sys} &= \left(\frac{\text{kW power out from wheel}}{\text{kW power into worm} + \text{kW power into sonotrode}} \right) 100 \\ &= \left(\frac{T_R n_2 / 9550}{(T_B n_1 / 9550) + 100(V_p \times i_p)} \right) 100 \end{aligned} \quad (147)$$

The earlier determined gearset efficiency without vibration $\eta_{z1-2} = 72\%$, is reduced to an efficiency η_{sys} under vibration of just 9 to 13% (Figure 7.15a). Therefore, while vibration improves the gearset mechanical advantage, power required to generate the vibration causes a drop in overall efficiency. This may be acceptable in a system where vibration is only activated for a temporary boost in mechanical advantage.

7.4.7. Limitations of Modelling and Error Mitigation

A limitation of FEA is that to improve computational efficiency and mitigate simulation errors the worm and wheel CAD models have had to be simplified. To minimise simulation durations, gear component features that are away from the contact

area have been excluded. In line with this, the torsional stiffness of the worm shaft is represented by a torsional spring. Furthermore, the worm gear has been assumed rigid and the wheel teeth have had to undergo topology adjustments that are assumed to have minimal impact on flank geometry near the contact area. Finally, the maximum elastic contact deformation has been assumed $s_{max} = 7 \cdot 10^{-8}$ m.

As stated in 5.3.5, the mathematical model behind an FEA simulation (5.2.4), the applied boundary conditions (5.3.1), and the contact properties (5.2.1-5.2.45.2.3) are all factors that can affect the accuracy of FEA results regardless of how well they represent reality. The friction subroutine has been validated against the analytical execution of previous mathematical models for contact between two planar surfaces. However, FEA simulations of the worm gearset with consideration of the limitations and assumptions can only be validated by performing gear tests for comparison.

As a step towards error mitigation, a mesh study has been performed to assess the influence of mesh density on simulation results and thereby select the appropriate mesh size.

7.5. Chapter Discussion and Conclusions

This chapter has combined the learning from worm gearing theoretical assessment (chapter 3) with friction modelling of vibration (chapter 4), and FEA simulations (chapter 5), to develop 3D finite element simulations for studying the effect of vibration on mechanical advantage and efficiency of a worm gearset.

The method used to reduce the complexity of the simulation and therefore the computing power and time required to run the simulation has been detailed. The friction model for coupled longitudinal-transverse vibration developed in 4.5 has been revised to align with vibration applied on the sliding part, as opposed to previously applied on the mating part. The worm gear, being the sliding part, is actuated with vibration due to its lighter mass in comparison to the wheel.

Simulations have shown that axial vibration of the worm gear reduces its input torque by up to 80%. This constitutes up to five-fold increase in gearset mechanical advantage, meaning a gearset that normally requires 33.8 Nm of input to generate 366 Nm of output now only requires 7.4 Nm of input to generate the same output torque. Consequently, the motor driving the worm gear could potentially be downsized by 50 mm in diameter and 30 mm in length, with mass reduction of 6 kg and a huge cost saving of £23 per build associated just with this single gearset variant. The influence of vibration on mechanical advantage is governed by the ratio between vibration velocity amplitude and gear contact sliding velocity, $k_w = v_a/v_g$.

Mechanical advantage M_a and gear efficiency η_{z1-2} are interrelated. Efficiency η_{z1-2} exceeds 100% if M_a exceeds the gear ratio U . This is physically not possible; efficiency analysis must consider the electrical power consumed by the vibration generating device. While vibration greatly improves gearset mechanical advantage, power required to generate the vibration causes a drop in overall system efficiency. This may be acceptable in a system where vibration is only activated for a temporary boost in mechanical advantage.

Chapter 8

Conclusions and Future Work

8.1. Overall Conclusions

This research has expanded current knowledge by showing that friction in lubricated sliding-rolling contact can be reduced using imposed vibration. Vibration can be applied in worm gearing to improve mechanical advantage, but the overall system efficiency is impacted.

The overall conclusions of this thesis are presented with reference to the research objectives outlined in chapter 1.

- i. Identify existing and emerging methods of reducing friction between loaded contacts.*

Review of literature in chapter 2 has highlighted that of all the types of losses in a worm gearbox, tooth friction losses are most significant. Reduction of these losses thus yields the greatest benefit from an efficiency standpoint. A hardened steel worm with an alloyed bronze wheel have long been established as the best tribological pair for worm gears. Other methods for friction reduction currently employed and widely researched include a wide variety of lubricants, and surface coatings. Synthetic lubricants have shown to outperform mineral oils, and the use of nanoparticle additives have been tested with promising results. Meanwhile, development of new coatings continues with a drive to reduce surface damage at high loads.

Control of friction using vibration is a developing field with minimal research exploring the science behind the phenomenon despite its exploitation in many applications. One patent (Mori, Kukita and Shimada, 2014) has indicated it can be successfully applied to worm gearing but lack of literature has highlighted a knowledge gap that is explored by this thesis.

- ii. Use worm gearing design standards to calculate the theoretical efficiency improvement gained by imposing vibration compared to other methods of reducing friction.*

In chapter 3 a spreadsheet to calculate efficiency and load capacity of worm gearsets based on theory from three different standards has been created. This has been used to investigate the sensitivity of efficiency to different worm gearset design parameters. To maintain gearset space envelope and avoid major redesign of other system

components, only four design parameters can be optimised, namely normal pressure angle α_n , diameter factor q_1 , axial module m_{x1} and surface roughness Ra_1 . Theoretically, the studied gearsets can be improved in efficiency by 7% due to design optimisation, without impacting load capacity.

The effect of different lubricants and coatings on efficiency has also been evaluated. However, the best worm gearing efficiency benefit is projected from use of vibration, outperforming the use of synthetic oils, the addition of oil nanoparticles and use of coatings. This further exemplifies the previously identified knowledge gap and the need to research control of friction using vibration imposed between sliding surfaces.

- iii. Develop mathematical models to describe the contact mechanics associated with friction force reduction in the presence of in-plane vibration and validate the analytical models against pre-existing simulation results.*

Chapter 4 has introduced pre-existing mathematical models describing the mechanics of contacting asperities when vibration is applied. Due to incorporation of the dynamic Dahl (1968; 1976) friction model within these analytical models, they are in good agreement with empirical results of friction reduction under longitudinal and transverse vibration modes. Combining the separate models of the two vibration modes into a single friction model for coupled longitudinal-transverse vibration has established a comprehensive understanding of contact mechanics. Analytical evaluation of the new model via Simulink[®] has validated it against pre-existing simulation results and empirical data.

- iv. Develop numerical simulations of friction force reduction by in-plane vibration using finite element method and compare results with analytical method.*

Chapter 5 has evaluated the same system as in Chapter 4 but numerically by implementing the new friction model for coupled longitudinal-transverse vibration into a subroutine (Appendix D) for 3D finite element simulations using Abaqus[®]. It has been shown that numerical method produces the same friction reduction effect as analytical, proving the suitability of numerical technique for simulating worm gearing in chapter 7.

- v. *Produce a custom friction test rig to conduct vibration experiments of a contact representative of worm gearing and evaluate empirical results.*

Chapter 6 has described a custom disc-on-disc test rig developed to imitate real application conditions as closely as possible using test specimen geometry that can be manufactured simply and consistently. The test rig enables experimentation of sliding-rolling contact interaction typical of worm gearing using a representative material pair while allowing vibration to be applied. Test variables include lubricant type, vibration mode, vibration waveform, vibration frequency f , and sliding speed v_{sl} . The effect of vibration on disc drive torques and rotational speeds, as well as voltage and current drawn by the motors has been measured. This data has allowed changes in efficiency of the steel disc drive system to be determined.

The most favourable results in both longitudinal and transverse vibration modes are achieved in oil at $f = 750$ Hz using sinusoidal waveform. Recorded accelerometer data supports these results by measuring the highest vibration velocity at this frequency. At $f = 750$ Hz vibration velocities are $v_a = 59$ mm/s during transverse vibration (Figure 6.36), and $v_a = 87$ mm/s during longitudinal vibration (Figure 6.45). Despite of smaller v_a during transverse mode, disc drive torque is reduced by up to 86% compared to 78% reduction in longitudinal mode. This is contrary to previous researchers (Gutowski and Leus, 2015) who report greater friction reduction in longitudinal vibration tests performed with two planar surfaces in contact. Wear test performed to 1.8 metres of sliding under longitudinal vibration indicates that the rate of wear may double due to vibration.

- vi. *Perform 3D finite element simulations of vibration applied to a worm gearset, evaluate efficiency results, and quantify the benefits.*

By combining knowledge of worm gearing theory from chapter 3 with friction modelling from chapter 4, and the conduct of numerical simulations from chapter 5, chapter 7 has developed 3D simulations to study the effect of vibration on efficiency of a single worm gearset. Axially vibrating the worm gear is shown to reduce its input torque by up to 80% (Figure 7.15a). The extent of reduction is governed by the ratio of vibration

velocity amplitude v_a and the gearset sliding velocity v_g , $k_w = v_a/v_g$. The shape of the curve plotting normalised input torque against k_w depends on the mechanical system being evaluated. Simulated T_{Bv}/T_{Bs} of the worm gearset (Figure 7.15a) matches closely with disc-on-disc transverse vibration test results (Figure 7.15b) only in the range $k_w \leq 3$.

Up to five-fold increase in gearset mechanical advantage due to vibration means a gearset that normally requires 33.8 Nm of input to generate 366 Nm of output now only requires 7.4 Nm of input to generate the same output torque. Consequently, the motor driving the worm gear can potentially be downsized by 50 mm in diameter and 30 mm in length, with mass reduction of 6 kg and a huge cost saving of £23 per build associated just with this single gearset variant.

Energy consumed to generate the vibration must also be considered in the overall system efficiency η_{sys} calculation. η_{sys} is dependent on changes of input mechanical power to the worm gear as well as input electrical power to the sonotrode. While vibration improves the gearset mechanical advantage, power required to generate the vibration causes a drop in overall efficiency. The extent of this reduction depends on the dynamics of the system and characteristics of the piezo actuator employed. Tests with worm gearsets are necessary to confirm this.

If applied continuously, vibration will impact wear life, therefore, its activation must be controlled such that it is used only when the application requires the most torque output from the gearset. Otherwise, under normal operation or when gearing is idle the vibration must be inactive. In this manner the self-locking capability of worm gearing described in 2.1.5 can be maintained. Furthermore, if vibration is only needed for a small percentage of the application's operating cycle, then the temporary boost in mechanical advantage can far outweigh any system efficiency and wear life concerns.

8.2. Recommendations for Future Work

Recommendations that would merit further investigation based on outcomes of this thesis:

- i. Disc-on-disc experiments have proven the friction reduction effect of vibration in a sliding-rolling contact, while simulations have shown encouraging results when vibration is applied to a single worm gearset. The next logical step for progressing this research would be to support gear simulation results with worm gearset vibration experiments. To enable like-for-like comparison of results,

recommendation is to develop another custom rig so that the gearset can be tested in isolation. The simulation can be fine-tuned, if necessary, by tuning variables μ , s_{max} , i and η_y in the friction model (7.3) to align with experimental results.

- ii. Testing and simulation should be extended to a range of gearsets to study whether the benefits of induced vibration are more prominent with certain gear ratios and sizes. This would enable an assessment of motor downsizing and cost reduction opportunities across a wider range of products.
- iii. As well as testing for mechanical advantage and efficiency improvements, the effect of vibration on gearset self-locking capability should also be studied. It is likely that a control system would need development for activating vibration only when higher mechanical advantage is desired, and subsequently deactivating it to maintain self-locking when gearing is idle. The control system itself would need to be tested for reliability.
- iv. With regards to the method of applying vibration, instead of electronic control it may be possible to induce vibration by a mechanical coupling to the worm gear rotation. A benefit of this is vibration control without additional electronics, but the drawback is vibration applied mid-stroke where torque reduction is generally not necessary. A mechanical decoupling method would thus also need to accompany this development.
- v. System testing, where gearsets are housed in their respective gearboxes, would allow for an overall system evaluation. It is recommended that the effects of vibration on other integral measurement and data logging devices be assessed. It may be necessary to electronically filter the vibration noise from data recorded by integral devices.
- vi. Wear testing is recommended at system level to assess impact on overall product functionality during its intended life, as well as to assess impact on gearset operations to failure.

Bibliography

Abaqus®. (2014a) *Abaqus Analysis User's Guide. 28.1.1 Solid (continuum) elements* [online]. Available from: <http://130.149.89.49:2080/v6.14/books/usb/default.htm> [Accessed 07/08/2022].

Abaqus®. (2014b) *Abaqus Analysis User's Guide. 36.1.1 Contact interaction analysis: overview* [online]. Available from: <http://130.149.89.49:2080/v6.14/books/usb/default.htm> [Accessed 07/08/2022].

Abaqus®. (2014c) *Abaqus Analysis User's Guide. 38.1.1 Contact formulations in Abaqus/Standard* [online]. Available from: <http://130.149.89.49:2080/v6.14/books/usb/default.htm> [Accessed 07/08/2022].

Abaqus®. (2014d) *Abaqus Analysis User's Guide. 38.1.2 Contact constraint enforcement methods in Abaqus/Standard* [online]. Available from: <http://130.149.89.49:2080/v6.14/books/usb/default.htm> [Accessed 07/08/2022].

Abdo, J. and Tahat, M. (2008) The Effect of Frequency and Amplitude of Vibration on the Coefficient of Friction for Metals. *WSEAS Transactions on Applied and Theoretical Mechanics*. 3 (7), pp. 265-274.

Abdullah, M. and Jameel, A. (2015) Reduction of Noise and Vibration of Spur Gear by Using Asymmetric Teeth Profiles with Tip Relief. *University of Baghdad Engineering Journal*. 21 (9), pp. 105-118.

Aboua, K., Umehara, N., Kousaka, H., Tokoroyama, T., Murashima, M., Tasdemir, H., Mabuchi, Y. and Higuchi, T. (2018) Effect of ZnDTP tribofilm's morphology on friction behaviors of DLC coatings: tribofilm characterization by 3D scanning electron microscope observation. *Journal of Advanced Mechanical Design Systems and Manufacturing*. 12 (7), pp. 1-7.

Amaro, R., Martins, R., Seabra, J., Renevier, N. and Teer, D. (2005) Molybdenum disulphide/titanium low friction coating for gears application. *Tribology International*. 38 (4), pp. 423-434.

American Gear Manufacturers Association. (1992) *ANSI/AGMA 6034-B92. Practice for Enclosed Cylindrical Wormgear Speed Reducers and Gearmotors*. Virginia: American Gear Manufacturers Association.

Amini, S. and Amiri, M. (2014) Study of ultrasonic vibrations' effect on friction stir welding. *International Journal of Advanced Manufacturing Technology*. 73 (1-4), pp. 127-135.

Arnold, G., Leiteritz, L., Zahn, S. and Rohm, H. (2009) Ultrasonic cutting of cheese: Composition affects cutting work reduction and energy demand. *International Dairy Journal*. 19 (5), pp. 314-320.

Baker, H., Claypoole, W. and Fuller, D. (1952) Further developments in the measurement of the coefficient of static friction. In: Sternberg, E., ed. *Proceedings of the First U.S. National Congress of Applied Mechanics*. Chicago, 11-15 June 1951. American Society of Mechanical Engineers.

Bartels, T. and Bock, W. (2017) Gear Lubrication Oils. In: Mang, T. and Dresel, W. (2017) *Lubricants and Lubrication*. 3rd ed. Weinheim: Wiley-VCH, pp. 83-115.

Benedetti, M., Fontanari, V., Torresani, E., Girardi, C., Giordanino, L. (2017) Investigation of lubricated rolling sliding behaviour of WC/C, WC/C-CrN, DLC based coatings and plasma nitriding of steel for possible use in worm gearing. *Wear*, 378-379, pp. 106-113.

Bird, J. (2001) *Newnes Engineering Science Pocket Book*. 3rd ed. Oxford: Newnes.

Bobak, T. (2009) *White Paper. How Green is Your Gearbox?* [online]. Sumitomo Drive Technologies. Available from: <https://entermediadb.sumitomodrive.com/assets/emshare/views/modules/asset/downloads/originals/2018/06/93/68b1c71ac//How%20Green%20is%20Your%20Gearbox%20Update.pdf> [Accessed 20 October 2020].

Brandão, J., Meheux, M., Ville, F., Seabra, J., Castro, J. (2021) Comparative overview of five gear oils in mixed and boundary film lubrication. *Tribology International*. 47, pp. 50-61.

British Standards Institution. (1983) BS 721-2:1983 British Standard Specification for Worm Gearing. Part 2. Metric Units. UK: British Standards Institution.

British Standards Institution. (2011) *PD ISO/TR 14521:2010 Gears – Calculation of load capacity of wormgears*. UK: British Standards Institution.

Budynas, R. and Nisbett, J. (2011) *Shigley's Mechanical Engineering Design*. 9th ed. New York: McGraw Hill.

Calkins, C. (1926) *Worm-Gears and Worm-Geared Axles*. Report number: 260044. SAE International.

Cao, M., Zhao, L., Wang, W., Han, H. and Lang, W. (2019) Effects of dopants Ti and Al on microstructure, mechanical and tribological behaviors of ZnO/MoS₂ coating deposited by magnetron co-sputtering. *AIP Advances*. 9 (4), pp. 1-10.

Childs, P. (2019) *Mechanical Design Engineering Handbook*. 2nd ed. Oxford: Butterworth-Heinemann.

Chowdhury, M. and Helali, M. (2007) The effect of frequency of vibration and humidity on the wear rate. *Tribology International*. 262 (1-2), pp. 198-203.

Chowdhury, M. and Helali, M. (2008) The effect of amplitude of vibration on the coefficient of friction for different materials. *Tribology International*. 41 (4), pp. 307-314.

Chu, H., Hsu, W. and Lin, J. (2010) The anti-scuffing performance of diamond nanoparticles as an oil additive. *Wear*. 268 (7-8), pp. 960-967.

Cirelli, M., Giannini, O., Valentini, P. and Pennestrì, E. (2020) Influence of tip relief in spur gears dynamic using multibody models with movable teeth. *Mechanism and Machine Theory*. 152 (103948), pp. 1-18.

Dahl, P. (1968) *A Solid Friction Model*. Report number: TOR-0158H3107-181-1. California: The Aerospace Corporation.

Dahl, P. (1976) Solid friction damping of mechanical vibrations. *AIAA Journal*. 14 (12), pp. 1675-82.

Daniel, R. and Paulus, T. (2019) *Lock Gates and Other Closures in Hydraulic Projects*. Oxford: Butterworth-Heinemann.

Davis, J. (2005) *Gear Materials, Properties, and Manufacture*. Ohio: ASM International.

Designatronics Inc. (2020) *Gear Types and Axial Arrangements; Details of Involute Gearing, Elements of Metric Gear Technology* [online]. Available from: <https://www.sdp-si.com/resources/elements-of-metric-gear-technology/page2.php> [Accessed 06 October 2020].

Deng, X., Wang, J. and Horstemeyer, M. (2013) Modification design method for an enveloping hourglass worm gear with consideration of machining and misalignment errors. *Chinese Journal of Mechanical Engineering*. 26 (5), pp. 948-956.

Dowson, D. (1998) *History of Tribology*. 2nd ed. London: Professional Engineering Publishing.

Dresel, W. (2017) Synthetic Base Oils. In: Mang, T. and Dresel, W. (2017) *Lubricants and Lubrication*. 3rd ed. Weinheim: Wiley-VCH, pp. 83-115.

Dwyer-Joyce, R., Sayles, R. and Ioannides, E. (1994) An investigation into the mechanisms of closed three-body abrasive wear. *Wear*. 175 (1-2), pp. 133-142.

Earl, R. and Nicholson, J. (2021) *The Concise Oxford Dictionary of Mathematics*. 6th ed. Oxford: Oxford University Press.

Egashira, K., Mizutani, K. and Nagao, T. (2002) Ultrasonic vibration drilling of microholes in glass. *CIRP Annals*. 51 (1), pp. 339-342.

Eriksson, P. and Kovalainen, A. (2016) *Quantitative Methods in Business Research*. London: Sage Publications Ltd.

Espejo, C., Thiébaud, B., Jarnias, F., Wang, C., Neville, A. and Morina, A. (2018) MoDTC tribochemistry in steel/steel and steel/DLC systems lubricated with model lubricants and fully formulated engine oils. *Journal of Tribology*. 141 (1), pp. 1-12.

Fang, H., Tsay, C. (2000) Mathematical model and bearing contacts of the ZN-type worm gear set cut by oversize hob cutters. *Mechanism and Machine Theory*. 35 (12), pp. 1689-1708.

Feng, X., and Xia, Y. (2012) Tribological properties of Ti-doped DLC coatings under ionic liquids lubricated conditions. *Applied Surface Science*. 258 (7), pp. 2433-2438.

Fontanari, V., Benedetti, M., Straffelini, G., Girardi, C. and Giordanino, L. (2013) Tribological behaviour of the bronze-steel pair for worm gearing. *Wear.* 302 (1-2), pp. 1520-1527.

Fontanari, V., Benedetti, M., Girardi, C. and Giordanino, L. (2016) Investigation of the lubricated wear behavior of ductile cast iron and quenched and tempered alloy steel for possible use in worm gearing. *Wear.* 350-351, pp. 68-73.

Fridman, H. and Levesque, P. (1959) Reduction of static friction by sonic vibrations. *Journal of Applied Physics.* 30 (10), pp. 1572-1575.

Fuchs. (2011) *Product Information. Titan Gear MP SAE 80* [online]. Mannheim: Fuchs Europe Schmierstoffe GmbH. Available from: https://www.general oils.net/PI_TITAN-GEAR-MP-80_e.pdf [Accessed 15 December 2020].

Gao, S., Wu, S. and Padhy, G. (2017) Material flow, microstructure and mechanical properties of friction stir welded AA 2024-T3 enhanced by ultrasonic vibrations. *Journal of Manufacturing Processes.* 30, pp. 385-395.

Global Industry Analysts Inc. (2020) *Industrial Gearbox – Global Market Trajectory & Analytics* [online] Document Number: MCP12628. California: Global Industry Analysts Inc. Available from: <https://www.strategyr.com/market-report-industrial-gearbox-forecasts-global-industry-analysts-inc.asp> [Accessed 04 October 2020].

Global Info Research. (2020) *Global Worm Gear Market 2020 by Manufacturers, Regions, Type and Application, Forecast to 2025* [online]. Hong Kong: Global Info Research. Available from: https://www.globalinfo research.com/Global-Worm-Gear_p476434.html [Accessed 04 October 2020].

Godfrey, D. (1967) Vibration reduces metal to metal contact and causes an apparent reduction in friction. *Tribology Transactions.* 10 (2), pp. 183-192.

Gonzalez, C. (2015) *What's the Difference Between Spur, Helical, Bevel, and Worm Gears?* [online]. Machine Design. Available from: https://cdn.baseplatform.io/files/base/ebm/machinedesign/document/2019/03/machinedesign_3397_spur_helical_bevel_and_worm_gears.pdf [Accessed 06 October 2020].

Gutowski, P. and Leus, M. (2011) Practical possibilities of utilization of tangential longitudinal vibrations for controlling the friction force and reduction of drive force in sliding. *Mechanics and Mechanical Engineering*. 15 (4), pp. 103-113.

Gutowski, P. and Leus, M. (2012) The effect of longitudinal tangential vibrations on friction and driving forces in sliding motion. *Tribology International*. 55 (6), pp. 108-118.

Gutowski, P. and Leus, M. (2015) Computational model for friction force estimation in sliding motion at transverse tangential vibrations of elastic contact support. *Tribology International*. 90, pp. 455-462.

Gutowski, P. and Leus, M. (2020) Computational model of friction force reduction at arbitrary direction of tangential vibrations and its experimental verification. *Tribology International*. 143, pp. 1-13.

Hargreaves, D., Planitz, A. (2009) Assessing the energy efficiency of gear oils via the FZG test machine. *Tribology International*. 42 (6), pp. 918-925.

He, H., Lyu, S. and Her, C. (2010) Effect of MoS₂-based composite coatings on tribological behavior and efficiency of gear. *International Journal of Precision Engineering and Manufacturing*. 11 (6), pp. 937-943.

Hess, D. and Soom, A. (1991) Normal vibration and friction under harmonic loads: Hertzian contacts. *Journal of Tribology*. 113 (1), pp. 80-86.

Hof, L. and Abou Ziki, J. (2017) Micro-Hole Drilling on Glass Substrates - A Review. *Micromachines*. 8, pp. 1-23.

Höhn, B., Michaelis, K. and Hinterstoißer, M. (2009) Optimization of Gearbox Efficiency. *Gomabn*. 48 (4), pp. 441-480.

Hulka, I., Utu, D., Serban, V., Dan, M., Matikainen, V. and Vuoristo, P. (2015) Corrosion Behavior of WC-Ni Coatings Deposited by Different Thermal Spraying Methods. *Chemical bulletin of the "Politehnica" University of Timișoara*. 60 (2), pp. 60-65.

Hutchings, I. (2016) Leonardo da Vinci's studies of friction. *Wear*. 360-361, pp. 51-66.

- Ingole, S., Charanpahari, A., Kakade, A., Umare, S., Bhatt, D. and Menghani, J. (2013) Tribological behavior of nano TiO₂ as an additive in base oil. *Wear*. 301 (1-2), pp. 776-785.
- Jimma, T., Kasuga, Y., Iwaki, N., Miyazawa, O., Mori, E., Ito, K. and Hatano, H. (1998) An application of ultrasonic vibration to the deep drawing process. *Journal of Materials Processing Technology*. 80, pp. 406-412.
- Jin, Y., Liu, Z. and Zhou, X. (2019) Theoretical, numerical, and experimental studies on friction vibration of marine water-lubricated bearing coupled with lateral vibration. *Journal of Marine Science and Technology*. 25 (3), pp. 1-14.
- Joachim, F., Kurz, N., Glatthaar, B. (2004) Influence of coatings and surface improvements on the lifetime of gears. *Proceedings of the International Conference on Gears, VDI-Berichte NR 1665*. pp. 565-82.
- Kajdas, C., Karpińska, A. and Kulczycki, A. (2010) Industrial Lubricants. In: Mortier, R., Fox, M. and Orszulik, S. (2010) *Chemistry and Technology of Lubricants*. 3rd ed. London: Springer, pp. 239-292.
- Klüber Lubrication. (2018) *Klübersynth UH1 6 oils* [online]. Munich: Klüber Lubrication München KG. Available from: <http://oilmart.com/data/products/pds/1625/TDS%20Kluber%20Klübersynth%20UH1%2006.pdf> [Accessed 16 December 2020].
- Kondo, Y., Koyama, T., Tsuboi, R., Nakano, M., Miyake, K. and Sasaki, S. (2013) Tribological performance of halogen-free ionic liquids as lubricants of hard coatings and ceramics. *Tribology Letters*. 51 (2), pp. 243-249.
- Kumar, V. and Hutchings, I. (2004) Reduction of the sliding friction of metals by the application of longitudinal or transverse ultrasonic vibration. *Tribology International*. 37 (10), pp. 833–840.
- Laderou, A., Mohammadpour, M., Theodossiades, S., Daubney, R. and Meeks, G. (2020) On the Effect of DLC and WCC Coatings on the Efficiency of Manual Transmission Gear Pairs. *Applied Sciences*. 10 (9), pp. 1-20.

Lenkiewicz, W. (1969) The sliding friction process-effect of external vibrations. *Wear*. 13 (2), pp. 99-108.

Li, L., Lu, Z., Pu, J., Wang, H., Li, Q., Chen, S., Zhang, Z. and Wang, L. (2020) The superlattice structure and self-adaptive performance of C–Ti/MoS₂ composite coatings. *Ceramics International*. 46 (5), pp. 5733-5744.

Liang, J., Fillmore, S. and Ma, O. (2012) An extended bristle friction force model with experimental validation. *Mechanism and Machine Theory*. 56, pp. 123-137.

Linquip. (2021) *What is a Worm Gearbox?* [online]. Available from: <https://www.linquip.com/blog/worm-gearbox-working-principle/> [Accessed 18 April 2022].

Littmann, W., Storck, H. and Wallaschek, J. (2001) Sliding friction in the presence of ultrasonic oscillations: superposition of longitudinal oscillations. *Archive of Applied Mechanics*. 71 (8), pp. 549-554.

Litvin, F., Gonzalez-Perez, I., Yukishima, K., Fuentes, A. and Hayasaka, K. (2007) Design, simulation of meshing, and contact stresses for an improved worm gear drive. *Mechanism and Machine Theory*. 42 (8), pp. 940–959.

Liu, J., Niu, Z., Zhu, H. and Zhao, C. (2019) Design and Experiment of a Large-Aperture Hollow Traveling Wave Ultrasonic Motor with Low Speed and High Torque. *Applied Sciences*. 9 (19), pp. 1-16.

Liu, L., Jia, W., Xu, D., Li, R. (2014) Applications of ultrasonic cutting in food processing. *Journal of Food Processing and Preservation*. 39, pp. 1762-1769.

Magalhães, L., and Seabra, J. (1998) Wear and scuffing of austempered ductile iron gears. *Wear*. 215 (1-2), pp. 237-246.

Magalhães, L., Seabra, J. and Sá, C. (2000) Experimental observations of contact fatigue crack mechanisms for austempered ductile iron (ADI) discs. *Wear*. 246 (1-2), pp. 134-148.

Magalhães, L., Martins, R. and Seabra, J. (2012) Low-loss austempered ductile iron gears: Experimental evaluation comparing materials and lubricants. *Tribology International*. 46 (1), pp. 97-105.

Mao, K., Sun, Y. and Bell, T. (2006) An initial approach to the link of multi-layer coatings contact stresses and the surface engineered gears. *Surface & Coatings Technology*. 201 (12), pp. 5796-5803.

Mao, K. (2007) Gear tooth contact analysis and its application in the reduction of fatigue wear. *Wear*. 262 (11-12), pp. 1281-1288.

Marques, P., Fernandes, C., Martins, R. and Seabra, J. (2014) Efficiency of a gearbox lubricated with wind turbine gear oils. *Tribology International*. 71, pp. 7-16.

Martins, R., Seabra, J., Brito, A., Seyfert, C., Luther, R. and Igartua, A. (2005) Friction coefficient in FZG gears lubricated with industrial gear oils: Biodegradable ester vs. mineral oil. *Tribology International*. 39 (6), pp. 512-521.

Martins, R., Amaro, R. and Seabra, J. (2008) Influence of low friction coatings on the scuffing load capacity and efficiency of gears. *Tribology International*. 41 (4), pp. 234-243.

Martins, R., Seabra, J. and Magalhães, L. (2008) Austempered ductile iron (ADI) gears: power loss, pitting and micropitting. *Wear*. 264 (9-10), pp. 838-849.

Mautner, E., Sigmund, W., Stemplinger, J. and Stahl, K. (2015) Efficiency of worm gearboxes. *Proceedings of the Institution of Mechanical Engineers, Part C: Journal of Mechanical Engineering Science*. 230 (16), pp. 2952-2956.

Mitskevich, A. (1968) Motion of a body over tangentially vibrating surface, taking into account of friction. *Soviet Physics-Acoustics*. 13 (3), pp. 343-351.

Moorthy, V., Shaw, B. (2012) Contact fatigue performance of helical gears with surface coatings. *Wear*. 276-277, pp. 130-140.

Mori, M., Kukita, D. and Shimada, S. (2014) *Actuator* [online]. Mori, M., Kukita, D. and Shimada, S. US8847533B2. Available from: <https://patents.google.com/patent/US8847533/ja> [Accessed 05 December 2020].

Mutuonga, S. and Onoda, J. (1995) New gravity compensation method by dither for low-g simulation. *Journal of Spacecraft and Rockets*. 32 (2), pp. 364-369.

Oden, J., Martins, J. (1985) Models and Computational Methods for Dynamic Friction Phenomena. *Computer Methods in Applied Mechanics and Engineering*. 52 (1-3), pp. 527-634.

Pitenis, A., Dowson, D. and Sawyer, W. (2014) Leonardo da Vinci's Friction Experiments: An Old Story Acknowledged and Repeated. *Tribology Letters*. 56 (3), pp. 509-515.

Popova, E. and Popov, V. (2015) The research works of Coulomb and Amontons and generalized laws of friction. *Friction*. 3 (2), pp. 183-190.

Radzevich, S. (2012) Dudley's Handbook of Practical Gear Design and Manufacture. 2nd ed. Florida: CRC Press.

Rotork PLC. (2020) *IQ Mk3 (IQ3) Multi-turn (IQ) / Part-turn (IQT) Sales Brochure* [online]. Document Number: pub002-038-00-0820. Bath: Rotork PLC. Available from: <https://www.rotork.com/en/documents/publication/8923> [Accessed 03 October 2020].

Russo, M. (2013) *High Tin Bronze Alloys for Gear Applications* [online]. Available from: <https://www.nationalbronze.com/News/high-tin-bronze-alloys-for-gear-applications> [Accessed 07 November 2020].

Schneider, Y., Zahn, S., Schindler, C. and Rohm, H. (2009) Ultrasonic excitation affects friction interactions between food materials and cutting tools. *Ultrasonics*. 49 (6-7), pp. 588-593.

Sohn, J. and Park, N. (2016) Geometric interference in cylindrical worm gear drives using oversized hob to cut worm gears. *Mechanism and Machine Theory*. 100, pp. 83-103.

Sohn, J. and Park, N. (2017) Modified worm gear hobbing for symmetric longitudinal crowning in high lead cylindrical worm gear drives. *Mechanism and Machine Theory*. 117, pp. 133-147.

Sharif, K., Evans, H. and Snidle, R. (2006) Prediction of the wear pattern in worm gears. *Wear*. 261 (5-6), pp. 666-673.

Shen, M., Luo, J. and Wen, S. (2001) The Tribological Properties of Oils Added with Diamond Nano-Particles. *Tribology Transactions*. 44 (3), pp. 494-498.

Siebert, H. (2011) *Worm Gears - Higher Energy Efficiency and Less Strain on Resources* [online]. Available from: http://www.klueber.com/ecomaXL/files/PDF_Fachartikel_Worm_Gears.pdf [Accessed 06 November 2020].

Siegert, K. and Ulmer, J. (2001) Influencing the Friction in Metal Forming Processes by Superimposing Ultrasonic Waves. *CIRP Annals*. 50 (1), pp. 195-200.

Singh, H., Mutyala, K., Mohseni, H., Scharf, T., Evans, R. and Doll, G. (2015): Tribological Performance and Coating Characteristics of Sputter Deposited Ti Doped MoS₂ in Rolling and Sliding Contact. *Tribology Transactions*. 58 (5), pp. 767-777.

Skåre, T. and Ståhl, J. (1992) Static and dynamic friction processes under the influence of external vibrations. *Wear*. 154 (1), pp. 177-192.

Socoliuc, A., Gnecco, E., Maier, S., Pfeiffer, O., Baratoff, A., Bennewitz, R. and Meyer, E. (2006) Atomic-scale control of friction by actuation of nanometer-sized contacts. *Science*. 313 (5784), pp. 207-210.

Storck, H., Littmann, W., Wallaschek, J. and Mracek, M. (2002) The effect of friction reduction in presence of ultrasonic vibrations and its relevance to travelling wave ultrasonic motors. *Ultrasonics* 40 (1–8): 379-383.

Su, D. and Qin, D. (2003) Integration of numerical analysis, virtual simulation and finite element analysis for the optimum design of worm gearing. *Journal of Materials Processing Technology*. 138 (1-3), pp. 429-435.

Tamura, Y., Zhao, H., Wang, C., Morina, A. and Neville, A. (2016) Interaction of DLC and B₄C coatings with fully formulated oils in boundary lubrication conditions. *Tribology International*. 93, pp. 666-680.

Taylor Hobson®. (2004) HB-103 Surtronic 3+ Operating Instructions.

Tong, R., Han, B., Quan, Z. and Liu, G. (2019) Molecular dynamics simulation of friction and heat properties of Nanotexture GOLD film in space environment. *Surface & Coatings Technology*. 358, pp. 775-784.

Tsukamoto, N., Maruyama, H., Taki, T. and Kato, M. (1990) Characteristics of a Worm Gear of Austempered Ductile Cast Iron. *Transactions of the Japan Society of Mechanical Engineers Series C*. 56 (531), pp. 3000-3004.

Udaykant Jadav, P., Amali, R. and Adetoro, O. (2018a) Analytical friction model for sliding bodies with coupled longitudinal and transverse vibration. *Tribology International*. 126, pp. 240-248.

Udaykant Jadav, P., Amali, R. and Adetoro, O. (2018b) Analytical friction model for sliding bodies with coupled longitudinal and transverse vibration. In: Abdollah, M., ed. *Proceedings of Asia International Conference on Tribology*. Sarawak, Malaysia, 17-20 September 2018. Kuala Lumpur: Malaysian Tribology Society, pp. 129-130.

Wang, Z., Duan, Z., Dong, Y. and Zhang, Y. (2020) Molecular dynamics simulation of lateral ultrasonic excitation in atomic-scale friction. *Materials Research Express*. 7 (1), pp. 1-10.

Wang, D., Mo, J., Wang, X., Ouyang, H. and Zhou, Z. (2018) Experimental and numerical investigations of the piezoelectric energy harvesting via friction-induced vibration. *Energy Conversion and Management*. 171, pp. 1134-1149.

Watanabe, K., Shimizu, Y. and Terada, Y. (2006) *A Study of Worm Gear to Size Reduction and Performance Enhancement for EPS*. Report number: 2006-01-1177. Detroit: SAE International.

Weck, M., Hurasky-Schönwerth, O., Bugiel, C. (2002) Service behaviour of PVD-coated gearing lubricated with biodegradable synthetic ester oils. *Proceedings of the International Conference on Gears, VDI-Berichte NR 1665*. pp. 667-690.

Wriggers, P. (2006) *Computational Contact Mechanics*. 2nd ed. Berlin: Springer-Verlag.

Wu, H., Zhao, J., Cheng, X., Xia, W., He, A., Yun, J., Huang, S., Wang, L., Huang, H., Jiao, S. and Jiang, Z. (2018) Friction and wear characteristics of TiO₂ nano-additive water-based lubricant on ferritic stainless steel. *Tribology International*. 117, pp. 24-38.

Wu, L., Zhao, C., Cao, M. and Han, X. (2021) Effect of ultrasonic and low frequency vibrations on friction coefficient at die radius in deep drawing process. *Journal of Manufacturing Processes*. 71, pp. 56-69.

Xiao, Y., Shi, W., Luo, J. and Liao, Y. (2014) The tribological performance of TiN, WC/C and DLC coatings measured by the four-ball test. *Ceramics International*. 40 (5), pp. 6919-6925.

Xiaochao, L., Chuansong, W., Haoting, Z. and Maoai, C. (2013) Effect of ultrasonic vibration on the friction stir weld quality of aluminium alloy. *China Welding*. 22 (3), pp. 12-17.

Xu, T., Zhao, J. and Xu, K. (1996) The ball-bearing effect of diamond nanoparticles as an oil additive. *Journal of Physics D: Applied Physics*. 29 (11), pp. 2932-2937.

Xu, W., Qin, D. and Shi, W. (2006) Direct digital design and simulation of meshing in worm-gear drive. *Chinese Journal of Mechanical Engineering*. 19 (3), pp. 428-433.

Yang, F., Su, D. and Gentle, C. (2001) Finite element modelling and load share analysis for involute worm gears with localized tooth contact. *Proceedings of the Institution of Mechanical Engineers, Part C: Journal of Mechanical Engineering Science*. 215 (7), pp. 805-816.

Yang, C., Wu, C. and Shi, L. (2018) Analysis of friction reduction effect due to ultrasonic vibration exerted in friction stir welding. *Journal of Manufacturing Processes*. 35, pp. 118-126.

Yazawa, S., Minami, I. and Prakash, B. (2014) Reducing friction and wear of tribological systems through hybrid tribofilm consisting of coating and lubricants. *Lubricants*. 2 (2), pp. 90-112.

Yongliang, L. and Sunkyu, K. (2006) Microstructural and tribological behavior of TiAlN/MoS₂-Ti coatings. *Rare Metals*. 25 (4), pp. 326-330.

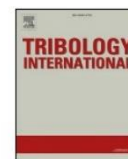
Zahid, R., Hassan, M., Alabdulkarem, A., Varman, M., Mufti, R., Kalam, M., Zulkifli, N., Gulzar, M. and Lee, T. (2017) Investigation of the tribochemical interactions of a tungsten-doped diamond-like carbon coating (W-DLC) with formulated palm trimethylolpropane ester (TMP) and polyalphaolefin (PAO). *RSC Advances*. 7 (43), pp. 26513-26531.

BIBLIOGRAPHY

Zahn, S., Schneider, Y. and Rohm, H. (2006) Ultrasonic cutting of foods: Effects of excitation magnitude and cutting velocity on the reduction of cutting work. *Innovative Food Science & Emerging Technologies*. 7 (4), pp. 288-293.

Zhou, G., Zhu, Y., Wang, X., Xia, M., Zhang, Y. and Ding, H. (2013) Sliding tribological properties of 0.45% carbon steel lubricated with Fe₃O₄ magnetic nano-particle additives in base oil. *Wear*. 301 (1-2), pp. 753-757.

Appendices



Analytical friction model for sliding bodies with coupled longitudinal and transverse vibration



Priyang Udaykant Jadav^{a,c,*}, Ramin Amali^a, Oluwamayokun B. Adetoro^b

^a Department of Engineering Design and Mathematics, University of the West of England, Bristol, BS16 1QY, United Kingdom

^b Department of Mechanical and Aerospace Engineering, Brunel University London, Uxbridge, UB8 3PH, United Kingdom

^c Rotork plc, Bath, BA1 3JQ, United Kingdom

ARTICLE INFO

Keywords:
Friction reduction
In-plane vibration
Modelling
Contact compliance

ABSTRACT

An analytical friction model is developed to calculate the drive force required to slide a body over a surface that is subjected to coupled longitudinal and transverse vibration. Previously, this computation was only possible under either longitudinal or transverse vibration using a separate analytical model for each mode. This paper presents a development of recent research in which it is possible to use a single analytical model, developed in Matlab[®]/Simulink[®], to compute the friction force and drive force during longitudinal, transverse and coupled longitudinal-transverse vibration. The new model is also evaluated numerically by use of a specially developed friction subroutine which can be integrated into any Abaqus[®] dry contact simulation. Results agree very well with those in previously published literature.

1. Introduction

In mechanical systems that involve predominantly dry sliding contacts the efficiency of the system can be significantly improved by reducing the friction force between the rubbing surfaces. This is usually achieved by improving the surface quality of the contacting pair, utilising conventional lubricants [1–3] or those enhanced with nano-particles [4–6], or by applying surface coatings [7,8]. A less typical method of friction reduction and one that has been the subject of theoretical analyses for several decades is the phenomenon of reduced friction force of surfaces when subjected to vibration. Frictional forces may cause undesired vibrations in a system as a result of stick-slip motion at the contact, conversely, many studies [9–25] have shown that imposed vibration can significantly reduce the friction force between two contacting surfaces. In such studies the vibration is applied to the contact by exciting one of the contacting bodies in the normal, longitudinal or transverse direction.

Considerable research has been devoted to exploiting this phenomenon in various manufacturing processes. Jimma et al. [26] found that vibration applied to the deep drawing process enables deeper cups to be formed whilst avoiding cracks in steel drawn parts, Siegert and Ulmer [27] showed that it is possible to further reduce the friction force by having the drawing dies vibrate parallel to the drawing direction at frequencies ranging 20–22 kHz. Egashira et al. [28] utilised vibration whilst drilling micro holes in glass to reduce the cutting force and

extend tool life. In the food industry, vibrating blades are used to reduce friction when cutting through foods [29]. Screws can also be tightened with considerably less torque through an instantaneous reduction in the friction force supplied by vibration.

The first work investigating the influence of vibration on friction dates back to a 1952 study by Baker et al. [9] in which they determined that the coefficient of static friction under the influence of imposed normal vibration can be minimised to almost zero. Experiments by Fridman and Levesque [10] and also by Godfrey [11] showed that pulling a block of mass over a plate vibrating perpendicular to the contact, with increasing vibration amplitude, reduces the static friction coefficient by almost 100%. One of the first attempts to explain friction force reduction due to normal vibration was made by Lenkiewicz [12]; vibrations forced perpendicularly or at an angle to the friction surface generally cause changes in the value of the real contact area, and consequently changes in the value of the friction force. This is in agreement with Hess and Soom [13] who concluded that a temporary debonding of the contact surfaces leads to a reduction in the mean area of contact and a corresponding reduction in friction. In this century, normal vibration applied in custom built pin-on-disk tribometers have shown a decrease in friction coefficient with increasing vibration frequency and amplitude, between both metallic [14] and non-metallic surfaces [15].

In the case of longitudinal vibration conjecture, until recently, has been that the reduction of average friction force occurs as a result of

* Corresponding author. Rotork plc, Bath, BA1 3JQ, United Kingdom.

E-mail addresses: Priyang.Jadav@rotork.com (P. Udaykant Jadav), Ramin2.Amali@uwe.ac.uk (R. Amali), Mayo.Adetoro@brunel.ac.uk (O.B. Adetoro).

<https://doi.org/10.1016/j.triboint.2018.04.018>

Received 5 April 2018; Accepted 16 April 2018

Available online 21 April 2018

0301-679X/ © 2018 Elsevier Ltd. All rights reserved.

cyclic instantaneous changes in the direction of the friction force vector, caused by changes in the sign of relative velocity when the amplitude of vibration velocity is greater than the velocity of sliding motion [16–22]. Gutowski and Leus [23] have shown that this commonly accepted view is erroneous. Reduction of average friction force may also take place without the change in sign of the friction force vector. One of the reasons behind the antiquated view is that in friction force estimations, the simplified static friction models based on the Coulomb model of friction are assumed. In these models the deformation in the contact zone of two surfaces moving in relation to one another is not taken into consideration. This creates significant difficulties in the conduct of simulational analyses due to their insufficient consistency with experimental results. Gutowski and Leus [23] have shown that significantly better results can be achieved by conducting the analyses using dynamic friction models, such as the Dahl or Dupont model in which the real elasto-plastic characteristics of the contact are considered. Analyses carried out with the use of Dahl friction model yield very good agreement between computations and experimental results.

During transverse vibration a variable vector of relative velocity of sliding causes oscillations of the friction force vector around the sliding direction, resulting in a sub-division of this force into two components, one parallel (F_x) and one perpendicular (F_y) to the direction of motion, see Fig. 3c. Consequently, only the parallel component of friction force acts in the direction of motion, resulting in the reduction of driving force F_d required in this direction. Investigations [18–22] based on this mechanism have also shown a large discrepancy between analytical and experimental results since the analytical models are based on the Coulomb friction model. Gutowski and Leus [24] again demonstrated that a much better agreement can be achieved by utilising an analytical model which considers dynamic friction together with dynamic equations of motion, whilst also including terms to describe the compliance of the mechanical drive system.

This paper focuses on the latter two modes of vibration that are tangential to the plane of contact. Tsai and Tseng [25] assumed that tangential vibrations are imposed directly onto the sliding body and analysed the effect on friction force reduction. They used the Dahl friction model [30,31] on a single lumped elastic asperity to investigate the reduction phenomenon. Gutowski and Leus [23,24] on the other hand, applied vibration to the base and assumed that this vibration is transferred to the sliding body. They developed an analytical model for longitudinal vibration and a separate model for transverse vibration, however, a model for coupled longitudinal-transverse vibration does not exist in literature. This paper proposes a new model, based on the approach of Gutowski and Leus [23,24], to describe the changes in friction force and drive force for sliding surfaces subjected to coupled vibration. The previous models [23,24] are used as basis for validating the new model.

There are four objectives of the work presented in this paper; (i) derivation of a mathematical model that can be used to determine quantitative changes in the friction force occurring at the contact between the sliding body and the base which is under the influence of longitudinal, transverse or coupled vibration (ii) simulation of the new model both analytically in Matlab/Simulink* and numerically in Abaqus* (iii) validation of the new model by comparison of results with analogous ones in previous publications (iv) analysis of how the drive force F_d is influenced by different modes of imposed coupled vibration.

2. Model formulation

Dahl [30] discovered that when an external drive force is applied on a static body that is in contact with another, an intermediate motion of one surface over the other occurs before the bodies enter macroscopic relative motion. This intermediate motion is often described as pre-sliding displacement, otherwise termed “elastic slip”, and is the result of real surfaces having asperities that interlock when two surfaces are in

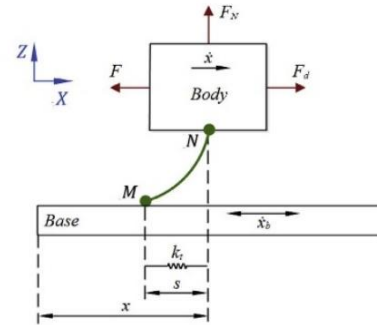


Fig. 1. Elastic strain 's' of contact zone assumed in Dahl's friction model.

contact. The application of external drive force on the body initially creates an elastic deformation of the contacting asperities. As the asperities undergo increased strain, yielding occurs and the two surfaces then start to break free of each other. During this time plastic deformation of asperities takes place. Finally, asperity rupture occurs leading to formation of further surface irregularities which will continuously undergo strain and rupture as sliding takes place [30]. Thus, in Dahl's dynamic friction model it is assumed that the friction force F is associated with the elastic deformation s of the contact (Fig. 1) measured in the direction of sliding:

$$F = k_t s \tag{1}$$

where k_t is the stiffness of the contact in the tangential direction. This is illustrated in Fig. 1 where the deformable contacting asperities of the sliding body and the base are thought of as a single lumped asperity MN.

The force-displacement relationship is modelled by Dahl [31] with the following differential equation:

$$\frac{dF}{dx} = \begin{cases} k_t \left[1 - \frac{F}{F_C} \text{sgn}(\dot{x}) \right]^i & \text{if } i > 0 \\ k_t & \text{if } i = 0 \end{cases} \tag{2}$$

where dF and dx are the incremental friction force and incremental displacement respectively, and \dot{x} is the instantaneous velocity of the body in the direction of sliding. F_C is the magnitude of Coulomb friction force, given by:

$$F_C = \mu F_N \tag{3}$$

where μ is the coefficient of static friction and F_N is the normal reaction force.

The parameter i in equation (2) determines the shape of the relationship between the tangential displacement x and friction force F . $i = 0$ describes brittle material behaviour, where the friction force linearly increases with tangential displacement at a gradient k_t (Fig. 2), until the maximum friction force is reached and the surfaces break away. This maximum force is equal to the Coulomb friction force F_C . As the value of $i \rightarrow 2$ the material behaviour becomes ductile producing a non-linear response of F which is asymptotic to the value of F_C [31]. The value $i = 1$ is used for all computations in this paper.

By substituting (1) and (3) into (2), the relationship can be written in the form of (4), which describes the relationship between the velocity of contact deformation ds/dt and the velocity \dot{x} of the sliding body.

$$\frac{ds}{dt} = \dot{x} \left[1 - \frac{k_t s}{\mu F_N} \text{sgn}(\dot{x}) \right]^i \tag{4}$$

The instantaneous velocity \dot{x} can be thought of as the relative velocity v_r of the sliding body in relation to the base velocity \dot{x}_b (Fig. 1), where:

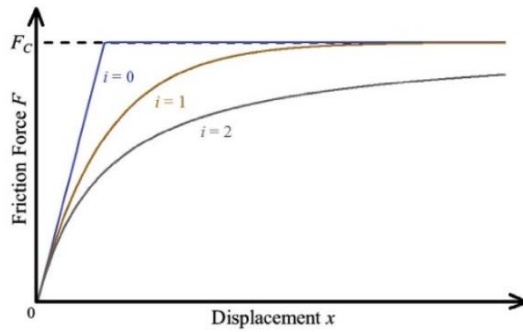


Fig. 2. The effect of parameter i on the relationship between friction force F and displacement x .

$$v_r = \dot{x} - \dot{x}_b = \begin{cases} \dot{x} & \text{if } \dot{x}_b = 0, \text{ i. e. stationary base} \\ v_r & \text{if } \dot{x}_b \neq 0, \text{ i. e. vibrating base} \end{cases} \quad (5)$$

Therefore (4) can be written in a generalised form which takes into account both the non-vibrating and vibrating cases:

$$\frac{ds}{dt} = v_r \left[1 - \frac{k_t s}{\mu F_N} \text{sgn}(v_r) \right] \quad (6)$$

Fig. 1 depicts the case of longitudinal vibration which is a one-dimensional problem; the vibration of the base acts parallel to the direction of sliding of the body therefore deformation s of elastic asperity MN occurs in one dimension. Equation (6) can be readily used in this case.

In transverse, or coupled longitudinal-transverse vibration, the problem becomes two dimensional since the deformation s no longer occurs parallel to the direction of sliding. Equation (6) therefore cannot be readily used in these cases. Gutowski and Leus [24] developed a mathematical model for computing friction force during transverse vibration. In the following work it is shown that the transverse vibration model can be extended for use with longitudinal and coupled longitudinal-transverse vibration.

Mathematical computational procedures were developed assuming the Dahl model in combination with the experimental setup described by Gutowski and Leus [23,24]. Their specially designed test rig comprises a body of known mass m moved over a base that can be vibrated by a piezoelectric element either in the longitudinal or transverse mode. Fig. 3a is a schematic representation of their setup with the assumption,

for the purposes of this paper, that vibration can be applied not only in longitudinal (X) or transverse (Y) mode but can also be coupled so that longitudinal and transverse components act simultaneously and in phase. Mathematically this is equivalent to applying the vibration along an axis that is at an arbitrary angle θ (Fig. 3b) relative to the direction of sliding. Angle θ thus describes the mode of vibration. The displacement of the base during this coupled vibration can be separated into longitudinal and transverse components x_b and y_b respectively.

The movement of mass m over the base is imposed by a constant drive velocity v_d applied at point B (Fig. 3a), while sinusoidal vibration applied to the base is also transferred to the body, corresponding to an instantaneous external drive force F_d . The drive force is transferred to point A of the sliding body via the drive system of which the stiffness coefficient k_d is known and zero structural damping is assumed, hence $h_d = 0$. Endpoint N of the lumped asperity is attached to the sliding body, while the free endpoint M interfaces with the vibrating base. N' is the projection of N on the plane of sliding XY . Relative displacement of points M and N' creates the deformation s of the contact at an angle β measured in the XY plane.

In transverse vibration [24] the motion of the body sliding over the vibrating base is a superposition of two motions; the first caused by the driving force F_d , and the second by the transfer of transverse motion y_b from the base to the sliding body. When coupling longitudinal vibration to the transverse, a third motion must also be superimposed; the motion of the sliding body caused by the transfer of longitudinal motion x_b from the base. All three of these motions influence the magnitude and direction of elastic deformation s of the contact zone. This deformation directly decides the magnitude and direction of the friction force F .

The new model is a development of previous models [23,24] and follows the formulation described by the sequence of equations henceforth using notations presented in Fig. 4. Boxed parameters indicate state variables; their value calculated in the previous increment is carried forward for use in the current increment. During a consecutive time increment Δt , points M and N' change their relative positions thus elastic deformation of the contact undergoes a change in its magnitude and direction from $s(t)$ at the beginning of the increment to $s_1(t + \Delta t)$ at the end of the increment. Coordinates of M and N' , and magnitude of $s(t)$ at the start of the increment are given by:

$$M(t) = [M_x(t), M_y(t)] = \begin{bmatrix} \boxed{M_{1x}} \\ \boxed{M_{1y}} \end{bmatrix} \quad (7)$$

$$N'(t) = [N'_x(t), N'_y(t)] = \begin{bmatrix} \boxed{N_{1x}} \\ \boxed{N_{1y}} \end{bmatrix} = \begin{bmatrix} \boxed{x} \\ \boxed{y} \end{bmatrix} \quad (8)$$

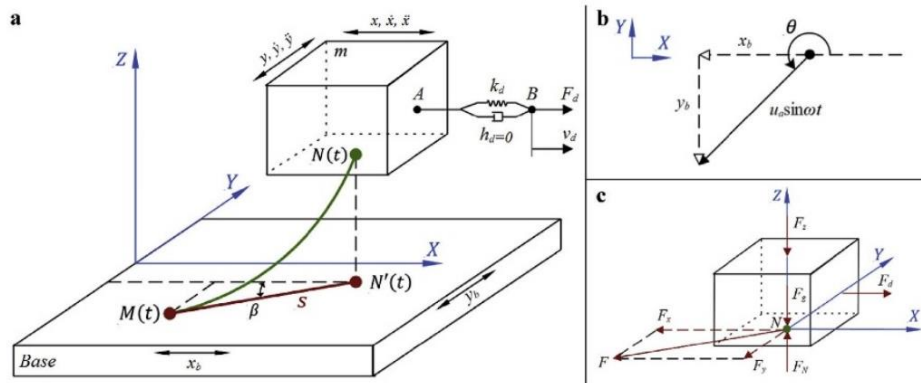


Fig. 3. (a) Contact's elastic deformation modelled as a lumped elastic asperity MN [24] (b) instantaneous displacement vector of base vibrating along an axis at angle θ , separated into components x_b and y_b (c) instantaneous forces acting on sliding body [24].

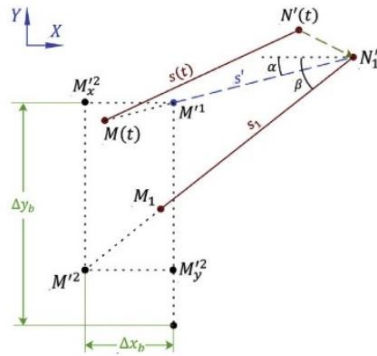


Fig. 4. Change in magnitude and direction of deformation from s to s_1 over a single time increment Δt .

$$s(t) = [s_1] \tag{9}$$

and at the end of the increment by:

$$M(t + \Delta t) = M_1 = [M_{1x}, M_{1y}] \tag{10}$$

$$N'(t + \Delta t) = N'_1 = [N'_{1x}, N'_{1y}] = [x, y] \tag{11}$$

The position of points M and N' at any instance is a result of superposition of the motion caused by the driving force F_d , the base longitudinal vibration component x_b and transverse component y_b . At consecutive instances M and N' change their relative position, thus elastic deformation of the contact undergoes a change in its magnitude and direction from s to s_1 . This change during any consecutive time increment Δt is separated into two phases. In the first phase the intermediate deformation s' is analysed as a result of motion of point N' to N'_1 position. In the second phase the final deformation s_1 is analysed as a result of motion of point M^1 to M^2 position. The displacement from M^1 to M^2 is described by components $M^1M^2_x$ and $M^1M^2_y$. Since N is rigidly connected with the sliding body, its coordinates $[x, y]$ in the XY plane can be described by equations (14) and (16).

$$m\ddot{x} = F_d - F_x \tag{12}$$

$$\Delta x = \iint \frac{F_d - F_x}{m} dt dt - \left[\iint \frac{F_d - F_x}{m} dt dt \right] \tag{13}$$

$$x = \Delta x - [\Delta x_b] + [x] \tag{14}$$

where F_d , F_x and Δx_b are calculated by equations (17), (28) and (38) respectively.

$$m\ddot{y} = F_y \tag{15}$$

$$y = \iint \frac{F_y}{m} dt dt \tag{16}$$

where F_y is calculated by equation (39). F_x and F_y are components of the friction force F acting parallel to the X and Y axes respectively (Fig. 3c). Point B moves at a constant drive velocity v_d whereas the velocity of point A , being rigidly connected to the sliding body, is affected by the transfer of vibrating motion from the base to the body. Due to a continually changing position of point A relative to B , the driving force F_d does not have a constant value. It is a function of the variable elastic deformation of the mechanical drive's components. Assuming the drive system has a linear elastic characteristic, the drive force is calculated by:

$$F_d = k_d[x_B - x_A] = k_d[v_d t - N'_{1x}] \tag{17}$$

where t is time, and $N'_{1x} = x$ is the instantaneous displacement of the sliding body in the X direction, determined by equation (14).

2.1. First phase of motion

During a consecutive time interval Δt , in the first phase of motion, displacement of the sliding body occurs which moves N' to the N'_1 position (Fig. 4). At the same instance, M moves along the path MN'_1 to the M^1 position. Consequently, deformation s changes to an intermediate s' with a new magnitude and direction. Instantaneous direction of this deformation is determined by angle α , whilst the change in its magnitude by an increment Δs [24]. The increment Δs can be evaluated using relationship (6), therefore, the magnitude of deformation s' after this first phase of motion is calculated by:

$$s' = s + \Delta s = [s_1] + v_{r1} \left[1 - \frac{k_c [s_1]}{\mu F_N} \text{sgn}(v_{r1}) \right] \Delta t \tag{18}$$

Relative velocity v_{r1} along the line of action of the lumped elastic asperity can be determined from the following expression:

$$v_{r1} = \frac{MN'_1 - MN'}{\Delta t} = \frac{MN'_1 - s}{\Delta t} = \frac{MN'_1 - [s_1]}{\Delta t} \tag{19}$$

where

$$MN'_1 = \sqrt{[N'_{1x} - M_x(t)]^2 + [M_y(t) - N'_{1y}]^2} \\ = \sqrt{[x - [M_{1x}]]^2 + [[M_{1y}] - y]^2} \tag{20}$$

Direction of v_{r1} in relation to axis X is determined by angle α (Fig. 4) where:

$$\sin \alpha = \begin{cases} \frac{[M_{1y}] - y}{MN'_1} & \text{if } t > t_v \\ 0 & \text{if } t \leq t_v \end{cases} \tag{21}$$

$$\cos \alpha = \begin{cases} \frac{x - [M_{1x}]}{MN'_1} & \text{if } t > t_v \\ 1 & \text{if } t \leq t_v \end{cases} \tag{22}$$

and t_v is the time at which vibration is switched on. The *if* conditions in (21) and (22) are necessary to avoid nan errors in the formulation when $MN'_1 = 0$.

2.2. Second phase of motion

Within the same time increment Δt , in the second phase of motion, in accordance with Fig. 3b, the base undergoes coupled longitudinal-transverse vibration such that the longitudinal component x_b and transverse component y_b act simultaneously and in phase. Mathematically this coupled motion can be treated as vibration applied along an axis that is at an arbitrary angle θ . The instantaneous displacement u of this sinusoidal vibrating motion along the axis of vibration is given by:

$$u = \begin{cases} u_a \sin \omega t & \text{if } t \geq t_v \\ 0 & \text{if } t < t_v \end{cases} \tag{23}$$

where u_a is the amplitude of the displacement of vibration and ω is the angular frequency in rad/s. The above equation acts as a switch that activates the sinusoidal vibration at $t \geq t_v$. The displacement components x_b and y_b in Fig. 3b are thus given by:

$$x_b = u \cos \theta \tag{24}$$

$$y_b = u \sin \theta \tag{25}$$

and the instantaneous velocity v of this sinusoidal motion along the axis of vibration is given by:

$$v = \begin{cases} u_a \omega \cos \omega t & \text{if } t \geq t_v \\ 0 & \text{if } t < t_v \end{cases} \tag{26}$$

where $u_a\omega$ is the amplitude of the velocity of vibration v_a , and hence:
 $v_a = u_a\omega = 2\pi f u_a$ (27)

In longitudinal vibration, where θ is 0° or 180° , only x_b changes direction and y_b remains zero. In transverse vibration, where θ is 90° or 270° , only y_b changes direction and x_b remains zero. During any other mode of vibration, the vector direction of both x_b and y_b will change.

At the beginning of increment Δt the base touches the sliding body at point M . After the lapse of Δt , the base incremental displacements Δx_b and Δy_b (Fig. 4) are:

$$\Delta x_b = x_b - \boxed{x_b} \quad (28)$$

$$\Delta y_b = y_b - \boxed{y_b} \quad (29)$$

The effect of incremental displacement Δx_b is described by (14), whereas the effect of Δy_b by (30). Δy_b is only partially transferred to endpoint M [24], therefore, the displacement $M^1M_y^{22}$ of point M^1 caused by the transverse component of vibrating motion comprises only a part of the incremental displacement Δy_b of the base:

$$\overline{M^1M_y^{22}} = \eta_y \Delta y_b \quad (30)$$

where η_y is the transverse vibration transfer coefficient defining the proportion of Δy_b that is transferred to move the free endpoint from M^1 to the M^2 position. The consequence of this second phase of motion is a further change of asperity deformation from an intermediate s' to final magnitude s_1 (Fig. 4). Instantaneous direction of this deformation is determined by angle β , whilst the change in its magnitude by an increment $\Delta s'$ [24]. In similarity with the previous phase, $\Delta s'$ can be evaluated using relationship (6), therefore, the final magnitude of deformation s_1 after this second phase of motion is calculated by:

$$s_1 = s' + \Delta s' = s' + v_{r2} \left[1 - \frac{k_t s'}{\mu F_N} \text{sgn}(v_{r2}) \right] \Delta t \quad (31)$$

Relative velocity v_{r2} along the new line of action of the lumped elastic asperity can be determined from the following expression:

$$v_{r2} = \frac{N_1^2 M^{r2} - N_1^1 M^{r1}}{\Delta t} = \frac{N_1^1 M^{r2} - s'}{\Delta t} \quad (32)$$

where

$$\begin{aligned} N_1^1 M^{r2} &= \sqrt{[s' \cos \alpha]^2 + [s' \sin \alpha + M^1 M_y^{22}]^2} \\ &= \sqrt{[s' \cos \alpha]^2 + [s' \sin \alpha + \eta_y \Delta y_b]^2} \end{aligned} \quad (33)$$

Direction of v_{r2} in relation to axis X is determined by angle β (Fig. 4) where:

$$\sin \beta = \begin{cases} \frac{s' \sin \alpha + \eta_y \Delta y_b}{N_1^1 M^{r2}} & \text{if } t > t_v \\ 0 & \text{if } t \leq t_v \end{cases} \quad (34)$$

$$\cos \beta = \begin{cases} \frac{s' \cos \alpha}{N_1^1 M^{r2}} & \text{if } t > t_v \\ 1 & \text{if } t \leq t_v \end{cases} \quad (35)$$

The if conditions in (34) and (35) are necessary to avoid nan errors in the formulation when $N_1^1 M^{r2} = 0$. At the end of increment Δt , knowing the magnitude of deformation s_1 and its direction β , as well as coordinates $[x, y]$ of point N_1^1 , it is possible to determine the coordinates of point M_1 at which the endpoint M is placed after lapse of increment Δt :

$$M_{1x} = N_{1x}' - s_1 \cos \beta = x - s_1 \cos \beta \quad (36)$$

$$M_{1y} = N_{1y}' + s_1 \sin \beta = y + s_1 \sin \beta \quad (37)$$

In accordance with relationship (1) and notations per Figs. 3 and 4, an instantaneous value of friction force components F_x and F_y can also

Table 1
State variables.

State variable	Computed during Δt by	Carried forward to Δt_2 for use as
$\iint \frac{F_d - F_x}{m} dt dt$	(13)	$\boxed{\iint \frac{F_d - F_x}{m} dt dt}$ in (13)
x	(14)	\boxed{x} in (8) and (14)
y	(16)	\boxed{y} in (8)
x_b	(24)	$\boxed{x_b}$ in (28)
y_b	(25)	$\boxed{y_b}$ in (29)
Δx_b	(28)	$\boxed{\Delta x_b}$ in (14)
s_1	(31)	$\boxed{s_1}$ in (18) and (19)
M_{1x}	(36)	$\boxed{M_{1x}}$ in (7), (20) and (22)
M_{1y}	(37)	$\boxed{M_{1y}}$ in (7), (20) and (21)

be determined:

$$F_x(t + \Delta t) = k_t s_1 \cos \beta \quad (38)$$

$$F_y(t + \Delta t) = k_t s_1 \sin \beta \quad (39)$$

2.3. Consecutive time increments

The values of state variables listed in Table 1 computed during increment Δt are carried forward to the next consecutive time increment Δt_2 . The sequence of equations (7)–(37) is then repeated to determine the coordinates of point M_2 at which the endpoint M is placed after lapse of time increment Δt_2 . Equations (38) and (39) compute the components of friction force at the end of Δt_2 . At consecutive increments ($3\Delta t, 4\Delta t, \dots, n\Delta t$) the cycle described by these equations is repeated.

3. Methodology

The new model was evaluated by two methods; (i) in the Matlab[®]/Simulink[®] environment an analytical computation procedure was developed with equations (7)–(39) (ii) in Abaqus[®] the three-dimensional domain was numerically simulated by finite element method, with the model implemented via a specially developed friction subroutine defining the tangential contact behaviour between the body and base. The sliding body, Fig. 5, was a cuboid with contact area $0.030 \text{ m} \times 0.040 \text{ m}$ and height 0.053 m , made up of deformable hexahedral elements. The base was a $0.1 \text{ m} \times 0.1 \text{ m}$ analytical rigid shell. The material definition applied to deformable elements had Young's modulus 209 GPa and Poisson's ratio 0.3 . There are two body masses m used in this paper; the density was set to 7850 kg/m^3 for a mass of 0.5 kg , or 31400 kg/m^3 for

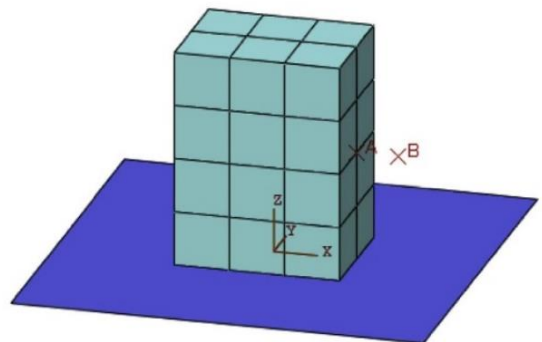


Fig. 5. 3D domain in Abaqus[®].

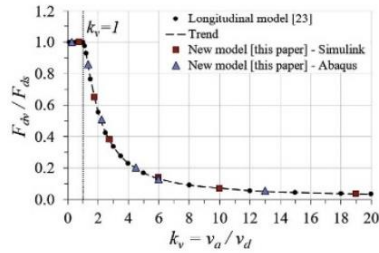


Fig. 6. Change in F_{dv}/F_{db} as k_v increases in longitudinal vibration.

mass 2 kg. A spring element with stiffness k_d was applied between points A and B. A normal pressure load in addition to gravitational load was applied to attain a normal reaction force F_N . The base orientation can be set between $0^\circ \leq \theta < 360^\circ$ in the XY plane, thereby applying any mode of in-plane vibration.

4. Results and discussion

In 4.1 and 4.2, results of longitudinal and transverse vibration are compared with analogous ones accepted in previous literature [23,24] that have shown a good match to experiments. Coupled longitudinal-transverse vibration is then evaluated in 4.3.

4.1. Longitudinal vibration

The longitudinal vibration model accepted in literature [23] was executed with the same parameters as utilised therein; $v_d = 0.0005$ m/s, $m = 0.5$ kg, $f = 4000$ Hz, $\mu = 0.1$, $F_N = 55$ N, $k_t = 80E6$ N/m. The value $k_d = 96068$ N/m was estimated by extracting data from graphs [23] and substituting into relationship (17). The total simulation time was set to 1 s and a fixed time step of $1E-6$ s was utilised with vibration of the base

starting at 0.14 s. Fig. 6 illustrates the computed variability of drive force F_{dv} under the influence of longitudinal vibration in relation to the magnitude F_{db} of this force without vibration as a function of a dimensionless coefficient $k_v = v_a/v_d$. Each data point on the graph corresponds to the result of a single simulation. The data points collectively form a trend indicated by the dashed line.

The new coupled vibration model proposed in this paper was then executed in Matlab[®]/Simulink[®] and Abaqus[®] using the same parameters while varying the value of k_v . To reduce computation effort in Abaqus[®] a larger time step of $1E-5$ s was utilised. The vibration mode was set to longitudinal by setting $\theta = 0^\circ$. Since y_b given by (25) remains zero at $\theta = 0^\circ$, $\overline{M}^T \overline{M}_y^T$ given by (30) also remains zero, therefore, the value of transverse vibration transfer coefficient η_y has no effect on the results of longitudinal vibration. Longitudinal vibration results obtained from the new model are also plotted in Fig. 6 and agree very well with the plotted trend. There is no reduction in drive force due to longitudinal vibration when $k_v \leq 1$.

Changes in drive force F_d and friction force F_x with time, computed using the new model when $k_v = 6$ ($v_a = 0.003$ m/s), are plotted in Fig. 7 and Fig. 8 in comparison to results obtained from the longitudinal vibration model [23]. Simulations begin with the body stationary, hence initially there is no elastic slip at the contact, resulting in $F_d = 0$ N at $t = 0$ s (Fig. 7). Application of constant drive velocity v_d at $t > 0$ s causes elastic deformation s to increase, resulting in a steady rise in F_d until $t \approx 0.12$ s at which time breakaway occurs due to F_d reaching the magnitude of $\mu F_N = 5.5$ N. Switching on vibration at $t = 0.14$ s significantly reduces the magnitude of F_d as the body continues to slide.

Also shown in Fig. 7, the new model when evaluated in Matlab[®]/Simulink[®] produces greater undulation of F_d . This is a characteristic of the new model and is due to the computation of x , equation (14), being different to how x is determined in the longitudinal model [23]. This undulation decreases as the vibration mode θ approaches transverse at 90° and 270° , see Fig. 10. F_{dv} is thus determined by averaging its magnitude within a single vibration cycle:

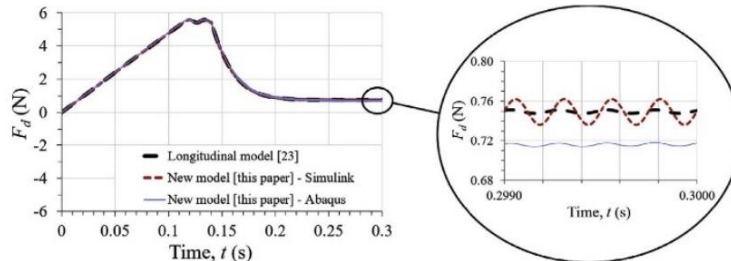


Fig. 7. Comparison of change in F_d when longitudinal vibration is switched on, $k_v = 6$.

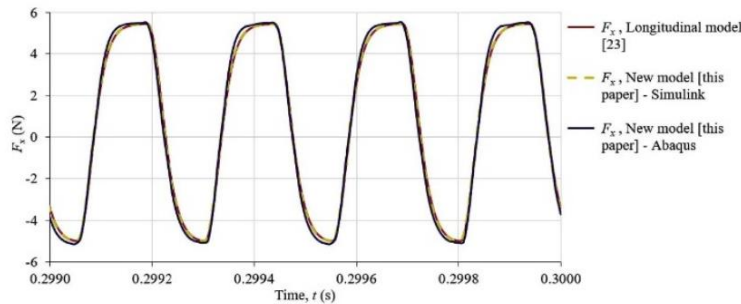


Fig. 8. Comparison of friction force changes during longitudinal vibration, $k_v = 6$.

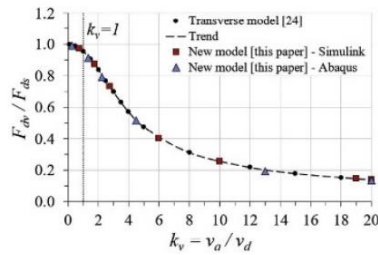


Fig. 9. Change in F_{dv}/F_{dv0} as k_v increases in transverse vibration.

$$F_{dv} = \frac{1}{n} \sum_{i=1}^n F_{dv}(t + \Delta t_i) \quad (40)$$

where n is the number of time intervals into which a single vibration cycle is divided:

$$n = \frac{1}{f\Delta t} \quad (41)$$

At $k_v = 6$ friction force component F_x undergoes cyclic changes in magnitude and direction (Fig. 8), therefore, its average value over a single vibration cycle reduces from $\mu F_N = 5.5$ N when there is no vibration to a lower value when vibration is initiated, hence the drive force is also reduced. Analytical results of the new model obtained via Matlab[®]/Simulink[®] show an exact match of F_x to the longitudinal model [23], however, numerical results from Abaqus[®] show subtle differences. These differences can be attributed to the Abaqus[®] solver which evaluates the model iteratively in each time increment to compute an approximation while enforcing equilibrium of internal structure forces with externally applied loads, whereas Matlab[®]/Simulink[®] performs an analytical calculation that outputs the exact solution to the formulation.

These subtle differences in F_x affect the correlation of the Abaqus[®] computed drive force in Fig. 7, otherwise the new model agrees very well with previous work.

4.2. Transverse vibration

The new coupled model was executed for transverse vibration with parameters matching those utilised in literature [24]; $v_d = 0.0005$ m/s, $m = 2$ kg, $f = 3000$ Hz, $\mu = 0.1$, $F_N = 50.8$ N, $k_t = 67.29E6$ N/m, $k_d = 96068$ N/m. The total simulation time was set to 0.5 s and a fixed time step of 1E-6 s in Matlab[®]/Simulink[®], and 1E-5 s in Abaqus[®], was utilised with vibration of the base starting at 0.14 s. The vibration mode was set to transverse by setting $\theta = 270^\circ$. The transverse vibration transfer coefficient was assumed $\eta_y = 0.71$. This is the value estimated by Gutowski and Leus [24] at which their transverse vibration model produces a good match to results of all experiments carried out at $f = 3000$ Hz in the range $v_d = 0.0001$ – 0.0033 m/s.

Fig. 9 illustrates the variability of normalised drive force F_{dv}/F_{dv0} under the influence of transverse vibration as a function of a dimensionless coefficient k_v , computed using the transverse vibration model [24]. The data points, each corresponding to the result of a single simulation, overlaid in Fig. 9, agree very well with the trend. Unlike longitudinal vibration, in transverse vibration there is reduction of drive force even when $k_v \leq 1$.

Changes in drive force F_d , and friction force components F_x and F_y with time, computed using the new model when $k_v = 20$ ($v_d = 0.010$ m/s), are plotted in Figs. 10 and 11 in comparison to results obtained from the transverse vibration model [24]. Application of constant drive velocity v_d at $t > 0$ s causes elastic deformation s to increase, resulting in a steady rise in F_d until $t \approx 0.11$ s at which time breakaway occurs due to F_d reaching the magnitude of $\mu F_N = 5.08$ N. Switching on vibration at $t = 0.14$ s significantly reduces the magnitude of F_d as the body continues to slide.

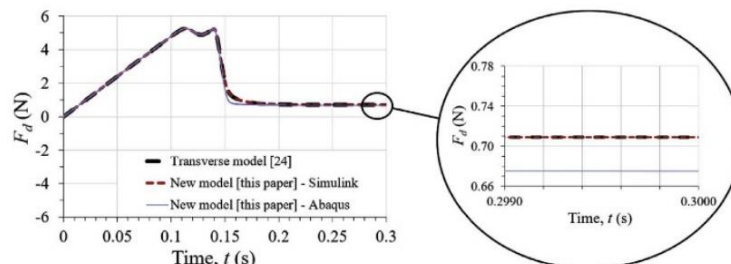


Fig. 10. Comparison of change in F_d when transverse vibration is switched on, $k_v = 20$.

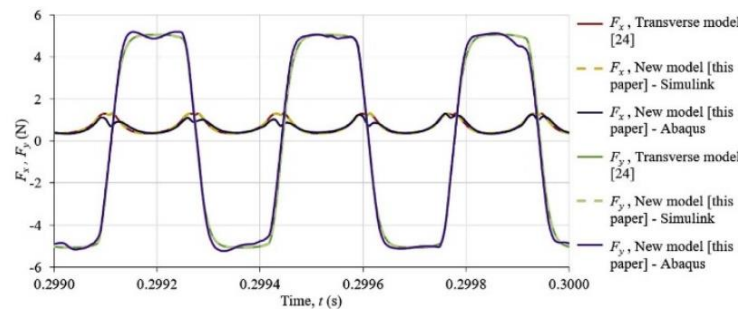


Fig. 11. Comparison of friction force changes during transverse vibration, $k_v = 20$.

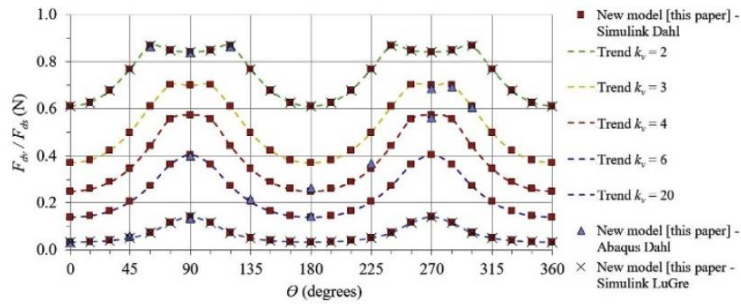


Fig. 12. Changes in F_{dv}/F_{ds} with θ at different values of k_v .

At $k_v = 20$, friction force component F_x undergoes cyclic changes only in magnitude whereas F_y changes in magnitude and direction, Fig. 11. The average value of F_x over a single vibration cycle reduces from $\mu F_N = 5.08$ N when there is no vibration to a lower value when vibration is initiated, hence the drive force is also reduced. Analytical results of the new model obtained via Matlab[®]/Simulink[®] show an exact match to the transverse model [24], and numerical results via Abaqus[®] show subtle differences attributed to the iterative solver.

4.3. Coupled longitudinal-transverse vibration

The new model can also determine the influence of coupled longitudinal-transverse vibration on drive force F_d . Simulations were performed in different vibration modes θ at selected values of k_v (2, 3, 4, 6 and 20) with parameters described in 4.2; $v_d = 0.0005$ m/s, $m = 2$ kg, $f = 3000$ Hz, $\mu = 0.1$, $F_N = 50.8$ N, $k_t = 67.29E6$ N/m, $k_d = 96068$ N/m. The total simulation time was set to 0.5 s and a fixed time step of 1E-6 s in Matlab[®]/Simulink[®], and 1E-5 s in Abaqus[®], was utilised with vibration of the base starting at 0.14 s. At $\eta_y = 0.71$ the transverse vibration model [24] produces a good match to results of all transverse vibration experiments performed at $f = 3000$ Hz in the range $v_y = 0.0001$ – 0.0033 m/s. Since the vibration frequency in the transverse direction will remain 3000 Hz at all vibration modes θ , and v_d is also in the range 0.0001– 0.0033 m/s, it is reasonable to assume $\eta_y = 0.71$ for all vibration modes.

For each selected value of k_v , simulations in 25 different vibration modes θ were performed in Matlab[®]/Simulink[®]. The results in terms of normalised drive force F_{dv}/F_{ds} are plotted in Fig. 12 and the corresponding trend for each value of k_v is also plotted. 3 further simulations for each value of k_v were performed in Abaqus[®] and their results are also overlaid in Fig. 12. Abaqus[®] and Matlab[®]/Simulink[®] results are in good agreement; an increase in k_v results in a decrease in the drive force in all modes of vibration. Regardless of the value of k_v , the greatest reduction in drive force is always achieved by longitudinal vibration ($\theta = 0^\circ, 180^\circ$). During transition from longitudinal to transverse vibration ($\theta = 90^\circ, 270^\circ$), and vice versa, the shape of curve F_{dv}/F_{ds} varies depending on the value of k_v , however, the curve is always symmetrical about $\theta = 180^\circ$. This suggests the same result can be obtained at multiple values of θ .

5. Substituting Dahl with LuGre friction model

The new model is based on friction behaviour per the Dahl model [31], however, it is possible to substitute other dynamic friction models into the formulation, for example, the LuGre friction model [32] which is an extension of the Dahl model and defines the friction force by extending relationship (1) to:

$$F = k_t s + h_t \frac{ds}{dt} + h_v v_r \tag{42}$$

where h_t is the contact damping coefficient, h_v is the viscous damping coefficient, and ds/dt is given by:

$$\frac{ds}{dt} = v_r - \frac{k_t |v_r|}{\mu F_N + (F_S - \mu F_N) e^{-(v_r/v_s)}} s \tag{43}$$

where F_S is the stiction force and v_s is the Stribeck velocity. Equations (18) and (31) are then substituted by (44) and (45):

$$s' = \left[\frac{s_1}{s_1} + \left[v_{r1} - \frac{k_t |v_{r1}|}{\mu F_N + (F_S - \mu F_N) e^{-(v_{r1}/v_s)}} \right] \frac{s_1}{s_1} \right] \Delta t \tag{44}$$

$$s_1 = s' + \left[v_{r2} - \frac{k_t |v_{r2}|}{\mu F_N + (F_S - \mu F_N) e^{-(v_{r2}/v_s)}} \right] s' \Delta t \tag{45}$$

and, (38) and (39) substituted by (46) and (47):

$$F_x(t + \Delta t) = \left[k_t s_1 + h_t \left(\frac{s_1 - [s_1]}{\Delta t} \right) + h_v \left(\frac{N_1' M'^2 - [s_1]}{\Delta t} \right) \right] \cos \beta \tag{46}$$

$$F_y(t + \Delta t) = \left[k_t s_1 + h_t \left(\frac{s_1 - [s_1]}{\Delta t} \right) + h_v \left(\frac{N_1' M'^2 - [s_1]}{\Delta t} \right) \right] \sin \beta \tag{47}$$

Setting $h_t = h_v = F_S = v_s = 0$ in the LuGre model reverts to Dahl friction behaviour. To prove this the LuGre model was implemented into the new coupled vibration model for execution in Matlab[®]/Simulink[®] at $k_v = 2$ and 20. Results using the LuGre model are overlaid in Fig. 12 and show an exact match to those with Dahl friction.

If h_t, h_v, F_S and v_s are non-zero, or if another friction model is used then the value of the transverse vibration transfer coefficient η_y may change since $\eta_y = 0.71$ is based on a fit fidelity exercise performed by Gutowski and Leus [24] to match their model, which is also based on Dahl friction, to experimental data. If the friction model is changed it is advisable to check the fit fidelity of the model to experimental results and use a new value of η_y if necessary.

6. Conclusion

A new analytical model has been developed based on two separate models presented in previous literature [23,24]. The new model is able to describe changes in friction force and drive force during sliding motion of a body over a surface vibrating not only in the longitudinal or transverse mode but also in any mode of coupled longitudinal-transverse vibration. The model has been evaluated analytically in Matlab[®]/Simulink[®] and numerically via a specially developed friction subroutine in Abaqus[®]. Simulations yield good agreement with the models for longitudinal [23] and transverse vibration [24] in previous literature.

The new model can be used in any three-dimensional domain, such as the flat-on-flat contact domain used in this paper where the normal contact pressure has been assumed constant, or a more complex case of gears for example, where the normal contact pressures change as gear

teeth move over one another, while multiple teeth enter and exit the gear mesh forming multiple contacts simultaneously. An advantage with Abaqus[®] is that the complexity of the domain can be increased by modifying the geometry of parts within it and the way in which they interact, whereas in Matlab[®]/Simulink[®] additional relationships would have to be introduced to describe these aspects which may result in time-varying contact geometry. In the case of flat-on-flat contact, the greatest reduction in F_d is achieved by longitudinal vibration, however, friction is in nearly all engineering problems and in other applications a different vibration mode may be more beneficial.

To simulate coupled vibration the value of transverse vibration transfer coefficient η_y must be known and can be estimated using transverse vibration experimental data with the method described by Gutowski and Leus [24]. It is assumed that η_y does not change in value as vibration mode θ changes. The new model can then be used to compute changes in friction force and drive force in any mode of in-plane vibration. The longitudinal model and transverse model have previously been validated against experiments [23,24] and have been used in this paper as basis for validating the new model, however, experimental results for coupled vibration are not currently available. This provides scope for future work. Also, the influence on η_y of using dynamic friction models other than the Dahl model is currently unknown.

References

- [1] Hargreaves DJ, Planitz A. Assessing the energy efficiency of gear oils via the FZG test machine. *Tribol Int* 2009;42(6):918–25.
- [2] Marques PMT, Fernandes CMCG, Martins RC, Seabra JHO. Efficiency of a gearbox lubricated with wind turbine gear oils. *Tribol Int* 2013;71:7–16.
- [3] Cardoso NFR, Martins RC, Seabra JHO, Igartua A, Rodríguez JC, Luther R. Micropitting performance of nitrided steel gears lubricated with mineral and ester oils. *Tribol Int* 2009;42(1):77–87.
- [4] Shen M, Luo J, Wen S. The tribological properties of oils added with diamond nanoparticles. *Tribol Trans* 2001;44(3):494–8.
- [5] Chu HY, Hsu WC, Lin JF. The anti-scuffing performance of diamond nano-particles as an oil additive. *Wear* 2010;268(7):960–7.
- [6] Zhou G, Zhu Y, Wang X, Xia M, Zhang Y, Ding H. Sliding tribological properties of 0.45% carbon steel lubricated with Fe₃O₄ magnetic nano-particle additives in base oil. *Wear* 2013;301(1–2):753–7.
- [7] Moorthy V, Shaw BA. Contact fatigue performance of helical gears with surface coatings. *Wear* 2012;276–277:130–40.
- [8] Xiao Y, Shi W, Luo J, Liao Y. The tribological performance of TiN, WC/C and DLC coatings measured by the four-ball test. *Ceram Int* 2013;40(5):6919–25.
- [9] Baker HD, Claypoole W, Fuller DD. Proceedings of the first US national congress of applied mechanics. 1952. p. 23.
- [10] Fridman HD, Levesque P. Reduction of static friction by sonic vibrations. *J Appl Phys* 1959;30(10):1572–5.
- [11] Godfrey D. Vibration reduces metal to metal contact and causes an apparent reduction in friction. *Tribol Trans* 1967;10(2):183–92.
- [12] Lenkiewicz W. The sliding friction process-effect of external vibrations. *Wear* 1969;13(2):99–108.
- [13] Hess DP, Soom A. Normal vibration and friction under harmonic loads: Part I - Hertzian contacts. *J Tribol* 1991;113(1):80–6.
- [14] Abdo J, Tahat M. The effect of frequency and amplitude of vibration on the coefficient of friction for metals. *WSEAS Trans Appl Theor Mech* 2008;3(7):265–74.
- [15] Chowdhury MA, Helali MM. The effect of amplitude of vibration on the coefficient of friction for different materials. *Tribol Int* 2008;41(4):307–14.
- [16] Mitskevich AM. Motion of the body over tangentially vibrating surface taking account of friction. *Sov Phys Acoust* 1968;13(3):343–51.
- [17] Skare T, Stahl JE. Static and dynamic friction processes under the influence of external vibrations. *Wear* 1992;154(1):177–92.
- [18] Mutuanga S, Onoda J. New gravity compensation method by dither for low-g simulation. *J Spacecraft Rockets* 1995;32(2):364–9.
- [19] Littmann W, Storck H, Wallaschek J. Sliding friction in the presence of ultrasonic oscillations: superposition of longitudinal oscillations. *Arch Appl Mech* 2001;71(8):549–54.
- [20] Littmann W, Storck H, Wallaschek J. Reduction of friction using piezoelectrically excited ultrasonic vibrations. *Proceedings of SPIE - The International Society for Optical Engineering* 2001;4331:302–11.
- [21] Storck H, Littmann W, Wallaschek J, Mracek M. The effect of friction reduction in presence of ultrasonic vibrations and its relevance to travelling wave ultrasonic motors. *Ultrasonics* 2002;40(1–8):379–83.
- [22] Kumar VC, Hutchings IM. Reduction of sliding friction of metals by the application of longitudinal or transverse ultrasonic vibration. *Tribol Int* 2004;37(10):833–40.
- [23] Gutowski P, Leus M. The effect of longitudinal tangential vibrations on friction and driving forces in sliding motion. *Tribol Int* 2012;55(6):108–18.
- [24] Gutowski P, Leus M. Computational model for friction force estimation in sliding motion at transverse tangential vibrations of elastic contact support. *Tribol Int* 2015;90:455–62.
- [25] Tsai CC, Tseng CH. The effect of friction reduction in the presence of in-plane vibrations. *Arch Appl Mech* 2006;75(2):164–76.
- [26] Jimma T, Kasuga Y, Iwaki N, Miyazawa O, Mori E, Ito K, Hatano H. An application of ultrasonic vibration to the deep drawing process. *J Mater Process Technol* 1998;80–81:406–12.
- [27] Stegert K, Ulmer J. Influencing the friction in metal forming processes by superimposing ultrasonic waves. *CIRP Ann - Manuf Technol* 2001;50(1):195–200.
- [28] Egashira K, Mizutani K, Nagoa T. Ultrasonic vibration drilling of microholes in glass. *CIRP Ann - Manuf Technol* 2002;51(1):339–42.
- [29] Schneider Y, Zahn S, Schindler C, Rohm H. Ultrasonic excitation affects friction interactions between food materials and cutting tools. *Ultrasonics* 2009;49(6–7):588–93.
- [30] Dahl PA. Solid friction model. Technical report TOR-0158H3107-181-1. El Segundo, CA: The Aerospace Corporation; 1968.
- [31] Dahl P. Solid friction damping of mechanical vibrations. *AIAA J* 1976;14(12):1675–82.
- [32] Canudas de Wit C, Olsson H, Astrom KJ, Lischinsky P. A new model for control of systems with friction. *IEEE Trans Automat Contr* 1995;40(3):419–25.

Appendix B: Conference Article

Proceedings of Asia International Conference on Tribology 2018, pp. 129-130, September 2018

Analytical friction model for sliding bodies with coupled longitudinal and transverse vibration

P. Udaykant Jadav^{1,3,*}, R. Amali¹, O.B. Adetoro²

¹) Department of Engineering Design and Mathematics, University of the West of England, Bristol, BS16 1QY, United Kingdom.

²) Department of Mechanical and Aerospace Engineering, Brunel University London, Uxbridge, UB8 3PH, United Kingdom.

³) Rotork Controls Ltd., Bath, BA1 3JQ, United Kingdom.

*Corresponding e-mail: Priyang.Jadav@rotork.com

Keywords: Friction; vibration; modelling

ABSTRACT – An analytical friction model is developed to compute the drive force required to slide a body over a surface subjected to coupled longitudinal and transverse vibration. Previously, this computation was only possible under either longitudinal or transverse vibration using a separate analytical model for each mode. The model proposed in this paper is applied to longitudinal, transverse, and coupled vibration modes. Results are in good agreement with existing literature. Analytical results are replicated numerically by use of a specially developed friction subroutine which can be integrated into any Abaqus® dry contact simulation.

1. INTRODUCTION

The efficiency of mechanical systems that involve predominantly dry sliding contacts can be significantly improved by friction reduction via the use of conventional lubricants or surface coatings. A less typical method, and one that has been the subject of theoretical analyses for several decades, is the phenomenon of reduced friction force of surfaces when subjected to vibration. In such studies vibration is applied by exciting one of the contacting bodies either in the longitudinal [1], transverse [2] or normal [3] direction.

In recent research Gutowski and Leus [1-2] have shown that good agreement between analytical and experimental results can be achieved by utilising models that have dynamic equations of motion, while also including terms to describe compliance of both the contact and the drive system. A model for longitudinal vibration and a separate model for transverse vibration were developed [1-2], however, a model for coupled longitudinal and transverse vibration does not exist in literature. This paper proposes a new friction model to describe changes in friction force and drive force for sliding surfaces subjected to coupled longitudinal and transverse vibration. The new model is validated against previous models [1-2] that have shown good agreement with experiments.

2. METHODOLOGY

The domain, Figure 1, consists of a body of known mass m moved over a base that can be oscillated sinusoidally such that the longitudinal and transverse components of motion, x_b and y_b , act simultaneously and in phase. Mathematically this coupled motion can

be treated as vibration applied along an axis which is at angle θ relative to direction X , Figure 2. Movement of mass m over the base is imposed by a constant drive velocity v_d applied at point B , while vibration of the base is also transferred to the body. This corresponds to an instantaneous external drive force F_d that is transferred to point A of the body via a mechanical drive system of which the stiffness k_d is known. No structural damping of the drive system is assumed, hence $h_d = 0$.

Contact compliance is included by assuming Dahl friction behaviour [4]. The deformable contacting asperities of the sliding body and base are modelled as a single lumped asperity MN . Endpoint N is attached to the sliding body, while the free endpoint M interfaces with the vibrating base. During vibration, change in relative displacement of M and N creates change in magnitude s and direction β of the contact's elastic deformation. This causes changes in the friction force between the two bodies.

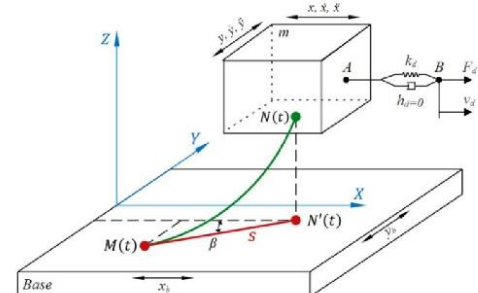


Figure 1 Schematic of domain [2] showing coupled vibration with base motion components x_b and y_b

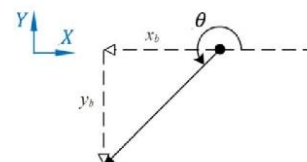


Figure 2 Mode of vibration defined by angle θ .

The new analytical model is a development of previous models [1-2] and is described by a mathematical computational procedure developed in Matlab®/Simulink®. The model enables computation of

F_d under different conditions, with the variable inputs being mass m , drive velocity v_d , amplitude of vibration velocity v_a , vibration frequency f , contact normal force F_N , coefficient of friction μ , contact stiffness k_t , drive system stiffness k_d , and angle θ .

The same domain has also been generated by finite element method in Abaqus® and the new model has been implemented via a specially developed friction subroutine. The base orientation can be set between $0^\circ \leq \theta < 360^\circ$ in the XY plane to apply vibration in any mode.

3. RESULTS AND DISCUSSION

Results of the new model when set to longitudinal vibration mode, $\theta = 0^\circ$, are plotted in Figure 3, and with transverse vibration mode, $\theta = 90^\circ$, in Figure 4. Results of previous models are overlaid for validation. Simulations begin with the body stationary, hence $F_d = 0N$ at $t = 0s$. Constant drive velocity v_d at $t > 0s$ causes elastic deformation s to increase, resulting in steady rise of F_d until $t \approx 0.04s$. At this time the magnitude of F_d is large enough to cause the body to breakaway. At $t = 0.05s$, switching on vibration significantly reduces the magnitude of F_d as the body continues to slide.

A characteristic of the new model when evaluated in Matlab®/Simulink® is that it produces a continuous small undulation of F_d in longitudinal mode (Figure 3). The undulation diminishes as vibration mode approaches transverse, Figure 4.

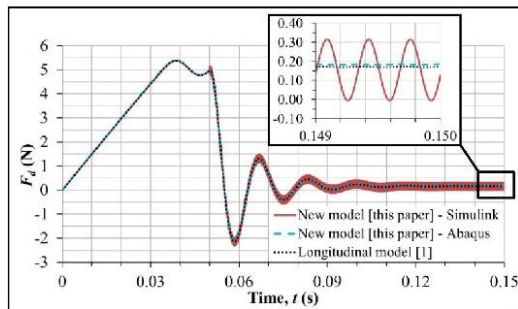


Figure 3 Validation of longitudinal vibration results.

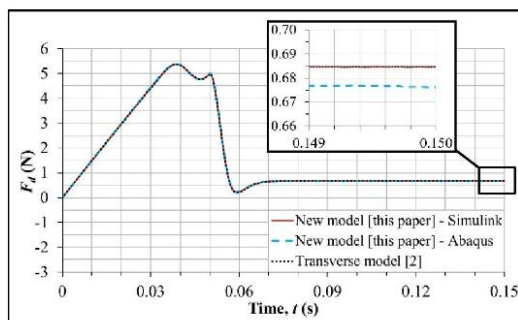


Figure 4 Validation of transverse vibration results.

Further simulations in Abaqus®, Figure 5, illustrate the influence of θ and k_v on F_{dv} / F_{ds} , where $k_v = v_a/v_d$, and F_{dv} / F_{ds} is the drive force under vibration in relation to drive force without vibration.

Each data point in Figure 5 corresponds to the result of a single simulation. For each value of k_v , seven simulation results in the range $0^\circ \leq \theta \leq 90^\circ$ allow a trend to be established. Trends for different values of k_v are indicated by dashed lines. A reduced number of simulations at $\theta > 90^\circ$ agree with the expected trends. Increasing k_v decreases the drive force in all vibration modes. The greatest reduction in drive force is always achieved by longitudinal vibration ($\theta = 0^\circ, 180^\circ$) and the curve is always symmetrical about $\theta = 180^\circ$. The same result can thus be obtained at multiple values of θ .

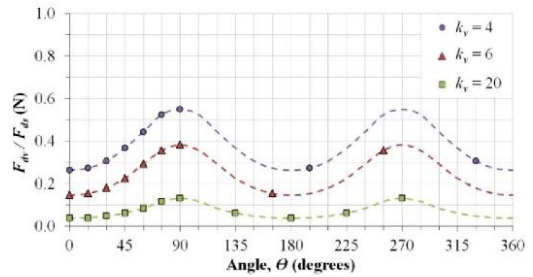


Figure 5 Influence of θ and k_v on F_{dv} / F_{ds} .

4. CONCLUSIONS

An analytical model has been developed that is able to describe changes in friction force and drive force during sliding motion of a body over an in-plane vibrating surface. The new model has been validated against existing models for longitudinal and transverse vibration, and can also be used to simulate any mode of coupled vibration.

The model can be used in any three-dimensional domain, such as the flat-on-flat contact domain used in this paper where the normal contact pressure has been assumed constant, or a more complex case of gears for example, where the normal contact pressures change as gear teeth move over one another, while multiple teeth enter and exit the gear mesh to form multiple contacts simultaneously. In the case of flat-on-flat contact, the greatest reduction in F_d is achieved by longitudinal vibration, however, friction is in nearly all engineering problems and in other applications a different mode of vibration may be more beneficial.

REFERENCES

[1] Gutowski, P., & Leus, M. (2012). The effect of longitudinal tangential vibrations on friction and driving forces in sliding motion. *Tribology International*, 55(6), 108-118.
 [2] Gutowski, P., & Leus, M. (2015). Computational model for friction force estimation in sliding motion at transverse tangential vibrations of elastic contact support. *Tribology International*, 90, 455-462.
 [3] Chowdhury, M., Helali, M. (2008). The effect of amplitude of vibration on the coefficient of friction for different materials. *Tribology International*, 41(4), 307-314.
 [4] Dahl, P. (1976). Solid friction damping of mechanical vibrations. *ALAA Journal*, 14(12), 1675-1682.

Appendix C: Theoretical Calculations of Worm Gearsets

Gearset 1

PD ISO/TR 14521 (British Standards Institution, 2011)					BS 721 (British Standards Institution, 1983)				
Parameter	Symbol	Value	Unit	Notes	Parameter	Symbol	Value	Unit	Notes
3	Normal pressure angle	α_n		deg	Speed factor for wear on worm	$X_{c,1}$			Per BS721, Figure 7
4	Centre distance	c		mm	Speed factor for wear on wheel	$X_{c,2}$			Per BS721, Figure 7
5	Gear ratio	U			Surface stress factor on worm	$\sigma_{cm,1}$			Per BS721, Table 7
6	Number of starts on worm	z_1			Surface stress factor on wheel	$\sigma_{cm,2}$			Per BS721, Table 7
7	Number of teeth on wheel	z_2			Zone factor	Z			Per BS721, Table 6
8	Diameter factor	q_1			Permissible wheel torque for wear (a)	M_{wa}	41.92	Nm	
9	Worm lead angle	Y_{m1}		deg	Permissible wheel torque for wear (b)	M_{wb}	29.36	Nm	
10	Max addendum modification coefficient	$x_{2,max}$			Permissible wheel torque for wear based on 26000 hr life	M_{wear}	29.36	Nm	Lowest of the two values M_{wa} and M_{wb}
11	Min addendum modification coefficient	$x_{2,min}$			Speed factor for strength on worm	$X_{b,1}$			Per BS721, Figure 8
12	Maximum axial module	m_{max}		mm	Speed factor for strength on wheel	$X_{b,2}$			Per BS721, Figure 8
13	Minimum axial module	m_{min}		mm	Bending stress factor on worm	$\sigma_{bm,1}$			Per BS721, Table 7
14	Axial module	m_{x1}		mm	Bending stress factor on wheel	$\sigma_{bm,2}$			Per BS721, Table 7
15	Axial pitch	p_{x1}		mm	Worm tooth reference addendum in axial section	h_{am1}		mm	
16	Worm reference diameter	d_{m1}		mm	Worm tip diameter	d_{a1}		mm	
17	Wheel reference diameter	d_{m2}		mm	Maximum clearance	c_{max}		mm	
18	Worm speed	n_1		RPM	Wheel effective face width	b_e		mm	
19	Wheel speed	n_2		RPM	Length of root of wheel teeth	$l_{f,2}$		mm	
20	Sliding velocity at worm reference diameter	v_g		m/s	Permissible wheel torque for strength (a)	M_{sa}	93.25	Nm	
21	Size factor	Y_s			Permissible wheel torque for strength (b)	M_{sb}	37.94	Nm	
22	Profile shift coefficient	x_2			Permissible wheel torque for strength based on 26000 hr life	$M_{strength}$	37.94	Nm	Lowest of the two values M_{sa} and M_{sb}
23	Kinematic viscosity at 40°C	ν_{40}		mm ² /s Per lubricant data	Permissible wheel torque based on 26,000 hours life	M_{26k}	29	Nm	Lowest of the two values M_{wear} and $M_{strength}$
24	Kinematic viscosity at 100°C	ν_{100}		mm ² /s Per lubricant data	Total equivalent running time for wear (500,000 cycles)	H_{ec}	173.61	hr	Based on 500,000 cycles wear life
25	Coefficient for kinematic viscosity	A			Permissible wheel torque for wear based on 500,000 cycles	M_w	83	Nm	Based on 500,000 cycles wear life
26	Coefficient for kinematic viscosity	B			Total equivalent running time for strength	H_{eb}	17.36	hr	Based on 1/10 of H_{ec}
27	Mean lubricant film thickness parameter	h^*			Permissible wheel torque for strength	M_s	75	Nm	
28	Geometry factor	Y_G			Safety factor at rated torque based on strength	$FoS_{strength}$	2.21		
29	Material factor	Y_W		Per PD ISO/TR 14521, Table 6	Safety factor at 1/3 rated torque based on wear	FoS_{wear}	7.37		
30	Arithmetic mean roughness	Ra_1		µm					
31	Roughness factor	Y_R							
32	Coefficient of friction	μ		In mineral oil					
33	Mean tooth coefficient of friction	μ_{zm}							
34	Worm gearing efficiency	η_{z1-2}	41	%					
35	Rated torque of valve actuator	T_R		Nm					
36	Wheel through-travel output torque	T_2		Nm	Based on 1/3 of T_R				
37	Meshing power loss	P_{vz1-2}		W					
38	Idle running power loss	P_{v0}		W					
39	Output power from wheel shaft	P_2		W					
40	Bearing power loss	P_{VLP}		W					
41	Sealing power loss	P_{VD}		W					
42	Total power loss	P_V		W					
43	Total efficiency of system	η_{ges1-2}	28	%					

	M	N	O	P	Q
1	AGMA 6034-B92 (American Gear Manufacturers Association, 1992; Budynas and Nisbett, 2011)				
2	Parameter	Symbol	Value	Unit	Notes
3	Transverse pressure angle	ϕ_t		deg	
4	Wheel pitch diameter	d_G		inch	
5	Wheel pitch line velocity	V_G		ft/min	
6	Sliding velocity	V_S		ft/min	Budynas and Nisbett (2011), Equation 15-30, pp. 810
7	Wheel face width	F		inch	
8	Wheel effective face width	F_e		inch	
9	Lewis form factor	y			Budynas and Nisbett (2011), pp. 812, for $\alpha_n = 20^\circ$
10	Transverse diametral pitch of wheel	P_d		teeth/inch	
11	Normal diametral pitch of wheel	P_n		teeth/inch	
12	Normal circular pitch of wheel	p_n		inch	
13	Size factor	K_s			Budynas and Nisbett (2011), Section 14-10, pp. 759
14	Application overload factor	K_o			Budynas and Nisbett (2011), Figure 14-17, pp. 766
15	AGMA quality number	Q_v			3-7 for commercial gears, 8-12 for precision quality.
16	Variable A for dynamic factor calculation	A_{Kv}			Budynas and Nisbett (2011), Equation 14-28, pp. 756
17	Variable B for dynamic factor calculation	B_{Kv}			Budynas and Nisbett (2011), Equation 14-28, pp. 756
18	Dynamic factor	K_v			Budynas and Nisbett (2011), Equation 14-27, pp. 756
19	Load correction factor	C_{mc}			Budynas and Nisbett (2011), pp. 760, for crowned teeth.
20	Pinion proportion factor	C_{pf}			Budynas and Nisbett (2011), Equation 14-32, pp. 760
21	Pinion proportion modifier	C_{pm}			Budynas and Nisbett (2011), pp. 760
22	Mesh alignment factor	C_{ma}			Budynas and Nisbett (2011), Equation 14-34, pp. 760
23	Mesh alignment correction factor	C_e			Budynas and Nisbett (2011), pp. 760
24	Load distribution factor	K_m			Budynas and Nisbett (2011), Equation 14-30, pp. 759
25	Design factor	n_d			Assumed 1. For unquantifiable exigencies factor is > 1 .
26	Output horsepower at rated torque	H_0		hp	
27	Coefficient of friction	μ_{AGMA}			
28	Worm gearing efficiency	η_{AGMA}	78	%	Budynas and Nisbett (2011), Equation 15-54, pp. 813
29	Tangential force on wheel tooth at rated torque	W_G^t		lb	
30	Wheel bending stress at rated torque T_R	σ_a	256	N/mm²	Budynas and Nisbett (2011), Equation 15-53, pp. 812
31	Elastic coefficient	C_p		lb/in ²	Budynas and Nisbett (2011), Table 14-8, pp. 757
32	Surface condition factor	C_f			Assumed 1. For detrimental surface finish factor is > 1 .
33	Geometry factor for pitting resistance	I			Budynas and Nisbett (2011), Equation 14-23, pp. 755
34	Wheel contact stress at through-travel torque T_2	σ_c	349	N/mm²	Budynas and Nisbett (2011), Equation 14-16, pp. 746
35	Materials factor	C_s			
36	Ratio correction factor	C_m			
37	Velocity factor	C_v			
38	Allowable tangential force on wheel tooth	$W_{G,all}^t$		lb	
39	Allowable wheel torque based on 25000 hours life	$T_{G,all}$	51	Nm	Budynas and Nisbett (2011), Equation 15-31, pp. 810
40					
41					
42					
43					

Gearset 2

PD ISO/TR 14521 (British Standards Institution, 2011)					BS 721 (British Standards Institution, 1983)							
1	A	B	C	D	E	F	G	H	I	J	K	L
2	Parameter	Symbol	Value	Unit	Notes	Parameter	Symbol	Value	Unit	Notes		
3	Normal pressure angle	α_n		deg		Speed factor for wear on worm	$X_{c,1}$				Per BS721, Figure 7	
4	Centre distance	c		mm		Speed factor for wear on wheel	$X_{c,2}$				Per BS721, Figure 7	
5	Gear ratio	U				Surface stress factor on worm	$\sigma_{cm,1}$				Per BS721, Table 7	
6	Number of starts on worm	z_1				Surface stress factor on wheel	$\sigma_{cm,2}$				Per BS721, Table 7	
7	Number of teeth on wheel	z_2				Zone factor	Z				Per BS721, Table 6	
8	Diameter factor	q_1				Permissible wheel torque for wear (a)	M_{wa}	114.45	Nm			
9	Worm lead angle	Y_{m1}		deg		Permissible wheel torque for wear (b)	M_{wb}	87.75	Nm			
10	Max addendum modification coefficient	$x_{2,max}$			Per BS721, Figure 5	Permissible wheel torque for wear based on 26000 hr life	M_{wear}	87.75	Nm		Lowest of the two values M_{wa} and M_{wb}	
11	Min addendum modification coefficient	$x_{2,min}$			Per BS721, Figure 6	Speed factor for strength on worm	$X_{b,1}$				Per BS721, Figure 8	
12	Maximum axial module	m_{max}		mm		Speed factor for strength on wheel	$X_{b,2}$				Per BS721, Figure 8	
13	Minimum axial module	m_{min}		mm		Bending stress factor on worm	$\sigma_{bm,1}$				Per BS721, Table 7	
14	Axial module	m_{x1}		mm		Bending stress factor on wheel	$\sigma_{bm,2}$				Per BS721, Table 7	
15	Axial pitch	p_{x1}		mm		Worm tooth reference addendum in axial section	h_{am1}		mm			
16	Worm reference diameter	d_{m1}		mm		Worm tip diameter	d_{a1}		mm			
17	Wheel reference diameter	d_{m2}		mm		Maximum clearance	c_{max}		mm			
18	Worm speed	n_1		RPM		Wheel effective face width	b_e		mm			
19	Wheel speed	n_2		RPM		Length of root of wheel teeth	$l_{f,2}$		mm			
20	Sliding velocity at worm reference diameter	v_g		m/s		Permissible wheel torque for strength (a)	M_{sa}	296.48	Nm			
21	Size factor	Y_S				Permissible wheel torque for strength (b)	M_{sb}	133.76	Nm			
22	Profile shift coefficient	x_2				Permissible wheel torque for strength based on 26000 hr life	$M_{strength}$	133.76	Nm		Lowest of the two values M_{sa} and M_{sb}	
23	Kinematic viscosity at 40°C	ν_{40}		mm ² /s	Per lubricant data	Permissible wheel torque based on 26,000 hours life	M_{26k}	88	Nm		Lowest of the two values M_{wear} and $M_{strength}$	
24	Kinematic viscosity at 100°C	ν_{100}		mm ² /s	Per lubricant data	Total equivalent running time for wear (500,000 cycles)	H_{ec}	347.22	hr		Based on 500,000 cycles wear life	
25	Coefficient for kinematic viscosity	A				Permissible wheel torque for wear based on 500,000 cycles	M_w	238	Nm		Based on 500,000 cycles wear life	
26	Coefficient for kinematic viscosity	B				Total equivalent running time for strength	H_{eb}	34.72	hr		Based on 1/10 of H_{ec}	
27	Mean lubricant film thickness parameter	h^*				Permissible wheel torque for strength	M_s	262	Nm			
28	Geometry factor	Y_G				Safety factor at rated torque based on strength	$FoS_{strength}$	1.29				
29	Material factor	Y_W			Per PD ISO/TR 14521, Table 6	Safety factor at 1/3 rated torque based on wear	FoS_{wear}	3.52				
30	Arithmetic mean roughness	Ra_1		µm								
31	Roughness factor	Y_R										
32	Coefficient of friction	μ			In mineral oil							
33	Mean tooth coefficient of friction	μ_{zm}										
34	Worm gearing efficiency	η_{z1-2}	38	%								
35	Rated torque of valve actuator	T_R		Nm								
36	Wheel through-travel output torque	T_2		Nm	Based on 1/3 of T_R							
37	Meshing power loss	P_{Vz1-2}		W								
38	Idle running power loss	P_{V0}		W								
39	Output power from wheel shaft	P_2		W								
40	Bearing power loss	P_{VLP}		W								
41	Sealing power loss	P_{VD}		W								
42	Total power loss	P_V		W								
43	Total efficiency of system	η_{ges1-2}	31	%								

	M	N	O	P	Q
1	AGMA 6034-B92 (American Gear Manufacturers Association, 1992; Budynas and Nisbett, 2011)				
2	Parameter	Symbol	Value	Unit	Notes
3	Transverse pressure angle	ϕ_t		deg	
4	Wheel pitch diameter	d_G		inch	
5	Wheel pitch line velocity	V_G		ft/min	
6	Sliding velocity	V_S		ft/min	Budynas and Nisbett (2011), Equation 15-30, pp. 810
7	Wheel face width	F		inch	
8	Wheel effective face width	F_e		inch	
9	Lewis form factor	y			Budynas and Nisbett (2011), pp. 812, for $\alpha_n = 20^\circ$
10	Transverse diametral pitch of wheel	P_d		teeth/inch	
11	Normal diametral pitch of wheel	P_n		teeth/inch	
12	Normal circular pitch of wheel	p_n		inch	
13	Size factor	K_s			Budynas and Nisbett (2011), Section 14-10, pp. 759
14	Application overload factor	K_o			Budynas and Nisbett (2011), Figure 14-17, pp. 766
15	AGMA quality number	Q_v			3-7 for commercial gears, 8-12 for precision quality.
16	Variable A for dynamic factor calculation	A_{Kv}			Budynas and Nisbett (2011), Equation 14-28, pp. 756
17	Variable B for dynamic factor calculation	B_{Kv}			Budynas and Nisbett (2011), Equation 14-28, pp. 756
18	Dynamic factor	K_v			Budynas and Nisbett (2011), Equation 14-27, pp. 756
19	Load correction factor	C_{mc}			Budynas and Nisbett (2011), pp. 760, for crowned teeth.
20	Pinion proportion factor	C_{pf}			Budynas and Nisbett (2011), Equation 14-32, pp. 760
21	Pinion proportion modifier	C_{pm}			Budynas and Nisbett (2011), pp. 760
22	Mesh alignment factor	C_{ma}			Budynas and Nisbett (2011), Equation 14-34, pp. 760
23	Mesh alignment correction factor	C_e			Budynas and Nisbett (2011), pp. 760
24	Load distribution factor	K_m			Budynas and Nisbett (2011), Equation 14-30, pp. 759
25	Design factor	n_d			Assumed 1. For unquantifiable exigencies factor is > 1.
26	Output horsepower at rated torque	H_0		hp	
27	Coefficient of friction	μ_{AGMA}			
28	Worm gearing efficiency	η_{AGMA}	69	%	Budynas and Nisbett (2011), Equation 15-54, pp. 813
29	Tangential force on wheel tooth at rated torque	W_G^t		lb	
30	Wheel bending stress at rated torque T_R	σ_a	480	N/mm²	Budynas and Nisbett (2011), Equation 15-53, pp. 812
31	Elastic coefficient	C_p		lb/in ²	Budynas and Nisbett (2011), Table 14-8, pp. 757
32	Surface condition factor	C_f			Assumed 1. For detrimental surface finish factor is > 1.
33	Geometry factor for pitting resistance	I			Budynas and Nisbett (2011), Equation 14-23, pp. 755
34	Wheel contact stress at through-travel torque T_2	σ_c	487	N/mm²	Budynas and Nisbett (2011), Equation 14-16, pp. 746
35	Materials factor	C_s			
36	Ratio correction factor	C_m			
37	Velocity factor	C_v			
38	Allowable tangential force on wheel tooth	$W_G^{t,all}$		lb	
39	Allowable wheel torque based on 25000 hours life	$T_{G,all}$	119	Nm	Budynas and Nisbett (2011), Equation 15-31, pp. 810
40					
41					
42					
43					

Gearset 3

A PD ISO/TR 14521 (British Standards Institution, 2011)					G BS 721 (British Standards Institution, 1983)					
1	Parameter	Symbol	Value	Unit	Notes	Parameter	Symbol	Value	Unit	Notes
3	Normal pressure angle	α_n		deg		Speed factor for wear on worm	$X_{c,1}$			Per BS721, Figure 7
4	Centre distance	c		mm		Speed factor for wear on wheel	$X_{c,2}$			Per BS721, Figure 7
5	Gear ratio	U				Surface stress factor on worm	$\sigma_{cm,1}$			Per BS721, Table 7
6	Number of starts on worm	z_1				Surface stress factor on wheel	$\sigma_{cm,2}$			Per BS721, Table 7
7	Number of teeth on wheel	z_2				Zone factor	Z			Per BS721, Table 6
8	Diameter factor	q_1				Permissible wheel torque for wear (a)	M_{wa}	244.96	Nm	
9	Worm lead angle	Y_{m1}		deg		Permissible wheel torque for wear (b)	M_{wb}	150.63	Nm	
10	Max addendum modification coefficient	$x_{2,max}$			Per BS721, Figure 5	Permissible wheel torque for wear based on 26000 hr life	M_{wear}	150.63	Nm	Lowest of the two values M_{wa} and M_{wb}
11	Min addendum modification coefficient	$x_{2,min}$			Per BS721, Figure 6	Speed factor for strength on worm	$X_{b,1}$			Per BS721, Figure 8
12	Maximum axial module	m_{max}		mm		Speed factor for strength on wheel	$X_{b,2}$			Per BS721, Figure 8
13	Minimum axial module	m_{min}		mm		Bending stress factor on worm	$\sigma_{bm,1}$			Per BS721, Table 7
14	Axial module	m_{x1}		mm		Bending stress factor on wheel	$\sigma_{bm,2}$			Per BS721, Table 7
15	Axial pitch	p_{x1}		mm		Worm tooth reference addendum in axial section	h_{am1}		mm	
16	Worm reference diameter	d_{m1}		mm		Worm tip diameter	d_{a1}		mm	
17	Wheel reference diameter	d_{m2}		mm		Maximum clearance	c_{max}		mm	
18	Worm speed	n_1		RPM		Wheel effective face width	b_e		mm	
19	Wheel speed	n_2		RPM		Length of root of wheel teeth	$l_{f,2}$		mm	
20	Sliding velocity at worm reference diameter	v_g		m/s		Permissible wheel torque for strength (a)	M_{sa}	519.65	Nm	
21	Size factor	Y_S				Permissible wheel torque for strength (b)	M_{sb}	193.07	Nm	
22	Profile shift coefficient	x_2				Permissible wheel torque for strength based on 26000 hr life	$M_{strength}$	193.07	Nm	Lowest of the two values M_{sa} and M_{sb}
23	Kinematic viscosity at 40°C	ν_{40}		mm ² /s	Per lubricant data	Permissible wheel torque based on 26,000 hours life	M_{26k}	151	Nm	Lowest of the two values M_{wear} and $M_{strength}$
24	Kinematic viscosity at 100°C	ν_{100}		mm ² /s	Per lubricant data	Total equivalent running time for wear (500,000 cycles)	H_{ec}	86.81	hr	Based on 500,000 cycles wear life
25	Coefficient for kinematic viscosity	A				Permissible wheel torque for wear based on 500,000 cycles	M_w	440	Nm	Based on 500,000 cycles wear life
26	Coefficient for kinematic viscosity	B				Total equivalent running time for strength	H_{eb}	8.68	hr	Based on 1/10 of H_{ec}
27	Mean lubricant film thickness parameter	h^*				Permissible wheel torque for strength	M_s	385	Nm	
28	Geometry factor	Y_G				Safety factor at rated torque based on strength	$FoS_{strength}$	1.05		
29	Material factor	Y_W			Per PD ISO/TR 14521, Table 6	Safety factor at 1/3 rated torque based on wear	FoS_{wear}	3.60		
30	Arithmetic mean roughness	Ra_1		µm						
31	Roughness factor	Y_R								
32	Coefficient of friction	μ			In mineral oil					
33	Mean tooth coefficient of friction	μ_{zm}								
34	Worm gearing efficiency	η_{z1-2}	73	%						
35	Rated torque of valve actuator	T_R		Nm						
36	Wheel through-travel output torque	T_2		Nm	Based on 1/3 of T_R					
37	Meshing power loss	P_{Vz1-2}		W						
38	Idle running power loss	P_{V0}		W						
39	Output power from wheel shaft	P_2		W						
40	Bearing power loss	P_{VLP}		W						
41	Sealing power loss	P_{VD}		W						
42	Total power loss	P_V		W						
43	Total efficiency of system	η_{ges1-2}	68	%						

	M	N	O	P	Q
1	AGMA 6034-B92 (American Gear Manufacturers Association, 1992; Budynas and Nisbett, 2011)				
2	Parameter	Symbol	Value	Unit	Notes
3	Transverse pressure angle	ϕ_t		deg	
4	Wheel pitch diameter	d_G		inch	
5	Wheel pitch line velocity	V_G		ft/min	
6	Sliding velocity	V_S		ft/min	Budynas and Nisbett (2011), Equation 15-30, pp. 810
7	Wheel face width	F		inch	
8	Wheel effective face width	F_e		inch	
9	Lewis form factor	y			Budynas and Nisbett (2011), pp. 812, for $\alpha_n = 20^\circ$
10	Transverse diametral pitch of wheel	P_d		teeth/inch	
11	Normal diametral pitch of wheel	P_n		teeth/inch	
12	Normal circular pitch of wheel	p_n		inch	
13	Size factor	K_s			Budynas and Nisbett (2011), Section 14-10, pp. 759
14	Application overload factor	K_o			Budynas and Nisbett (2011), Figure 14-17, pp. 766
15	AGMA quality number	Q_v			3-7 for commercial gears, 8-12 for precision quality.
16	Variable A for dynamic factor calculation	A_{Kv}			Budynas and Nisbett (2011), Equation 14-28, pp. 756
17	Variable B for dynamic factor calculation	B_{Kv}			Budynas and Nisbett (2011), Equation 14-28, pp. 756
18	Dynamic factor	K_v			Budynas and Nisbett (2011), Equation 14-27, pp. 756
19	Load correction factor	C_{mc}			Budynas and Nisbett (2011), pp. 760, for crowned teeth.
20	Pinion proportion factor	C_{pf}			Budynas and Nisbett (2011), Equation 14-32, pp. 760
21	Pinion proportion modifier	C_{pm}			Budynas and Nisbett (2011), pp. 760
22	Mesh alignment factor	C_{ma}			Budynas and Nisbett (2011), Equation 14-34, pp. 760
23	Mesh alignment correction factor	C_e			Budynas and Nisbett (2011), pp. 760
24	Load distribution factor	K_m			Budynas and Nisbett (2011), Equation 14-30, pp. 759
25	Design factor	n_d			Assumed 1. For unquantifiable exigencies factor is > 1.
26	Output horsepower at rated torque	H_0		hp	
27	Coefficient of friction	μ_{AGMA}			
28	Worm gearing efficiency	η_{AGMA}	91	%	Budynas and Nisbett (2011), Equation 15-54, pp. 813
29	Tangential force on wheel tooth at rated torque	W_t^r		lb	
30	Wheel bending stress at rated torque T_R	σ_a	402	N/mm²	Budynas and Nisbett (2011), Equation 15-53, pp. 812
31	Elastic coefficient	C_p		lb/in ²	Budynas and Nisbett (2011), Table 14-8, pp. 757
32	Surface condition factor	C_f			Assumed 1. For detrimental surface finish factor is > 1.
33	Geometry factor for pitting resistance	I			Budynas and Nisbett (2011), Equation 14-23, pp. 755
34	Wheel contact stress at rated torque T_R	σ_c	778	N/mm²	Budynas and Nisbett (2011), Equation 14-16, pp. 746
35	Materials factor	C_s			
36	Ratio correction factor	C_m			
37	Velocity factor	C_v			
38	Allowable tangential force on wheel tooth	W_t^{call}		lb	
39	Allowable wheel torque based on 25000 hours life	T_{call}	194	Nm	Budynas and Nisbett (2011), Equation 15-31, pp. 810
40					
41					
42					
43					

Gearset 4

PD ISO/TR 14521 (British Standards Institution, 2011)					BS 721 (British Standards Institution, 1983)				
Parameter	Symbol	Value	Unit	Notes	Parameter	Symbol	Value	Unit	Notes
3 Normal pressure angle	α_n		deg		Speed factor for wear on worm	$X_{c,1}$			Per BS721, Figure 7
4 Centre distance	c		mm		Speed factor for wear on wheel	$X_{c,2}$			Per BS721, Figure 7
5 Gear ratio	U				Surface stress factor on worm	$\sigma_{cm,1}$			Per BS721, Table 7
6 Number of starts on worm	z_1				Surface stress factor on wheel	$\sigma_{cm,2}$			Per BS721, Table 7
7 Number of teeth on wheel	z_2				Zone factor	Z			Per BS721, Table 6
8 Diameter factor	q_1				Permissible wheel torque for wear (a)	M_{wa}	742.17	Nm	
9 Worm lead angle	Y_{m1}		deg		Permissible wheel torque for wear (b)	M_{wb}	556.41	Nm	
10 Max addendum modification coefficient	$x_{2,max}$			Per BS721, Figure 5	Permissible wheel torque for wear based on 26000 hr life	M_{wear}	556.41	Nm	Lowest of the two values M_{wa} and M_{wb}
11 Min addendum modification coefficient	$x_{2,min}$			Per BS721, Figure 6	Speed factor for strength on worm	$X_{b,1}$			Per BS721, Figure 8
12 Maximum axial module	m_{max}		mm		Speed factor for strength on wheel	$X_{b,2}$			Per BS721, Figure 8
13 Minimum axial module	m_{min}		mm		Bending stress factor on worm	$\sigma_{bm,1}$			Per BS721, Table 7
14 Axial module	m_{x1}		mm		Bending stress factor on wheel	$\sigma_{bm,2}$			Per BS721, Table 7
15 Axial pitch	p_{x1}		mm		Worm tooth reference addendum in axial section	h_{am1}		mm	
16 Worm reference diameter	d_{m1}		mm		Worm tip diameter	d_{a1}		mm	
17 Wheel reference diameter	d_{m2}		mm		Maximum clearance	c_{max}		mm	
18 Worm speed	n_1		RPM		Wheel effective face width	b_e		mm	
19 Wheel speed	n_2		RPM		Length of root of wheel teeth	$l_{f,2}$		mm	
20 Sliding velocity at worm reference diameter	v_g		m/s		Permissible wheel torque for strength (a)	M_{sa}	3269.80	Nm	
21 Size factor	Y_S				Permissible wheel torque for strength (b)	M_{sb}	1388.41	Nm	
22 Profile shift coefficient	x_2				Permissible wheel torque for strength based on 26000 hr life	$M_{strength}$	1388.41	Nm	Lowest of the two values M_{sa} and M_{sb}
23 Kinematic viscosity at 40°C	ν_{40}		mm ² /s	Per lubricant data	Permissible wheel torque based on 26,000 hours life	M_{26k}	556	Nm	Lowest of the two values M_{wear} and $M_{strength}$
24 Kinematic viscosity at 100°C	ν_{100}		mm ² /s	Per lubricant data	Total equivalent running time for wear (500,000 cycles)	H_{ec}	231.48	hr	Based on 500,000 cycles wear life
25 Coefficient for kinematic viscosity	A				Permissible wheel torque for wear based on 500,000 cycles	M_w	1557	Nm	Based on 500,000 cycles wear life
26 Coefficient for kinematic viscosity	B				Total equivalent running time for strength	H_{eb}	23.15	hr	Based on 1/10 of H_{ec}
27 Mean lubricant film thickness parameter	h^*				Permissible wheel torque for strength	M_s	2743	Nm	
28 Geometry factor	Y_G				Safety factor at rated torque based on strength	$FoS_{strength}$	3.24		
29 Material factor	Y_W			Per PD ISO/TR 14521, Table 6	Safety factor at 1/3 rated torque based on wear	FoS_{wear}	5.52		
30 Arithmetic mean roughness	Ra_1		µm						
31 Roughness factor	Y_R								
32 Coefficient of friction	μ			In mineral oil					
33 Mean tooth coefficient of friction	μ_{zm}								
34 Worm gearing efficiency	η_{z1-2}	66	%						
35 Rated torque of valve actuator	T_R		Nm						
36 Wheel through-travel output torque	T_2		Nm	Based on 1/3 of T_R					
37 Meshing power loss	P_{Vz1-2}		W						
38 Idle running power loss	P_{V0}		W						
39 Output power from wheel shaft	P_2		W						
40 Bearing power loss	P_{VLP}		W						
41 Sealing power loss	P_{VD}		W						
42 Total power loss	P_V		W						
43 Total efficiency of system	η_{ges1-2}	58	%						

	M	N	O	P	Q
1	AGMA 6034-B92 (American Gear Manufacturers Association, 1992; Budynas and Nisbett, 2011)				
2	Parameter	Symbol	Value	Unit	Notes
3	Transverse pressure angle	ϕ_t		deg	
4	Wheel pitch diameter	d_G		inch	
5	Wheel pitch line velocity	V_G		ft/min	
6	Sliding velocity	V_S		ft/min	Budynas and Nisbett (2011), Equation 15-30, pp. 810
7	Wheel face width	F		inch	
8	Wheel effective face width	F_e		inch	
9	Lewis form factor	y			Budynas and Nisbett (2011), pp. 812, for $\alpha_n = 20^\circ$
10	Transverse diametral pitch of wheel	P_d		teeth/inch	
11	Normal diametral pitch of wheel	P_n		teeth/inch	
12	Normal circular pitch of wheel	p_n		inch	
13	Size factor	K_s			Budynas and Nisbett (2011), Section 14-10, pp. 759
14	Application overload factor	K_o			Budynas and Nisbett (2011), Figure 14-17, pp. 766
15	AGMA quality number	Q_v			3-7 for commercial gears, 8-12 for precision quality.
16	Variable A for dynamic factor calculation	A_{Kv}			Budynas and Nisbett (2011), Equation 14-28, pp. 756
17	Variable B for dynamic factor calculation	B_{Kv}			Budynas and Nisbett (2011), Equation 14-28, pp. 756
18	Dynamic factor	K_v		ft/min	Budynas and Nisbett (2011), Equation 14-27, pp. 756
19	Load correction factor	C_{mc}			Budynas and Nisbett (2011), pp. 760, for crowned teeth.
20	Pinion proportion factor	C_{pf}			Budynas and Nisbett (2011), Equation 14-32, pp. 760
21	Pinion proportion modifier	C_{pm}			Budynas and Nisbett (2011), pp. 760
22	Mesh alignment factor	C_{ma}			Budynas and Nisbett (2011), Equation 14-34, pp. 760
23	Mesh alignment correction factor	C_e			Budynas and Nisbett (2011), pp. 760
24	Load distribution factor	K_m			Budynas and Nisbett (2011), Equation 14-30, pp. 759
25	Design factor	n_d			Assumed 1. For unquantifiable exigencies factor is > 1.
26	Output horsepower at rated torque	H_0		hp	
27	Coefficient of friction	μ_{AGMA}			
28	Worm gearing efficiency	η_{AGMA}	82	%	Budynas and Nisbett (2011), Equation 15-54, pp. 813
29	Tangential force on wheel tooth at rated torque	W_t^r		lb	
30	Wheel bending stress at rated torque T_R	σ_a	356	N/mm²	Budynas and Nisbett (2011), Equation 15-53, pp. 812
31	Elastic coefficient	C_p		lb/in ²	Budynas and Nisbett (2011), Table 14-8, pp. 757
32	Surface condition factor	C_f			Assumed 1. For detrimental surface finish factor is > 1.
33	Geometry factor for pitting resistance	I			Budynas and Nisbett (2011), Equation 14-23, pp. 755
34	Wheel contact stress at through-travel torque T_2	σ_c	534	N/mm²	Budynas and Nisbett (2011), Equation 14-16, pp. 746
35	Materials factor	C_s			
36	Ratio correction factor	C_m			
37	Velocity factor	C_v			
38	Allowable tangential force on wheel tooth	W_t^{call}		lb	
39	Allowable wheel torque based on 25000 hours life	T_{call}	517	Nm	Budynas and Nisbett (2011), Equation 15-31, pp. 810
40					
41					
42					
43					

APPENDIX C: THEORETICAL CALCULATIONS OF WORM GEARSETS

Cell	Formula	Unit
C7	$z_2 = Uz_1$	
C9	$\gamma_{m1} = \tan^{-1}\left(\frac{z_1}{q_1}\right)$	degree
C12	$m_{max} = \frac{2c}{z_2 + q_1 - 2x_{2,min}}$	mm
C13	$m_{min} = \frac{2c}{z_2 + q_1 + 2x_{2,max}}$	mm
C15	$p_{x1} = \pi m_{x1}$	mm
C16	$d_{m1} = q_1 m_{x1}$	mm
C17	$d_{m2} = 2c - d_{m1}$	mm
C19	$n_2 = \frac{n_1}{U}$	RPM
C20	$v_g = \frac{d_{m1} n_1}{19098 \cos \gamma_{m1}}$	m/s
C21	$Y_S = \left(\frac{100}{c}\right)^{0.5}$	
C22	$x_2 = \frac{2c - d_{m1} - (m_{x1} z_2)}{2m_{x1}}$	
C25	$A = \frac{\log\left(\frac{\log(v_{40} + 0.7)}{\log(v_{100} + 0.7)}\right)}{\log\left(\frac{313}{373}\right)}$	
C26	$B = \log(\log(v_{40} + 0.7)) - A \log(313)$	
C27	$h^* = -0.393 + 2.9157 \cdot 10^{-6} z_2^{-0.0847}$ $\cdot \alpha_n^{0.0595} (7.947 \cdot 10^{-7} x_2 + 5.927 \cdot 10^{-5})$ $\cdot (q_1 (1 - 0.038 q_1) + 65.576)$ $\cdot \left(\left(\frac{108.8547 z_1}{q_1} - 1 \right) \left(\frac{z_1}{q_1} \right) - 3294.921 \right)$ $\cdot \left((3.291 \cdot 10^{-3} B + 1) B - 13064.58 \right)$	
C28	$Y_G = \left(\frac{0.07}{h^*}\right)^{0.5}$	
C31	$Y_R = \left(\frac{Ra_1}{0.5}\right)^{0.25}$	
C32	$\mu = 0.033 + \left(\frac{0.079}{(v_g + 0.2)^{1.55}}\right)$	
C33	$\mu_{zm} = \mu Y_S Y_G Y_W Y_R$	

APPENDIX C: THEORETICAL CALCULATIONS OF WORM GEARSETS

Cell	Formula	Unit
C34	$\eta_{z1-2} = \left(\frac{\tan \gamma_{m1}}{\tan(\gamma_{m1} + \tan^{-1} \mu_{zm})} \right) 100$	%
C36	$T_2 = \frac{T_R}{3}$	Nm
C37	$P_{Vz1-2} = \left(\frac{0.1T_2n_1}{U} \right) \left(\left(\frac{100}{\eta_{z1-2}} \right) - 1 \right)$	W
C38	$P_{V0} = 0.89 \cdot 10^{-4} cn_1^{(4/3)}$	W
C39	$P_2 = \frac{2\pi n_2 T_2}{60}$	W
C40	$P_{VLP} = \frac{0.03P_2 c^{0.44} U}{d_{m2}}$	W
C41	$P_{VD} = 11.78 \cdot 10^{-6} d_{m1}^2 n_1$	W
C42	$P_V = P_{Vz1-2} + P_{V0} + P_{VLP} + P_{VD}$	W
C43	$\eta_{ges1-2} = \frac{100P_2}{P_2 + P_V}$	%
I8	$M_{wa} = 0.00191 X_{c,1} \sigma_{cm,1} Z d_{m1}^{1.8} m_{x1}$	Nm
I9	$M_{wb} = 0.00191 X_{c,2} \sigma_{cm,2} Z d_{m2}^{1.8} m_{x1}$	Nm
I10	$M_{wear} = \min(M_{wa}, M_{wb})$	Nm
I15	$h_{am1} = m_{x1}$	mm
I16	$d_{a1} = d_{m1} + 2h_{am1}$	mm
I17	$c_{max} = 0.25m_{x1} \cos \gamma_{m1}$	mm
I18	$b_e = 2m_{x1}(1 + q_1)^{0.5}$	mm
I19	$l_{f,2} = (d_{a1} + 2c_{max}) \sin \left(\frac{b_e}{d_{a1} + 2c_{max}} \right)$	mm
I20	$M_{sa} = 0.0018 X_{b,1} \sigma_{bm,1} m_{x1} l_{f,2} d_{m2} \cos \gamma_{m1}$	Nm
I21	$M_{sb} = 0.0018 X_{b,2} \sigma_{bm,2} m_{x1} l_{f,2} d_{m2} \cos \gamma_{m1}$	Nm
I22	$M_{strength} = \min(M_{sa}, M_{sb})$	Nm
I23	$M_{26k} = \min(M_{wear}, M_{strength})$	Nm
I24	$H_{ec} = \frac{500000}{60n_2}$	hours
I25	$M_w = M_{wear} \left(\frac{27000}{1000 + H_{ec}} \right)^{(1/3)}$	Nm
I26	$H_{eb} = \frac{H_{ec}}{10}$	hours

APPENDIX C: THEORETICAL CALCULATIONS OF WORM GEARSETS

Cell	Formula	Unit
I27	$M_s = M_{strength} \left(\frac{26200}{200 + H_{eb}} \right)^{(1/7)}$	Nm
I28	$FOS_{strength} = \frac{M_s}{T_R}$	
I29	$FOS_{wear} = \frac{M_w}{T_2}$	
O3	$\varphi_t = \tan^{-1} \left(\frac{\tan \alpha_n}{\gamma_{m1}} \right)$	degree
O4	$d_G = z_2 \left(\frac{m_{x1}}{25.4} \right)$	inch
O5	$V_G = \frac{\pi d_G n_2}{12}$	ft/min
O6	$V_s = \frac{\pi n_1 \left(\frac{d_{m1}}{25.4} \right)}{12 \cos \gamma_{m1}}$	ft/min
O8	$F_e = \begin{cases} F & \text{if } F \leq 0.67d_{m1}/25.4 \\ 0.67d_{m1}/25.4 & \text{if } F > 0.67d_{m1}/25.4 \end{cases}$	inch
O10	$P_d = \frac{z_2}{d_G}$	teeth/ inch
O11	$P_n = \frac{P_d \tan \varphi_t}{\tan \alpha_n}$	teeth/ inch
O12	$p_n = \frac{\pi}{P_n}$	inch
O13	$K_s = 1.192 \left(\frac{F \sqrt{y}}{P_d} \right)^{0.0535}$	
O16	$A_{Kv} = 50 + 56(1 - B_{Kv})$	
O17	$B_{Kv} = 0.25(12 - Q_v)^{2/3}$	
O18	$K_v = \left(\frac{A_{Kv} + \sqrt{V_G}}{A_{Kv}} \right)^{B_{Kv}}$	ft/min
O20	$C_{pf} = \begin{cases} \frac{F}{10d_G} - 0.025 & \text{if } F \leq 1 \text{ in} \\ \frac{F}{10d_G} - 0.0375 + 0.0125F & \text{if } 1 < F \leq 17 \text{ in} \\ \frac{F}{10d_G} - 0.1109 + 0.0207F - 0.000228F^2 & \text{if } 17 < F \leq 40 \text{ in} \end{cases}$	
O22	$C_{ma} = 0.0675 + 0.0128F - 0.0000926F^2$	
O24	$K_m = 1 + C_{mc}(C_{pf}C_{pm} + C_{ma}C_e)$	

APPENDIX C: THEORETICAL CALCULATIONS OF WORM GEARSETS

Cell	Formula	Unit
O26	$H_0 = \frac{0.7375T_R n_2}{5252}$	hp
O27	$\mu_{AGMA} = \begin{cases} 0.15 & \text{if } V_S = 0 \\ 0.124 \exp(-0.074V_S^{0.645}) & \text{if } 0 < V_S \leq 10 \text{ ft/min} \\ 0.103 \exp(-0.110V_S^{0.450}) + 0.012 & \text{if } V_S > 10 \text{ ft/min} \end{cases}$	
O28	$\eta_{AGMA} = \left(\frac{\cos \alpha_n - \mu_{AGMA} \tan \gamma_{m1}}{\cos \alpha_n + \mu_{AGMA} \cot \gamma_{m1}} \right) 100$	%
O29	$W_G^t = \left(\frac{33000n_d H_0 K_o}{V_G \eta_{AGMA}} \right) 100$	lb
O30	$\sigma_a = \frac{W_G^t}{145.0377 p_n F y}$	N/mm ²
O33	$I = \left(\frac{\cos \alpha_n \sin \alpha_n}{2} \right) \left(\frac{U}{U+1} \right)$	
O34	$\sigma_c = 0.00689 C_p \sqrt{W_G^t K_o K_v K_s \frac{K_m C_f}{d_G F I}}$	N/mm ²
O35	$C_s = \begin{cases} 1000 & \text{if } F \leq 0.67d_{m1}/25.4 \\ 1251 - 180 \log d_G & \text{if } F > 0.67d_{m1}/25.4 \end{cases}$	
O36	$C_m = \begin{cases} 0.02(-U^2 + 40U - 76)^{0.5} + 0.46 & \text{if } 3 < U \leq 20 \\ 0.0107(-U^2 + 56U + 5145)^{0.5} & \text{if } 20 < U \leq 76 \\ 1.1483 - 0.00658U & \text{if } U > 76 \end{cases}$	
O37	$C_v = \begin{cases} 0.659 \exp(-0.0011) & \text{if } V_S < 700 \text{ ft/min} \\ 13.31V_S^{-0.571} & \text{if } 700 \leq V_S < 3000 \text{ ft/min} \\ 65.52V_S^{-0.774} & \text{if } V_S > 3000 \text{ ft/min} \end{cases}$	
O38	$W_{G,all}^t = C_s d_G^{0.8} F_e C_m C_v$	lb
O39	$T_{G,all} = \left(\frac{W_{G,all}^t d_G}{2} \right) 0.11$	Nm

Appendix D: Abaqus® Friction Subroutine for Chapter 5

```
SUBROUTINE FRIC(LM,TAU,DDTDDG,DDTDDP,DSLIP,SED,SFD,
1 DDTDDT,PNEWDT,STATEV,DGAM,TAULM,PRESS,DPRESS,DDPDDH,SLIP,
2 KSTEP,KINC,TIME,DTIME,NOEL,CINAME,SLNAME,MSNAME,NPT,NODE,
3 NPATCH,COORDS,RCOORD,DROT,TEMP,PREDEF,NFDIR,MCRD,NPRED,
4 NSTATV,CHRLNGTH,PROPS,NPROPS)
C
C   INCLUDE 'ABA_PARAM.INC'
C   The INCLUDE statement includes source from another file.
C
C   CHARACTER*80 CINAME,SLNAME,MSNAME
C   The CHARACTER statement is used when the data being manipulated is
C   in the form of characters and words rather than numbers. This
C   CHARACTER statement declares 3 variables which can each contain 80
C   characters.
C   CINAME = User-specified surface interaction name associated with
C           the friction definition.
C   SLNAME = Slave surface name
C   MSNAME = Master surface name
C
C   DIMENSION TAU(NFDIR),DDTDDG(NFDIR,NFDIR),DDTDDP(NFDIR),
1 DSLIP(NFDIR),DDTDDT(NFDIR,2),STATEV(*),DGAM(NFDIR),
2 TAULM(NFDIR),SLIP(NFDIR),TIME(2),COORDS(MCRD),
3 RCOORD(MCRD),DROT(2,2),TEMP(2),PREDEF(2,*),PROPS(NPROPS)
C   The DIMENSION statement specifies the number of dimensions for an
C   array, including the number of elements in each dimension
C
C   user coding to define LM, TAU, DDTDDG, DDTDDP,
C   and, optionally, DSLIP, SED, SFD, DDTDDT, PNEWDT, STATEV
C
C   PARAMETER(ZERO=0.0D0,ONE=1.0D0,PRECIS=1.D-14,XKS=1.D6)
C   The PARAMETER statement specifies named constants.
C   Double-precision floating-point format is a computer number format
C   that occupies 8 bytes (64 bits) in computer memory and represents
C   a wide, dynamic range of values by using a floating point.
C
C   IMPLEMENTATION OF DAHL FRICTION
C
C   Variables used:
C   DS           = Change in elastic slip during current increment
C   S1           = Elastic slip at end of current increment
C   GAMMA1      = Total slip in direction X
C   GAMMA2      = Total slip in direction Y
C   DGAM(1)     = Increment of sliding motion in direction X
C   DGAM(2)     = Increment of sliding motion in direction Y
C   STIFF       = Contact stiffness
C   TAUCRIT     = Critical frictional stress
C   XMU         = PROPS(1)      !Coefficient of friction
C   XI          = PROPS(2)      !Dahl friction shape parameter
C   SMAX        = PROPS(3)      !Max allowable elastic slip
C   ETA         = PROPS(4)      !Transverse vibration transfer coefficient
C   THETA       = PROPS(5)      !Angle describing the vibration mode
C   VIBSTART    = PROPS(6)      !Time at which vibration is initiated
C   F           = PROPS(7)      !Vibration frequency in Hertz
C   VA         = PROPS(8)      !Amplitude of the velocity of vibration
C
C   IF (LM .EQ. 2) THEN
C   If LM = 2 frictionless sliding is assumed
C   If LM = 1 no relative motion is allowed (rigid sticking condition
C           at the interface)
```

```

C      If LM = 0 relative motion is allowed
C      Gap is opened at start of the current increment. Frictionless
C      sliding is assumed. In this case no further variables need to be
C      updated.
C
C      IF (XMU .LE. PRECIS) RETURN
C      END IF
C
C      LM = 0
C      Relative motion is allowed (either due to slip or elastic stick).
C      In this case the subroutine must specify the frictional stress TAU
C      (in 2 directions for 3D analysis) as a function of:
C      -the relative sliding motion (slip rate dependant data),
C      -the interface contact pressure (contact pressure dependant data),
C      and other predefined or user-defined state variables. In addition,
C      the subroutine must define the derivatives of TAU with respect to
C      relative sliding motion and interface contact pressure.
C
C      CHECK IF PRESSURE IS NON-POSITIVE
C      IF (PRESS .LE. ZERO) THEN
C          STATEV(1) = ZERO
C          GAMMA = DGAM(1)
C      If pressure is less than zero then there is no elastic slip, and
C      total slip is equal to the increment of sliding motion in the
C      current time increment.
C          IF (XMU .LE. PRECIS) THEN
C              DDTDDG(1,1) = ZERO
C              DDTDDP(1) = XMU*GAMMA/GCRIT
C          ELSE
C              DDTDDG(1,1) = XKS
C              DDTDDP(1) = ZERO
C          END IF
C          TAU(1) = ZERO
C          DSLIP(1) = ZERO
C          RETURN
C      ELSE
C      If pressure is not less than zero then there is elastic slip
C      COMPUTE FOR CRITICAL STRESS AND ARTIFICIAL STIFFNESS
C          TAUCRIT = XMU*PRESS
C          STIFF = TAUCRIT/SMAX
C      END IF
C
C      COMPUTE FOR THE TOTAL SLIP AND FRICTIONAL SHEAR STRESS
C      PI = ACOS(-ONE)
C      IF (TIME(2) .GE. VIBSTART) THEN
C          YB = (SIN(THETA*PI/180))*((VA/(2*PI*F))*SIN(2*PI*F*TIME(2)))
C      ELSE
C          YB = 0
C      END IF
C      DYB = YB-STATEV(6)
C
C      GAMMA1 = STATEV(2)+DGAM(1)
C      GAMMA2 = STATEV(4)+DGAM(2)+DYB
C
C      AMNA1 = SQRT(((GAMMA1-STATEV(3))**2)+((STATEV(5)-GAMMA2)**2))
C      VR1 = (AMNA1-ABS(STATEV(1)))/DTIME
C      DS = VR1*((1-(STIFF*ABS(STATEV(1))*SIGN(ONE,VR1)/TAUCRIT)**
1      XI)*DTIME
C      SA = ABS(STATEV(1))+DS
C
C      IF (TIME(2) .GT. VIBSTART) THEN
C          COSA = (GAMMA1-STATEV(3))/AMNA1
C          SINA = (STATEV(5)-GAMMA2)/AMNA1
C      ELSE

```

```

        COSA = ONE
        SINA = ZERO
    END IF
C
ANA1MA2 = SQRT(((SA*COSA)**2)+(((SA*SINA)+(DYB*ETA))**2))
VR2      = (ANA1MA2-SA)/DTIME
DSA      = VR2*((1-(STIFF*SA*SIGN(ONE,VR2)/TAUCRIT))**XI)*DTIME
S1       = SA+DSA
C
    IF (TIME(2) .GT. VIBSTART) THEN
        COSB = (SA*COSA)/ANA1MA2
        SINB = ((SA*SINA)+(DYB*ETA))/ANA1MA2
    ELSE
        COSB = ONE
        SINB = ZERO
    END IF
C
    TAU(1) = STIFF*S1*COSB
    TAU(2) = STIFF*S1*SINB
C
    STATEV(1) = S1
    STATEV(2) = GAMMA1
    STATEV(3) = GAMMA1-(S1*COSB)
    STATEV(4) = GAMMA2
    STATEV(5) = GAMMA2+(S1*SINB)
    STATEV(6) = YB
C
    WRITE(06,*) "NODE:",NODE,"TIME:",TIME
C
    RETURN
    END

```


Appendix E: Abaqus[®] Friction Subroutine for Chapter 7

```

SUBROUTINE FRIC(LM,TAU,DDTDDG,DDTDDP,DSLIP,SED,SFD,
1 DDTDDT,PNEWDT,STATEV,DGAM,TAULM,PRESS,DPRESS,DDPDDH,SLIP,
2 KSTEP,KINC,TIME,DTIME,NOEL,CINAME,SLNAME,MSNAME,NPT,NODE,
3 NPATCH,COORDS,RCOORD,DROT,TEMP,PREDEF,NFDIR,MCRD,NPRED,
4 NSTATV,CHRLNGTH,PROPS,NPROPS)
C
C   INCLUDE 'ABA_PARAM.INC'
C   The INCLUDE statement includes source from another file.
C
C   CHARACTER*80 CINAME,SLNAME,MSNAME
C   The CHARACTER statement is used when the data being manipulated is
C   in the form of characters and words rather than numbers. This
C   CHARACTER statement declares 3 variables which can each contain 80
C   characters.
C   CINAME = User-specified surface interaction name associated with
C           the friction definition.
C   SLNAME = Slave surface name
C   MSNAME = Master surface name
C
C   DIMENSION TAU(NFDIR),DDTDDG(NFDIR,NFDIR),DDTDDP(NFDIR),
1 DSLIP(NFDIR),DDTDDT(NFDIR,2),STATEV(*),DGAM(NFDIR),
2 TAULM(NFDIR),SLIP(NFDIR),TIME(2),COORDS(MCRD),
3 RCOORD(MCRD),DROT(2,2),TEMP(2),PREDEF(2,*),PROPS(NPROPS)
C   The DIMENSION statement specifies the number of dimensions for an
C   array, including the number of elements in each dimension
C
C   user coding to define LM, TAU, DDTDDG, DDTDDP,
C   and, optionally, DSLIP, SED, SFD, DDTDDT, PNEWDT, STATEV
C
C   DIMENSION GAMMA(2)
C
C   PARAMETER(ZERO=0.0D0,ONE=1.0D0,ASMALL=1.0D-27,PRECIS=1.D-14,
1 XKS=1.D6)
C   The PARAMETER statement specifies named constants.
C   Double-precision floating-point format is a computer number format
C   that occupies 8 bytes (64 bits) in computer memory and represents
C   a wide, dynamic range of values by using a floating point.
C
C   IMPLEMENTATION OF DAHL FRICTION
C
C   Variables used:
C   XMU      = Coefficient of friction
C   I        = Shape parameter
C   SMAX     = Critical elastic slip
C   DS       = Change in elastic slip during current increment

```

Change: Line added.

Change: ASMALL definition added.

```

C      S1          = Elastic slip at end of current increment
C      GAMMA       = Total slip
C      STIFF       = Contact stiffness
C      TAUCRIT    = Critical frictional stress
C
C      XMU         = PROPS(1)
C      XI          = PROPS(2)
C      SMAX       = PROPS(3)
!      ETA        = PROPS(4)
!      THETA      = PROPS(5)
!      VIBSTART   = PROPS(6)
!      F          = PROPS(7)
!      VA        = PROPS(8)
C
C      IF (LM .EQ. 2) THEN
C      If LM = 2 frictionless sliding is assumed
C      If LM = 1 no relative motion is allowed (rigid sticking condition
C      at the interface)
C      If LM = 0 relative motion is allowed
C      Gap is opened at start of the current increment. Frictionless
C      sliding is assumed. In this case no further variables need to be
C      updated.
C
C      IF (XMU .LE. PRECIS) RETURN
C      END IF
C
C      LM = 0
C      Relative motion is allowed (either due to slip or elastic stick).
C      In this case the subroutine must specify the frictional stress TAU
C      (in 2 directions for 3D analysis) as a function of:
C      -the relative sliding motion (slip rate dependant data),
C      -the interface contact pressure (contact pressure dependant data),
C      and other predefined or user-defined state variables. In addition,
C      the subroutine must define the derivatives of TAU with respect to
C      relative sliding motion and interface contact pressure.
C
C      CHECK IF PRESSURE IS NON-POSITIVE
C      IF (PRESS .LE. ZERO) THEN
C      STATEV(1) = ZERO
C      STATEV(2) = ZERO
C      GAMMA(1) = DGAM(1)
C      GAMMA(2) = DGAM(2)
C      If pressure is less than zero then there is no elastic slip, and
C      total slip is equal to the increment of sliding motion in the
C      current time increment.
C      IF (XMU .LE. PRECIS) THEN
C      DDTDDG(1,1) = ZERO
C      DDTDDG(1,2) = ZERO
C      DDTDDG(2,1) = ZERO
C      DDTDDG(2,2) = ZERO
C      DDTDDP(1) = XMU*GAMMA(1)/SMAX

```

Change: Variable no longer used, removed from formulation.
Change: Variable no longer used, removed from formulation.
Change: Variable no longer used, removed from formulation.
Change: Variable no longer used, removed from formulation.

Change: Line added.
Change: Line added.

Change: Line added.
Change: Line added.
Change: Line added.
Change: Modified formulation.

```

        DDTDDP(2) = XMU*GAMMA(2)/SMAX
ELSE
        DDTDDG(1,1) = XKS
        DDTDDG(1,2) = ZERO
        DDTDDG(2,1) = ZERO
        DDTDDG(2,2) = XKS
        DDTDDP(1) = ZERO
        DDTDDP(2) = ZERO
END IF
TAU(1) = ZERO
TAU(2) = ZERO
DSLIP(1) = ZERO
DSLIP(2) = ZERO
RETURN
ELSE
C   If pressure is not less than zero then there is elastic slip
C   COMPUTE FOR CRITICAL STRESS AND ARTIFICIAL STIFFNESS
        TAUCRIT = XMU*PRESS
        STIFF = TAUCRIT/SMAX
END IF
C
C   COMPUTE FOR THE TOTAL SLIP AND FRICTIONAL SHEAR STRESS
!   PI = ACOS(-ONE)
!   IF (TIME(2) .GE. VIBSTART) THEN
!       YB = (SIN(THETA*PI/180))*((VA/(2*PI*F))*SIN(2*PI*F*TIME(2)))
!   ELSE
!       YB = 0
!   END IF
!   DYB = YB-STATEV(6)
C
GAMMA(1) = STATEV(1)+DGAM(1)
GAMMA(2) = STATEV(2)+DGAM(2)!+DYB
C
AMNAA = SQRT(((GAMMA(1)-STATEV(3))**2)+((STATEV(2)-STATEV(4))**2
1))
DDAMNAADDG1 = (GAMMA(1)-STATEV(3))/AMNAA
DDAMNAADDG2 = ZERO
DDAMNAADDP = ZERO
VR1 = AMNAA-STATEV(5)
DDVR1DDG1 = DDAMNAADDG1
DDVR1DDG2 = ZERO
DDVR1DDP = ZERO
DS = VR1*((1-(STATEV(5)*SIGN(ONE,VR1)/SMAX))**XI)
1 DSDSDG1 = DDVR1DDG1*((1-(STATEV(5)*SIGN(ONE,VR1)/SMAX))**
XI)
DSDSDG2 = ZERO
DSDSDDP = ZERO
SA = STATEV(5)+DS
DDSADDG1 = DSDSDG1
DDSADDG2 = ZERO
DDSADDP = ZERO

```

Change: Line added.

Change: Line added.
Change: Line added.
Change: Line added.

Change: Line added.

Change: Line added.

Change: No longer used, removed from formulation.
Change: No longer used, removed from formulation.
Change: No longer used, removed from formulation.
Change: No longer used, removed from formulation.
Change: No longer used, removed from formulation.
Change: No longer used, removed from formulation.

Change: GAMMA with 1 in brackets to signify dimension 1, now used throughout.
Change: GAMMA with 2 in brackets to signify dimension 2, now used throughout. DYB no longer used.

Change: Modified formulation for vibration applied directly to sliding body.

Change: New line for partial derivative of AMNAA with respect to GAMMA(1).
Change: New line for partial derivative of AMNAA with respect to GAMMA(2).
Change: New line for partial derivative of AMNAA with respect to PRESS.
Change: Modified formulation for vibration applied directly to sliding body.
Change: New line for partial derivative of VR1 with respect to GAMMA(1).
Change: New line for partial derivative of VR1 with respect to GAMMA(2).
Change: New line for partial derivative of VR1 with respect to PRESS.
Change: Modified formulation for vibration applied directly to sliding body.
Change: New line for partial derivative of DS with respect to GAMMA(1).
Change: New line for partial derivative of DS with respect to GAMMA(1).
Change: New line for partial derivative of DS with respect to GAMMA(2).
Change: New line for partial derivative of DS with respect to PRESS.
Change: Modified formulation for vibration applied directly to sliding body.
Change: New line for partial derivative of SA with respect to GAMMA(1).
Change: New line for partial derivative of SA with respect to GAMMA(2).
Change: New line for partial derivative of SA with respect to PRESS.

	DDSA2DDG1 = 2*SA*DDSADDG1		Change: New line for partial derivative of (SA**2) with respect to GAMMA(1).
	DDSA2DDG2 = ZERO		Change: New line for partial derivative of (SA**2) with respect to GAMMA(2).
	DDSA2DDP = ZERO		Change: New line for partial derivative of (SA**2) with respect to PRESS.
C	IF (TIME(2) .GT. VIBSTART) THEN		Change: IF condition not necessary, removed from formulation.
!	COSA = (GAMMA(1)-STATEV(3))/AMNAA		
	DDCOSADDG1 = (AMNAA-((GAMMA(1)-STATEV(3))*DDAMNAADDG1))/		Change: New line for partial derivative of COSA with respect to GAMMA(1).
1	(AMNAA**2)		Change: New line for partial derivative of COSA with respect to GAMMA(1).
	DDCOSADDG2 = ZERO		Change: New line for partial derivative of COSA with respect to GAMMA(2).
	DDCOSADDP = ZERO		Change: New line for partial derivative of COSA with respect to PRESS.
	DDCOSA2DDG1 = (2*(GAMMA(1)-STATEV(3))*((AMNAA**2)-((GAMMA(1)-		Change: New line for partial derivative of (COSA**2) with respect to GAMMA(1).
1	STATEV(3))**2)))/(AMNAA**4)		Change: New line for partial derivative of (COSA**2) with respect to GAMMA(1).
	DDCOSA2DDG2 = ZERO		Change: New line for partial derivative of (COSA**2) with respect to GAMMA(2).
	DDCOSA2DDP = ZERO		Change: New line for partial derivative of (COSA**2) with respect to PRESS.
	SINA = (STATEV(2)-STATEV(4))/AMNAA		Change: Modified formulation for vibration applied directly to sliding body.
	DD SINADDG1 = (ZERO-((STATEV(2)-STATEV(4))*DDAMNAADDG1))/		Change: New line for partial derivative of SINA with respect to GAMMA(1).
1	(AMNAA**2)		Change: New line for partial derivative of SINA with respect to GAMMA(1).
	DD SINADDG2 = ZERO		Change: New line for partial derivative of SINA with respect to GAMMA(2).
	DD SINADDP = ZERO		Change: New line for partial derivative of SINA with respect to PRESS.
	DD SINA2DDG1 = (ZERO-(2*(GAMMA(1)-STATEV(3))*((STATEV(2)-		Change: New line for partial derivative of (SINA**2) with respect to GAMMA(1).
1	STATEV(4))**2)))/(AMNAA**4)		Change: New line for partial derivative of (SINA**2) with respect to GAMMA(1).
	DD SINA2DDG2 = ZERO		Change: New line for partial derivative of (SINA**2) with respect to GAMMA(2).
	DD SINA2DDP = ZERO		Change: New line for partial derivative of (SINA**2) with respect to PRESS.
!	ELSE		Change: ELSE condition removed as IF condition no longer used above.
!	COSA = ONE		Change: ELSE condition removed as IF condition no longer used above.
!	SINA = ZERO		Change: ELSE condition removed as IF condition no longer used above.
!	END IF		Change: END IF removed as IF condition no longer used above.
C	AMANA1 = SQRT(((SA*COSA)**2)+((GAMMA(2)-STATEV(2)+SA*SINA)**2))		Change: Modified formulation for vibration applied directly to sliding body.
	DD SACOSA2DDG1 = (((COSA**2)*DDSA2DDG1)+((SA**2)*DDCOSA2DDG1)		Change: New line for partial derivative of ((SA*COSA)**2) with respect to GAMMA(1).
	DD SASINA2DDG1 = ((SINA**2)*DDSA2DDG1)+((SA**2)*DD SINA2DDG1)		Change: New line for partial derivative of ((SA*SINA)**2) with respect to GAMMA(1).
	DD2G2SASINADDG1 = (SINA*2*(GAMMA(2)*DDSADDG1)+(2*(GAMMA(2)*SA*		Change: New line for partial derivative of (2*(GAMMA(2)*SA*SINA) with respect to GAMMA(1).
1	DD SINADDG1)		Change: New line for partial derivative of (2*(GAMMA(2)*SA*SINA) with respect to GAMMA(1).
	DD2SV2SASINADDG1= (SINA*2*STATEV(2)*DDSADDG1)+(2*STATEV(2)*SA*		Change: New line for partial derivative of (2*STATEV(2)*SA*SINA) with respect to GAMMA(1).
1	DD SINADDG1)		Change: New line for partial derivative of (2*STATEV(2)*SA*SINA) with respect to GAMMA(1).
	DDAMANA1DDG1 = (0.5/AMANA1)*(DD SACOSA2DDG1+DD2G2SASINADDG1-		Change: New line for partial derivative of AMANA1 with respect to GAMMA(1).
1	DD2SV2SASINADDG1+DD SASINA2DDG1)		Change: New line for partial derivative of AMANA1 with respect to GAMMA(1).
	DDAMANA1DDG2 = (0.5/AMANA1)*((2*(GAMMA(2))-(2*STATEV(2)))+(2*		Change: New line for partial derivative of AMANA1 with respect to GAMMA(2).
1	SA*SINA))		Change: New line for partial derivative of AMANA1 with respect to GAMMA(2).
	DDAMANA1DDP = ZERO		Change: New line for partial derivative of AMANA1 with respect to PRESS.
	VR2 = AMANA1-SA		Change: Modified formulation for vibration applied directly to sliding body.
	DDVR2DDG1 = DDAMANA1DDG1-DDSADDG1		Change: New line for partial derivative of VR2 with respect to GAMMA(1).
	DDVR2DDG2 = DDAMANA1DDG2		Change: New line for partial derivative of VR2 with respect to GAMMA(2).
	DDVR2DDP = ZERO		Change: New line for partial derivative of VR2 with respect to PRESS.
	DSA = VR2*(1-(SA*SIGN(ONE,VR2)/SMAX)**XI)		Change: Modified formulation for vibration applied directly to sliding body.
	DD SADDG1 = (((1-(SA*SIGN(ONE,VR2)/SMAX))**XI)*DDVR2DDG1)-		Change: New line for partial derivative of DSA with respect to GAMMA(1).
1	(VR2**XI*((1-(SA*SIGN(ONE,VR2)/SMAX))**XI-1))*		Change: New line for partial derivative of DSA with respect to GAMMA(1).
2	(SIGN(ONE,VR2)/SMAX)*DDSADDG1)		Change: New line for partial derivative of DSA with respect to GAMMA(1).
	DD SADDG2 = ((1-(SA*SIGN(ONE,VR2)/SMAX))**XI)*DDVR2DDG2		Change: New line for partial derivative of DSA with respect to GAMMA(2).
	DD SADDP = ZERO		Change: New line for partial derivative of DSA with respect to PRESS.
	S1 = SA+DSA		

	DDS1DDG1 = DDSADDG1+DDDSADDG1		Change: New line for partial derivative of S1 with respect to GAMMA(1).
	DDS1DDG2 = DDDSADDG2		Change: New line for partial derivative of S1 with respect to GAMMA(2).
	DDS1DDP = ZERO		Change: New line for partial derivative of S1 with respect to PRESS.
C	!		
	IF (TIME(2) .GT. VIBSTART) THEN		Change: IF condition not necessary, removed from formulation.
	COSB = (SA*COSA)/AMANA1		
	DDCOSBDDG1 = ((AMANA1*((COSA*DDSADDG1)+(SA*DDCOSADDG1)))-(SA		Change: New line for partial derivative of COSB with respect to GAMMA(1).
	*COSA*DDAMANA1DDG1))/(AMANA1**2)		Change: New line for partial derivative of COSB with respect to GAMMA(1).
	DDCOSBDDG2 = ZERO-(SA*COSA*DDAMANA1DDG2/(AMANA1**2))		Change: New line for partial derivative of COSB with respect to GAMMA(2).
	DDCOSBDDP = ZERO		Change: New line for partial derivative of COSB with respect to PRESS.
	SINB = (GAMMA(2)-STATEV(2)+SA*SINA)/AMANA1		Change: Improved formulation.
	DDSinBDDG1 = ((AMANA1*((SINA*DDSADDG1)+(SA*DDSinADDG1)))-		Change: New line for partial derivative of SINB with respect to GAMMA(1).
	((GAMMA(2)-STATEV(2)+SA*SINA)*DDAMANA1DDG1))/		Change: New line for partial derivative of SINB with respect to GAMMA(1).
	(AMANA1**2)		Change: New line for partial derivative of SINB with respect to GAMMA(1).
	DDSinBDDG2 = (AMANA1-((GAMMA(2)-STATEV(2)+SA*SINA)*		Change: New line for partial derivative of SINB with respect to GAMMA(2).
	DDAMANA1DDG2))/(AMANA1**2)		Change: New line for partial derivative of SINB with respect to GAMMA(2).
	DDSinBDDP = ZERO		Change: New line for partial derivative of SINB with respect to PRESS.
	!		Change: ELSE condition removed as IF condition no longer used above.
	ELSE		Change: ELSE condition removed as IF condition no longer used above.
	! COSB = ONE		Change: ELSE condition removed as IF condition no longer used above.
	! SINB = ZERO		Change: ELSE condition removed as IF condition no longer used above.
	! END IF		Change: END IF removed as IF condition no longer used above.
C			
	TAU(1) = STIFF*S1*COSB		
	TAU(2) = STIFF*S1*SINB		
	TAUEQV = SQRT(TAU(1)**2 + TAU(2)**2)		Change: Line added.
C			
	CHECK IF THE FRICTIONAL STRESS EXCEEDS THE CRITICAL STRESS		
C	IF (TAUEQV .LT. TAUCRIT) THEN		Change: IF condition added.
C	BEHAVIOR REMAINS ELASTIC		
	DDTDDG(1,1) = STIFF*((COSB*DDS1DDG1)+(S1*DDCOSBDDG1))		Change: New line for partial derivative of TAU(1) with respect to GAMMA(1).
	DDTDDG(1,2) = STIFF*((COSB*DDS1DDG2)+(S1*DDCOSBDDG2))		Change: New line for partial derivative of TAU(1) with respect to GAMMA(2).
	DDTDDG(2,1) = STIFF*((SINB*DDS1DDG1)+(S1*DDSinBDDG1))		Change: New line for partial derivative of TAU(2) with respect to GAMMA(1).
	DDTDDG(2,2) = STIFF*((SINB*DDS1DDG2)+(S1*DDSinBDDG2))		Change: New line for partial derivative of TAU(2) with respect to GAMMA(2).
	DDTDDP(1) = (S1*COSB*XMU/SMAX)		Change: New line for partial derivative of TAU(1) with respect to PRESS.
	DDTDDP(2) = (S1*SINB*XMU/SMAX)		Change: New line for partial derivative of TAU(2) with respect to PRESS.
	STATEV(1) = GAMMA(1)		Change: Modified formulation for vibration applied directly to sliding body.
	STATEV(2) = GAMMA(2)		Change: Modified formulation for vibration applied directly to sliding body.
	STATEV(3) = GAMMA(1)-(S1*COSB)		Change: Modified formulation for vibration applied directly to sliding body.
	STATEV(4) = GAMMA(2)-(S1*SINB)		Change: Modified formulation for vibration applied directly to sliding body.
	STATEV(5) = S1		Change: STATEV(6) no longer necessary, removed from formulation.
	! STATEV(6) = YB		Change: ELSE condition added.
C	ELSE		
	BEHAVIOR IS PLASTIC		
	TAU(1) = TAUCRIT*COSB		Change: TAU(1) definition added for ELSE condition.
	TAU(2) = TAUCRIT*SINB		Change: TAU(2) definition added for ELSE condition.
	DDTDDG(1,1) = TAUCRIT*DDCOSBDDG1		Change: New line for partial derivative of TAU(1) with respect to GAMMA(1).
	DDTDDG(1,2) = TAUCRIT*DDCOSBDDG2		Change: New line for partial derivative of TAU(1) with respect to GAMMA(2).
	DDTDDG(2,1) = TAUCRIT*DDSinBDDG1		Change: New line for partial derivative of TAU(2) with respect to GAMMA(1).
	DDTDDG(2,2) = TAUCRIT*DDSinBDDG2		Change: New line for partial derivative of TAU(2) with respect to GAMMA(2).
	DDTDDP(1) = COSB*XMU		Change: New line for partial derivative of TAU(1) with respect to PRESS.
	DDTDDP(2) = SINB*XMU		Change: New line for partial derivative of TAU(2) with respect to PRESS.

```
STATEV(1) = GAMMA(1)  
STATEV(2) = GAMMA(2)  
ENDIF  
END
```

Change: STATEV(1) definition added for ELSE condition.
Change: STATEV(2) definition added for ELSE condition.
Change: ENDIF added to close out new IF condition.